ADVANCED DAYTIME RADIATIVE COOLING: WORLDWIDE POTENTIAL IN THE BUILT-ENVIRONMENT

Doctoral Thesis

Laura Carlosena

Escuela Técnica Superior de Arquitectura de San Sebastián

Universidad del País Vasco / Euskal Herriko Unibertsitatea UPV/EHU

San Sebastián, April 2021

eman ta zabal zazu

Universidad del País Vasco
Euskal Herriko Unibertsitatea

ADVANCED DAYTIME RADIATIVE COOLING: WORLDWIDE POTENTIAL IN THE BUILT-ENVIRONMENT

Doctoral Thesis

Laura Carlosena

Dissertation presented at the University of the Basque Country (UPV/EHU) in fulfillment of the requirements for the Degree of Doctor of Philosophy in Architecture of the Sustainability and Efficiency in Engineering and Architecture

Supervisors

Rufino J. Hernández Minguillón

Olatz Irulegi Garmendia

Escuela Técnica Superior de Arquitectura de San Sebastián

Universidad del País Vasco / Euskal Herriko Unibertsitatea UPV/EHU

San Sebastián, April 2021

FOREWORD

The present thesis received funding from the Government of Navarra financing plan for Industrial Doctorates "AYUDAS 2017 PARA LA CONTRATACIÓN DE DOCTORANDOS Y DOCTORANDAS POR EMPRESAS Y ORGANISMOS DE INVESTIGACIÓN Y DIFUSIÓN DE CONOCIMIENTOS: "DOCTORADOS INDUSTRIALES 2018-2020" DEL GOBIERNO DE NAVARRA". With the code: 0011-1408-2017-000028. This economical grant has allowed the architecture studio "Alonso Hernández & Asociados Arquitectura, S.L. (AH Asociados) to hire the author to develop her doctoral research. The Thesis field of research, radiative cooling, is a part of an integrated project "CBC". The materials were developed with the grant "AYUDAS A PROYECTOS DE I+D CONVOCATORIA DE 2019 DEL GOBIERNO DE NAVARRA" awarded to AH Asociados, with file number 0011-1365-2019-000051.

The industrial grant allowed the author to conduct two research stays as a "Junior Research Visiting Fellow" at the University of New South Wales (UNSW), in 2018 and 2020, under the supervision of Professor Mattheos Santamouris and a research stay in 2019 at the University of Sevilla under the supervision of Professor Servando Álvarez Domínguez. As a result of the research and the collaboration with UNSW, "On the energy potential of daytime radiative cooling for urban heat island mitigation" was published in Solar Energy. in September 2020. Moreover, an association was made with the nanophotonic research team led by Professor Joaquín Sevilla of the Public University of Navarra who assisted with material optimization.

ACKNOWLEDGEMENTS

I have been highly privileged for the opportunity to spend three years devoted to research, surrounded by colleagues, friends, and family willing to help, listen, and sometimes distract me from my duties. To all of you, I dedicate these lines.

First of all, I would like to thank my supervisors, Olatz, for making sure architecture was present through my research and pushing me towards achieving the goals in due time, and Rufino, for presenting this exciting topic and being open-minded about the Ph.D. direction.

I am very grateful to ah asociados, especially to Miguel Ángel Alonso del Val and Rufino J. Hernández, for accepting to host an industrial doctorate in your architecture studio. To the R+D Department in ah asociados, Luis Torres and María José Alonso, for your support during this period. To my colleagues in ah asociados.

It has been a true honor to work with Mattheos Santamouris, who always has a smile and kind words amidst his busy agenda, for being a rigorous researcher from whom to learn. This Ph.D. has veered into material development and has directed me towards photonics. During these times of despair, I was lucky to meet the right people at the right time. Álvaro Ruiz helped me with his thermodynamics expertise and welcomed me to Sevilla. Enrique Rodríguez, for your support with the thermal simulations and willingness to review the work. Joaquín Sevilla, who had the interest and took the time to listen to my problems and found solutions, for our conversations on radiative cooling and architecture. Ángel Andueza, for always being willing to run “another simulation” and helping me to understand the microscopic interaction of matter. Even though research has many backlashes, Jaione Bengoechea was always there to answer questions and present alternatives.

To the Thesis reviewers, Benoit Beckers, Francesco Fiorito, José Antonio Millán and Gianluca Ranzi, for your valuable time and kind comments. To many others, who have dedicated valuable time to explain, listen and orient me.

To my fellow researchers in Sydney, Chantal Basurto, Jie Feng, and Ioannis Kousis, for sharing great times inside and outside the lab.

To my lifelong friends and new additions, for making everything, including this Ph.D., more bearable, Anna Cases, Carla Davidson, María José Hasta, Mónica Montes, Paula Orio, Lide Plazaola, Juan Carlos Salas and Aimar Santos

To my mother, Malú, for nurturing me throughout this period. To my father, Alfonso, for being a director in the shadow and guiding me towards this surprising endeavor. To my antipode family, my beloved sister Alicia and her always supporting boyfriend Luke. They were kind enough to do anything I needed during both of my stays in Sydney.

Finally, to Guillermo, for your unconditional understanding, support, and love during this challenging period. For always believing I could do anything even if I thought otherwise.

HOW TO READ THIS THESIS

This Thesis studies daytime radiative cooling materials' potential for architecture, as they can reduce the problems associated with the increased cooling demand without adding to the vicious cycle of rejecting heat to the streets. The dissertation is divided into three main parts. Figure 1 summarizes the Thesis's layout with the main topics discussed in each chapter. The various objectives in this Thesis require differentiated methodological approaches. Therefore, to satisfy this requirement while having a systematic discourse, the same outline is used throughout the dissertation. Each chapter is divided into introduction, methodology, results, and summary and discussion. It has to be noted, that some data in each chapters' introduction is repeated to be able to read the chapter independently while having a broad view on the topic covered.

The first part introduces the topic of radiative cooling through a literature review and a theoretical background. Chapter 2 presents the state-of-the-art, research trends, and knowledge gaps; vital for understanding this proposal's context. To conclude this initial stage, the third chapter presents the theoretical background of daytime radiative cooling by studying the ideal material's optical characteristics. Hence, a sensitivity analysis is used to determine the ideal spectrum. The cooling power is calculated using a heat transfer model that includes radiation, convection, and conduction and two background conditions that assimilate an active and a passive approach.

The second part englobes the development and testing of daytime radiative cooling materials for architecture. The fourth chapter discusses material design, optimization, development, and characterization. Simulations and optimization techniques are vital for the success of the material's design. Moreover, fabrication techniques are researched, and finally, the materials' resulting characterization is discussed. The fifth chapter delves into material testing in two different temperate climates, a humid subtropical climate, and a temperate oceanic climate under non-ideal meteorological conditions.

The third part comprises chapter 6 and studies radiative cooling materials' worldwide potential of the developed materials in this Thesis, among others, in several different cities suffering from the Urban Heat Island effect englobed in the world's most prevalent climates.

Finally, chapter 7 presents the general conclusions and recommendations for future research.

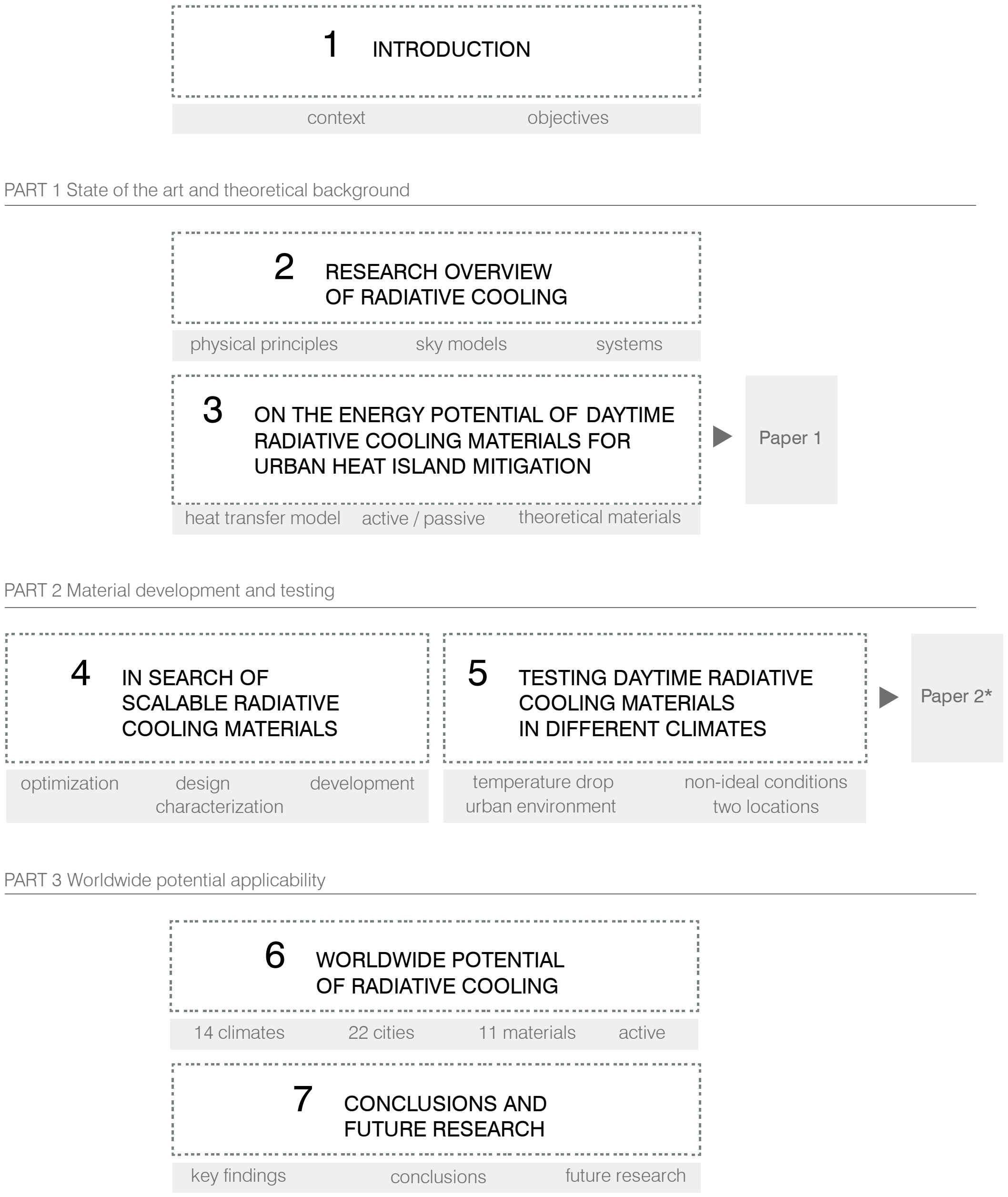

Figure 1: Thesis outline diagram.

CONTENT

ABSTRACT

The thesis “Advanced Daytime Radiative Cooling: Worldwide Potential in the Built-Environment” aims to determine the worldwide application potential of radiative cooling for future applications in architecture. Thus, it considers a broad range of aspects, from the material’s ideal optical configuration (reflectivity/emissivity), type of application (active or passive), material design (layers, thicknesses), fabrication and deposition technique, material testing under variable meteorological conditions, climate suitability to calculating the cooling potential in different climates.

The current energy context strengthens the importance of radiative cooling techniques as they do not require energy input. Fossil fuel energy consumption and other non-renewable sources have increased in the last decades. Moreover, the global population is rising, while more stringent thermal comfort inside buildings is required. Increasing global temperatures, the occurrence of heatwaves, and other extreme meteorological events present an unfavorable scenario. The widespread use of air conditioning has appeared alongside; most used air conditioning systems are based on vapor compression, which rejects the exceeding heat towards the exterior, exacerbating outside temperatures and inhibiting the thermal exchange.

Radiative cooling materials are proposed as an alternative cooling source, as they emit radiation through the atmospheric window using the space as the heat sink. Most of the material and system proposals are based on complex material designs that hinder the built environment’s applicability. Moreover, studies on climate suitability are scarce and under ideal conditions.

In this research work, the material optical properties were simulated through a sensitivity analysis to determine the impact of solar absorbance and infrared emissivity. Once the material ideal characteristics were known, low-cost scalable 1D photonic structures were successfully designed, optimized, developed, and tested. Since future applicability in architecture is a prerequisite, the materials' designs were based on abundant materials, favorable for use in the built environment due to their availability. The spray coating technique was successfully developed for broad application. The emissive coatings had the potential to lower any substate's potential temperature, resulting in a potential mitigating technique for the Heat Island. Finally, the developed materials and other radiative cooling materials were simulated in 22 different cities suffering from the Urban Heat Island Effect. The cities are grouped under the worldwide most prevalent 14 climates. The simulation results showed that the developed materials could compete against other more complex materials produced in the current literature. They have an excellent heat evacuation potential by radiation, especially in arid and temperate climates.

To conclude, this Thesis includes valuable information regarding the theoretical and experimental background for the development of daytime radiative cooling materials for future application in architecture. The easy deposition technique here presented, the small costs and the materials' performance have narrowed the gap to apply daytime radiative cooling materials as envelope coatings and as part of active systems. The materials here presented are great candidates to counteract the Urban Heat Island effect and lower building cooling loads.

KEYWORDS: daytime radiative cooling; Urban Heat Island; cooling potential; architecture application; scalable material development; sub-ambient cooling.

RESUMEN

La tesis “Advanced Daytime Radiative Cooling: Worldwide Potential in the Built-Environment” tiene como objetivo calcular el potencial mundial de enfriamiento radiativo para su futura aplicación en arquitectura. Para ello, se consideran diferentes aspectos necesarios para su correcta implementación, desde el diseño de la configuración óptica ideal del material (emisividad/reflectividad), el tipo de aplicación (activa o pasiva), el diseño de material (capas y espesores), la fabricación y las técnicas de deposición, la experimentación de los materiales bajo diferentes condiciones meteorológicas, adecuación climática y el cálculo del potencial de enfriamiento radiativo en diferentes climas.

El contexto energético actual hace que las propuestas de refrigeración basadas en enfriamiento radiativo sean de especial interés ya que no requieren de energía. El consumo de energías fósiles y otras fuentes no renovables, ha aumentado considerablemente en los últimos años. Por otro lado, la población mundial sigue creciendo junto a las demandas cada vez más exigentes de confort térmico en el interior de los edificios. El aumento simultáneo de temperatura, la aparición creciente de olas de calor y eventos meteorológicos extremos no presentan un escenario nada halagüeño. La proliferación de equipos de refrigeración ha ido de la mano con el aumento de temperaturas. En general, los sistemas de refrigeración basados en la compresión de vapor expulsan al exterior los excedentes de calor interior, elevando la temperatura del exterior, y dificultado el intercambio térmico.

El enfriamiento radiativo diurno aparece como una fuente de refrigeración alternativa, ya que los materiales consiguen enfriarse incluso con radiación solar incidente al emitir radiación infrarroja a través de la ventana de transparencia de la atmósfera al espacio. La mayoría de los estudios de enfriamiento radiativo hasta la fecha consideran unos materiales complejos, difíciles de fabricar y de elevado coste; dificultando su aplicación en el mundo de la arquitectura. Por otro lado, los experimentos al exterior se hacen, en la mayoría de los casos, en condiciones ideales, cielos despejados y sin edificios colindantes que puedan emitir radiación.

En este trabajo de investigación, se hizo un análisis de sensibilidad de las propiedades ópticas de los materiales para determinar el impacto de la absorción solar y la emisión infrarroja. Tras determinar las características del material ideal, se diseñaron, optimizaron, fabricaron y ensayaron materiales basados en estructuras fotónicas de una dimensión (1D) escalables y de bajo coste. Como su posterior aplicación en la arquitectura era un prerrequisito, los diseños de los materiales se basaron en materias primas abundantes, que facilitarán su uso en la construcción debido a su disponibilidad. La técnica de deposición basada en los espráis se desarrolló para su posible aplicación en grandes formateos.

Los recubrimientos emisivos tienen el potencial de bajar la temperatura superficial de cualquier tipo de sustrato, aunque no se consigan temperaturas subambiente, puede resultar beneficioso para mitigar las Islas de Calor.

Finalmente, los materiales desarrollados se simularon junto a otros materiales de enfriamiento radiativo en 22 ciudades con Isla de Calor Urbana. Las ciudades estudiadas se localizan en los 14 climas más prevalentes del mundo. Los resultados de las simulaciones demuestran que los materiales desarrollados pueden competir con otros materiales más complejos de la literatura actual. Los materiales desarrollados muestran un gran potencial de evacuación de calor, especialmente por radiación, en los climas áridos y en los climas templados.

Para concluir, esta Tesis incluye información relevante sobre el contexto teórico y experimental para el desarrollo de materiales de enfriamiento radiativo para su aplicación posterior en arquitectura. La sencilla técnica de deposición presentada, el bajo coste y el rendimiento de los materiales han reducido el salto para la aplicación de los materiales diurnos de enfriamiento radiativo como materiales de la envolvente y como sistemas activos. Los materiales presentados son unos candidatos excelentes para contrarrestar el efecto de la Isla de Calor Urbana y reducir la carga de refrigeración.

PALABRAS CLAVE: enfriamiento radiativo diurno; Isla de Calor Urbana; potencial de enfriamiento; aplicación en arquitectura; desarrollo de materiales escalables; enfriamiento subambiente.

“Thousands of years before Christ, man made ice when the temperature was above freezing and did it naturally. This was accomplished in Iran with ice walls which were actually made of Earth. The tapered vertical walls to the left and right partially enclose the freezing zone. The ice is stored inside the earth pyramid where the temperature hardly varies, and ice can be stored well into the summer. A shallow layer of water behind this pyramid is protected from solar radiation by the wall to the right and that insolation striking the wall to the left is partially reflected or reradiates back to the sky and not down on the ground. Also, the wind passes over the walls causing air stratification between them. Though the ambient temperature at the top of the wall is 50 °F, water will freeze to ice at ground level. In a desert, this is the power of radiation of the sky. Instead of using this principle for cooling where it can be successful, we have tried in the last 150 years, to forget what the people have known and used for thousands of years.”

“We must return to working with the climate — not against it.”

-Harold Hay, 1976

LIST OF FIGURES[1]

---

[1] All figures are by author unless otherwise noted

APPENDIX FIGURES

LIST OF TABLES

APPENDIX TABLES

NOMENCLATURE

Abbreviations

AC	Air Conditioning
BEM	Boundary element method
CDD	Cooling Degree Days
COP	UN Climate Change Conference
DRC	Daytime Radiative Cooling
EU	European Union
ESR	Enhanced Solar Reflector
FDTD	Finite Difference Time Domain
FEM	Finite Element Method
FIR	Far Infrared
FIT	Finite Integration Time-Domain Technique
GHG	Greenhouse Gases
HFC	Hydrofluorocarbons
HW	Heatwaves
IEA	International Energy Agency
IR	Infrared
IRENA	International Renewable Energy Agency

NIR	Near Infrared
NRC	Nighttime Radiative Cooling
nZEB	Near Zero Energy Buildings
PCM	Phase Change Material
PECVD	Plasma-Enhanced Chemical Vapor Deposition
PV	Photovoltaic
TDRC	Tunable Daytime Radiative Cooling
TMY	Typical Meteorological Year
SC	Solar Collector
SCR	Solar Collector Sky Radiator
UHI	Urban Heat Island
UV	Ultraviolet

Symbols

A	Surface area
c	Fraction of sky covered by clouds
c	Speed of light in the medium
E_b	Blackbody radiation (W·m^{-2})
G	Irradiance (W·m^{-2})
h	Convective heat transfer (W·m^{-2} ·K^{-1})
h	Planck's constant
I	Solar irradiation (W·m^{-2})
J	Radiosity (W·m^{-2})
k_B	Boltzmann's constant
n(λ)	Refractive index real part
k(λ)	Refractive index complex part
P	Total power

q	Heat flux (W·m^{-2})
T	Temperature (K or °C)
v	Wavenumber (m^{-1})

Greek letters

α	Absorptivity
ε	Emissivity
λ	Wavelength
σ	Stefan-Boltzmann constant
τ	Transmissivity

Subscripts

air	Air
amb	Ambient
BB	Blackbody
cd	Conduction
cv	Convection
r	Radiation
s	Surface studied
sun	Solar
t	Transition
Δv	A wavenumber range or band

Chemical formulas

Al	Aluminum
Al_2O_3	Aluminum oxide
BN	Boron nitride

CO_2	Carbon dioxide
FTO	Fluorine doped tin oxide
MgF_2	Magnesium fluoride
PDMS	Polydimethylsiloxane
PE	Polyethylene
PET	polyethylene terephthalate
PMSQ	Polymethylsilsesquioxane
PVF	Polyvinyl fluoride
Si_3N_4	Silicon nitride
SiC	Silicon carbide
SiO	Silicon monoxide
SiO_2	Silicon dioxide
TiO_2	Titanium dioxide
TPX	Polymethylpentene
$V_{1-x}W_xO_2$	Vanadium dioxide doped with tungsten
VO_2	Vanadium dioxide
ZnS	Zinc sulfide
ZnSe	Zinc selenide
ZnTe	Zinc telluride

1 INTRODUCTION

This thesis "Advanced Daytime Radiative Cooling: Worldwide Potential in the Built-Environment" aims to determine the future potential for the worldwide application of radiative cooling in architecture.

The current energy context, combined with the effects of heat islands and rising global temperatures, point towards a highly demanding cooling scenario in the years to come. Over the last decade, there has been an increasing interest in the new possibilities that daytime radiative coolers, which evacuate heat passively, can offer. Radiative cooling materials that rely on particular spectral configurations could lower the energy demands of buildings when applied as passive coatings, or make the cooling cycle more efficient when integrated into active systems. This research presents a broad overview of this technology potential through several experimental and numerical approaches, which are based on the future integration of this technology as a prerequisite in architecture (performance, scalability, costs, and easy to apply methods). Thus, it considers aspects ranging from material design, development, testing and climate suitability to cooling potential.

This first chapter introduces the research within the present context and outlines the basic concept of radiative cooling with a brief overview of the existing literature on radiative cooling. The knowledge gaps are identified, and the main research problems and drawbacks are detailed. The research questions and objectives are formulated. Finally, the scientific relevance and contribution of the thesis is discussed.

1.1 Background

1.1.1 Energy context

The consumption of fossil fuels and other non-renewable energy sources is rising at a fast pace. At the same time, population growth and rising living standards lead to a higher demand for energy production. Therefore, relying on fossil fuels to meet energy demand is neither viable in the long run nor sustainable in environmental terms. As has been well established, carbon dioxide emissions are closely related to the transformation of fossil fuels into energy, and are the leading cause of the greenhouse effect. Carbon dioxide (CO_2) molecules in the atmosphere create a barrier that inhibits heat from escaping the Earth. Greenhouse gas emissions are a threat to the environment, and although governments have implemented policies to keep them at a minimum, CO_2 emissions continue to grow. Emissions linked to coal, oil, and natural gas have increased in the last 25 years, as seen in Figure 2.

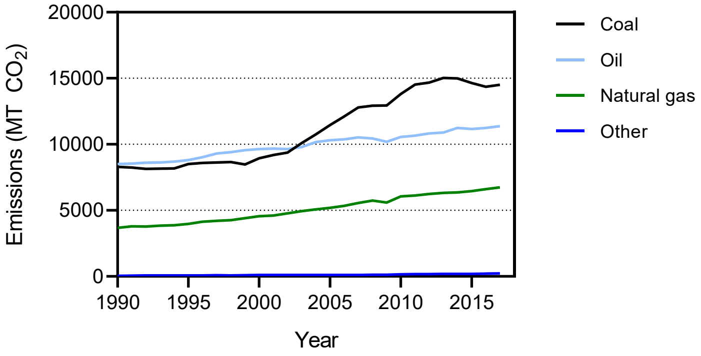

Figure 2: CO_2 emissions by energy source. Data from (IEA, 2020a).

At present, half of the world's population lives in urban areas (*World Urbanization Prospects*, 2014) and consumes 75% of the primary energy sources, emitting between 50 and 60% of greenhouse gases ("Energy – UN-Habitat," n.d.). Furthermore, the world's urban population is expected to grow more than two thirds by 2050, reaching 6.3 billion, with nearly 90% of this increase in Asian and African cities (*World Urbanization Prospects*, 2014) Carbon dioxide emissions increase in proportion with the population due to energy use (O'Neill et al., 2012). A 1% increase in the urban population is estimated to raise energy consumption by 2.2% (Santamouris et al., 2001). Global energy demand is predicted to increase by more than 25% if the International Energy Agency's New Policies Scenario (rising incomes and an extra 1.7 billion people) becomes a reality (UN Environment and International Energy Agency, 2018). In addition to increased energy demand, urbanization is expected to raise the projected emissions by more than 25% in developing countries, due to population growth, especially in China and India (O'Neill et al., 2010). Therefore, if energy consumption patterns follow the current trends, it could lead to a scenario of unforeseen environmental consequences. Reducing primary energy demand, as well as the emissions of polluting gases, is of utmost importance. Depending on the emissions path model followed, the temperature of the atmosphere would increase from 1 °C to 4 °C by the end of the 21st Century (Fiorito and Santamouris, 2017).

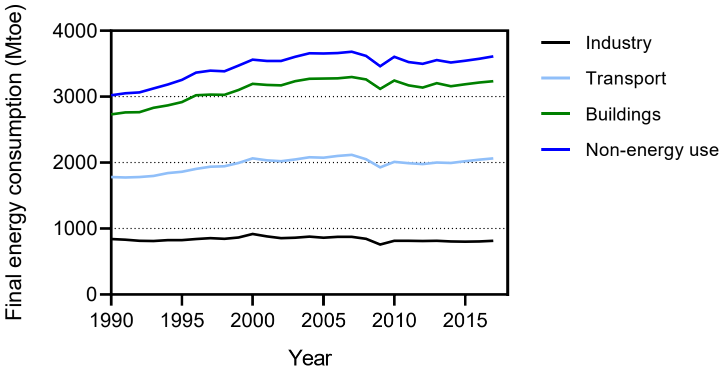

Figure 3: Final energy consumption by sector in the OECD, 1990-2017. Data from (IEA, 2019a).

Buildings account for a third of global energy consumption (Figure 3) (UN Environment and International Energy Agency, 2017). Studies show that refrigeration and air conditioning (AC) is responsible for 18.5% of the total electricity consumption globally in 2016, up from 13% in 1990 (IEA, 2018a). Air conditioning penetration and the energy demand for cooling depend on factors such as the economy, climate, demography, policies and technology (Santamouris, 2016a). Although there are many air conditioning types, these systems can be classified into three main categories, according to the final energy used to operate them: electrical systems, thermal systems and hybrid systems (Afonso, 2006). The most prevalent AC throughout the world is based on vapor-compression refrigeration, which discharges latent waste heat to the ambient air. Studies in urbanized areas of central Paris have shown an increase in the street air temperature, ranging from 0.5 °C to 2 °C depending on the AC equipment employed (Munck et al., 2013). Although these systems worsen the outdoor conditions, especially in cities, vapor-compression systems constitute 90% of the air conditioning systems installed worldwide (Daniels, 2003).

From 1990 to 2016, annual sales of AC systems nearly quadrupled, reaching 135 million units. Over recent years, this trend has grown consistently worldwide, with only a brief recess during the 2008 financial crisis (IEA, 2018a). Most households in Japan and the United States of America already have an AC unit; however, the share of AC units in developing countries such as India and South America is scant (Figure 4). Moreover, as seen in Figure 4, the number of units is predicted to increase, especially in countries where the current stock is low, such as India and Africa. Aside from the excess heat rejection to the ambient air, the energy consumption of AC systems is their main contribution to greenhouse gas emissions (GHG).

In 2016, energy used for cooling accounted for 65% of the total generation of emissions (coal for 37%, gas 24%, and oil 4%), resulting in average emissions of around 505 grams of carbon dioxide (CO_2) per kWh (gCO_2/kWh) generated (IEA, 2018a).

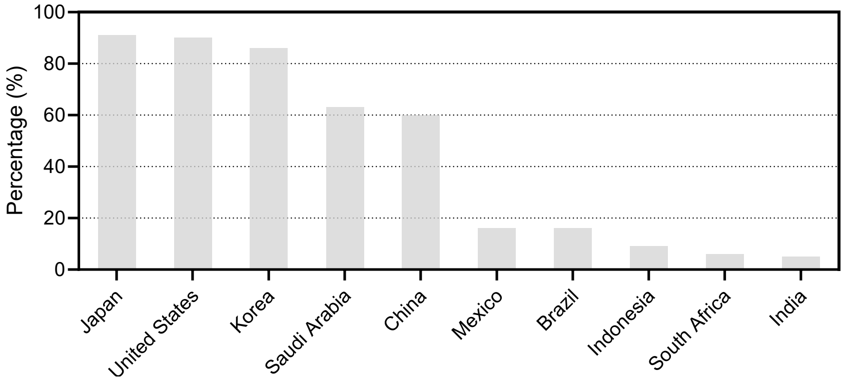

Figure 4: Share of households with AC. Data from (IEA, 2019b).

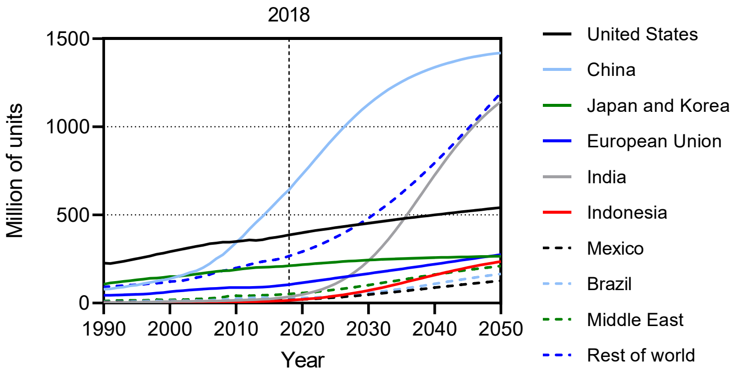

Figure 5: Global air conditioner stock from 1990 to 2018, with predicted values up till 2050. Updated 19. November 2019. Data from (IEA, 2019c, pp. 1990–2050).

Moreover, the leakage or improper disposal of refrigerants contributes to emissions since they are usually comprised of greenhouse gases such as hydrofluorocarbons (HFC). As a result of population growth, household income increases and higher urban temperatures, cooling degree days (CDD), defined as the sum of the positive deviations of the mean daily temperatures from a base value (Asimakopoulos and Santamouris, 1996, p. 78), are expected to increase 25% by 2050 globally, leading to a more demanding scenario for cooling (IEA, 2018a).

Overheating will increase in the future, and so will the occurrences of heatwaves. Buildings will need cooling mechanisms; therefore, if energy consumption patterns, population growth, and AC systems installations follow the current trends and predictions are fulfilled, this would lead to an unmanageable scenario of unforeseen consequences as GHG emissions continue to increase.

Several worldwide agreements have been arranged throughout the years to stop the Earth from warming and to reduce emissions. In the Paris Agreement of 2015, a series of parameters were determined to stem the route towards climate change and to maintain the Earth 2 °C under preindustrial values (*COP21*, 2015). Moreover, the European Union (EU) established the EU/2016/2281 regulation (European Parliament, Council of the European Union, 2016) – a framework for the setting of "ecodesign requirements for energy-related products, with regard to ecodesign requirements for air heating products, cooling products, high-temperature process chillers, and fan coil units." The application of these regulations aims at achieving savings of the equivalent of 5 million-tons of petroleum (Mtep) per year by 2030, approximately 9 million tons of CO_2. By 2030, all decarbonizing hypotheses assume a 30% increase in the use of renewable energies (European Commission, 2011). Finally, in December of 2019, during COP25, energy scenarios were discussed to keep global temperatures from rising more than 1.5 °C ("COP25 • UN Climate Change Conference," 2020). As pointed out by the Intergovernmental Panel on Climate Change (IPCC, 2018), achieving the goal is possible but requires strong transitions in social aspects. This tendency towards renewable energy has been adopted in the European Union, over the past 20 years, by creating a series of "directives", legislative acts which set out goals that all EU countries must achieve (European Union, 2016). **Error! Not a valid bookmark self-reference.** details directives related to the phasing down of CO_2 emissions, energy efficiency and air conditioning equipment since 1990.

Table 1: European Union Regulation Framework (CO2 emissions, energy efficiency, and air conditioning equipment).

YEAR	DIRECTIVE
1993	Council Directive 93/76/EEC to limit carbon dioxide emissions by improving energy efficiency (SAVE).
1996	Directive 96/92/EC of the European Parliament and of the concerning common rules for the internal market in electricity.
2002	Commission Directive 2002/31/EC implementing Council Directive 92/75/EEC with regard to energy labelling of household air-conditioners.
2002	Directive 2002/91/EC on the energy performance of buildings.
2005	Directive 2005/32/EC establishing a framework for the setting of ecodesign requirements for energy-using products and amending 92/42/EEC, 96/57/EC and 2000/55/EC.
2006	Directive 2006/32/EC on energy end-use efficiency and energy services and repealing 93/76/EEC.

2008	Directive 2008/50/EC of the European Parliament and of the Council of 21 May 2008 on ambient air quality and cleaner air for Europe.
2009	Directive 2009/28/EC of the European Parliament and of the Council of 23 April 2009 on the promotion of the use of energy from renewable sources and amending and subsequently repealing Directives 2001/77/EC and 2003/30/EC (Text with EEA relevance).
2009	Directive 2009/72/EC of the European Parliament and of the Council of 13 July 2009 concerning common rules for the internal market in electricity and repealing Directive 2003/54/EC (Text with EEA relevance).
2010	Directive 2010/31/EU of the European Parliament and of the Council of 19 May 2010 on the energy performance of buildings.
2010	Directive 2010/30/EU on the indication by labelling and standard product information of the consumption of energy and other resources by energy-related products.
2012	Directive 2012/27/EU of the European Parliament and of the Council of 25 October 2012 on energy efficiency.
2013	Council Directive 2013/12/EU adapting Directive 2012/27/EU of the European Parliament and of the Council on energy efficiency.
2018	Directive (EU) 2018/410 amending Directive 2003/87/EC to enhance cost-effective emission reductions and low-carbon investments.
2018	Directive (EU) 2018/844 amending Directive 2010/31/EU on the energy performance of buildings and Directive 2012/27/EU on energy efficiency.
2018	Directive (EU) 2018/2001 on the promotion of the use of energy from renewable sources.
2018	Directive (EU) 2018/2002 amending Directive 2012/27/EU on energy efficiency.
2019	Directive (EU) 2019/944 on common rules for the internal market for electricity and amending Directive 2012/27/EU (Text with EEA relevance).

As seen in Figure 6, policy regulation has increased; however, its implementation degree varies across countries. The IEA analyzed energy efficiency policy implementation across the globe and found that even though energy efficiency policies for buildings continued to progress in 2018 (40%), the rate was lower than in 2017 (38%) (IEA, n.d.). Moreover, these slowdowns can be attributed to market changes such as the shift of energy demand from China to other emerging economies (IEA, 2020b).

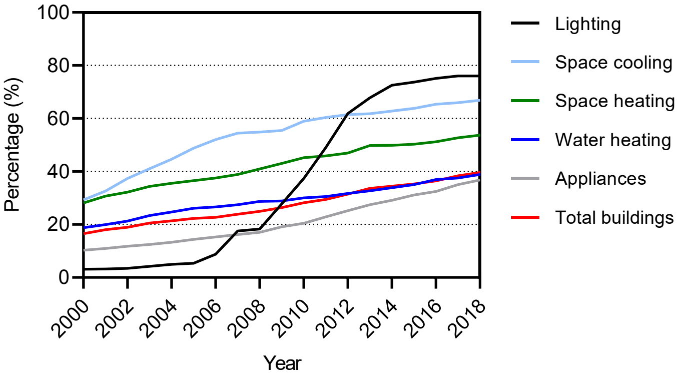

Figure 6: Policy coverage of total final energy consumption in buildings, 2000-2018. Data from (IEA, 2020c).

1.1.2 Urban Heat Islands

Cities have been reported to have higher thermal differences in comparison with surrounding rural areas (Figure 7) due to significant releases of anthropogenic heat, the excess storage of solar radiation by the city structures, the lack of green spaces and cold sinks, the non-circulation of air in urban canyons and the low ability of the emitted infrared radiation to escape in the atmosphere (Oke et al., 1991).

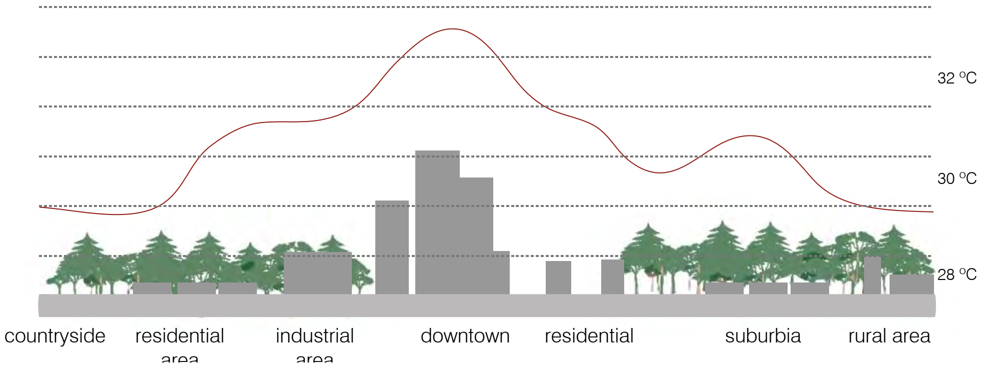

Figure 7: Urban Heat Island Effect.

Urban Heat Islands (UHI) are the most documented phenomena of climate change. Urban overheating is associated with higher urban temperatures in dense parts of cities compared to surrounding suburban or rural areas (Akbari et al., 2016). Overheating sources include the released anthropogenic heat, high absorption of solar radiation by the urban materials and structures, decreased airflow and urban ventilation, reduced evapotranspiration, and limited radiative losses (Santamouris, 2015a). The phenomenon is documented in more than 400 cities worldwide, and the amplitude of urban overheating may range from 1 to 10 °C, averaging 5 to 6 °C (Santamouris, 2015b). Synergies with global climate change and heatwaves further intensify the scale of urban overheating (Founda and Santamouris, 2017). The number of cities that experience this phenomenon is increasing quickly (Santamouris, 2019).

Urban overheating has a severe impact on the cooling energy consumption of buildings, outdoor pollution levels, heat-related mortality and morbidity, urban ecological footprint, and survival levels (Santamouris, 2020). It is reported that urban overheating raises the peak electricity load, which varies from 0.45% to 4.6%, equivalent to an electricity penalty of about 21 (±10.4) W per degree of temperature increase and per person (Santamouris et al., 2015). Moreover, the additional energy penalty induced by urban overheating is close to 0.74 kWh/m^2/C, while the Global Energy Penalty per person is close to 237 (±130) kWh/p (Santamouris, 2014). Similarly, recent research has found that populations living in cities with warmer precincts have a close to 6% higher risk of mortality than those living in cooler urban neighborhoods (Schinasi et al., 2018).

The urban climate is strongly determined by morphological characteristics and the properties of the materials comprising the urban landscape (Lemonsu et al., 2015). Therefore, several mitigation strategies have been presented besides improving AC systems such as green roofs, vertical gardens, open spaces, street trees, blue infrastructure, photovoltaics, coolroofs, urban form, reduced AC use, low-energy transport, and solar-passive design (Bosomworth et al., 2013). Many strategies that focus on new material developments have been suggested to mitigate the UHI effect in cooling demand aggravated by heatwaves. Increasing the global albedo of cities has demonstrated a reduction of peak ambient temperature by up to 3 °C, leading to a 20% reduction of peak cooling demand in residential buildings. Studies have widely shown that coolroofs reduce cooling demand (Bell et al., 2003; Berdahl and Bretz, 1997; Erell et al., 2006; Kolokotroni et al., 2013; Kolokotsa et al., 2018; Miller et al., 2015; Radhi et al., 2017; Santamouris, 2013; Santamouris et al., 2008). Green roofs and vegetation have been proposed as a mitigation strategy (Foustalieraki et al., 2017; Herrera-Gomez et al., 2017; Kolokotsa et al., 2013; Zinzi and Agnoli, 2012).

Figure 8 summarizes the optical response of different materials, ranging from conventional to thermochromic materials. Conventional construction materials have a constant behavior and are usually very absorptive. On the other side of the spectrum, cool materials are reflective under all conditions, which leads to heat penalties during the winter. Radiative cooling materials can be considered a subgroup within cool materials, with more selective optical requirements. Their goal is usually to achieve sub-ambient cooling. Thus, they need to reflect most solar radiation and emit highly on the infrared wavelengths, where the incoming radiation is negligible. Fluorescent materials behave similarly to coolmaterials but using another mechanism, photoluminescence, which shifts the reemission of energy in time. Finally, thermochromic materials respond thermally to the environment and change their color reversibly once they reach the transition temperature. Figure 9 classifies cooling techniques based on passive principles that do not require energy input and active cooling, such as electrochromism, that require energy input to work.

Me suena raro pero no sé si es la palabra que usa Santamouris así que no lo cambio pero pondría 'survival' si no.

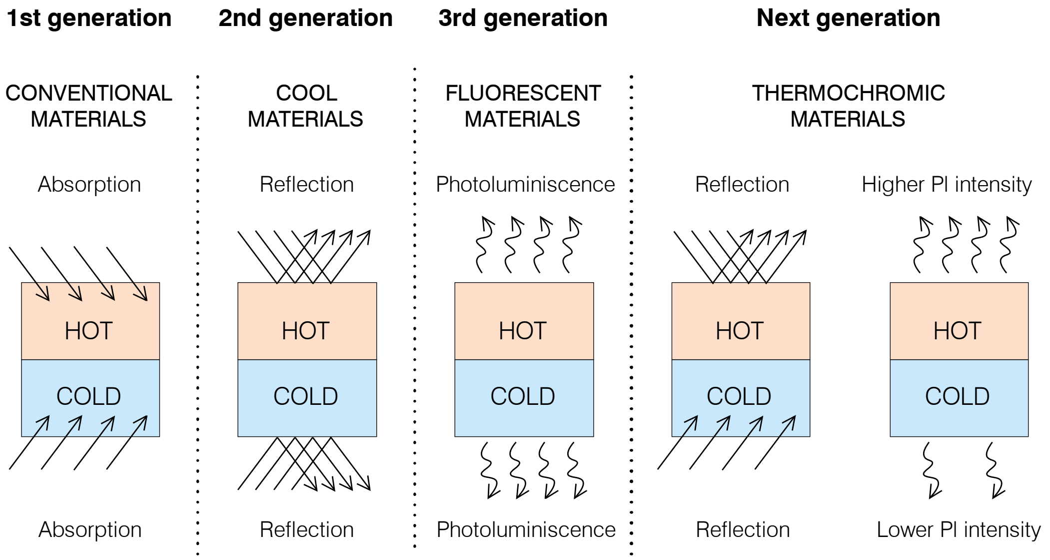

Figure 8: The optical response of different generations of construction materials in the cold (bottom part) and warm periods (upper side). Based on (Garshasbi and Santamouris, 2019).

The development of coatings that respond thermally to the environment and reversibly change their color presents tremendous advantages. These thermochromic coatings present a thermally reversible transformation of their molecular structure, causing a spectral change of visible color (Santamouris et al., 2011). Thermochromic materials have a high absorption during winter and high reflectance during summer and can decrease both the heating and cooling needs of buildings (Santamouris et al., 2011). These materials applied as coatings achieved reductions in the cooling demand during the summer (Akbari et al., 1997; Perez et al., 2018; Santamouris et al., 2011; Sharma et al., 2017; Zheng et al., 2015). The studied thermochromic materials were discarded due to their lack of ultraviolet (UV) resistance. However, recent progress in the production of thermochromic materials offers a renewed opportunity to research their potential in the built environment (Garshasbi and Santamouris, 2019). Fluorescent materials presented high advantages for cooling. Nevertheless, they are not suitable candidates for all seasons or even a day since they increase the heating demand during cold periods. (Santamouris et al., 2011; Synnefa et al., 2007). In photoluminescent materials, the absorbed photons are partly reemitted as visible light rather than long-wave radiation (Kousis et al., 2020). These materials can complement the high cooling potential of albedo materials in a twofold solar rejection mechanism defined as Effective Solar Reflectance (ESR) (Garshasbi and Santamouris, 2019). With regard to fluorescent materials, a recently introduced type of heat mitigation technology is quantum dots. They reached 2 °C reductions compared to non-fluorescent reference samples under two different boundary conditions in Sydney, Australia (Garshasbi et al., 2020b).

The radiative cooling phenomenon has been applied since ancient times, as discussed in the next section. Progress in achieving daytime radiative cooling materials has been studied since the ‘70s, as will be summarised in Chapter 2. Current advances in material engineering and photonic research are resulting in an increased interest in radiative cooling materials, since many achieved daytime sub-ambient temperatures (Gentle and Smith, 2015; Raman et al., 2014; Zhai et al., 2017b). This type of material might significantly decrease the current and future cooling demand of buildings (Santamouris and Feng, 2018). On the one hand, radiative cooling materials might be applied passively to decrease the cooling demand of buildings, similarly to coolmaterials. On the other hand, they can be coupled to AC systems to evacuate the excess heat to space instead of the ambient air (Aili et al., 2019b; Goldstein et al., 2017; Zhang et al., 2018).

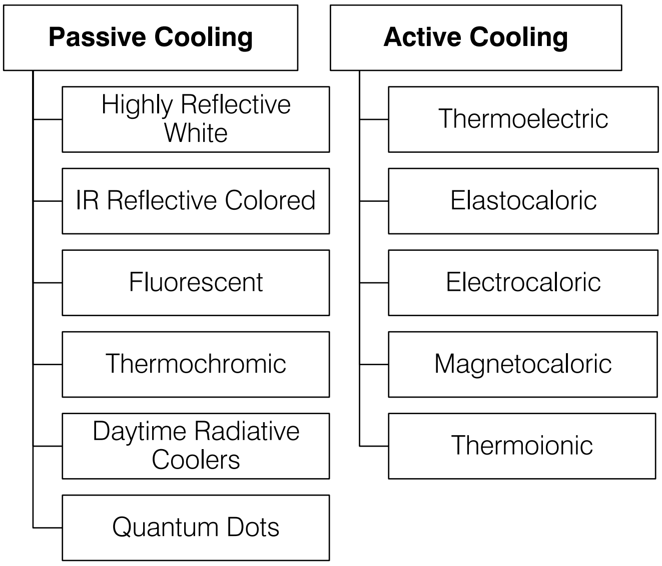

Figure 9: Classification of materials for passive and active cooling. Based on: (Santamouris and Feng, 2018).

1.1.3 Radiative cooling

Radiative cooling is the physical phenomenon through which an object dissipates heat as infrared radiation. All bodies over 0 K (-273 °C) emit electromagnetic radiation depending on their temperature and surface nature. According to Wien's displacement law, the sun can be considered a blackbody at the temperature of 5778 K, whose peak of emission is at 0.5 μm.

The Earth receives average solar radiation of 1368 $W\cdot m^{-2}$ from the sun, however since half of the Earth is continuously shadowed, the average amount of energy incident on a level surface outside the atmosphere is one-fourth 342 $W\cdot m^{-2}$ (Trenberth, 2004). The atmospheric gasses scatter and reflect 31% of the incoming radiation to space, leaving 235 $W\cdot m^{-2}$ to warm the Earth's surface (Bhattacharyya, 2019).

Over mid-infrared wavelengths, from 8 to 13 μm, the Earth's atmosphere is transparent to electromagnetic radiation, its transmittance is near unity, and its radiation is minimum. This wavelength range is called the atmospheric transparency window and it coincides with the peak wavelength of thermal radiation from terrestrial structures at typical ambient temperatures (Figure 10). Blackbody radiation from an object between -53 °C and 47 °C coincidentally matches the atmospheric window shown in Figure 11. Thus, a sky-facing object can radiate its heat into space. If the incoming heat (conduction, convection, and radiation) is lower than the outgoing heat, the object cools down.

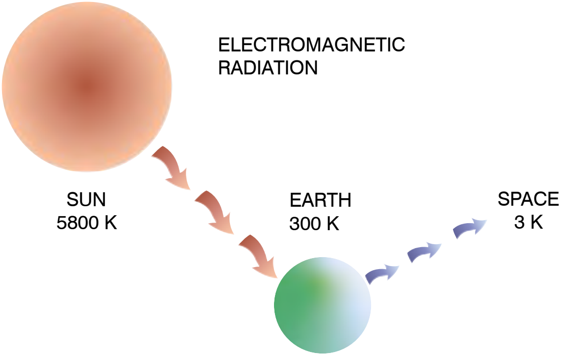

Figure 10: Radiative cooling phenomenon of the Earth.

Planck's law of blackbody radiation gives the relationship of the dependent emission and temperature:

$$I_{BB}(T,\lambda) = \frac{2\pi hc^2}{\lambda^5} \frac{1}{e^{\frac{hc}{\lambda kT}} - 1} \tag{1}$$

Where I_{BB} is the spectral irradiance per unit area per unit wavelength, h is Planck's constant, c is the speed of light, k is Boltzmann's constant, and T denotes the temperature in K (Sun et al., 2017). By integrating the spectral irradiance over an area and the whole wavelength range, it can be found that the total emitted power is proportional to the fourth power of the emitter temperature, as described by the Stefan-Boltzmann law:

$$P = \varepsilon A \sigma T^4 \tag{2}$$

where P is the total emissive power, A is the surface area of the emitting object, σ is the Stefan-Boltzmann constant, and ε denotes the averaged emittance of the object. Therefore, the higher the temperature, the stronger its emissive power. Kirchhoff's Law states that at a point on the surface of a thermal radiator at any temperature and wavelength, the spectral directional emittance is equal to the spectral absorptance for radiation incident from the same direction (Kelly, 1965).

$$\varepsilon_\lambda = \alpha_\lambda \tag{3}$$

Therefore, if an object is very reflective in the solar wavelengths (solar absorptivity is almost zero) and is very absorbent or emissive (Equation (3)) in the atmospheric window wavelengths since the atmospheric radiation is negligible, the object is able to cool down.

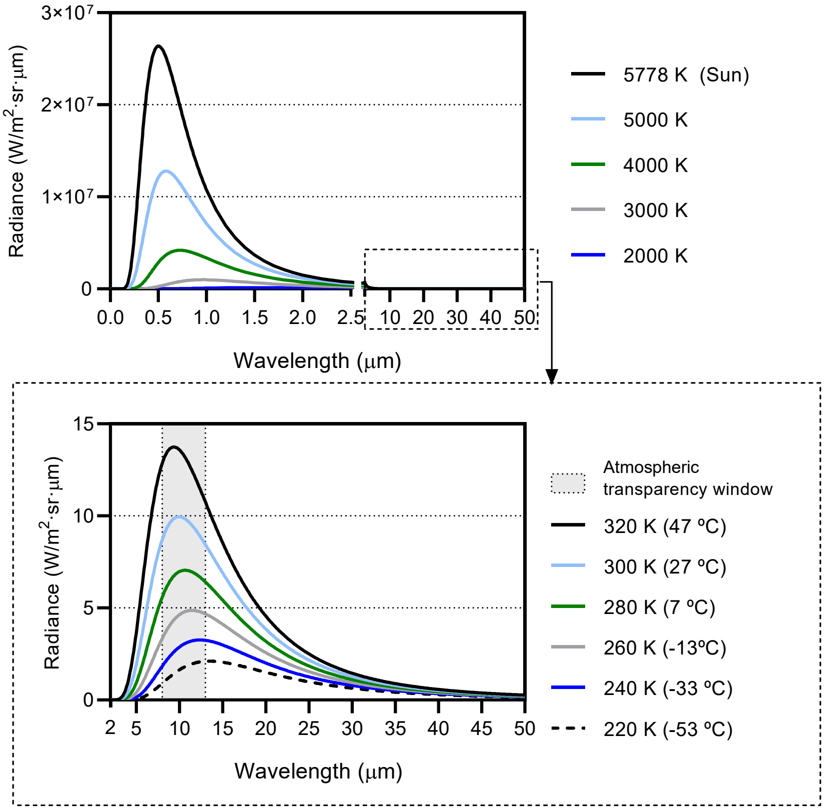

Figure 11: Blackbody radiance at several temperatures. The top image shows high temperatures such as the sun (5778 K) and at the bottom temperatures of black bodies at Earth temperatures.

The research on radiative cooling has been grouped into understanding the physical phenomenon and applying the technique to the real world (D. Zhao et al., 2019b). According to the same authors, the first category researches the physics behind the phenomenon, such as the emissivity properties of radiative cooling surfaces, spectral emissivity of the atmosphere, and the dependence of radiative cooling on the wavelength, incident angle, and geographic locations. The second group investigates new materials with desirable optical properties and their application in different scenarios (e.g., residential and commercial buildings refrigeration, cooling of solar cells, dew harvesting, outdoor personal thermal management, and supplemental cooling for condensers of air conditioners and power plants).

Radiative cooling is a refrigeration mechanism present in nature. Plants and some animals, such as the Saharan silver ants (Shi et al., 2015), the Bisotnina biston butterflies (Cheng-Chia Tsai et al., 2017), and the Namib desert beetle (Guadarrama-Cetina et al., 2014) use this mechanism to avoid overheating, or for water harvesting. For example, the exterior wings of desert beetles have a spectrally selective coating that allows sub-ambient cooling. Consequently, the ambient water condenses and drips into the wings to obtain water under extreme weather conditions. Tree leaves convert incident solar radiation into energy by photosynthetic reduction of CO_2 to hydrocarbons. This absorption heats the leaves to 40-50 °C, where many processes start to be affected, so besides water evaporation, leaves use spectral selectivity to reduce their temperature with limited water loss (Granqvist, 1981).

Nighttime radiative cooling

The nighttime radiative cooling phenomenon was first known to be used in Iran's arid areas to produce ice during the night (Hosseini and Namazian, 2012). Iran’s vernacular architecture developed two kinds of buildings, icehouses, and cisterns, for making and storing ice using this thermodynamic principle. The structure of the Yakhchals, literally meaning ice-houses (Hosseini and Namazian, 2012; Kazemi and Shirvani, 2011; Mahdavinejad and Javanrudi, 2012), generally has three main parts: a shading wall, a provisioning pool, and an ice reservoir (Figure 12). Water is poured during the night to the north of the shade wall. As the Earth's temperature and the water are higher than the sky during the night hours, the water loses its heat and quickly freezes.

Radiative cooling has been empirically applied in vernacular Mediterranean architecture with the widespread use of whitewashed roofs, with high reflectance in solar during daytime and high emissivity in the infrared during the night (Psiloglou et al., 1996). This optical characteristic allows the roofs to dissipate the heat accumulated during the day to a colder heat sink, the space. Radiative cooling occurs during the entire day; however, the incoming heat counteracts this phenomenon and heat up during the daytime. Most commonly available materials do not have the needed optical properties to achieve daytime radiative cooling.

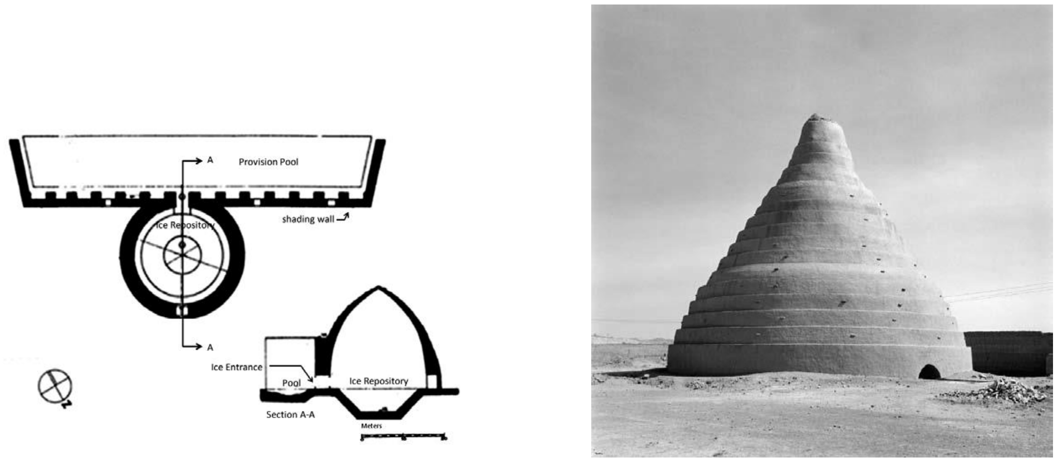

Figure 12: Meiboud Icehouse in Yazd (Ghobadian, 2001) and Yakhchal in abarku-Yazd (Lynn Davis, 2001). Cited in (Hosseini and Namazian, 2012).

First prototypes

In the mid-60s and after the petroleum crisis of 1973, researchers started to apply radiative cooling principles into systems to reduce the energy demand of cooling and, as a result, electricity. The first designs were passive systems such as high inertia roofs, concrete slabs, and movable insulation. The latter protected the inertia element from incoming solar radiation and was retired during the night to expose the surface to the night sky. Despite their simplicity, these systems rely on electromechanical devices to move daily the insulation layer, although the authors refer to these designs as passive systems.

In the past, radiative cooling was applied as a nocturnal passive system for cooling in some temporary buildings and prototypes (Awanou, 1986; Baer, 1976; Ezekwe, 1986; Yellot, 1976; Yellot, John I., 1976). The results showed that the cooling capacity provided by those pioneering experiences was limited. Moreover, the locations of those experiments usually took place in hot and dry areas around the world, such as Arizona, California (Yellot, John I., 1976), Nigeria (Ezekwe, 1986), and Israel (Erell and Etzion, 2000).

In 1967 Harold Hay constructed in Phoenix a one-story 16 m^2 demonstrator with a water deposit on its roof covered by movable insulation panels (Figure 13). During summer days, the panels protected the water from heating. At night, they were removed, letting the accumulated heat to be radiated towards the sky. In winter, the process was reversed. The water beds were exposed during sunny days to accumulate solar radiation, and during the night, the insulation protected them to avoid losses. The interior temperature was under 26 °C even though exterior temperatures surpassed 46 °C (Yellot, 1976).

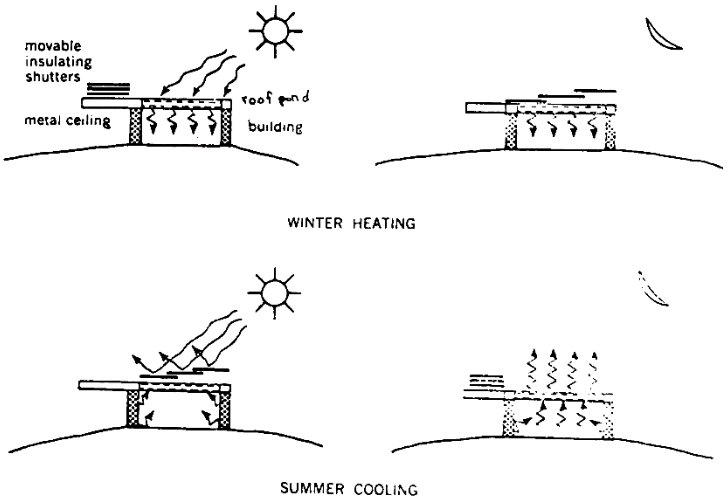

Figure 13: Skytherm operation modes (Anderson, 1976).

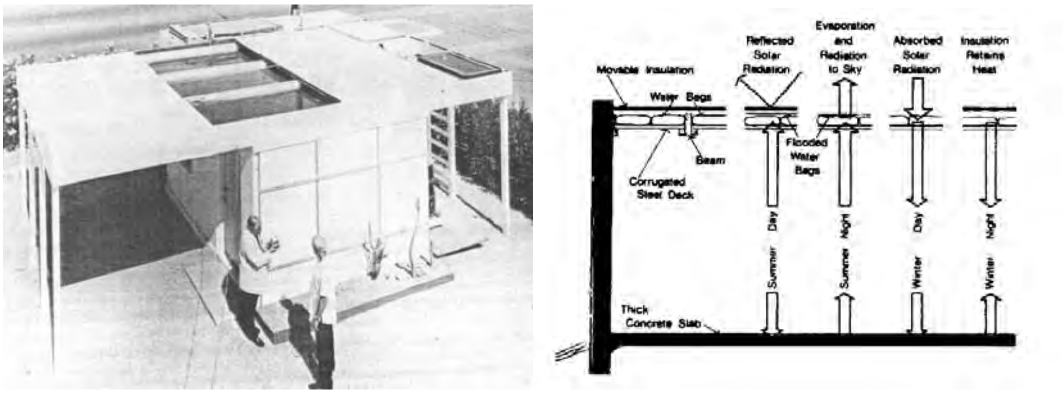

Figure 14: Skytherm in Atascadero photograph ("Wie du mit der Kälte des Weltraums kühlst," n.d.) and operation principles of Skytherm (Yellot, 1976).

In 1973 John Yellot joined Harold Hay to construct a third prototype: the Atascadero House in California (Figure 14). This prototype was 100 m^2. In this proposal, the water was hosted in plastic bags to avoid evaporation and dirt accumulation. The interior temperatures achieved thermal comfort throughout the year, even with extreme exterior temperatures of -4 °C in winter and 47 °C in summer (Yellot, 1976). According to a study published in 2000 (Raeissi and Taheri, 2000), Skytherm houses achieved cooling powers between 7 and 18 W·m^{-2}.

Holly Baer and Steven Baer proposed a similar system located on the walls called "Water Walls." The New Mexico prototype, as seen in Figure 15, used 55-gallon containers filled with water as thermal inertia. The glass south façade was covered by reflective panels that were open during sunny winter days and covered during the night (Baer, 1976).

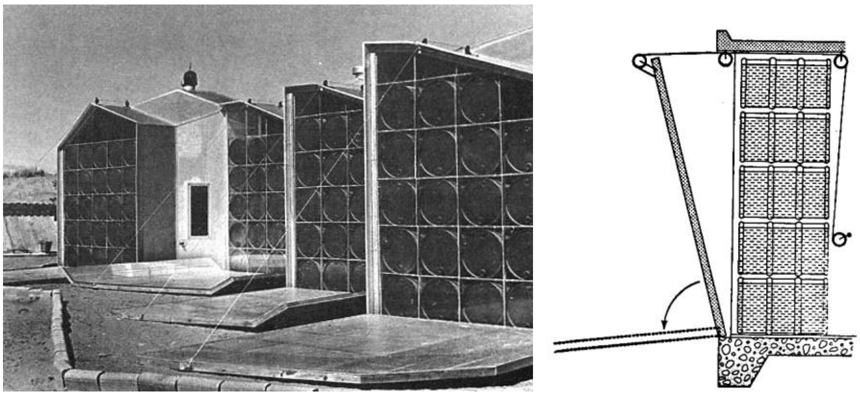

Figure 15: (left) photo “Double Play Solar Heating and Cooling System” Source: (the MOTHER EARTH NEWS editors, 1973)and (right) drawing of the system operation. Source: (Anderson, 1976).

Radiator designs

Nocturnal longwave radiation from materials commonly found on the earth’s surface can rarely achieve cooling powers of more than 100 W·m$^{-2,}$ even under ideal meteorological conditions (Erell and Etzion, 1992). The potential for radiative cooling of buildings is inherently limited; therefore, any system designed to use this phenomenon must be very efficient (Erell and Etzion, 1992). Fluids, such as water, may be employed by taking advantage of its circulation through a radiator to cool down. The chosen fluids may go through a radiator system or be integrated into the roofing itself. Afterward, the cooled material is introduced into the building via a radiant cooling floor. This technology likewise allows storing the cooled fluid in an accumulator; consequently, it can be used during peak demand periods or as an add-on to a fan-coil-based system, reducing the air's initial temperature providing a marginal performance improvement.

Erell and Etzion (Erell et al., 2006; Erell and Etzion, 1999, 1992; Molina et al., 2013) conducted their research on cooling radiators between 1992 and 1996 (Figure 20). They were among the first groups to analyze the parameters that affected radiators’ performance, presenting favorable results without clouds or wind (Erell and Etzion, 1996). Besides the contribution in systems, they studied the cooling potential under typical desert meteorological conditions reaching a cooling power of 90 W·m^{-2}. Moreover, they studied different transmission fluids – water and air– and established sizing methods. In 2008 an air-based system was tested in Greece using a metallic plate radiator painted white (Bagiorgas and Mihalakakou, 2008), achieving temperatures between 2.5 and 4 °C lower than the one without a cooling device.

Material development

White paints have been commonly used in hot regions to reflect solar radiation. Several additives have been used to enhance their performance. Titanium dioxide particles (TiO_2) were tested, reporting a cooling of 15 °C below the ambient in Calgary (Harrison and Walton, 1978). In 1993 the incorporation of barium sulfate ($BaSO_4$) into paint coatings demonstrated improved performance as infrared selective radiators, showing a difference of 3.2 °C with paints without it (Orel et al., 1993).

In 1979 Michell and Biggs tested two different huts: one roofed with a galvanized steel decking painted white and an aluminum decking with aluminized Tedlar (Michell and Biggs, 1979). The white paint, which from 3 μm onwards acted as a blackbody, achieved better behavior than the Tedlar cover. They achieved a cooling power of 22 $W \cdot m^{-2}$ at a roof temperature of 5 °C and ambient 10 °C.

In 1985 a concept called diode roof in which a metallic roof was covered with closed bags painted with titanium dioxide (TiO_2) containing rock mass for insulation was tested (Awanou, 1986). They reported passive cooling of 7 °C below the outside maximum air temperature. Another experiment conducted in Australia in 1989 (Phuong Dung Dan and Chinnappa, 1989) used water initially heated to 35-40 °C was tricked over a solar collector's cover glass exposed to the sky, achieving to cool down a 400-liter deposit to the minimum diurnal temperature.

In 1987, Matsuta et al. designed a dual system that combined solar heating during the day and radiative cooling at night using a solar collector (Matsuta et al., 1987). However, it is considered that the performance of Solar Collector-Sky Radiator (SCR) as a solar collector is worse than a Solar Collector (SC) owing to its lower reflectance for $8 < \lambda < 13\ \mu$m. Ito and Miura researched experimentally and theoretically the thermal performance of an uncovered radiator and a radiative cooling system (Ito and Miura, 1989). The black painted radiator panel's cooling power at ambient temperature was 40-60 $W \cdot m^{-2}$ on clear nights in the summer and 60-80 $W \cdot m^{-2}$ in the fall and winter. The radiative cooling technique to cool down a refrigerator was researched in (Ezekwe, 1990) for developing countries. It provided an average cooling capacity of 628 $kJ \cdot m^{-2}$ reaching 7 °C below ambient temperature.

Although several studies have calculated the radiative cooling potential of different devices and materials in several cities (Vall et al., 2018), countries (Li et al., 2019), or world areas (Argiriou et al., 1992), a more detailed study contrasting calculation with empirical data applied in worldwide climates has not been yet presented. Moreover, when experiments are conducted, they are monitored under clear sky conditions (Raman et al., 2014; Zhai et al., 2017) and during brief periods.

This Thesis deals with the application, development, and climate potential of daytime radiative cooling materials as architecture coatings or active applications to reduce cooling loads without electricity. Moreover, these types of materials can provide free cooling even under incident sunlight. These materials present the opportunity to counteract the increasing penetration of air conditioning equipment while reducing long-wave radiation emissions towards the streets. The next section states the main problems detected in the literature and the aspects this Thesis addresses considering the needs for future application in architecture both as envelope coatings and as part of active systems.

1.2 Problem statement

This central hypothesis of this research is that radiative cooling materials are a promising efficient cooling alternative (active and passive applications) depending on the location's climate. Reflective materials can decrease the surface temperature of roofs, minimize the transfer of sensible heat towards the building's interior, and decrease their cooling demand (Synnefa et al., 2012). There has been renewed interest, especially significant in the last decade, in developing radiative cooling materials; their optimization is seen as evidence of the importance of the technique as a free cooling alternative. However, several aspects need to be addressed if they are to be applied as part of the built environment. The proposed research will deal with some of the main problems detected in state-of-the-art radiative cooling (climate relevance; manufacturing and costs; active and passive application; and adaptability):

Climate relevance

Most of the research on radiative cooling has focused on the development of new materials. However, the use of these materials needs to be studied considering the climate of application. Besides optimizing the optical spectrum, the climate is a crucial determinant of success. Some climates may have the harvesting potential and a low cooling need while others a high need but low potential. Moreover, many recent studies warn of the impact of increasing temperatures on the cooling loads of buildings (Brown and Caldeira, 2017; Campbell et al., n.d.; José et al., 2017; Popovich et al., 2018). This thesis offers a holistic approach towards diminishing the impact of rising temperatures on thermal comfort and decreasing overall electricity consumption linked with refrigeration. Considering the significant energy consumption associated with cooling, this thesis proposes an efficient reduction of cooling loads by developing a series of coatings for architecture that can be applied to roofs, horizontal surfaces and surfaces exposed to the sky (heat sink).

Manufacturing and costs

Current manufacturing methods are complex and not geared towards application in architecture. As a result of intricate manufacturing procedures, the cost of new materials is not suitable for broad application in architecture. At first, the implementation costs of new technology might be high, but prices tend to drop due to improving technologies, economies of scale, competitive supply chains, and growing developer experience (IRENA, 2020a). In this thesis, alternative application and material development techniques will be researched to achieve cost-effective and scalable solutions suitable for application in architecture. The built environment needs easy-to-apply methods and relatively low costs since the surfaces to cover are vast. In this thesis, low-cost and easy-to-apply methods will be proposed to narrow the application gap in architecture.

Active and passive application

Daytime radiative cooling materials have two main possible applications in the built environment. They can be applied as part of an active air conditioning system alleviating the excess heat rejection while improving the equipment's efficiency. Moreover, they can be applied passively as coating materials to reduce the building envelope's temperature and, as a result, the cooling demand. This thesis studies both types of applications. In a passive application, the maximum temperature drop of daytime radiative cooling materials is calculated and compared with traditional materials and daytime radiative cooling materials from other research. As an active application, the maximum radiated heat and total heat losses are determined. For both instances, the climate plays a significant role; therefore, this study will be carried out in different climates.

Adaptability

Daytime radiative cooling materials offer new possibilities that go beyond those of coolmaterials, as they allow cooling throughout the entire day and can achieve lower temperatures thanks to their low solar absorption. However, when applied as passive technology, they might lead to heat penalties since they always reflect and emit heat. To avoid such an effect, the possibility of adding a switchable layer is a promising option, especially in temperate climates. This tunable layer will enable daytime radiative cooling materials to adapt to changes in ambient temperature. This solution has received little interest and needs to be further researched. The present thesis researches the possibility of including a tunable layer to turn the radiative cooling material "on" and "off".

1.3 Objectives and questions

1.3.1 Research questions

- What is the impact of each wavelength on radiative cooling? What is the theoretical temperature drop limit on a given climate? (Chapter 3)
- What kind of designs, materials, and manufacturing techniques should be used to manufacture scalable, low-cost radiative cooling materials and tunable radiative cooling materials for applications in the built environment? (Chapter 4)
- What is the maximum temperature drop achieved by the developed materials in different climates? Are the developed tunable radiative cooling materials able to successfully switch their optical properties? (Chapter 5)
- Which climate conditions benefit the most from a daytime radiative cooling (DRC) material? (Chapter 6)
- How much energy can be radiated by a radiative cooling material (active application)? (Chapter 6)

Why is it worth answering the research questions?

- The exact contribution of each wavelength must be determined in order to effectively design radiative cooling materials. The maximum theoretical limit of the system needs to be determined to observe the behavior of the existing material and the improvements presented by radiative cooling materials.
- Radiative cooling has been widely studied, but easy manufacturing and low-cost materials are needed if they are to be applied in architecture where size requirements, aging, and costs are prerequisites.
- Tests must be performed to ascertain whether the proposed materials can achieve sub-ambient cooling in certain conditions. Moreover, adaptative radiative cooling offers the ability to tune the optical properties of the materials to the ambient temperature to avoid cooling when it is not needed.
- Determining which climates can harvest energy for cooling by using radiative cooling materials is critical; certain climates might have high cooling demands and no potential, while others might be ideal locations to apply systems or coatings using these materials. Targeting where this technology is helpful is crucial. A climate study determines and evaluates the cooling need versus the potential of radiative cooling materials.
- Besides knowing which climates benefit the most from this technology, the potential radiated heat must be quantified before integrating these materials in systems or as envelope coatings in roofs and other horizontal surfaces.

1.3.2 Objectives

OBJECTIVE 1 Define the current radiative cooling possibilities and restrictions.

OBJECTIVE 2 Calculate the energy savings potential of daytime radiative cooling materials.

OBJECTIVE 3 Develop and characterize daytime radiative cooling materials and tunable radiative cooling materials for architecture applications.

OBJECTIVE 4 Test radiative cooling materials under different conditions and in different climates.

OBJECTIVE 5 Calculate the worldwide cooling potential of daytime radiative cooling materials and determine the most suitable climates.

If the predicted increase in worldwide temperature occurs, radiative cooling materials could play a relevant role, especially in locations suffering from the Urban Heat Island effect. Radiative cooling materials have already achieved temperature drops of up to 12 °C below ambient air temperature (Atiganyanun et al., 2018) and cooling power of up to 120 $W{\cdot}m^{-2}$. Therefore, the application of these materials might lower the build-up of heat in cities and significantly reduce their cooling load.

1.4 Methodology

This research aims to expand current knowledge on radiative cooling for future application in the built environment with a holistic and interdisciplinary approach. This thesis addresses the current state-of-the-art in material development and application scenarios and how they could be integrated into architecture. Among other elements, it therefore takes into account manufacturing cost and techniques to be applied onto large surfaces considering the climates of application.

The various objectives in this thesis require different methodological approaches since they deal with different disciplines ranging from heat transfer mechanisms, material design, optimization and development to material testing and climate simulations. The methodology is explained in each chapter within a dedicated section.

After extensive state-of-the-art research, the cooling potential of theoretical and currently available materials is estimated using a heat transfer model that considers different scenarios of sky cover. Afterward, several structures, including daytime radiative cooling material and tunable daytime radiative cooling materials, are designed, optimized, developed, and characterized. The resulting materials have different spectral properties and are tested in two cities with different climate conditions, and finally, their worldwide cooling potential is calculated.

1.5 Scientific relevance

The research deals with specific knowledge gaps detected in the field, especially in the potential worldwide application of radiative cooling. The numerical and experimental assessment of current materials, newly developed materials for reducing the cooling loads of buildings, is regarded as a relevant contribution to the field. This contribution might guide further research coming from architecture in the development of spectrally selective materials for cooling. Furthermore, the methodology followed in each chapter may be helpful not only for the case of daytime radiative cooling but to evaluate the potential of developments in new materials for architecture. Likewise, the research deals with specific research gaps, such as optimizing, developing, and testing materials. Therefore, the results and conclusions presented in Chapters 4 and 5 provide insights on general issues within material development, besides contributing to the main objective of this research project.

The contribution of each wavelength in the ability to cool by radiation was studied with a sensitivity analysis. The radiation spectrum was divided into bands; using the thermal sky emissivity band division, the contribution of each band to achieving sub-ambient cooling was calculated. The most critical bands regarding heat absorption are within the solar wavelength range (0.5-1 μm).

Simple material designs based on single emissive layers might be preferably used for applications in the built environment. Their manufacture is less stringent, and as a result, the costs are more competitive and scalable. Optical characterization of the materials is essential to understand any experimental result.

Two experiments with similar experimental settings were conducted in different temperate climate locations, Sydney and Pamplona, to test climate dependency. The materials managed to achieve a nighttime sub-ambient temperature in both locations under almost adiabatic conditions. Some of the materials were able to achieve significant cooling during the day, as will be further discussed in Chapter 5. Achieving values of 2.70 °C below ambient air temperature during the day and a maximum of 7.97 °C.

Finally, it is worth mentioning that this thesis takes a comprehensive perspective regarding the application of radiative cooling materials across climates, offering a thorough picture of the application of passive[2] cooling strategies. Some of the materials developed were simulated along with materials from the literature, as an active system in several locations experiencing the Urban Heat Island phenomenon, grouped in 14 of the worlds' most prevalent climates. The materials analyzed show great potential for heat evacuation in arid and temperate climates. Chapter 6 is expected to be a valuable reference for applying radiative cooling materials and related solutions across all climates globally.

---

[2] Here the passive concept refers to the radiative cooling phenomenon itself, as it requires no energy to cool down, although it can be applied as a passive or active solution, as will be further discussed in this thesis.

2 DAYTIME RADIATIVE COOLING LITERATURE REVIEW

This chapter presents an overview of recent daytime radiative cooling materials and systems, analyzing the trends in current research. The survey was conducted by reviewing the literature from the first research papers to the recently published investigation. Even though architects and engineers constructed some of the first prototypes, the newest literature on the field has arrived from physicists, material engineers, and chemists. To comprehend the different approaches, multidisciplinary and architecture-specific databases were consulted.

The achievement of daytime radiative cooling was a breakthrough in the field since it allowed reconsidering this technology to mitigate the problems linked with cooling peak demands during the day. Recent material developments are classified in the following categories: multilayer photonic structures, metamaterials, and 2D-3D photonic structures, polymer structures, and paints for radiative cooling. Geometry apertures and windshields are discussed as other aspects of the field, which could help achieve lower temperatures or higher cooling powers.

The final section of this chapter summarizes the research trends and presents the main knowledge gaps detected, offering valuable information for future developments.

2.1 Introduction

The current predictions on energy consumption, CO_2 emissions, and global temperatures' increase is leaning towards a highly demanding energetic scenario. Nevertheless, the number of renewable energy technology installations (hydropower, wind energy, solar, biomass, and geothermal) has been increasingly growing throughout the years (Figure 16), reducing CO_2 emissions and offering alternatives to fossil fuels.

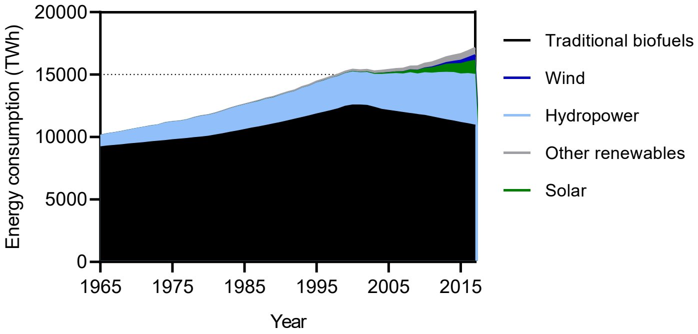

Figure 16: Global renewable energy consumption in the world by source (Ritchie and Roser, 2017).

The efficiency of these developments has improved while their costs have decreased, arriving to be a reliable alternative to traditional energy sources. As stated in the last report of the International Renewable Energy Agency (IRENA, 2020a), renewable power generation costs have dropped in the last decade due to improving technologies, economies of scale, competitive supply chains, and growing developer experience. The renewable power generation capacity has increased 3.4 fold from 2000 to 2019, from 754 gigawatts (GW) to 2,537 GW (IRENA, 2020b).

Most of these technologies are oriented towards producing electricity without emitting pollutants. As discussed in the Energy context section in Chapter 1, modifications of the thermal climate due to urbanization generally lead to a warmer climate compared to the surrounding non-urbanized areas, particularly at night. This event is known as the Urban Heat Island effect (Voogt and Oke, 2003). With rising temperatures, especially in cities, the increase of the cooling load might be unmanageable. As stated in the IEA report (IEA, 2018a), space cooling is the fastest-growing energy use in buildings, both in hot and humid emerging economies. Worldwide final energy use for space cooling in residential and commercial buildings more than tripled between 1990 and 2016, reaching 2,020 terawatt-hours (TWh).

Passive cooling techniques have been applied and researched to achieve thermal comfort in the built environment throughout the years. These techniques prevent heat gains and modulate unwanted heat gains. In contrast, natural cooling is the dissipation of heat from buildings by the processes of radiation, convection, conduction, and evaporation to a lower temperature environmental sink such as air, sky, water, and ground (Figure 17) (Aranovitch et al., 1990, p. 146).

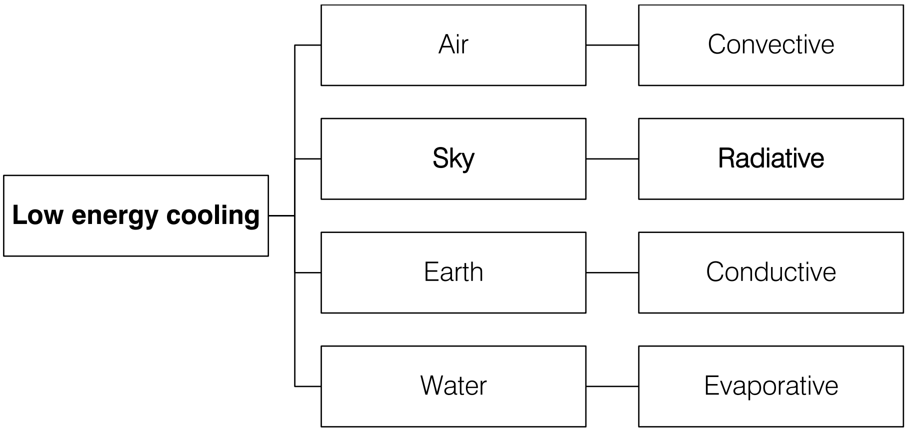

Figure 17: Heat sinks and cooling modes. Based on (Aranovitch et al., 1990, p. 146).

The limitations and intrinsic relationship of passive cooling techniques with climate are clearly stated in the following paragraph (Asimakopoulos and Santamouris, 1996):

> *The operation and efficiency of passive cooling techniques is more dependent on climate than passive heating ones. While the processes for passive solar heating are common throughout the world, passive cooling is based on processes fundamentally linked to climate (air temperature, relevant humidity, velocity and direction of winds). Passive solar heating will always make a positive contribution to the overall thermal performance of a building, whereas improper choice of a cooling technique could create an unpleasant internal environment. In addition, thermal comfort requirements during summer are different for each climate type.*

Besides natural cooling techniques, some active technologies started to emerge. In the second decade of the 20th Century, mechanically driven air conditioning systems were developed in the United States. The Carnot cycle refrigeration system's development using electrically driven compressors helped spread AC systems (Santamouris, 2018). New research has focused on making renewable-energy-based AC systems. As a result, in the last decades, solar-driven cooling systems have increased their popularity (Montagnino, 2018). These systems can be classified into two types depending on their energy input: solar electric process systems, which use photovoltaic cells to transform solar radiation into electric energy, and solar thermal process systems that use heat transformation process as a base for cooling (Prieto, 2018). Despite coupling renewable energy sources to AC systems, the problem still resides because the most widespread cooling system, vapor compression, rejects waste heat to the outside air, heating the streets.

Although the field of radiative cooling has been known since ancient times, as discussed in ▯, it has gained significant interest in recent years (Granqvist and Niklasson, 2018) thanks to new material development that have achieved daytime sub-ambient cooling. Radiative cooling materials use the outer space as a heat sink at 2.7 K, preventing the heat rejection to the ambient. They have the potential to help to mitigate the UHI, reduce buildings' cooling demand, or be coupled to traditional AC systems to avoid dumping heat excess to the streets.

2.2 Methodology

To survey the radiative cooling state-of-the-art, a series of searches in databases were conducted. The topic keywords were defined, starting with general concepts such as "radiative cooling" towards more particular "integration of radiative cooling systems in architecture." These keywords were searched, combining Boolean operators' series to refine the results according to the Thesis research scope. See APPENDIX 1: Research overview methodology for further information.

2.3 Recent advances on daytime radiative cooling

Achieving daytime sub-ambient cooling has been a breakthrough in the field since buildings require cooling during the peak day period (Santamouris and Feng, 2018). To efficiently convert solar radiation into heat, materials need two properties: a high absorptance in the solar spectrum (0.3-2.5 μm) and an almost zero longwave infrared emissivity, as can be seen in Figure 18. On the contrary, to refrigerate it needs high reflectivity outside the atmospheric window ($r \approx 1$ at $\lambda < 8$ μm; $\lambda > 13$ μm) and highly emissive in that band ($\varepsilon \approx 1$ at $8\ \mu m \leq \lambda \leq 13\ \mu m$) (Figure 18)(Granqvist, 1981) allows irradiating heat with high efficiency towards space whose temperature is -270 °C. Spectrally selective materials entail a very complex design process since they have differentiated optical properties along the spectrum, showing absorption or emission areas and others of high reflectance. In 1975, a polyvinyl fluoride (PVF) film produced by Dupont was coated on aluminum and reported in Napoli (Italy) a maximum sub-ambient temperature of 15 °C during the day (Catalanotti et al., 1975).

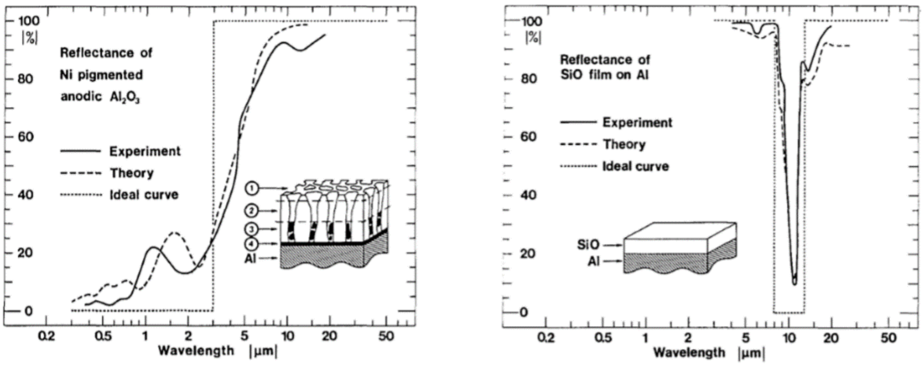

Figure 18: Ideal reflectivity properties. Left, comparison of the ideal solar absorber with a developed material. On the right, the ideal radiative cooler compared with aluminum and a layer of silicon monoxide. Source:(Granqvist, 1981).

Highly reflective selective emittance materials and coatings are a promising technology; they have achieved sub-ambient temperatures during the daytime due to their ability to reflect most incident solar radiation. Some of these materials and coatings are based on a photonic understanding of how their emission spectrum is engineered to achieve efficient radiation in the atmosphere's transparency window wavelengths. Daytime radiative cooling materials will be classified in this Thesis following the division in Figure 19, along with other elements and solutions that help achieve higher temperature drops by eliminating convection or blocking solar radiation.

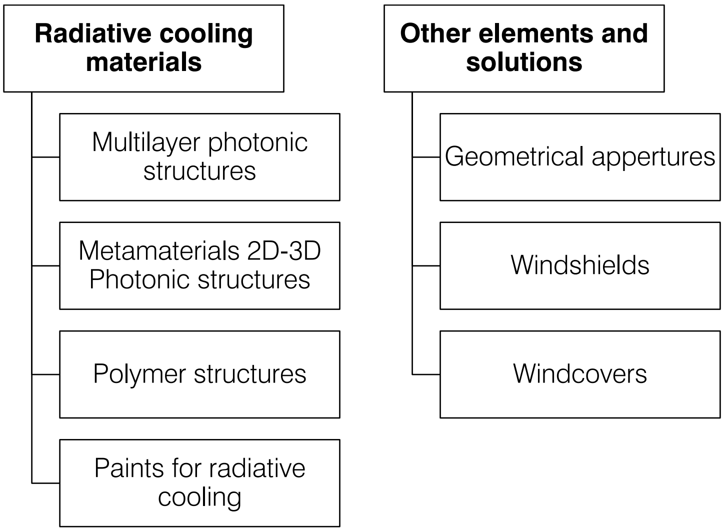

Figure 19: Scheme of material classification based on (Santamouris and Feng, 2018) and completed by the author.

Multilayer photonic structures

Multilayer photonic structures are materials made of several very thin layers of various materials optimized to achieve an ideal optical response. A group at Stanford University developed a selective emittance material used to build a series of radiative cooling prototypes. In 2014 they achieved to cool down the material 4 °C (Raman et al., 2014) below ambient temperature when the sample was exposed directly to the sun. The nanomaterial was composed of a multi-layer multi-stack pattern of different elements made of silicon nitride (Si_3N_4), amorphous silicon (Si), and aluminum (Al), with a thickness of 70, 700, and 150 nm, respectively. Other research proved that theoretically, it was possible to achieve a 60 °C (Chen et al., 2016) reduction below ambient temperature for a sample enclosed in a vacuum chamber, experimentally they achieve an average temperature reduction from the ambient of 37.4 °C and a maximum of 42.2 °C when exposed to the sun with a “sunshade/mirror-cone” for blocking the sunlight. Moreover, they researched the theoretical limits of exploitation of a material for heating and cooling enclosed in a single device. As an absorber it was 24 °C over the ambient temperature and 29 °C below ambient temperature when acting as an emitter (Chen et al., 2018).

The combination of polar materials like SiC and BN on reflective substrates exhibit selective thermal emission behavior whose peaks in the emission profile appear on either side of the restrahlen band, corresponding to wavelengths at which Fabry-Perot like resonances are capable of being sustained (Narayanaswamy et al., 2014). A double-layer coating composed of densely packed TiO_2 particles on top of densely packed SiO_2 or SiC nanoparticles reached a 90.7% reflectivity in the solar spectrum reaches and a 90.11% emittance in the sky window. This material can theoretically achieve 17 °C below ambient at night and 5 °C below ambient under direct solar radiation. However, experiments conducted in Shanghai did not achieve sub-ambient cooling due to high humidity (Bao et al., 2017).

Another polymer-coated fused (PDMS) silica mirror achieves radiative cooling below ambient air temperature under direct sunlight of 8.2 °C and 8.4 °C at night with an average net cooling power of about 127 $W \cdot m^{-2}$ (Kou et al., 2017). As an alternative to metallic substrates, repetitive high index-low index periodic layers were proposed to substitute reflective materials—one study designed two different thin-film stacks, improving the performance by adding an Al_2O_3 layer. The use of periodic TiO2 and SiO2 as high and low index layers obtained a radiative cooling power of 100 $W \cdot m^{-2}$ (Kecebas et al., 2017). Another research proposed optimized BN, SiC, and SiO_2 gratings on top of a metal-dielectric multi-layer structure, achieving a cooling power density of up to 80 $W \cdot m^{-2}$ and mean daytime radiative cooling power of 55 $W \cdot m^{-2}$ in Poitiers (Hervé et al., 2018).

Metamaterials and 2D-3D Photonic Structures

Two-dimensional and three-dimensional structures can be used to enhance resonances and, therefore, aid in designing radiative materials. A daytime equilibrium temperature of 260 K and a cooling power of 105 W·m^{-2} at ambient temperature was reported using two thermally emitting photonic crystal layers comprised of SiC and quartz, on top of a broadband solar reflector made of three sets of five bilayers made of MgF_2 and TiO_2 with varying periods on top of a silver substrate (Rephaeli et al., 2013). Another material made of symmetrically shaped conical metamaterial (CMM) pillars composed of alternating layers of aluminum and germanium can reach a daytime equilibrium temperature of 9 °C below the ambient temperature and 12 °C at night (Hossain et al., 2015).

A 2D photonic structure, fabricated by the focused ion beam technique, excited magnetic polaritons in SiC metasurfaces with three different periods, achieving an emission peak around 0.8 μm (Yang et al., 2017). The cell, coated with silver, consists of a thick phosphorus-doped n-type doped silicon substrate and two identical rectangular dielectric resonators placed perpendicular to each other. Doped silicon was selected to achieve the desired refractive index and loss at IR frequencies, while the silver layer is necessary for enhancing reflection at wavelengths that are not on resonance. It is calculated a minimum temperature decrease at the thermal equilibrium of 10.29 K at nighttime and 7.36 K at daytime, with a maximum net cooling power of 95.84 W·m^{-2} (Zou et al., 2017).

Based on the moth-eye structures, a two-dimensional pyramidal nanostructure for radiative cooling is made of alternating aluminum oxide (Al_2O_3) and silica (SiO_2) multi-layer thin films and a bottom silver layer. The structure achieved both broadband selective emissivity in the infrared atmospheric window and deficient absorption in the entire solar spectrum, achieving a net cooling power exceeding 122 W·m^{-2} at ambient temperature (Wu et al., 2018).

Besides achieving sub-ambient cooling or supercooling, radiative cooling has an exciting photovoltaics application to reduce their operating temperature and improve their efficiency. The proposal by (Jaramillo-Fernandez et al., 2019) is based on a single layer of silica microspheres self-assembled on soda-lime glass. A 14 K reduction on a silicon wafer was found when covered with the structure and 19 K if coated with silver. Under direct exposure to the sun and applied to hot surfaces around 50 K above the ambient achieved a radiative cooling power of 350 W·m^{-2}.

Polymer structures

Polymers are macromolecules formed by the chemical bonding of large numbers of smaller molecules, or repeating units, called monomers (Gad, 2014). Recently, polymer-based radiative cooling films and paints are gaining increasing interest due to their potential in mass production, low cost, and applicability to large systems (Aili et al., 2019a).

Gentle and Smith doped 25 μm thick polyethylene with SiC and SiO_2 nanoparticles on top of aluminum. They covered the device with an IR transparent 10 μm polyethylene (PE) film to avoid convective heat gains achieving a stagnation temperature of 17 °C below ambient in Sydney with about 3 mm of water vapor pressure (Gentle and Smith, 2010b). The same authors combined two polymers, one of them an Enhanced Solar Reflector (ESR) and a silver film on the bottom, and achieved a high solar reflectivity (r=0.97) and high emissivity (ε =0.96) in the transparency window. The reached temperature is 2 °C under solar radiation of 1060 W·m^{-2} with no convection shield (Gentle and Smith, 2015).

Another team developed a metamaterial film (Zhai et al., 2017b) made of a glass-polymer hybrid material that achieved a cooling power of 93 W·m^{-2} under direct sunshine at noon. They integrated this metamaterial into a system to generate “free cooling,” reducing energy consumption. They have achieved savings from 26% up to 46% for the modeled locations (Zhang et al., 2018). New research proposed a cost-effective double-layer coating embedded with titanium dioxide and carbon black particles, respectively responsible for reflecting the solar irradiation and emitting the heat in the atmospheric transparency window (Huang and Ruan, 2017). They predicted a net cooling power of 100 W·m^{-2} during the day and 180 W·m^{-2} at night.

A series of panels cooled water up to 5 °C below the ambient air temperature (Goldstein et al., 2017), covering the panels with a visibly reflective extruded copolymer mirror (3M Vikiuiti ESR film), the same material used in (Gentle and Smith, 2015) on top of an enhanced silver reflective surface. Moreover, they modeled the panel integrated on the condenser side of a building’s cooling system in Las Vegas and calculated an electricity reduction of 21% during the summer. More recently, a 0.2mm-thick transparent radiative film made of polyethylene terephthalate (PET) and silica microspheres was proposed by (Yi et al., 2020) and was previously used in (Zhai et al., 2017b). The silica microspheres are randomly distributed in the PET matrix. They compared two boxes’ performance where the inside air temperature was measured in August in Ningbo, China, showing a 21.6 °C difference between the one with the material and without it.

Paints for radiative cooling

Paints and sprays for radiative cooling offer the possibility to turn almost any surface into a radiative cooler, improving its emissivity in the mid-far infrared wavelengths.

A composite liquid material (Heltzel, 2017) that included up to ten layers of irregularly spaced silica particles embedded in a polymer medium achieved 82 W·m^{-2} radiation flux at an ambient temperature of 300 K (27 °C) when exposed to direct sunlight. A computational study of the aluminum-silver-silica combination yields a cooling potential of 250 W·m^{-2} when exposed at night and outperforms the ideal case. Another proposal avoided using costly metals such as silver to reflect solar radiation to cut expenses and researched silica microspheres that outperformed commercially available solar-reflective white paints for daytime cooling (Atiganyanun et al., 2018). The solar radiation is scattered from the microsphere coating without being absorbed, while the heat escapes from the surface by mid-infrared emission.

Mandal et al. presented (Mandal et al., 2018) a simple, inexpensive, and scalable phase-inversion-based method for fabricating hierarchically porous poly(vinylidene fluoride-co-hexafluoropropene) (P(VdF-HFP)HP) coatings to apply easily as paint. The material had a solar reflectivity of 0.96 and 0.97 emissivities in the infrared. It achieved sub-ambient temperature drops of 6°C and cooling powers of 96 W·m^{-2}. Spraying zinc phosphate sodium (NaZnPO4) onto an aluminum substrate, Ao et al. (Ao et al., 2019) reported a 7.3 °C sub-ambient temperature at noontime in Beijing with exceeding solar radiation of 430 W·m^{-2}.

Twelve samples were fabricated in (Yang et al., 2020) with various film thicknesses and silica sphere sizes made of a metamaterial radiative cooling film made of nanoporous SiO_2 microsphere-Poly-4-methyl -1-pentene (TPX) hybrid system deposited on fluorine-doped tin oxide (FTO) substrates via tape casting. The samples were tested in Shanghai. Although they showed temperatures about 20 °C lower than the black surface, 12 °C lower than the silver-coated glass, and 8 °C lower than the FTO sample, they did not achieve sub-ambient cooling. The samples showed an average temperature of 15 °C higher than ambient.

Geometry apertures

Besides material development, aperture dependency and geometrical designs have been widely studied. Trombe introduced this kind of device in 1967 (cited by (Smith, 2009)) by placing blackbody materials facing the sky and protecting them from the environment. Several authors have continued this research line (Aviv and Meggers, 2017; Smith, 2009; Zhou et al., 2019a, 2019b), showing temperature drops of up to 11 °C below ambient temperature. This type of device seeks to shadow the emitting surface to avoid any solar radiation from heating the surface.

Reducing convective heat gains: wind covers and windshields

Convective heat gains remain a problem to be solved. If sub-ambient temperatures are reached, the convection forces tend to augment the temperature of the radiative cooler. According to Lu et al., reducing the convective heat transfer can be done in two ways, with wind covers and windshields (Lu et al., 2016). The former are materials placed on top of the radiative cooling surface and suppress convection, and the latter are shield walls around the material. Wind covers depend on the material design, and several solutions have been proposed throughout the years. As a general criterion, wind covers for radiative cooling need to transmit highly all over the spectrum. Other authors extensively reviewed the solar transmittance and absorptance and the transmittance in the atmospheric window of 13 wind covers proposed throughout the years (Santamouris and Feng, 2018). Below, the most relevant solutions will be discussed.

Polyethylene (PE) has been one of the most researched wind covers. Its transmittance properties in the atmospheric window were researched (Berdahl et al., 1983; Landro and McCormick, 1980; Matsuta et al., 1987). An in-depth study (Ali et al., 1998) investigated the effect of aging, thickness, and color on polyethylene films' radiative properties. The authors concluded that polyethylene film aging by 100 days led to a substantial degradation in its radiative properties, causing a 33.3% reduction in the night cooling performance. Gentle et al. researched a PE-mesh that eliminated convective gain at night while having a black body transmittance (Gentle et al., 2013). They reported good mechanical stability, low cost, retractable, and an extended outdoor lifetime. Nevertheless, they do not provide data to support this claim (Vall and Castell, 2017). More recent research found that PE films with a pore size of 30-50nm can scatter 80% of the ultraviolet in the solar wavelength range and while simultaneously maintaining 96.6% transmittance, whereas the ordinary PE film with the same thickness transmits 87% (J. Liu et al., 2019).

Besides PE films, Nilsson et al. proposed ZnS and ZnSe due to their high solar and transmittance in the atmospheric window band(Nilsson et al., 1985). Laatioui et al. studied zinc monochalcogenide thin films ZnX (X = S, Se, Te) for radiative cooling applications. The films' properties and cooling potential were theoretically examined in the solar and atmospheric window wavelengths (Laatioui et al., 2018). The resulting cooling power was 159 $W \cdot m^{-2}$ at daytime, and 90 $W \cdot m^{-2}$ for ZnSe and ZnTe, respectively. However, Bosi et al. suggested ways to lower ZnSe cost: decreasing the thickness and subsequently increasing transmittance and developing a lower optical grade ZnSe (Bosi et al., 2014).

Moreover, numerical models suggest that a reduction from 5.0 to 2.5 mm in thickness would improve the transmittance by 10%. Nevertheless, inorganic and semiconductor alternatives for PE such as ZnS, ZnSe, and silicon, although durable present high costs to date (Lu et al., 2016). Moreover, and despite their strength, ZnS and ZnSe present low solar transmissivity (J. Liu et al., 2019). One of the drawbacks of using a convection cover is that when water is deposited on the cover, it reduces its transmittance and reduces thermal radiation's net output. However, when water drops directly on the cooler, it improves since water also has a high emissivity value (Gentle and Smith, 2010a).

Radiators

Many authors (Ahmadi et al., 2016; Ferrer Tevar et al., 2015; Hosseinzadeh and Taherian, 2012; Meir et al., 2002) tested several unglazed radiators with flowing water, achieving different results. An unglazed radiator performed well in clear and low humidity nights in Norway; nevertheless, the authors (Meir et al., 2002) suggested experimenting in climates with cooling demand. Similar research conducted in Iran achieved an average net cooling power of 45 W·m^{-2} and lowered the water accumulation tank up to 8 °C (Hosseinzadeh and Taherian, 2012). A group of Spanish researchers tested radiators with different infrared emissivities and achieved average cooling powers of 60 W·m^{-2}. A radiator insulated with polystyrene foam and bubbled plastic sheets used as top cover achieved temperatures of 20 °C below ambient temperature (Ahmadi et al., 2016).

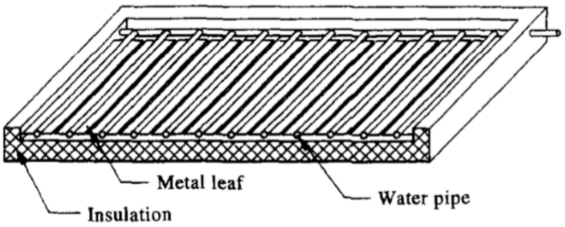

Figure 20: Radiator system. Source: (Erell and Etzion, 1996).

Finally, recent research proposed a single-phase thermosiphon (Zhao et al., 2017) for cold collection and radiative cooling storage. Instead of using an electric pump, their device used buoyancy force to drive heat transfer fluid and achieved an average cooling flux of 105 W·m^{-2} cooling flux.

2.4 Summary and discussion

Radiative cooling has recently diverted from its original approach, from a passive nighttime technology to evacuate heat, towards a daytime application with the development of new technologies and materials. The cooling demand peaks during the daytime, and nighttime radiative cooling does not have the potential to satisfy the cooling demand even with an accumulator. According to Vall and Castell, new functionalities of the device, apart from radiative cooling, are required for profitable reasons (Vall and Castell, 2017). Moreover, the cost of a system whose potential for cooling is around 100 W·m^{-2} needs to be competitive to be implemented.

Many studies have been published regarding the sky cooling capacity and the impact of the weather conditions of radiative cooling (Argiriou et al., 1992; Feng et al., 2020a; Li et al., 2019;

Vall et al., 2018). Nevertheless, no actual application of this knowledge has been considered in the studies exposed before, combining both the understanding of nano-photonics, nano-materials, thin films, and the surroundings' information (Vall and Castell, 2017). Some studies tried to replicate experiments under different climate conditions, Tso et al. (Tso et al., 2017) replicated in Hong Kong the experiment by Raman et al. (Raman et al., 2014), that achieved 5 °C below ambient in California, with two other setting variations and tested its cooling performance. The material in Hong Kong was not able to cool below the ambient temperature during the day.

Regardless of the material development approach, all technologies use the sky as the heat sink; in complex urban environments, the sky's visible portion is limited both from geographical obstacles and buildings. The current context restates the energy-saving strategies presented throughout the 20th and 21st Centuries. Construction materials are linked to energy demand and energy savings in buildings while impacting the urban environment (Santamouris et al., 2011). The increasing concern on global warming and UHI, due to infrared radiation absorption in construction materials (Prado and Ferreira, 2005; Taleghani, 2018) and the heating produced by convective refrigeration systems (Prado and Ferreira, 2005; Taleghani, 2018) highlights the relevance of radiative cooling materials study and application in the built environment. To control radiation absorption, careful study of spectrally selective materials is needed to augment the cooling capacity.

Nilsson and Nikklasson significantly contributed to the development of thin-films for radiative cooling (Nilsson et al., 1992); however, their developments did not result in systems of direct application in buildings. Besides, it is expected to impact the urban environment significantly, reducing the albedo, which lowers the urban heat island magnitude (Prado and Ferreira, 2005; Taleghani, 2018).

2.4.1 Current research trends

Several research trends are presented in the examined literature. They can be summarized in material optimization, scalability, tunability, integration, and new applications.

Material optimization

Designing spectrally selective materials depends on spectrum optimization, which has been possible thanks to several numerical solutions, such as finite element method (FEM), finite difference time domain (FDTD), and boundary element method (BEM), which are the most commonly employed methods (Feng and Santamouris, 2019). The radiative cooling field has dramatically improved thanks to the new possibilities of numerical optimization and material fabrication techniques. Different approaches have been used, ranging from multilayer photonic structures, 2D and 3D photonic structures, polymers, paints, to geometry apertures.

Scalability

Scalability for real-world application is being researched for all the available manufacturing techniques. The high costs of photonics, due to complex fabrication, remain a problem to be solved. Polymeric materials are promising, but their UV-degradation needs to be further studied if they are to be applied under extreme weather conditions throughout lengthy periods. Longer testing times are essential to prove their suitability. Paints and sprays could improve any subjacent material's characteristics, turning any surface into a radiative cooler.

Tunability

Supercooling remains a problem for the passive application of radiative cooling materials. Their cooling ability remains very stable throughout the year and day-night periods where refrigeration is not necessary. As with coolroofs, radiative cooling materials can generate heat penalties during the winter. Further research needs to be conducted for turning radiative cooling materials "on" and "off." Phase change materials, thermochromic materials have been proposed to address this matter.

New applications

Other applications besides building cooling are being researched. Radiative cooling has been proposed to lower operating temperatures of photovoltaic systems for space application or personal thermal management (Cai et al., 2019); however, the requirements are different depending on the target application.

2.4.2 Knowledge gaps

As explained in the introduction section of this chapter, the field has seen tremendous growth in the last years, resulting in several reviews on radiative cooling. Table 2 summarizes their main remarks. Moreover, other knowledge gaps have not been explicitly mentioned in the literature, such as climate adequation, passive vs. active application, and potential in the urban environment. These aspects are essential for a broad usage of radiative cooling techniques in the built environment.

Climate adequation

Daytime radiative cooling materials need to be very reflective in the solar wavelengths and very emissive in the transparency window. However, it is expected that the material's behavior might change depending on the location's climate. Therefore, the material's spectrum should be optimized according to that specific climate. The developed materials are usually tested under one determined condition; however, materials should be studied systematically under different climate conditions to test whether they have a broad or specific application. A material that works well under a particular climate and location might not work in another place.

Passive and active application development

Although some first attempts were made to integrate radiative cooling into AC systems, new systems need to be proposed and commercialized to test the thin layer's efficacy to cool down large amounts of fluid. A careful study should be conducted on the buildings' envelope composition when acting as a passive material such as an architectural coating.

Potential in urban environments

Radiative cooling material's thermal equilibrium depends on various heat transfer mechanisms: radiation, convection, and conduction. Longwave urban radiation has not been considered when calculating the potential of these materials. Experiments have been conducted with an unobstructed view of the sky, considering longwave radiation solely from the atmosphere. Further research to determine the potential of these materials in urban environments should be a priority.

Integration

One of the many possible applications of radiative cooling materials is in the built environment. Most radiative cooling materials are made of a reflective substrate where the glaring effect might not be suitable for integration in architecture. Moreover, different color ranges are needed to apply them in different urban contexts.

Table 2: Selection of knowledge gaps detected in reviews on radiative cooling published in the last decade.

Climate adequation
The atmospheric conditions in a particular geographical (Hossain and Gu, 2016).
Optimize radiative cooling devices in different areas of the world (Ko et al., 2018).
Climate dependence of the radiative coolers is location specific (Zeyghami et al., 2018).
Investigation of seasonal and regional applicability (B. Zhao et al., 2019).
Identify locations suitable for radiative sky cooling technology (D. Zhao et al., 2019b).
Determine the real potential of the technology (Vall and Castell, 2017).
Passive versus active application
Radiatively cooled water-collecting surfaces (Granqvist and Niklasson, 2018).
Undesired cooling during the heating period in buildings (Santamouris and Feng, 2018).
For sub-ambient applications finding a durable convection suppressant. (Zeyghami et al., 2018)
Development of a suitable wind cover for the sub ambient RC technology to improve the net cooling power, to protect radiative coolers, and to improve the stability. (J. Liu et al., 2019)
Development of new concepts and systems. (Vall and Castell, 2017)
Store the cold and effective coupling between the load and the cooler (Zeyghami et al., 2018).
Modeling on savings in energy expenditure and CO_2 (Yang and Zhang, 2020).
Integration
Combination with other passive cooling devices (Hossain and Gu, 2016) .
Building integration is an obstacles of radiative cooling (Lu et al., 2016).
Integration of thermal photonic structures into practical thermal systems (Fan, 2017).
Material development
The realization of strictly selective radiators with substantial solar reflection. (Hossain and Gu, 2016)
Optical properties obstacles of radiative cooling. (Lu et al., 2016)
Use of a material with appropriate properties. (Vall and Castell, 2017)
Multilayer designs with angular performance tailored to specific building sites and orientation. (Granqvist and Niklasson, 2018)
The choice of material and optimization of the nanosphere size and filling fractions. (Ko et al., 2018)
Angular, polarization, reciprocity and dynamic control, and thermal extraction. (Li and Fan, 2018)
Optical characteristics improvement may be of quite marginal importance. (Santamouris and Feng, 2018)
Stability and durability of different radiators, especially for polymer related. (B. Zhao et al., 2019)
Optimization of the device performance by simulation, material design, and system engineering. (Yang and Zhang, 2020)

Cost, fabrication, scalability
Cheap materials may be required to fabricate roof panels (Family and Mengüç, 2017).
Nanostructures widespread fabrication is still considered costly. (Family and Mengüç, 2017)
Photonic structures are relatively new in the market and expensive. (Zeyghami et al., 2018)
Alternative fabrication techniques and less complex designs (Zeyghami et al., 2018).
Scalation of photonic structures (Fan, 2017).
Scalable process for low-cost production (Sun et al., 2017).
Nanosphere design for future commercialization: large-scale production capabilities, and ease of fabrication and broad applicability. (Ko et al., 2018)
Scalability of the structures is a serious concern. (Santamouris and Feng, 2018)
The design and fabrication of large-scale cost-efficient radiators for commercial application. (B. Zhao et al., 2019)
Durability and cost analysis. (Yang and Zhang, 2020)
Consider cost, durability, and mechanical properties. (Yang and Zhang, 2020)
Tunability
Incorporating phase change materials to switch the radiative cooling on and off (Ko et al., 2018).
Integration of materials with temperature dependent emissivity (Santamouris and Feng, 2018).
Active radiative-cooling system to enable or disable cooling (Li and Fan, 2019).
The integration of daytime radiative sky cooling materials with new functionality, e.g., self-adaptive cooling, could significantly improve the efficiency of this technique. (D. Zhao et al., 2019b)

3

ON THE ENERGY POTENTIAL OF DAYTIME RADIATIVE COOLING MATERIALS FOR URBAN HEAT ISLAND MITIGATION[3]

This chapter presents the potential of daytime radiative cooling materials as a strategy to mitigate the Urban Heat Island effect. To evaluate the cooling potential of daytime radiative cooling materials, 15 theoretical materials and 7 existing materials were simulated: 2 daytime radiative cooling materials, a cool material, 2 white paints, a thermochromic paint and a typical construction material. A sensitivity analysis was performed to evaluate the impact of each wavelength emissivity on the ability to achieve sub-ambient radiative cooling. The heat transfer model, which includes conduction, convection, and radiation, was developed using a spectrally selective sky model for clear skies, with two correlations for partially covered skies and completely covered skies. Two background conditions were considered: a very conductive surface and a highly insulated one. All the materials were simulated in two cities that suffer from the Urban Heat Island effect—Phoenix and Sydney—under clear sky conditions during the summer solstice. The mean surface temperature reduction achieved was 5.30 °C in Phoenix and 4.21 °C in Sydney. The results presented suggest that the type of application is a determinant factor in the design of radiative cooling materials. Modifying the spectra of the materials led to a substantial change in the cooling potential and the surface

---

[3] This chapter was originally published as: Carlosena, L., Ruiz-Pardo, Á., Feng, J., Irulegi, O., Hernández-Minguillón, R.J., Santamouris, M., 2020. On the energy potential of daytime radiative cooling for urban heat island mitigation. Sol. Energy 208, 430–444. https://doi.org/10.1016/j.solener.2020.08.015

temperature obtained. A material that performs well in a dry climate as a passive solution could perform poorly as an active solution.

3.1 Introduction

Nowadays, half of the world's population lives in urban areas (*World Urbanization Prospects*, 2014) and consumes 75% of the primary energy sources, emitting between 50 and 60% of greenhouse gases ("Energy – UN-Habitat," n.d.). Furthermore, the world's urban population is expected to increase by more than two-thirds by 2050, reaching 6.3 billion (*World Urbanization Prospects*, 2014), with nearly 90% of this rise taking place in cities across Asia and Africa. CO_2 emissions increase proportionately with population due to energy use (O'Neill et al., 2012). A 1% increase in the urban population is estimated to increase energy consumption by 2.2% (Santamouris et al., 2001). The global energy demand is predicted to increase by more than 25% if the IEA's New Policies Scenario (rising incomes and an extra 1.7 billion people) is followed (IEA, 2018b).

Higher urban temperatures are due to the positive thermal balance of urban areas in comparison with rural areas, caused by (i) the significant release of anthropogenic heat, (ii) the excess storage of solar radiation by city structures, (iii) the lack of green spaces and cold sinks, (iv) the non-circulation of air in urban canyons, and (v) the reduced ability of emitted infrared radiation to escape into the atmosphere (Oke et al., 1991). This phenomenon, known as the Urban Heat Island (UHI), is well documented in more than 400 cities around the world (Santamouris, 2019), and the total number of reported cities is increasing rapidly. The average UHI varies between 0.5 °C to 7 °C, where 90% of the data is below 4.5 °C (Santamouris, 2020). As ambient air temperature increases, the carrying capacity of electric power cables decreases, a phenomenon that occurs more during the summer with the increase in electricity load caused by air-conditioning usage (Bartos et al., 2016). Moreover, UHI and heatwaves have a relevant environmental and financial impact, especially on vulnerable and low-income populations (Santamouris and Kolokotsa, 2015). Additionally, exposures to high ambient temperatures represent a serious health danger (Brooke Anderson and Bell, 2011).

The urban climate is strongly determined by morphological characteristics and the properties of the materials comprising the urban landscape (Lemonsu et al., 2015). Many strategies focusing on new material developments have been proposed to mitigate the rise in cooling demand, and the increase in urban temperatures. Increasing the global albedo of the city has resulted in a reduction in the peak ambient temperature of up to 3 °C and a 20% reduction in peak cooling demand in residential buildings (Santamouris et al., 2018). Cool roofs have been widely studied for reducing the cooling demand (Bell et al., 2003; Berdahl and Bretz, 1997; Erell et al., 2006; Kolokotroni et al., 2013; Kolokotsa et al., 2018; Miller et al., 2015; Radhi et al., 2017; Santamouris, 2013; Santamouris et al., 2008). Green roofs and vegetation have been proposed as a mitigation strategy as well (Foustalieraki et al., 2017; Herrera-Gomez et al., 2017; Kolokotsa et al., 2013; Zinzi and Agnoli, 2012).

Recently developed radiative cooling materials have achieved daytime sub-ambient temperatures even under direct solar radiation. Radiative cooling is the physical phenomenon by which an object dissipates heat as infrared radiation. Over mid-infrared wavelengths, between 8 and 13 μm, the Earth's atmosphere is transparent to electromagnetic radiation. Radiative cooling was applied as a nocturnal passive system for cooling in some experimental buildings and prototypes (Yellot, 1976; Yellot, John I., 1976). The results showed a limited nocturnal cooling capacity since longwave radiation from commonly-found materials can rarely achieve cooling powers of more than 100 W·m^{-2}, even under ideal meteorological conditions (Erell and Etzion, 1992). Material sciences have significantly evolved since the first designs were researched in the early '70s and radiative cooling materials have recently been developed (Kou et al., 2017; Li et al., 2017; Raman et al., 2014; Rephaeli et al., 2013; Shi et al., 2018; Zhai et al., 2017b; Zhu et al., 2015, 2019). Novel materials such as photonics, metasurfaces, and polymers have already achieved 120 W·m^{-2} under direct sunlight (Santamouris and Feng, 2018). Besides material development, aperture dependency and geometrical designs have been studied. This kind of device was introduced by Trombe in 1967 (cited by (Smith, 2009)) by placing blackbody materials facing the sky and protecting them from the environment. Several authors have continued this line of research (Aviv and Meggers, 2017; Smith, 2009; Zhou et al., 2019a, 2019b), showing temperature drops of up to 11 °C below ambient temperature.

In order to achieve daytime radiative cooling, the optical properties in each wavelength of a material are determinant. The material needs to emit highly in the atmospheric transparency window (7.9-13 μm) and reflect at least 94% of incident sunlight (0.3-3 μm) (Raman et al., 2014). Absorbing 10% of incident solar radiation is approximately 100 W·m^{-2} and therefore, the thermal equilibrium is reached at a higher temperature than the ambient temperature. Daytime radiative cooling materials have been coupled to air-conditioning (AC) systems to evacuate the excess heat to space instead of to the ambient air (Aili et al., 2019b; Goldstein et al., 2017; W. Wang et al., 2018; Zhang et al., 2018). In (D. Zhao et al., 2019a), the authors compared an air radiative cooling system with other materials and systems (shingle roof, attic ventilation, and coolroof). Using their proposed radiative cooling system, they achieved a reduction in the attic air temperature of 15.5-21 °C. Another system using the material developed by (Zhai et al., 2017b) reduced the energy consumption and achieved savings from 26% to 46% for the modeled locations (Zhang et al., 2018).

Radiative cooling depends on the optical properties of the material and the thermal exchange with the surroundings. The effect of climatic parameters such as the effect of air temperature, solar radiation, and ambient radiation have recently been discussed (Feng et al., 2020a). Moreover, the contribution of convection has been vastly researched (Chen et al., 2016; Cui et al., 2016; Huang and Ruan, 2017; Kou et al., 2017). Various studies have calculated the radiative cooling potential of several devices and materials in different cities (Feng et al., 2020a; Vall et al., 2018), countries (Li et al., 2019), and areas of the world (Argiriou et al., 1992). Nevertheless, a more detailed study showing the impact of the optical properties of each wavelength band on the ability to achieve sub-ambient cooling has not yet been presented.

This research aims to study the impact of the different spectral selectivity configurations in the cooling potential of radiative materials by conducting a sensitivity analysis. The effects of each wavelength's band emissivity on the ability to achieve sub-ambient cooling was determined. The authors compared the performance of several theoretical radiative cooling materials with newly developed ones and typical construction materials. The materials were studied under two conditions to assimilate a passive and active solution (for future integration in AC systems). Firstly, the passive solution was designed as a highly insulated surface on one side (an almost adiabatic condition). Secondly, the active condition was assimilated to a very conductive surface. Besides, several convective values were simulated to determine the maximum sub-ambient cooling. As a result, considerations for choosing the appropriate spectral emissivity configuration are given for each location. The restrictions to achieving daytime radiative cooling are detailed for both conditions.

The main novelty of this study is that it shows that the desired spectral emissivity characteristics of radiative cooling materials depend on the climate conditions and the type of application. It was discovered that the best spectral characteristics are different for a dry or humid climate and if the application is for a passive system or an active one. In-depth study of these two aspects is required in future research to establish the level of importance of these two observations using broader statistical data.

3.2 Methodology

The research methodology described was followed to determine the impact of the spectral emissivity configuration on the possibility of achieving sub-ambient temperatures. First, a heat transfer model was developed. This model simulated a horizontal flat plate, in which the conductive heat transfer was calculated using the finite difference method (implicit method). The boundary conditions on the lower side were convection and the temperature of a fluid. For a highly insulated condition, a nearly zero value is defined for the convective heat transfer coefficient. For the upper side, the boundary conditions defined were convection with air, incident solar radiation, and radiation exchange with the atmosphere. The optical properties varied spectrally, and the model considered this variation for both solar radiation and atmospheric radiation. Atmospheric radiation is based on the spectrally selective sky model presented in (Berger and Bathiebo, 1989), where the sky conditions were defined as clear sky, completely covered sky, and partially covered sky.

The model can perform transient and steady-state simulations with time steps specified at the beginning of each simulation (for this study, a 1-minute time step was used in all cases); the summary results presented are hourly, however. The main variables obtained in the results are surface temperatures and heat transfer on the surface. The heat transfer is discretized for each transfer mechanism: conduction, convection, radiation from the atmosphere, and solar radiation absorption. The power at the end of the hour is given for each heat transfer mechanism. Moreover, the cumulative energy transferred during the hour is presented. The previous results are used to obtain other related parameters, such as the hourly difference between air temperature and surface temperature, the daily mean of this difference, daily mean temperatures, and cumulative daily heat transfer.

The model was validated using outdoor experimental data from two newly developed radiative cooling materials (Raman et al., 2014; Zhai et al., 2017b). Following the validation, the sensitivity analysis was conducted with 90 theoretical materials and 7 existing materials in two locations: Sydney, with a mild climate and Phoenix, with an arid climate (Cfa and Bsh respectively according to (Kottek et al., 2006)). Moreover, the two boundary conditions—a high insulated and a very conductive surface—were simulated. Finally, the results are compared according to their radiative cooling potential and the surface temperature they reached. The suitability, restrictions, and limitations for each are presented for each location and boundary condition.

3.2.1 Heat transfer model

The objective of the heat transfer model is to simulate the thermal behavior of a horizontal surface that exchanges heat with its surroundings by convection and radiation. Radiation is divided into two components: solar radiation and radiation with the surroundings. The surrounding radiation will be assumed to be only from the sky. The heat transfer model calculated the heat transferred by conduction from the surface down with the finite difference method. The emphasis of the model is on the two radiation components, since it considers the spectral characteristics of the surface, sky, and solar radiation; therefore, only this component will be explained.

The radiosity of a surface with a view factor equal to one with the sky can be represented by:

$$J_s(v) = \varepsilon_s(v)E_b(v,T_s) + \left(1-\varepsilon_s(v)\right)G_s(v) \tag{4}$$

Where $J_s(v)$ is the radiosity of the surface for the wavenumber v, $\varepsilon_s(v)$ the emissivity of the surface for the wavenumber v, $E_b(v, T_s)$ the blackbody radiation in the wavenumber v when its temperature is T_s, $G_s(v)$ the irradiance received by the surface at a wavenumber v.

As the sky is the only radiation emitter that the surface faces, the irradiance received by the surface is:

$$G_s(v) = \varepsilon_{sky}(v) E_b(v, T_{air}) \tag{5}$$

Therefore:

$$J_s(v) = \varepsilon_s(v) E_b(v, T_s) + \big(1 - \varepsilon_s(v)\big) \varepsilon_{sky}(v) E_b(v, T_{air}) \tag{6}$$

On the other hand, the radiation heat flux in the surface for the wavenumber v is:

$$q_{r,s,v} = J_s(v) - G_s(v) \tag{7}$$

$$q_{r,s,v} = \varepsilon_s(v) \Big(E_b(v, T_s) - \varepsilon_{sky}(v) E_b(v, T_{air})\Big) \tag{8}$$

For the wavelength bands between wavenumbers v_i and v_j the heat flux is:

$$q_{r,s,\Delta v} = \int_{v_i}^{v_j} \varepsilon_s(v) \Big(E_b(v, T_s) - \varepsilon_{sky}(v) E_b(v, T_{air})\Big) dv \tag{9}$$

$$q_{r,s,\Delta v} = \int_{v_i}^{v_j} \varepsilon_s(v) E_b(v, T_s) dv - \int_{v_i}^{v_j} \varepsilon_s(v) \varepsilon_{sky}(v) E_b(v, T_{air}) dv \tag{10}$$

Selecting a range or band Δv where both $\varepsilon_s(v)$ and $\varepsilon_{sky}(v)$ can be considered approximately constant yields the following expression:

$$q_{r,s,\Delta v} = \varepsilon_{s,\Delta v} \left[\int_{v_i}^{v_j} E_b(v, T_s) dv - \varepsilon_{sky,\Delta v} \int_{v_i}^{v_j} E_b(v, T_{air}) dv\right] \tag{11}$$

The previous equation makes it possible to calculate the heat flux exchanged by radiation with the sky for each band in which the emissivity of the sky and the surface can be considered constant. The total heat flux is therefore the summation of the heat flux of each band:

$$q_r = \sum_{\Delta v_i} q_{r,s,\Delta v_i} \tag{12}$$

The second component of radiation is the solar radiation. In this case the heat can be calculated with:

$$q_{sun} = \int_0^{\infty} \varepsilon_s(v)\, I(v) dv \tag{13}$$

And similar to the previous considerations, if there are bands where emissivity can be considered as constant, the previous integral can be approximated by a summation:

$$q_{sun} \approx \sum_{\Delta v_i} \varepsilon_{s,\Delta v_i} I_{\Delta v_i} \tag{14}$$

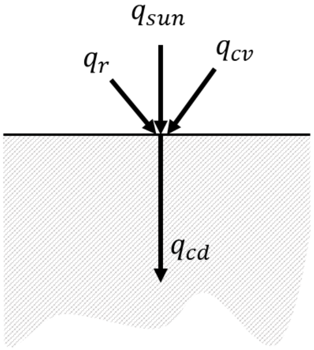

Figure 21. Heat flux in the surface

Finally, the balance of heat flux at the surface, following the schematic representation of Figure 21, can be expressed as:

$$q_{cd} = q_r + q_{sun} + q_{cv} \tag{15}$$

Where:

$$q_{cv} = h_{cv}(T_{air} - T_s) \tag{16}$$

And q_{cd}, as stated above, is calculated using the finite difference method.

Sky model review and development

Calculating the heat transfer with the atmosphere using equation (8) requires the spectral emissivity of the sky ($\varepsilon_{sky,\Delta v}$) to be known.

Although there is a vast literature on sky models (30 evaluated in (Vall and Castell, 2017), 35 in (Algarni and Nutter, 2015) and 70 in (Antonanzas-Torres et al., 2019)) both for clear sky conditions and cloudy conditions, most of them refer to global emissivity. Clouds act as a barrier to heat transfer, inhibiting the outgoing radiation through the atmospheric band and augmenting the effective temperature of the sky due to the absorption of heat by water vapor (Berdahl and Fromberg, 1982). Opaque clouds can be considered blackbody emitters at the temperature of the cloud base (Bliss, 1961) and their radiative effect close to the transparency window. The influence of cloud radiation decreases with altitude; higher clouds are colder than lower clouds (Sugita and Brutsaert, 1993). Nevertheless, measurements of the downward component emitted by clouds and aerosols in the atmosphere are scarce and not well understood (J Herrero and Polo, 2012).

Cloudy sky models are based on daytime clearness indexes and are transposed as a single value for the night; moving clouds cannot be considered (Eicker and Dalibard, 2011).

Moreover, at night there are no cloud coverage estimations. Malek (Malek, 1997) proposes a method to evaluate sky cloud cover without having to relate to any empirical and local constants. It is based on the cloud base height, cloud base temperature, and percentage of the sky covered by clouds. Emissivity value estimates are 1 under cloudy conditions (Martin and Berdahl, 1984) and above 0.95 for covered skies (J. Herrero and Polo, 2012). According to (Monteith and Unsworth, 2013), for a completely overcast sky (cloud fraction $c = 1$) in Oxford, England, the apparent emissivity of the sky can be calculated knowing the emissivity value for clear sky by:

$$\varepsilon_{sky,cloud} = \varepsilon_{sky}(1) = 0.84 + 0.16\varepsilon_{sky,clear} \quad (17)$$

And for a sky covered with a fraction "c" of cloud, emissivity can be calculated by interpolation:

$$\varepsilon_{sky}(c) = c\varepsilon_{sky}(1) + (1 + c)\varepsilon_{sky,clear} \quad (18)$$

Clear sky emissivity model

This research uses the Berger and Bathiebo 1989 (Berger and Bathiebo, 1989) spectral sky model to calculate the spectral radiation of the atmosphere. The model calculates the spectral and global emissivity of the sky in 21 wavelength ranges, using Equation (19).

$$\varepsilon_{sky,\Delta v_i} = 1 - exp\left(-k_{\Delta v_i} w_j\right) \quad (19)$$

Where $\varepsilon_{sky,\Delta v,i}$ is the clear sky emissivity for the range of wavenumbers Δv_i; $k_{\Delta v,i}$ is an absorption coefficient, and w_j an equivalent absorber that must be calculated using different correlations defined by (Berger and Bathiebo, 1989) for each band.

Completely covered sky emissivity

To the best knowledge of the authors, there are no correlations to calculate the spectral emissivity under completely covered skies with a similar degree of discretization that has been presented for clear skies. The model developed can calculate the emissivity of the sky using a correlation of Equation (17) or a constant value. By default, a value of 0.95 (J. Herrero and Polo, 2012) was used for the results calculated in this paper.

Partially covered sky emissivity

As shown in Equation 15, a linear relationship between the emissivity of clear skies and completely covered skies is presented in (Monteith and Unsworth, 2013). This principle can be applied for each spectral band. The parameter "c" is used as the fraction of sky covered by clouds, 1 being a completely covered sky. For a sky covered with a fraction c of cloud, interpolation gives:

$$\varepsilon_{sky,\Delta v_i}(c) = c\varepsilon_{sky}(1) + (1-c)\varepsilon_{sky,\Delta v_i} \tag{20}$$

The sky emissivity for a partially covered sky is the weighted average between the emissivity of clear sky and the completely covered sky, the ratio of the covered sky being the weighting factor. Note that emissivity for a completely covered sky $\varepsilon_{sky}(1)$ is not dependent on the wavenumber since there is no information about its spectral variation.

3.2.2 Model validation

The model was validated using data from two recently developed materials in the literature (Raman et al., 2014; Zhai et al., 2017b) and summarized in Table 3; the authors reported very high cooling rates even when exposed to the sun and achieved a substantial temperature drop from the ambient temperature. The model agreed well with experimental data (Figure 22 and 27) and is considered valid.

Table 3: Comparison of the experimental conditions of two radiative cooling materials, "Skycool" and "Radicool".

	Skycool (Raman et al., 2014)	**Radicool (Zhai et al., 2017b)**
Solar Reflectivity	0.90	0.90
Emissivity in the transparency window	0.80	0.93
Reported sub-ambient temperature	4.9 °C	-
Cooling potential	40.1 W·m^{-2}	93 W·m^{-2}
Location of experiment	Stanford, CA, USA	Cave Creek, AZ, USA
Köppen climate exp	Csb	BSh
Dates of the experiment	Clear winter day	16th Oct. to 19th Oct (Fall)

In the experiment conducted in 2014, the authors exposed the radiative cooling material protected by a low-density polyethylene cover to the sky. These polyethylene covers acted as a convection barrier (See APPENDIX 2: Model validation).

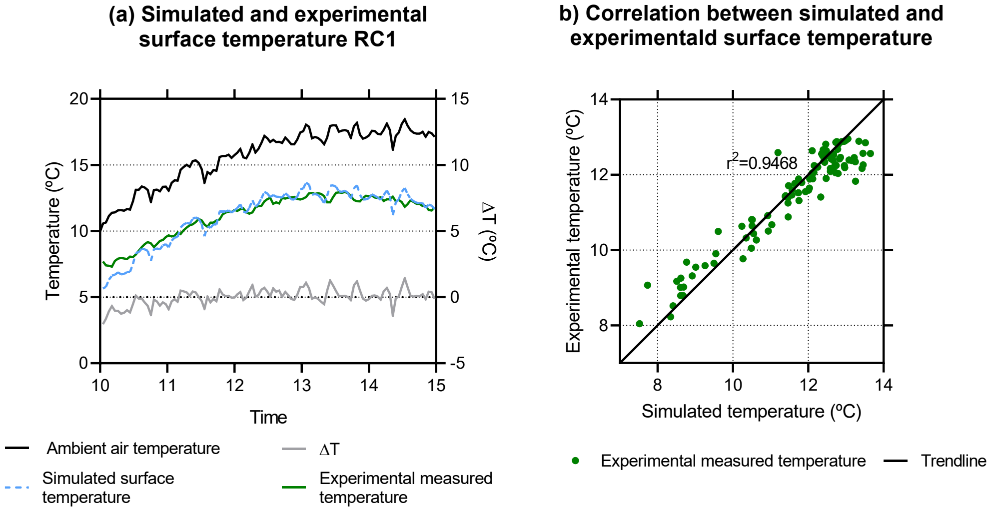

Figure 22. Validation of the thermal model with material 1 (RC1) "Skycool" (Raman et al., 2014).

The second experimental setting was different; they eliminated convection by applying a constant heat supply to the material to achieve ambient temperature.

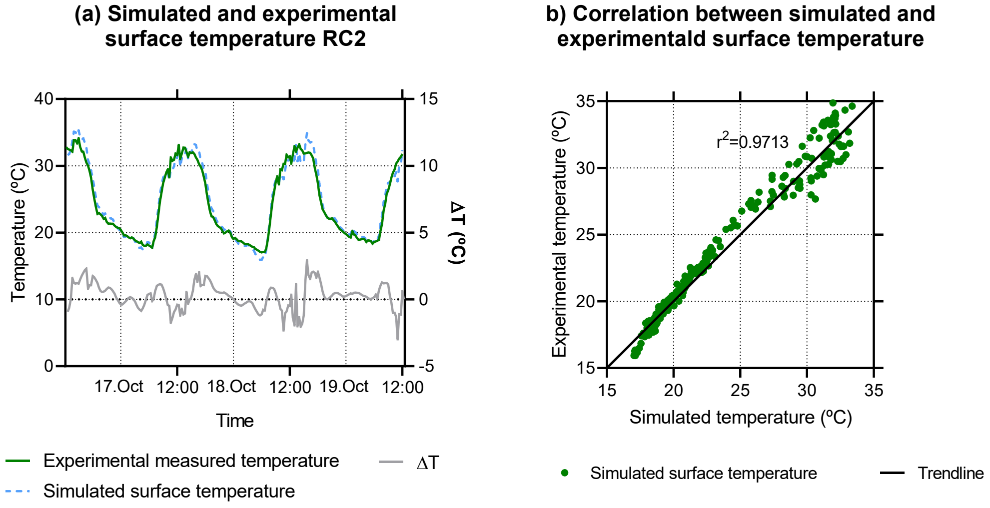

Figure 23. Validation of the thermal model with material 2 (RC2) "Radicool" (Zhai et al., 2017b).

3.2.3 Sensitivity analysis

The objective of this sensitivity analysis was to determine the impact of wavelength emissivity on the ability to achieve daytime radiative cooling. The radiation spectrum was divided into 39 bands (See APPENDIX 3: Band division), starting from the original 21 wavelength bands from the atmospheric radiation model (Berger and Bathiebo, 1989).

An emissivity value of zero or non-zero was assigned to each band; fifteen wavelength combinations were proposed. To establish the bandwidth for an ideal material, the non-zero emissivity values of the theoretical materials were selected to be centered in the transparency window of the atmosphere (infrared emission), shown in Figure 24. Similarly, for the visible region, the emissivity values were centered in the region with the highest solar irradiance. The band combinations resulted in the 15 theoretical materials (M1-M15) shown in Figure 25. Moreover, to quantify the impact of the emissivity value, six emissivity values (1, 0.9, 0.8, 0.7, 0.5, and 0.25) were assigned to the non-zero value, resulting in a total of 90 theoretical materials (See APPENDIX 4: Theoretical materials).

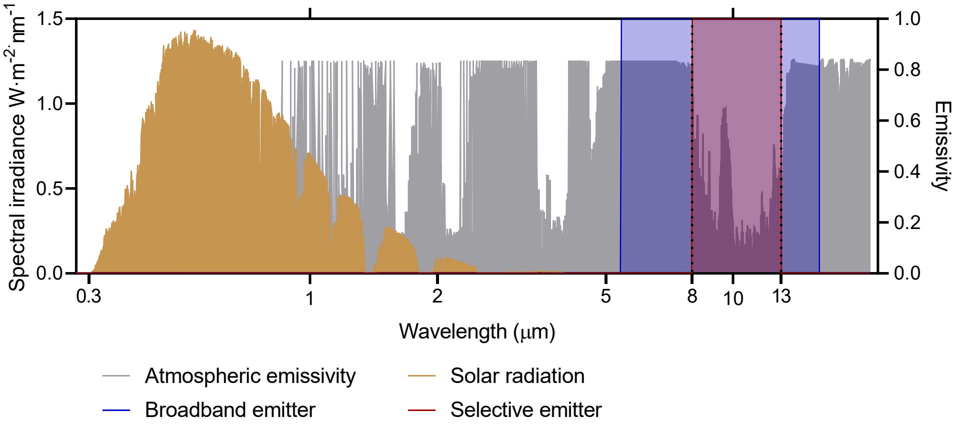

Figure 24. Solar spectrum, atmospheric emissivity, and two materials for radiative cooling, a broadband emitter material (blue) and a strictly selective emitter material (red) .

The performance of the theoretical radiative cooling materials (M1-M15), as shown in Figure 25 was compared with existing radiative cooling materials (Skycool (RC1) and Radicool (RC2)) and other construction materials (CM1-CM5 e.g., white paints, brick, and coolmaterials) (Figure 26) for the same boundary conditions. This provides a better understanding of the potential benefits and ways to improve these materials.

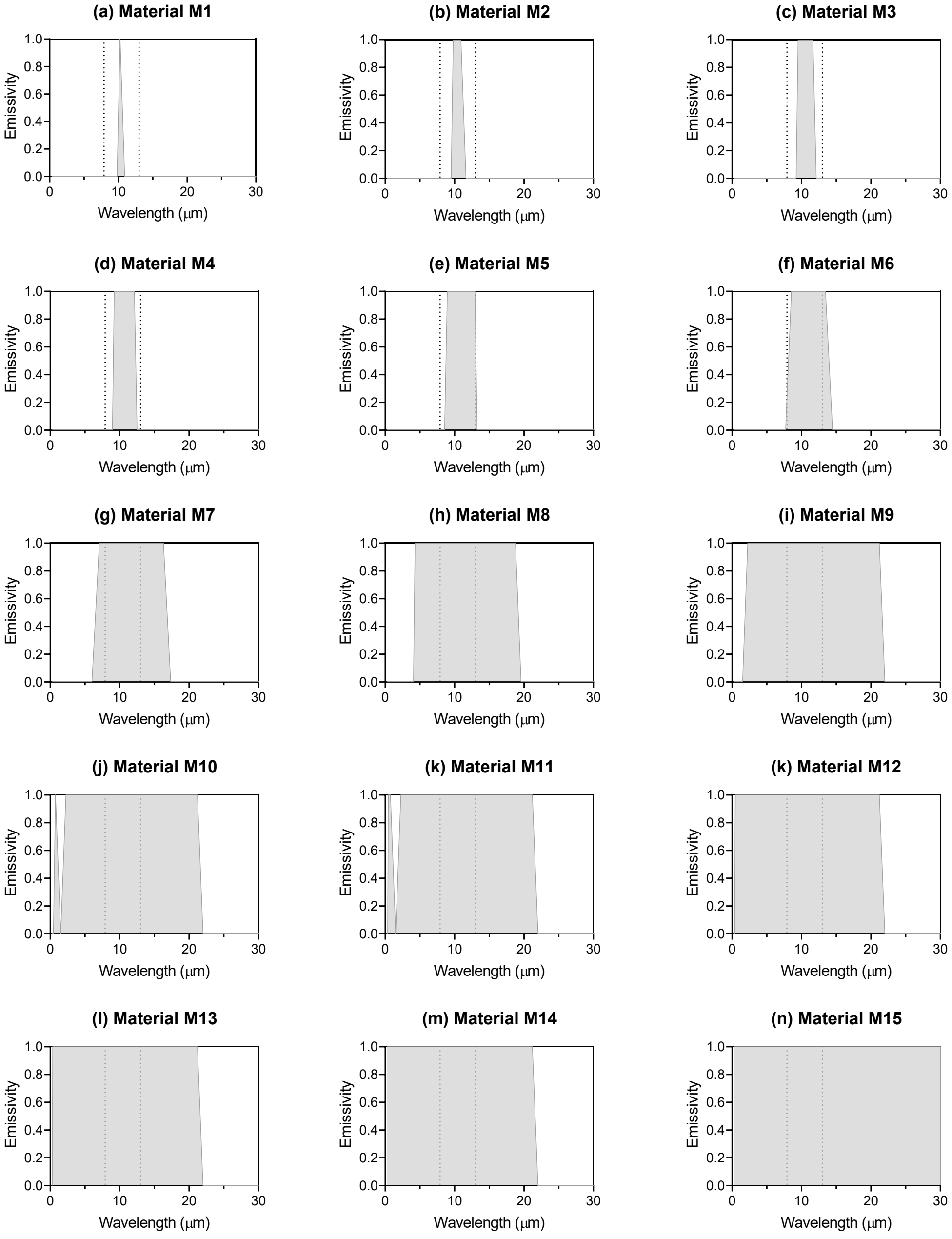

Figure 25. Emissivity of the theoretical materials (M1-M15) resulting from combining emissivity values of 1 and 0 in the 39 wavelength bands.

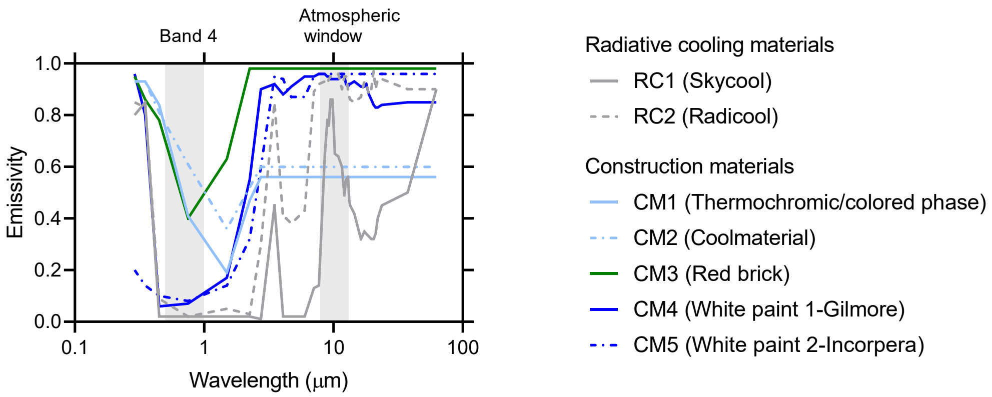

Figure 26. Emissivity comparison of existing radiative cooling materials (RC) and construction materials (CM).

The sample's thermal response was calculated in two different cities, Phoenix (hot and dry) and Sydney (mild and humid) during the summer solstice, on 21st June and 21st December, respectively. The climates of the selected cities obtained from Meteonorm (*Meteonorm 7*, 2017) represent completely clear skies and are shown in Figure 27.

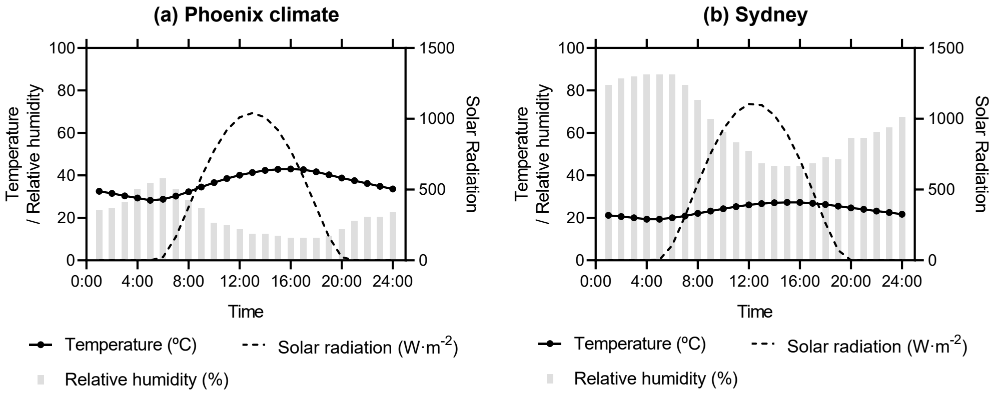

Figure 27. Hourly climatic parameters in summer solstice for Phoenix and Sydney.

3.3 Results

Two different simulation conditions were considered: a highly insulated and a very conductive surface (Table 4).

Table 4: Material substrate for two background conditions

Background conditions	Material	Thickness	Thermal conductivity
1. Insulated	Insulation	0.15 m	0.0001 W/m·K
2. Conductive	Metallic sheet	0.005 m	400 W/m·K

3.3.1 Performance of the samples over a highly insulated surface

The first thermal scenario considers the material insulated entirely on the bottom side to have almost no conductivity; there is negligible heat transfer by conduction. Therefore, this condition can be regarded as almost adiabatic. Below the insulation, the temperature was 25 °C, and the exterior convective heat transfer coefficient was 20 $W \cdot m^{-2} \cdot K^{-1}$. In this case, the resulting variable of interest is the surface temperature reached.

To study the effect of each of the 39 bands, the emissivity value in the selected band was 1 and 0 in the rest of the 38 bands. As Figure 28 shows, from "Band 2" (0.3-0.4 μm) to "Band 7" (2.5-3 μm), having an emissivity of 1 leads to heat gains, especially in "Band 4" (0.5-1 μm), where the material is 10.57 °C and 9.90 °C hotter than the ambient temperature in Sydney and Phoenix, respectively. On the other hand, "Band 15" (8.29-8.82 μm) and "Band 20" (9.98-10.50 μm) to "Band 22" (11.33-11.95 μm) have a high impact on the heat losses, reaching a reduction of 1.13 °C in Phoenix and 0.88 °C in Sydney when the emissivity of "Band 21" (10.5-11.325 μm) equals 1. Absorbing heat in the solar wavelengths has a more significant effect than the emissive power inside the atmospheric window, as can be seen in Figure 28.

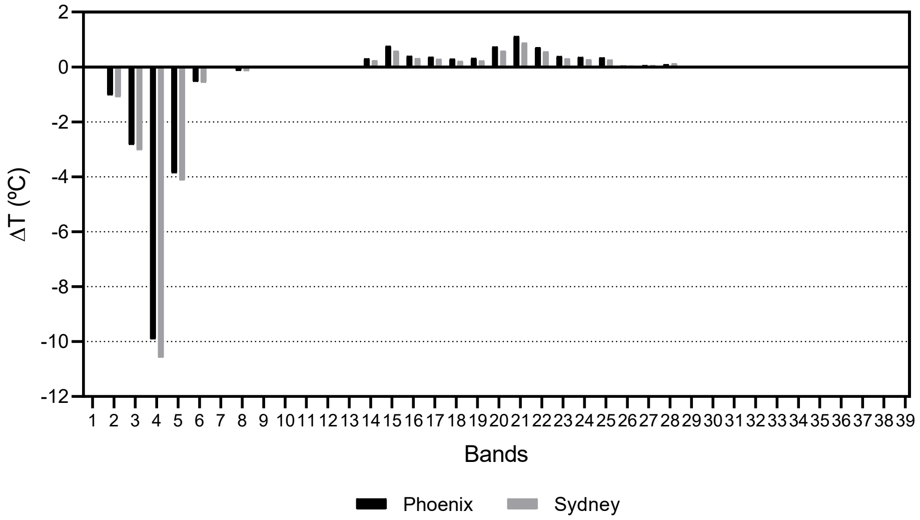

Figure 28. Contribution of each band's emissivity to the average temperature difference. Positive values are bands that achieved sub-ambient cooling and negative values are those that reached higher than ambient temperatures.

Once the effect of each band was known, the surface temperature of the 15 theoretical materials was calculated with the six possible emissivity values and the existing materials (Figure 29). The results for the theoretical materials were divided into two groups: those that achieved sub-ambient cooling during the day (M1-M9, Figure 29 a1, b1), and the ones that reached higher than ambient temperatures (M10-M15, Figure 29 a2, b2). All the materials achieved higher temperature reductions in Phoenix than in Sydney. M6 achieved a 5.29 °C reduction in Phoenix and M7 a reduction of 4.20 °C in Sydney (see Figure 30 a1, b1), whereas RC2 reached a mean temperature drop of 3.42 °C in Phoenix and 2.36 °C in Sydney. CM5 achieved a very similar temperature reduction, 3.12 °C, and 2.05 °C, respectively. The thermochromic paint (CM1), the cool material (CM2), and the red brick (CM3) did not achieve sub-ambient temperatures during the day (Figure 29 c, d).

Lowering the emissivity of the theoretical materials led to a reduction in the attained surface temperature, as seen in Figure 30 c, d; however, a material with an emissivity of 0.25 in the atmospheric window and 0 outside achieved a temperature reduction of 1.51 °C in Phoenix and 1.17 °C in Sydney. During the night, all the studied materials, theoretical and existing, achieved sub-ambient cooling.

Figure 29 and Figure 30 show summarized behavior and a comparison of the simulated materials considering a highly insulated condition. If the objective is to achieve the minimum surface temperature, the ideal material is M6 for Phoenix and M8 for Sydney. Nevertheless, in both cases (mainly for Phoenix), the difference between M6 and M8 is low. Therefore, the ideal material should have an emissivity of 1 approximately in the band between 5 and 17μm. The emissivity in the visible region has a powerful impact on the behavior of the material since the infrared emission cannot be compensated by solar absorption. The emissivity of the white paints (CM4 and CM5) was very similar to “Skycool” and “Radicool” (RC1 and RC2), and therefore their thermal behavior is similar to radiative cooling materials.

Finally, in order to study the effect of the convective coefficient, the mean surface temperature achieved by M1 to M15 was calculated and is shown in Figure 31. When the convection is reduced, Phoenix (M6, 37 °C) had the potential to achieve a lower sub-ambient temperature than Sydney (M6, 31 °C). On the other hand, a lower convective rate led to a higher surface temperature in Sydney (M15, 31 °C) than in Phoenix (M15, 23 °C).

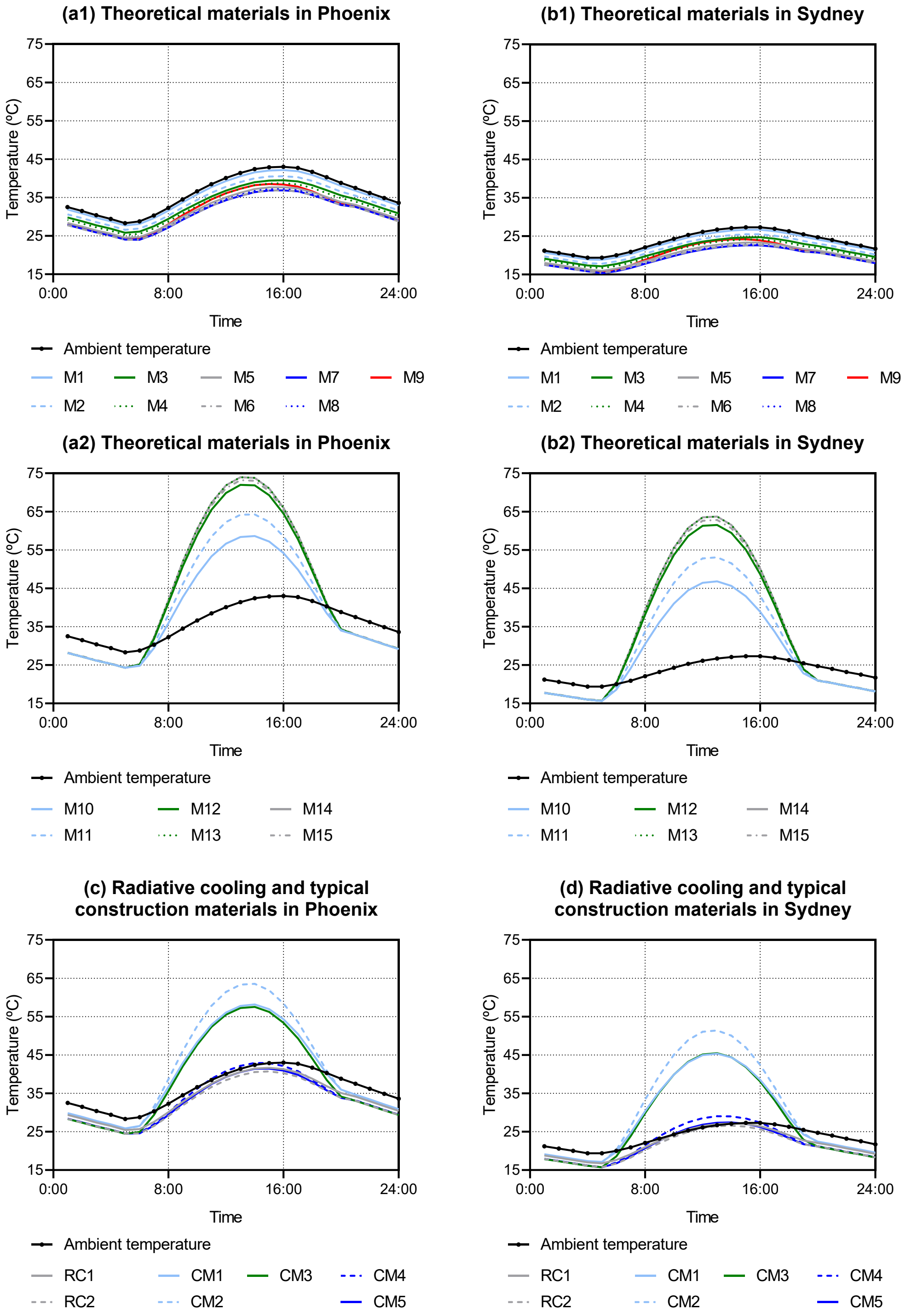

Figure 29. Hourly surface temperature achieved by the materials in Phoenix and Sydney.

(a) Theoretical materials with ε=1 in Phoenix

(b) Theoretical materials with ε=1 in Sydney

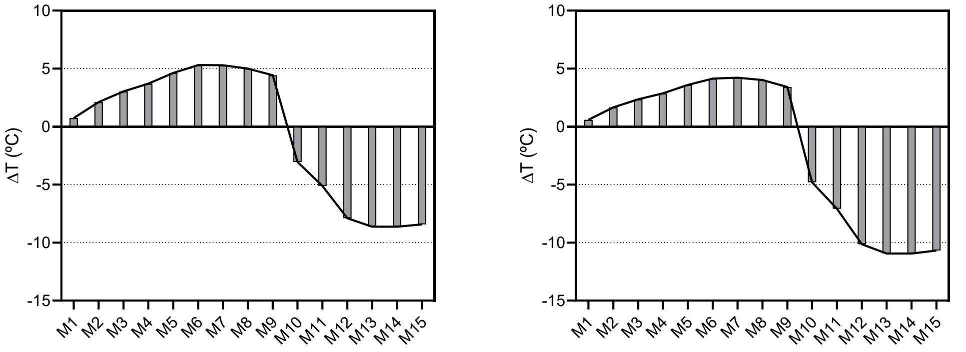

(c) Theoretical materials with emissivity variations in Phoenix

(d) Theoretical materials with emissivity variations in Sydney

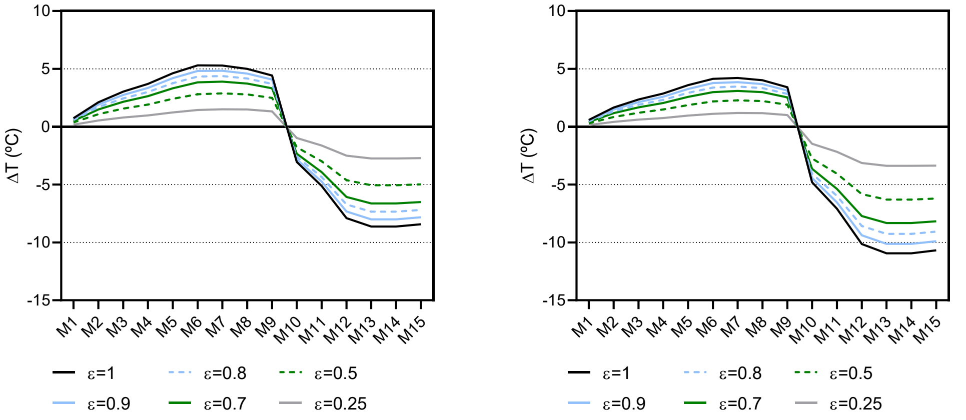

(e) Radiative cooling and typical construction materials in Phoenix

(f) Radiative cooling and typical construction materials in Sydney

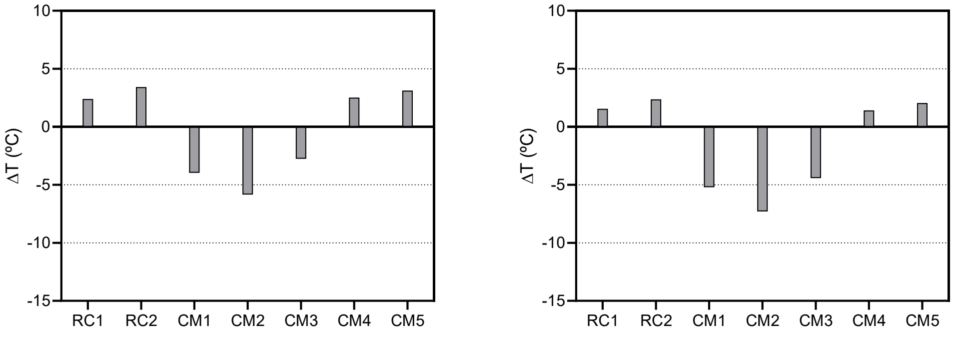

Figure 30. Difference between mean ambient and surface temperature for theoretical materials (M1-M15), radiative cooling materials (RC1-RC2) and typical construction materials (CM1-CM5) in Phoenix and Sydney. Positive values are materials that achieved sub-ambient cooling and negative values higher than ambient temperatures.

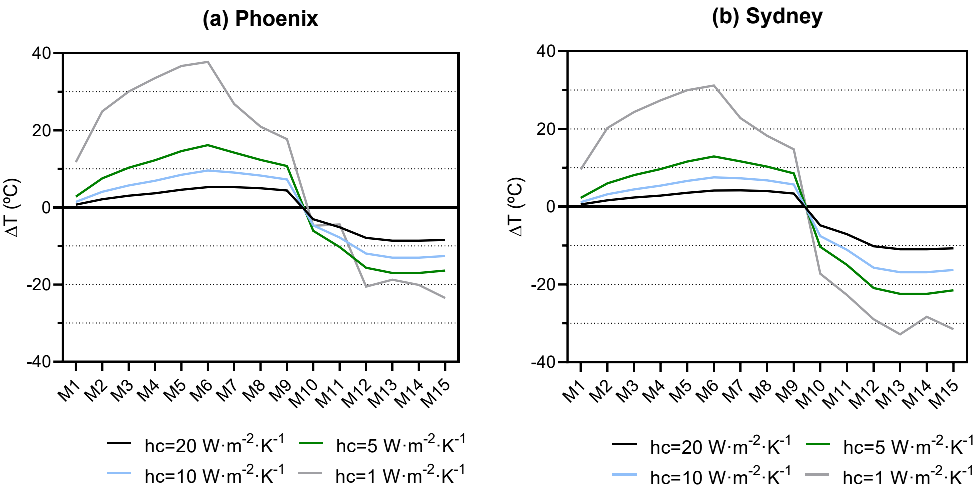

Figure 31. Difference between mean ambient and surface temperature for theoretical materials (M1-M15) with different convective values in Phoenix and Sydney. Positive values mean sub-ambient cooling and negative values higher than ambient temperatures.

3.3.2 Performance of the samples over a conductive surface

In the second scenario, materials are placed on top of a very conductive surface with no insulation. This scenario mimics the idea of having a fluid or a heat source at a constant temperature under the surface and calculates the cooling potential. Below the material, the temperature is 25 °C, the exterior heat transfer coefficient is 25 $W \cdot m^{-2} \cdot K^{-1}$, and the interior heat transfer coefficient is 1000 $W \cdot m^{-2} \cdot K^{-1}$.

The daily heat gains were calculated for all the materials in both cities and are represented in Figure 32. In the case of Phoenix (Figure 32 a), using a very conductive material leads to heat gains since the mean ambient temperature that day is 36.19 °C. Nevertheless, the theoretical material M6 with an emissivity of 1 achieves the lowest heat gain of 3091 $Wh \cdot m^{-2}$, followed by M7 (3306 $Wh \cdot m^{-2}$) and M5 (3384 $Wh \cdot m^{-2}$). Among the existing materials, the behavior of RC2 (4578 $Wh \cdot m^{-2}$) and CM4 (5240 $Wh \cdot m^{-2}$) is closer to that of RC1 (4645 $Wh \cdot m^{-2}$) and CM5 (4897 $Wh \cdot m^{-2}$). The mean ambient temperature in Sydney for that day is 23.6 °C (Figure 32 b). Materials M1-M9 achieved a substantial heat loss: theoretical material M8 attained the highest heat loss of -3176 $Wh \cdot m^{-2}$ followed by M7 (-3140 $Wh \cdot m^{-2}$), and M6 (-2916 $Wh \cdot m^{-2}$), when the emissivity value is 1 (Figure 32 b). Among the existing materials, the highest heat losses correspond to RC1 (-2212 $Wh \cdot m^{-2}$) and CM5 (-2077 $Wh \cdot m^{-2}$). Contrary to the situation in

Phoenix, despite having similar optical properties to RC1 and CM5, materials RC2 and CM4 achieved values that were around 700 Wh·m^{-2} lower.

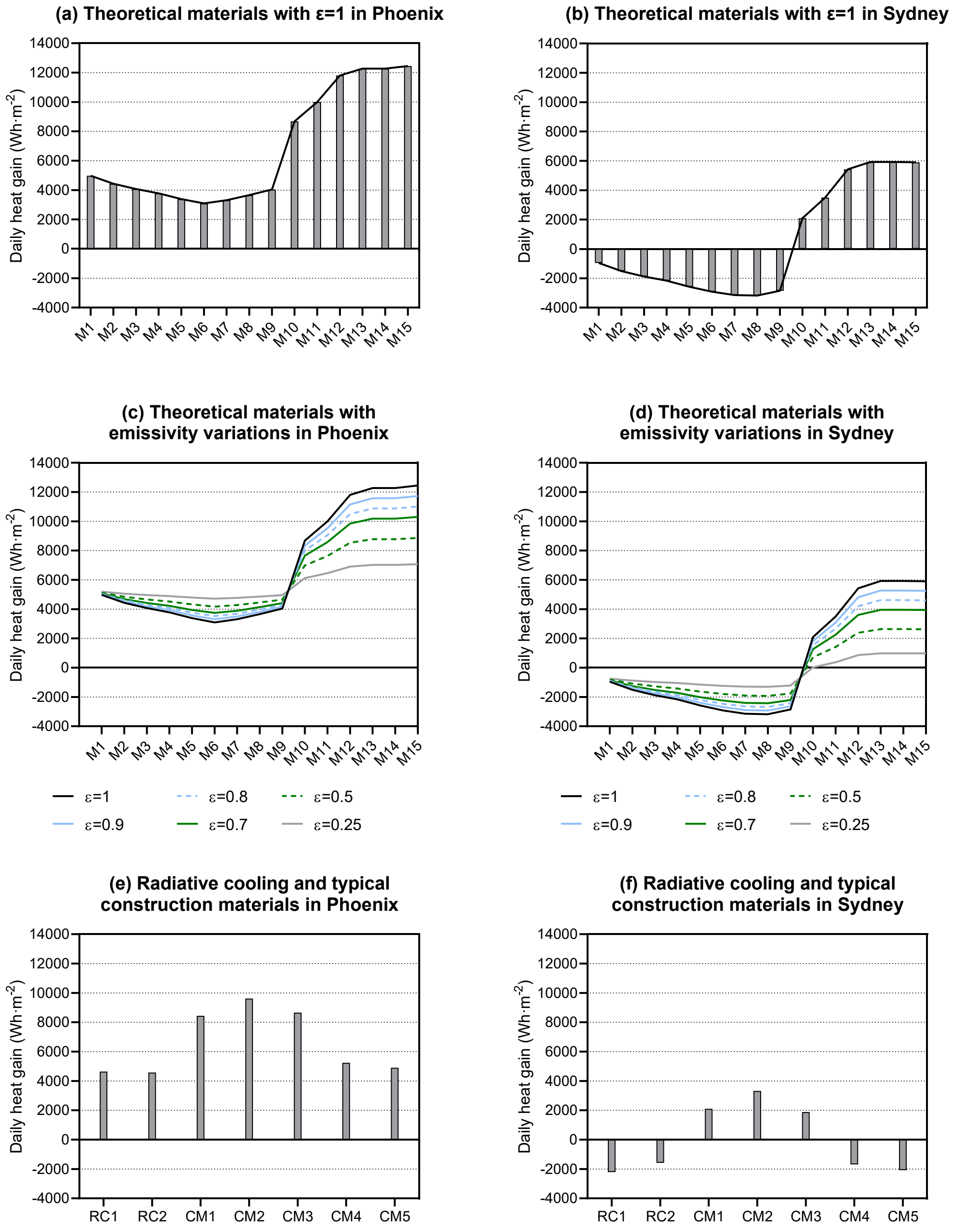

Figure 32. Daily gains or losses for theoretical materials (M1-M15), radiative cooling materials (RC1-RC2) and typical construction materials (CM1-CM5) in Phoenix and Sydney. Positive values are heat gains and negative are heat loses.

(a) Theoretical materials with ε=1 in Phoenix **(b) Theoretical materials with ε=1 in Sydney**

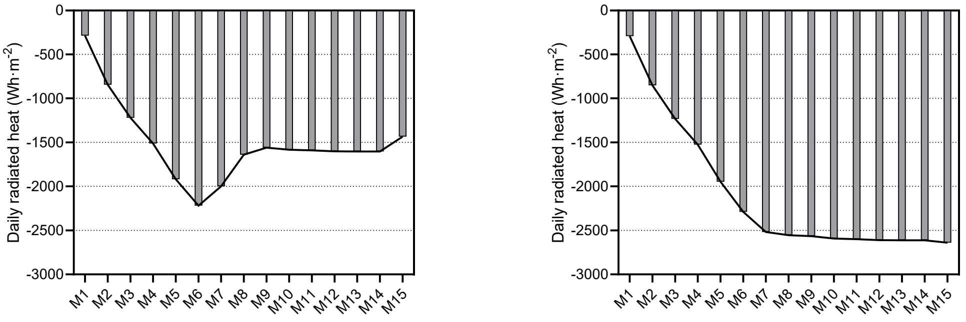

(c) Theoretical materials with emissivity variations in Phoenix **(d) Theoretical materials with emissivity variations in Sydney**

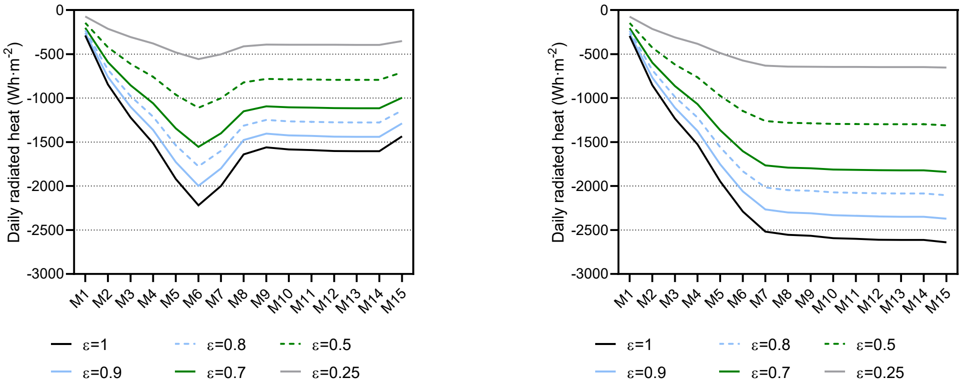

(e) Radiative cooling and typical construction materials in Phoenix **(f) Radiative cooling and typical construction materials in Sydney**

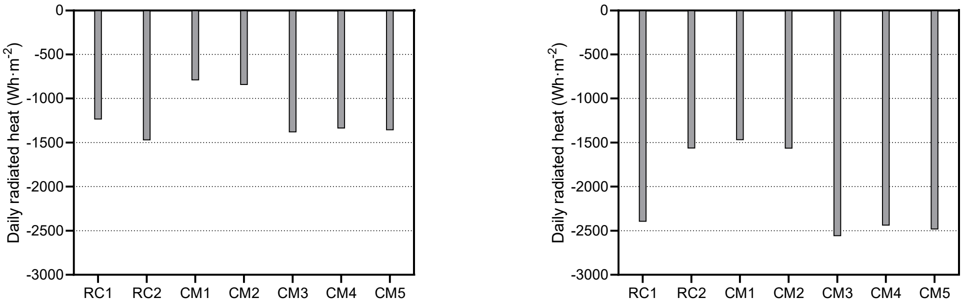

Figure 33. Daily radiated heat for theoretical materials (M1-M15), radiative cooling materials (RC1-RC2) and typical construction materials (CM1-CM5) in Phoenix and Sydney. Positive values are heat gains and negative are heat loses.

In the case of Phoenix (Figure 32 c), reducing the emissivity of the theoretical materials M1 to M9 leads to higher heat gains. Material M6 attains the best behavior since it has the lowest heat gains. Once the materials start to absorb in the solar wavelengths, the higher the emissivity, the greater the heat gains are. In the case of Sydney (Figure 32 d), reducing the emissivity of the theoretical materials leads to lower heat losses for M1 to M9. Material M8 attains the best behavior as it has the highest heat losses.

The daily accumulated radiated heat of each surface is represented in Figure 33. As can be seen, the potential is higher in Sydney than in Phoenix due to the difference in the ambient temperatures of both cites; that the bottom surface is at 25 °C hinders enormously the cooling ability in Phoenix, where M6 attains the highest radiation power, -2218 Wh·m^{-2}·(Figure 33 a). The difference between using one of the theoretical materials and the already developed ones is substantial, the radiated heat almost halving in the latter (Figure 33 e). RC2 achieved -1475 Wh·m^{-2} and CM5 -1359 Wh·m^{-2}. In the case of Sydney (Figure 33 b), from M7 (-2517 Wh·m^{-2}) onwards, all the materials achieve a similar radiation power. In this case, RC2, and RC5 achieve -2398 Wh·m^{-2}, -2484 Wh·m^{-2}, respectively. In both cities, lowering the emissivity leads to lower radiated heat (Figure 33 c, d). When the exchange temperature is higher, the theoretical radiative cooling materials perform better, as shown in Phoenix.

Finally, to study the effect of the convective coefficient, the thermal gains for materials M1 to M15 were calculated and are shown in Figure 34. As mentioned above, the mean ambient temperature of Phoenix is higher than the interior temperature considered. Therefore, in this case, the higher the convection, the lower the cooling capacity in Phoenix; the air temperature heats the surface leading to considerable heat gains. Convection plays a less significant role in Sydney since the interior temperature is closer to the ambient temperature.

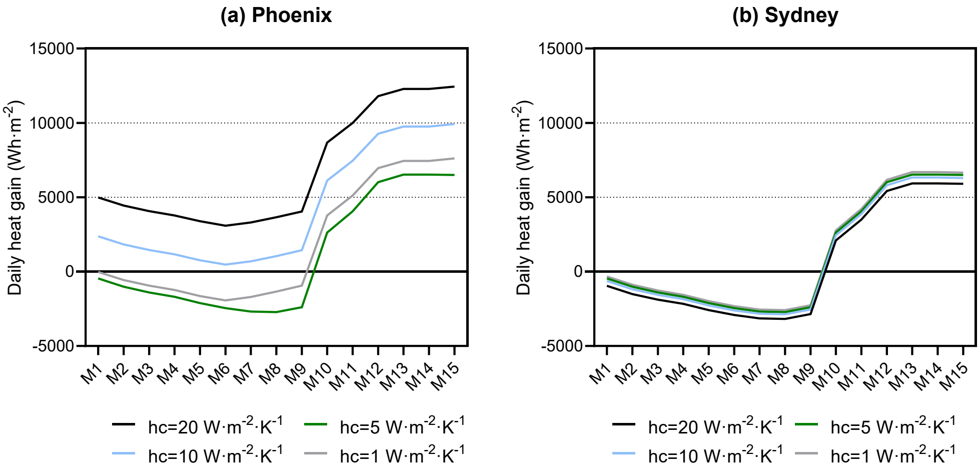

Figure 34. Daily gains or losses for theoretical materials (M1-M15) with different convective values in Phoenix and Sydney. Positive values are heat gains and negative are heat loses.

3.4 Summary and discussion

This chapter analyzed the sensitivity of the performance of daytime radiative cooling materials to different spectral selectivity configurations, type of application, and location. The results presented in this research (summarized in Table 5) suggest that the kind of application (active or passive) is a determinant factor in designing radiative cooling materials. A material that performs well in a dry climate as a passive solution could perform poorly as an active solution. When used as an active solution, the operating temperature and climate should be carefully studied.

The radiation spectrum was divided into 39 bands and the contribution of each band was calculated. The most critical bands regarding heat absorption are band 4 (0.5-1 μm) followed by band 5 (1-2 μm) and band 3 (0.4-0.5 μm). A material that solely emits in band 4 reaches a surface temperature up to 10.6 °C higher than the ambient temperature in Sydney and 9.9 °C in Phoenix. Therefore, it is important to achieve high reflectivity in the 0.5-1 μm region. The emissivity values should be especially high in Bands 20-22 (9.98-11.95 μm). Combining the 39 bands, a total of 15 theoretical materials with 6 different emissivity values were proposed and compared to existing daytime radiative cooling materials and typical construction materials. As many authors have previously mentioned, the results of the daytime radiative cooling materials could not be directly compared. However, the present research has made it possible to compare under the same conditions the results of theoretical materials (M1-M15) with two of the most innovative radiative cooling materials in recent years, "Skycool" RC1 and "Radicool" RC2.

Modifying the materials' optical properties leads to a substantial change in the heat gains or losses in an active system and the surface temperature reached as a passive application. The most suitable optical spectrum for a material is determined by the climate of each location (Sydney and Phoenix in this study) and the application type (boundary conditions). The highly insulated condition was more beneficial in Phoenix, where the theoretical materials achieved (M6, 5.30 °C) a higher sub-ambient cooling temperature than in Sydney (M6, 4.21 °C). On the other hand, the materials that did not present sub-ambient cooling during the day (M10-M15) showed worse behavior in Sydney than in Phoenix due to the higher humidity. M14 reached a surface temperature 10.93 °C higher than the ambient temperature in Sydney and 8.63 °C higher than in Phoenix. Using a radiative cooling material over a very conductive surface requires a different approach. In Sydney, a broader spectrum outside the atmospheric window was more beneficial than one solely within the transparency window. The theoretical material M8 achieved the highest daily heat losses (-3176 Wh·m^{-2}). In this case, the existing materials RC1 and CM5 are good alternatives to the theoretical materials. In Phoenix, on the other hand, restricting the emissivity to the atmospheric transparency window resulted in better behavior. Theoretical material M6, with an emissivity of 1, achieved the lowest heat gain of 3091 Wh·m^{-2}.

Table 5: Summary of simulations results.

Phoenix		**Sydney**	
Insulated			
Material	ΔT (°C) difference	Material	ΔT (°C) difference
M6	5.30 °C	M7	4.21 °C
RC2 Radicool	3.42 °C	RC2 Radicool	2.36 °C
RC1 Skycool	2.40 °C	RC1 Skycool	1.55 °C
CM5 White paint 2	3.12 °C	CM5 White paint 2	2.04 °C
CM4 White paint 1	2.52 °C	CM4 White paint 1	1.41 °C
Conductive			
Material	Daily heat gains	Material	Daily heat gains
M6	3091 W·m^{-2}	M8	-3176 W·m^{-2}
RC2 Radicool	4578 W·m^{-2}	RC2 Radicool	-2213 W·m^{-2}
RC1 Skycool	4644 W·m^{-2}	RC1 Skycool	-1574 W·m^{-2}
CM5 White paint 2	4897 W·m^{-2}	CM5 White paint 2	-2077 W·m^{-2}
CM4 White paint 1	5240 W·m^{-2}	CM4 White paint 1	-1689 W·m^{-2}

If the average temperature increase in urban areas reaches the predicted 4 to 5 °C, daytime radiative cooling materials are great candidates to counteract it. Radiative cooling is of special interest in cities suffering from the UHI effect since the heat accumulated during the day will be evacuated to outer space instead of to the streets, alleviating the heat buildup in cities and breaking the vicious cycle of increasing cooling demand. However, more research is necessary to determine how to apply this to the built environment. The impact of building radiation on the ability of these materials to cool down should be studied in more depth.

4 ON THE SEARCH FOR DAYTIME SCALABLE RADIATIVE COOLING MATERIALS[4]

This chapter explains the design, optimization, development, and characterization of two types of materials for daytime radiative cooling: tunable and non-tunable. The steps followed for the development of both types are (i) material selection and design, (ii) thickness optimization, (iii) fabrication, and (iv) characterization. After a literature review, the candidate materials were selected for the different parts and functions: reflective substrate, emissive layer particles, and tunable thermochromic material. The second step optimized the thickness of each layer both for the solar wavelengths and the atmospheric window. During the third step, the materials were fabricated using different substrates, formulations for the emissive layers, and two alternative pigments for the tunable thermochromic layer. The different layers were spray-coated on different substrates. In total, three types of materials were obtained with variations in their composition: (i) radiative cooling materials based on a polymeric matrix of polymethylsilsesquioxane and SiO_2 nanoparticles, (ii) tunable radiative cooling materials with commercial thermochromic pigments, (iii) and tunable radiative cooling materials with vanadium dioxide doped with tungsten. A total of 20 samples were obtained. Last, the materials' emissivity was measured. The first material's samples with the emissive layer had a 0.66 mean reflectivity in the solar wavelengths (0.3-0.8 μm), and its mean emissivity in the transparency window (8-13 μm) was 0.17. Therefore, the emissive layer's formulation was improved to achieve higher transparency in the solar wavelengths and higher emissivity in the

---

[4] The optimization and simulation of the samples was conducted by Dr. Ángel Andueza and supervised by Professor Joaquín Sevilla from the Public University of Navarra.

atmospheric window. The second type of radiative cooling materials with an aluminum substrate had a mean reflectivity in the solar wavelengths of 0.7, and 0.34 emissivity in the transparency window, the ones with the ESR Vikuiti film had 0.97 and 0.89, respectively.

4.1 Introduction

Materials in energy efficient buildings will increasingly involve nanostructure coatings, composites, and polymeric structures to use in windows, roof and wall coatings, energy storage, insulation, and other components (Geoff B. Smith, 2011). Material research has gained interest due to its numerous application for energy efficiency both in thermal applications and non-thermal applications such as photovoltaics (Parida et al., 2011), cleaning of water and air by solar-driven photocatalysis (Fujishima et al., 2008), and, in general, for solar-energy-effected chemical reactions (Granqvist and Niklasson, 2018). Materials for thermal applications have optical properties adapted for utilizing solar energy and achieving energy efficiency, especially in the built environment (Granqvist and Niklasson, 2018).

In recent years, the field of radiative cooling materials research has been very productive as it offers an alternative to traditional refrigeration techniques since it is an all-day free source of cooling. The ideal material properties were researched since the '70s but most commonly found materials cannot achieve sub-ambient cooling (Erell and Etzion, 1992). The ideal radiative cooling material needs to be highly reflective outside the atmospheric window ($r\approx1$ at $\lambda < 8\,\mu m$; $\lambda > 13\,\mu m$), to reradiate the highest possible amount of incoming solar radiation, and highly emissive in that band ($e\approx1$ at $8\,\mu m \leq \lambda \leq 13\,\mu m$) (Granqvist, 1981). Many authors have explained the need for strictly selective radiators with substantial solar reflection (Hossain and Gu, 2016; Raman et al., 2014; Vall et al., 2018). However, state of the art has reached a point in materials' development that further improvement in the optical characteristics of advanced materials may be of relatively marginal importance (Santamouris and Feng, 2018); they almost have the ideal spectrum.

There are two kinds of radiative cooling materials: broadband and spectrally selective. Broadband materials are highly emissive outside the solar radiation wavelengths, and spectrally selective materials' emissivity is 1 inside the atmospheric window and 0 outside. According to Gentle and Smith (Gentle and Smith, 2015), if super-cooling to near or below daytime is needed, the materials should reflect downwelling radiation. Therefore, broadband high emittance is thus preferred for above ambient cooling. Feng et al. (Feng et al., 2020a) found that broadband emitter exhibited better performance in an arid climate, being detrimental under humid climatic conditions. A similar analysis (Huang and Ruan, 2017) reported that the broadband emitter has better cooling performance when the surface temperature is above a certain threshold.

Several daytime radiative cooling materials have been produced in the last decade (Bao et al., 2017; Chen et al., 2016; Gentle and Smith, 2010b; Hervé et al., 2018; Kecebas et al., 2017;

Kou et al., 2017; Narayanaswamy et al., 2014; Raman et al., 2014; Rephaeli et al., 2013; Yang et al., 2017); however, the main concern now lays on their scalability (Santamouris and Feng, 2018). To broadly apply these materials, cheap solutions need to be found since their fabrication is still costly (Family and Mengüç, 2017; Zeyghami et al., 2018; D. Zhao et al., 2019a). Up until now, photonic structures were relatively new in the market and quite expensive (Zeyghami et al., 2018). Moreover, nanostructures' widespread use is far from reality; their fabrication is still considered costly (Family and Mengüç, 2017). The cost, durability, and mechanical properties must be solved (Yang and Zhang, 2020).

Besides their scalability, new functionalities are needed for daytime radiative cooling to improve this technique's efficiency, such as self-adaptative cooling (D. Zhao et al., 2019b). Two types of materials have been proposed, thermochromic and phase change materials. The incorporation of phase change materials that can switch on and off the radiative cooling material at specific temperatures might be of interest to avoid overcooling (Ko et al., 2018; Li and Fan, 2019, 2018; Santamouris and Feng, 2018). Latent heat storage materials, called phase change materials (PCMs), use chemical bonds to store and release heat. According to Zhang et al. (Zhang et al., 2007), latent heat storage is preferred due to the large energy storage density and nearly isothermal nature of the storage process during which the storage material, PCM, undergoes a phase change. On the other hand, thermochromic materials change the spectral properties of an organic or inorganic substrate by heating or cooling (Karlessi and Santamouris, 2013). They can be absorbent during the cold periods and reflective in the heating seasons, thus decreasing the built environment's energy consumption in any season (Granqvist et al., 2009; Kanu and Binions, 2010).

This research aims to develop a series of low-cost scalable radiative cooling structures for application in architecture and the built environment. Therefore, two types of materials are proposed, daytime radiative cooling materials (DRC) and tunable radiative cooling materials (TDRC). DRC materials have stable optical behavior, whereas TDRC tunes its optical spectrum depending on the surface temperature. The candidate materials for the different layers of the samples were researched and are made of a reflective substrate, an emissive layer, and a tunable layer. Once the materials for each layer were selected, the composition's thickness was optimized using a 3D electromagnetic optimization that solves Maxwell's equations. Afterward, the material's ideal spectrum was calculated, the fabrication of the samples was carried out using spray-coating as an easily scalable production method. During the fabrication, several adjustments were made to adapt to the manufacturing restrictions. The first set of samples were fabricated that included DRC and TDRC, based on SiO_2 nanospheres embedded on a matrix of a silica-based matrix of polymethylsilsesquioxane (PMSQ) and thermochromic commercially available pigments. Finally, the second set of samples included a formulation improvement in the emissive layer to augment its transparency in the solar wavelengths so that the reflective substrate works as its optimum performance.

4.2 Methodology

The proposed methodology follows the next steps. First, different types of multilayer materials were studied and compared as candidates to enhance the radiative cooling surfaces' emissivity in the transparency window for applications as architecture coatings. The design of the parameters of these multilayer structures was done considering industry fabrication capabilities for film deposition, and then, the dimensions of each design were analyzed to obtain maximum absorption from 8 to 13 μm. Secondly, a systematic process based on computer simulation using the CST MICROWAVE STUDIO™, a commercial code based on the Finite Integration time-domain Technique (FIT), was developed to determine the emissivity response of the analyzed samples. Moreover, the optical response in the visible range was simultaneously calculated and analyzed to evaluate the effect of the proposed structures in the reflected and transmitted power. Finally, the materials were fabricated and characterized.

4.2.1 Material selection and design

Material selection and design are of utmost importance to achieve the desired optical spectrum, in this case, to reflect solar radiation and emit in the atmospheric window, avoiding overheating in summer. For example, in hot and arid zones, whitewash (with solar absorptivity of less than 0.15 and emissivity in the infrared over 0.8), white clothes, and flat roofs are generally used (Awanou, 1986) as a passive strategy to control unwanted heat gains. Besides the inherent properties of the selected materials, the thickness of the layers plays a relevant role. A layer that is thick enough to produce complete absorption in the atmospheric window region begins to absorb outside it, reducing the selectivity and limiting access to low temperatures (Berdahl, 1983). The design of the material and its spectral properties depend on each wavelength's emissivity and its performance on the location and type of application (Carlosena et al., 2020).

This research focuses on the development of two types of daytime radiative cooling materials (Figure 35): daytime radiative cooling materials (DRC) and tunable daytime radiative cooling materials (TDRC). The first type is made of a reflective substrate and an emissive layer, and the latter includes a switch layer in the middle. A DRC material will have the same optical behavior and the same behavior throughout the year. The second type, TDRC has a switchable layer that allows changes in the spectrum depending on its temperature; hence it will regulate its optical behavior and thermal response depending on the ambient temperature.

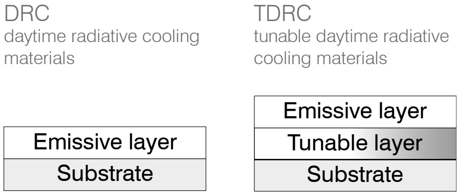

Figure 35: Two types of researched materials: DRC (left) and TDRC (right).

For both types of materials, 1D photonic structures have been proposed made of simple layers. Low-cost and scalable fabrication methods are researched to deposit the materials in large surfaces such as building roofs. The research takes after two approaches, for the DRC material, the structure from (Eriksson et al., 1985; Granqvist and Hjortsberg, 1981) is replicated, and for TDRC, an approximation of (Tazawa et al., 2006, 2000, 1996) is applied. Although Tazawa et al. used silicon monoxide (SiO) silicon dioxide was selected in this research, the amorphous silicon monoxide structure is a long-standing question because of the uncommon silicon valence state in the oxide form. Moreover, amorphous silicon monoxide undergoes an unusual disproportionation by forming silicon- and silicon-dioxide-like regions (Hirata et al., 2016).

Reflective layer

The material needs to reflect a high amount of solar radiation; otherwise, it will reach its thermal equilibrium at a temperature above the ambient. Metals have been proposed as reflective layers, but except silver, they cannot achieve solar reflectance above 96% (Figure 36). Moreover, the thermal emittance of common metals is too low. Therefore, when exposed to the sun, they cannot cool down (Gentle and Smith, 2015). However, the high silver cost reduces its scalability.

Aluminum was proposed as a substrate in several investigations. Several researchers coated aluminum with Tedlar (Addeo et al., 1978; Catalanotti et al., 1975; Michell and Biggs, 1979), others evaporated a series of silica derived chemical compounds such as silicon monoxide, silicon dioxide, and silicon nitride onto aluminized glass substrates (Eriksson et al., 1985; Eriksson and Granqvist, 1983; Granqvist and Hjortsberg, 1981; Hjortsberg and Granqvist, 1980). More recently, Gentle and Smith (Gentle and Smith, 2010b) doped 25 μm thick polyethylene with SiC and SiO_2 nanoparticles on top of aluminum and Ao et al. (Ao et al., 2019) sprayed zinc phosphate sodium ($NaZnPO_4$) onto an aluminum substrate.

Aluminum is used in this research as a low-cost, durable metal suitable for scaling into architecture applications such as roofs or façades. Aluminum offers a higher than 90%

reflectance from near UV to mid-IR except for a sharp dip at 0.8 μm, where the reflectance is significantly reduced, as seen in Figure 36. The best reflectance aluminum performance is obtained from mid-IR (2 μm), making it an excellent lossy reflector in the thermal wavelength range. Aluminum slowly oxidizes, resulting in a reduction of reflectance. Therefore, aluminum must include a protective dielectric overcoat that prevents oxidation. The reflectance of the substrate could be enhanced by adding a nanolayer of silver to improve its reflectivity (Gentle and Smith, 2015). A second substrate produced by 3M was used, Vikuiti Enhanced Solar Reflector ("3M^{TM} Enhanced Specular Reflector (3M ESR) | 3M United States," n.d.) due to its high reflectivity in the solar wavelengths. This substrate was used already in another research by Gentle and Smith (Gentle and Smith, 2015).

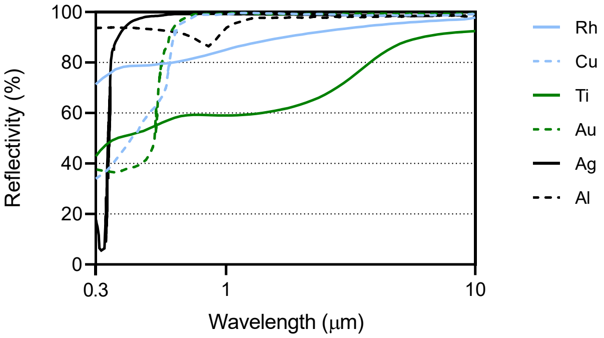

Figure 36: Reflectivity of some common metals versus wavelength at normal incidence. Based on: (Fabian et al., 2010).

Emissive layer

The emissive layer needs to be highly absorbent and therefore emissive in the atmospheric window, silica derived chemical compounds were proposed as emissive layers (Eriksson et al., 1985; Eriksson and Granqvist, 1983; Granqvist and Hjortsberg, 1981; Hjortsberg and Granqvist, 1980). Other authors studied ceramic oxide layers such as magnesium oxide (MgO) and lithium fluoride (LiF) (Berdahl, 1983).

Many researchers have proposed silica in their radiative cooling materials in the last years by embedding nanoparticles in polymers. Several authors embedded SiO_2 spheres on polymethylpentene (TPX) (Yang et al., 2020; Zhai et al., 2017b). (Kou et al., 2017) researched a polymer-silica mirror consisting of a fused silica wafer coated with a polymer top layer of polydimethylsiloxane (PDMS) and a silverback reflector. A numerical study researched the importance of silica spheres size on the emissivity properties of the material (Feng et al., 2020b). Other authors have made a single layer of silica microspheres self-assembled on a soda-lime glass for photovoltaic applications (Jaramillo-Fernandez et al., 2019). Due to its abundance and optimal infrared emissivity, SiO_2 was chosen in this research as an emissive layer, whose peak emissivity is at 9 μm precisely inside the atmospheric window.

The research takes after the approach proposed in (Eriksson et al., 1985; Granqvist and Hjortsberg, 1981), which includes a reflective substrate and an emissive coating. Therefore, the selected materials for optimization are silica and aluminum. Silica is transparent in the visible range presenting a refractive index almost constant of 1.4. The transmittance of silica is high until 2.5 μm; from that wavelength onwards, silica is almost opaque, its absorption rises strongly, and the transmitted power can be considered zero. Therefore, silica presents a significantly different refractive index in the visible region and the atmospheric window (AW) (8 to 13 μm), influenced by the vibrational modes of oxygen atoms (Kirk, 1988). The excitation of these vibrational modes by infrared (IR) radiation is macroscopically observed as absorption bands in the IR spectrum at 9 and 20 μm (Amma et al., 2015) [57].

When calculating a silica layer's absorption, we find two different situations depending on the layer thickness. When the layer thickness is greater than the incident wavelength, most of the energy is absorbed by the material at the atmospheric window wavelengths. However, silica layers with a thickness smaller than the IR light wavelength transmit radiation for all wavelengths except for the abovementioned bands. Therefore, strong absorption is obtained using thin silica layers in narrow spectral regions centered at 9 and 20 μm, as seen in Figure 37.

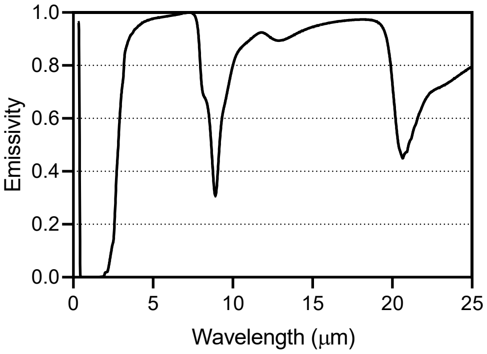

Figure 37: Simulated emissivity of a 3.2 mm bulk silica layer.

Tunable layer

A recent review summarized the presented modulation techniques on infrared emissivity in terms of design, materials, size, fabrication and modulation capacity (Ulpiani et al., 2020). The first attempt to include a tunable layer was conducted by a group of researchers (Tazawa et al., 1996) who proposed an innovative combination of two materials, a radiative cooling film based on silicon monoxide and a vanadium dioxide thermochromic layer, enabling both cooling and heating.

The most significant interest in thermochromic materials has been in the transition metal oxides since they exhibit discontinuous changes in electrical conductivity of up to eight orders of magnitude, with attendant changes in their infrared transmittances (Jorgenson and Lee, 1986). Vanadium dioxide is one of the most researched metals due to its characteristic phase transition at 68 °C. As shown in Figure 38, VO_2 is the only metal whose hysteresis and transition temperature (T_t) are closer to ambient. Therefore, research has focused on lowering its transition temperature. Jorgeson and Lee studied dopants to lower vanadium dioxide's transition temperature (T_t) around 68 °C, the closest to operational temperature. Tungsten (W) doping decreases T_t the most on a per atomic percent basis, followed by molybdenum (Mo), tantalum (Ta), and niobium (Nb) (Jorgenson and Lee, 1986). Goodenough pointed to ruthenium (Ru) to lower its T_t and to germanium (Ge), aluminum (Al), and gallium (Ga) to increase the transition temperature of vanadium dioxide (Goodenough, 1971).

Vanadium–oxygen phase diagram is complex and includes almost 20 different phases, frequently with only minor compositional differences; the challenges for the synthesis of VO_2 are related to the coexistence of these various oxide forms and the existence of various polymorphs (Granqvist and Niklasson, 2016). Therefore, it is rarely easy to make phase pure VO_2 produced in a very narrow interval of oxygen partial pressure.

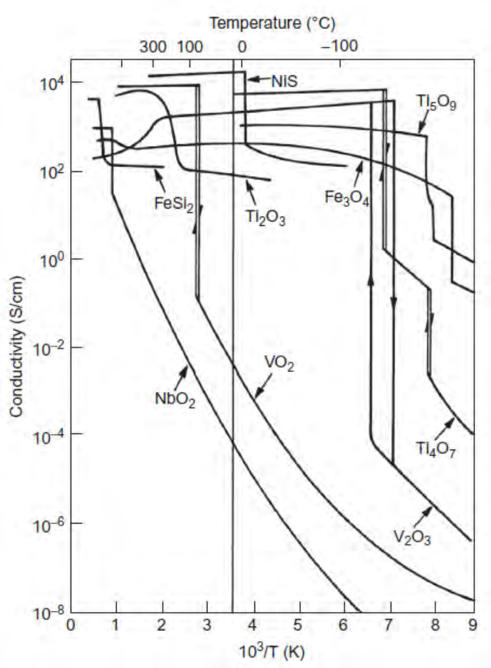

Figure 38: Electrical conductivity as a function of reciprocal temperature (lower horizontal axis) and temperature (upper horizontal axis) for several metal-based compounds elaborated by (Granqvist, 2015) from (Jorgenson and Lee, 1986).

4.2.2 Optimization

To optimize the material design, simulations are needed to obtain the desired optical response. As pointed out before, daytime radiative cooling materials as cool materials might lead to heat penalties during the heating period (Ascione et al., 2018). Therefore, the strategy to add a thermochromic layer to act as a switch was researched as well. Once the material goes below a specific threshold temperature, it will change its optical properties and absorb heat.

After the materials and the structure design compositions were selected (SiO_2 as an emissive layer, VO_2 as a tunable layer, and Al as substrate), a series of numerical optimizations were made to determine the ideal thickness of each layer. The target was to obtain the highest reflectivity in the solar wavelengths and the highest emissivity possible in the atmospheric window. Bulk aluminum was selected as the substrate with a thickness of 1 mm; several thicknesses of SiO_2 were simulated on top. The second set of simulations had an intermediate layer of vanadium dioxide doped with tungsten. The complex refractive indexes from vanadium dioxide doped with tungsten ($V_{1-x}W_xO_2$) were obtained from (Tazawa et al., 1995) for the range 0.25-2.5 μm and from 0.8-20 μm from (Paone et al., 2015). The maximum doping percentage, or power in the second case, was used for the simulation. Since the refractive index values were obtained from the literature, they might not exactly correspond to the deposited materials' actual values.

Simulations in the thermal wavelength range (8–13 μm) were carried out using the CST MICROWAVE STUDIO™, a commercial code based on the Finite Integration time-domain Technique (FIT) (Clemens and Weiland, 2001). The Finite Integration Technique (FIT) is a consistent discretization scheme that provides a reformulation of Maxwell's equations in their integral form suitable for computers, and it allows to simulate electromagnetic field problems with complex geometries and materials. This program is an electromagnetic field simulation software package especially suited for analysis and design in the microwave, terahertz, and optical range. The meshing algorithm employed by CST to calculate the absorptivity depends on the dimension (thickness) of the unit cell concerning the shorter wavelength of the calculation. This fact implies that the meshing employed by CST in the visible range exceeds the memory capacities of any computer. Therefore, to calculate the absorptivity of the structures in the visible and NIR ranges, we used Grating Diffraction Calculator (GD-Calc) code (Johnson, 2005), a commercial software package developed by Kenneth C. Johnson and integrated into Matlab that uses rigorously coupled-wave analysis (RCWA)(Moharam and Gaylord, 1981). GD-Calc resolves the Maxwell equations for a single frequency and analyzes the weight of each diffraction order separately in the power balance. A summation of the power density in all diffraction orders provides the reflection and transmission values, obtaining the absorption. The unit cell geometry simulated in GD-Calc is built up of discrete rectangular bricks arranged in strata divided into lateral stripes and subdivided into blocks to fill 3D space. These properties of GD-Calc resolve the meshing CST problems visible for large-sized samples since it is possible to simulate structures much larger than the shorter wavelength of the calculation in a reasonable time (Gjessing, 2011).

Daytime radiative cooling materials (DRC)

The composition of aluminum with an emissive layer of SiO_2 was simulated. As shown in Figure 39, the thicker the silica coating is, the more emissive it is in the atmospheric window. On the other hand, the increasing thickness does not hinder the reflectivity on the solar wavelengths. The progressive increase of thickness above 1 μm leads to a second emission peak around 13 μm, which, up to 5 μm it is inside the atmospheric window. Once the thickness is around 10 μm, it becomes a broadband emitter.

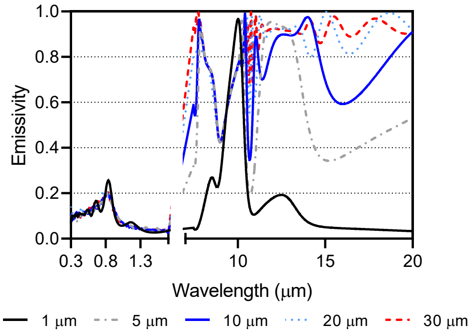

Figure 39: Emissivity simulation of a radiative cooling material: an aluminum substrate with different thicknesses of SiO_2 (author).

A layer of silver was included to improve the reflectivity in the solar wavelength range. Two thickness values were simulated, 100 nm and 200 nm. The result in Figure 40 compares the reflectivity with the same structure without silver coating. As can be seen, the material without the silver coating (black curve) is less reflective in the solar wavelengths; nevertheless, its average emissivity is higher without silver. Both thicknesses of silver result in an almost identical emissivity.

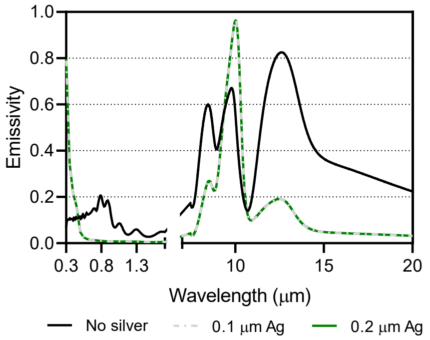

Figure 40: Emissivity simulation of an aluminum substrate with different thicknesses of silver and 2 μm SiO_2 layer(author).

Tunable daytime radiative cooling materials (TDRC)

To control the unwanted high emissivity during the heating periods, a switch layer was added, in this case, a layer of vanadium dioxide doped with tungsten. Based on previous literature (Tazawa et al., 2000), which coated aluminum with a 180 nm $V_{1-x}W_xO_2$ layer and several thicknesses of SiO_2 were simulated in Figure 41.

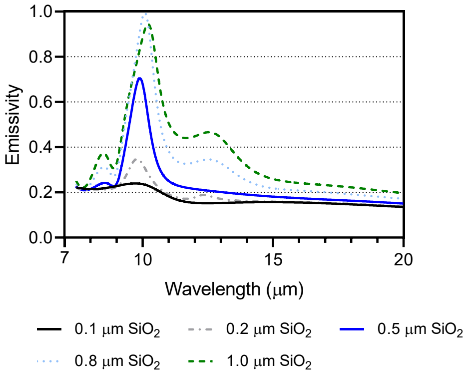

Figure 41: Emissivity simulation of an aluminum substrate with a 180 nm $V_{1-x}W_xO_2$ layer and several thicknesses of SiO_2 at 90 °C (author).

Finally, to optimize the ideal thickness of vanadium dioxide, iterative simulations were made with aluminum, different thicknesses of $V_{1-x}W_xO_2$, and 1 μm of SiO_2 (Figure 42). The vanadium's optical behavior is more stable at high temperatures, but once it reaches a 2 μm thickness, it presents a stable behavior at low temperatures.

Afterward a composition of an aluminum substrate, a 2 μm layer of $V_{1-x}W_xO_2$ with different emissive coatings, was simulated for two temperatures, 30 °C and 90 °C (Figure 43). Since the reference paper simulations included silicon oxide and silicon monoxide, both emissive layers were considered to see the difference. The vanadium oxide layer leads to a differentiated emissivity in the atmospheric window, being spectrally selective at high temperatures and a broadband emitter at low temperatures. Comparing to the material without coating (black line), the emissive silica layer accentuates this behavior. At low temperatures, the composition with SiO had a broadband emitter behavior while the SiO2 layer had a slightly worse behavior.

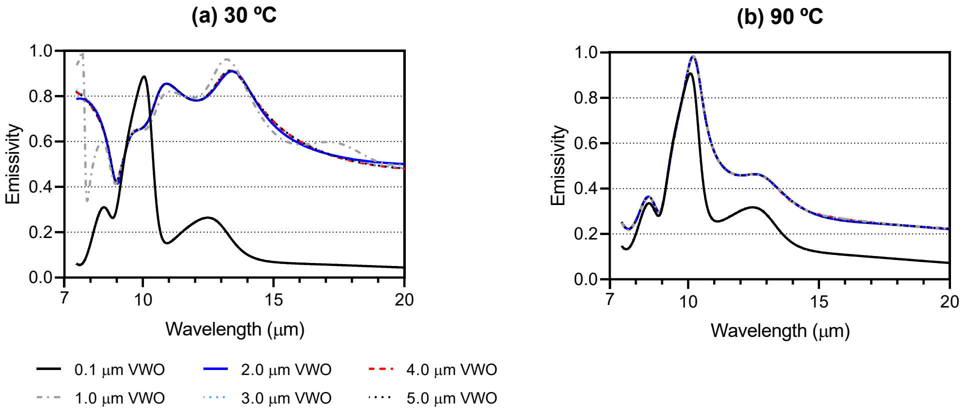

Figure 42: Emissivity simulation of an aluminum substrate with different thicknesses of $V_{1-x}W_xO_2$and 1 μm of SiO_2, at 30 °C and 90°C (author).

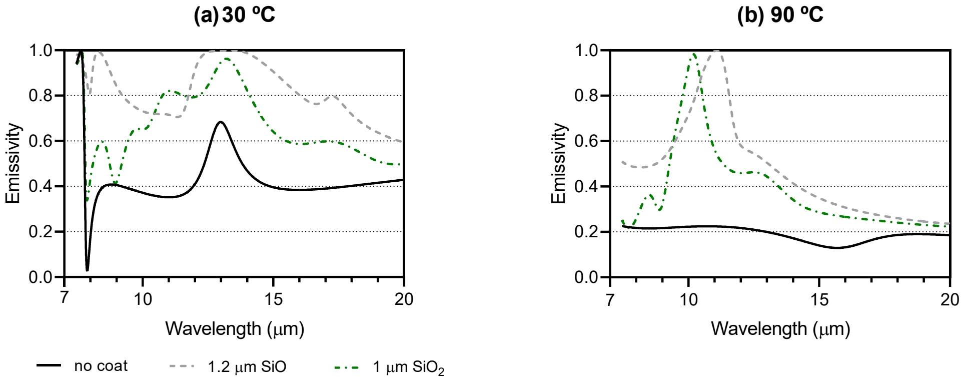

Figure 43: Emissivity simulation of aluminum with a 2 μm $V_{1-x}W_xO_2$ and different top coatings (author).

Once the optimal thickness of the $V_{1-x}W_xO_2$ layer was determined, 2 μm, a simulation was carried to determine the energy absorption inside the thermochromic layer (Figure 44). A very thick layer of SiO_2 generates NIR energy absorption due to its resonance in 9-10 μm, leading to no energy arriving at the $V_{1-x}W_xO_2$ layer. In the atmospheric window, at 90 °C, the absorptivity is lower than at 25 °C (from 10 μm to 20 μm). In this range, SiO_2 does not absorb energy, doing so around at 9 μm. Almost all the energy in the IR is reflected. At 90 °C, the material is more reflective than at 25 °C, where $V_{1-x}W_xO_2$ absorbs most energy. In the visible wavelengths, the finite size of the layers (1 μm SiO_2 and 2 μm $V_{1-x}W_xO_2$) lead to the characteristic wavy response when the structure thickness is similar to the wavelength of analysis. At 25 °C, $V_{1-x}W_xO_2$ absorbs more energy in the visible than at 90 °C being especially significant in the NIR (0.8 - 2 μm), where the mean absorption is 0.8 at 25 °C and 0.5 at 90 °C.

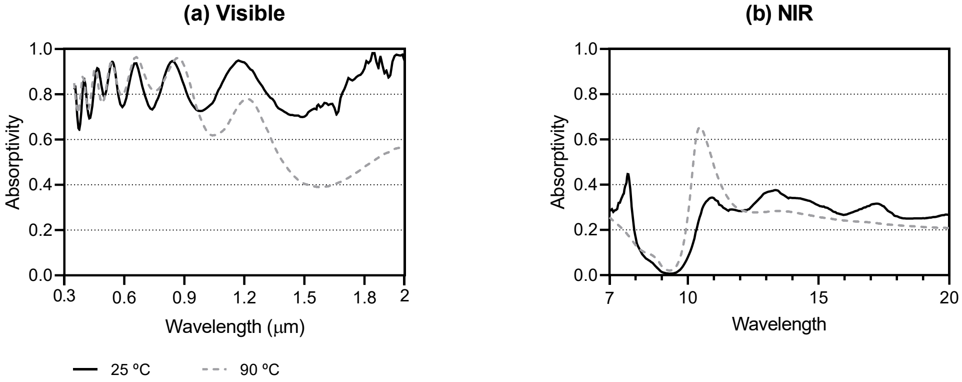

Figure 44: Absorptivity simulation of the $V_{1-x}W_xO_2$ layer, composite of Aluminum, 2μm $V_{1-x}W_xO_2$, and 1μm SiO_2 (author).

4.2.3 Development[5]

Several deposition technique options were researched, such as plasma-enhanced chemical vapor deposition (PECVD) and sputtering; however, since the deposition's scalability was a requisite, spray coating was chosen. As a result of choosing this deposition method, instead of working with SiO_2 as a bulk material, silica-derived polymer, polymethylsilsesquioxane (PMSQ), was chosen to be applied to the substrate. The simulation study established the importance of having two layers (reflective and absorptive) and the required thickness's magnitude to obtain their optimal characteristics.

The emissive layer was made of 20 nm silica SiO_2 nanoparticles embedded at a 5% weight in a PMSQ matrix. The aluminum substrate finish was a mirror polished, alloy 1050A H18, which is the most reflective on the market. Nevertheless, once its reflectivity was measured, it was lower than the theoretical maximum. Therefore, 3M Vikuiti Enhanced Solar Reflector ("3M™ Enhanced Specular Reflector (3M ESR) | 3M United States," n.d.) was an alternative substrate to aluminum, used previously in two works (Gentle and Smith, 2015; Goldstein et al., 2017). The emissive layer (PMSQ with embedded SiO_2 particles) approximate cost is 450-500 euros/kg, about 0.3 euros/m^2 for a layer of 2 μm.

Although the final product differed from the one designed and optimized in 4.2.2., unfortunately, no new optimizations could be carried out. The complex refractive index of the PMSQ with the embedded SiO_2 particles had to be known to optimize the thickness., several universities and research centers were contacted to measure the refractive index (University

---

[5] The samples were fabricated by the Technological Center L'Urederra following the instructions provided by author related to the materials and thicknesses to be deposited. The emissive coatings made of PMSQ and the $V_{1-x}W_xO_2$ were fabricated as part of the project "SERA".

of New South Wales, University of Sydney, University of Technology Sydney, Centro Nacional de Energías Renovables, Consejo Superior de Investigaciones Científicas, and Universidad de Barcelona). However, none of them could characterize the complex index due to the impossibility of measuring rough samples in the mid-infrared (2 to 20 μm). The refractive index measurement requires perfectly planar specular surfaces and is usually measured with an ellipsometer from 200 to 1500 nm and a spectrophotometer for the infrared. If the samples are rough, as in this case, complex models specifically developed are used and require several different measurements (diffuse reflectance in solid sample and powder absorption). The second alternative to optimize the thickness was to use information from the literature, but the complex index of PMSQ was not available in the literature as far as the author knows. Hence, the materials could not be optimized with the real refractive indexes.

The samples were developed using spray deposition on top of squares samples of 200 by 200 mm of two different materials: aluminum and Vikuiti ESR films. The substrates were washed with ethanol paper to clean the surface from impurities, allowing a correct deposition of the emissive layer. Depending on the substrate's nature, metallic or plastic, two different emissive layers were applied (Figure 45). The emissive layer contains silica nanoparticles embedded in a PMSQ matrix. Two formulations were developed for the metallic substrates since the first matrix was not transparent enough in the visible wavelengths. A third composition was explicitly developed for plastic substrates and was deposited on top of the Vikuiti substrates. The metallic samples were curated for an hour on a stove at 200 °C.

Nevertheless, the samples with a plastic substrate did not have a post-application treatment, and the emissive layer was curated at ambient temperature. The aluminum samples were applied, changing the deposition speed and quantity to achieve a layer of approximately 1 μm. Target thickness was 10 μm, but due to viscosity restrictions of deposition, the maximum deposited thickness was 3.7 μm. The Vikuiti substrates received two and three layers of the emissive coating to achieve the minimum 1 μm target.

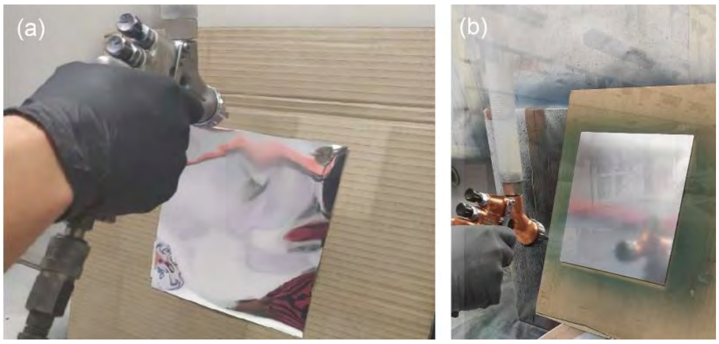

Figure 45: Deposition procedure (a) spray coating onto a plastic substrate and (b) spray on top of the aluminum metallic substrate.

For the development of the tunable layer, another approach was researched. Although the ideal material was $V_{1-x}W_xO_2$, it is not a commercially available product, and it had to be produced. Due to the difficulty in synthesizing vanadium dioxide doped with tungsten, the first thermochromic layer was fabricated using commercial thermochromic pigments ("Materiales inteligentes, S.L.," 2020). The chosen pigment had a transition temperature around 26 °C where the color changed reversibly from the colored to colorless phase. The used color was green; previous literature showed that it had the best solar reflectance ratio in the colorless phase and the highest absorbance in the colored phase (Karlessi et al., 2009). The thermochromic layer application was made using spray coating, and the pigment was encapsulated in the matrix, admitting a 5% weight of the thermochromic pigment. The second type of thermochromic layer was based on vanadium dioxide doped with tungsten. The thermochromic layer based on vanadium dioxide doped with tungsten was developed by L'Urederra Technological Center using the sol-gel method presented in (Cao et al., 2008). This component was developed explicitly for this research, and it is a very sensitive process; vanadium has a particle size very similar to that of tungsten and therefore does not readily admit a molecule with comparable properties. Two components were obtained during the reaction: $V_{1-x}W_xO_2$, the target component but in very little quantities, and vanadium pentoxide V_2O_5, which is the stable form of VO_2. Even though, ideally, the material is deposited straight into the substrate the same process as with the commercial organic pigment was employed. The $V_{1-x}W_xO_2$ component had to be encapsulated in a polymeric matrix with a maximum quantity of 5% in weight (see APPENDIX 5: Synthesis of vanadium dioxide doped with tungsten).

4.2.4 Characterization[6]

The reflectance of the first set of samples (Table 6) was characterized in the visible and near-infrared (0.3 to 2 μm) at the University of New South Wales, using a spectrophotometer (Agilent Technologies Cary Series UV-Vis-Nir Spectrophotometer) with an unpolarized light source and a calibrated high specular reflectance standard. In the infrared (1.66 to 55 μm), a Fourier transform infrared spectrometer at the University of Sydney (Bruker Invenio R) with an unpolarized light source is used to characterize the cooler's reflectance with a gold film used as a reflectance standard.

The reflectance of the second samples (Table 7) was characterized in the visible and near-infrared (from 200 to 1100 nm), using a combined Deuterium Halogen light source (Top

---

[6] See APPENDIX 6: Spectral characterizationfor more information on the spectral characterization.

Sensor System DH-2000-S) with an integrating sphere and a CCD spectrometer (OceanOptics USB2000-FLG) with an unpolarized light source and a calibrated high specular reflectance standard. This measurement was carried out at the Jerónimo de Ayanz facilty from the Universidad Pública de Navarra. A Fourier transform infrared spectrometer (Bruker Vertex 80V) equipped with an infrared microscope (Hyperion 3000) was employed to perform measurements in the near-infrared (NIR, 0.78-2.5 μm) and mid-infrared (MIR, 2.5-25 μm). The excitation was done with unpolarized light sources (halogen lamp in the NIR and a Globar source in the MIR) and the detection with an InGaAs detector (NIR) and a nitrogen-cooled MCT detector (MIR). The cooler's reflectance was characterized in normal reflection with a gold mirror used as a reflectance standard. This part of the characterization was done at the Navarra Biomed.

Besides the emissivity and reflectivity measurements, all samples[7] had their coating thickness, adherence and hardness characterized. The coating thickness of the aluminum samples was measured with an "Elcometer 456 standard model with range 0-1500 μm. Adherence measurements were made according to the ISO 2409 norm, where the metallic substrates were scratched with a metallic awn (6 horizontal and 6 vertical lines with an offset of 2 mm). Afterward, an adhesive film was placed on top of the grid to see detachments of the coating. The hardness test was based on ISO 15184 norm using different pencils and a hardness test instrument. The gloss was measured using a gloss meter Zehntner ZGM 1110 at three angles, 20°, 60°, and 85°.

4.3 Results

Twenty samples were fabricated, 10 in the first batch, 10 in the second batch. The second set enhanced the formulation to improve the emissive layer's solar transparency and the substrate's reflectivity. Vikuiti ESR was added as a substrate due to its high reflectivity in the solar wavelengths; therefore, a new formulation for plastics was developed.

A summary of the reflective layer, emissive coating, and tunable coating combinations is represented in Figure 46. The first row shows the different composition combinations, and the samples are grouped in the first set where the reflective substrate is based on aluminum, the tunable layer made of commercial thermochromic pigment, and the emissive layer of PMSQ with SiO_2 nanoparticles. The second set includes the aluminum samples with the improved

---

[7] Unfortunately, the third set of samples was not characterized on time to be included in this dissertation since they arrived by the end of November 2020.

emissive layer based on the PMSQ and SiO_2 nanoparticles and the tunable layer with the developed vanadium dioxide doped with tungsten. The last set included two types of plastic substrate Vikuiti with a PMSQ and SiO_2 layer formulated specifically for plastic applications.

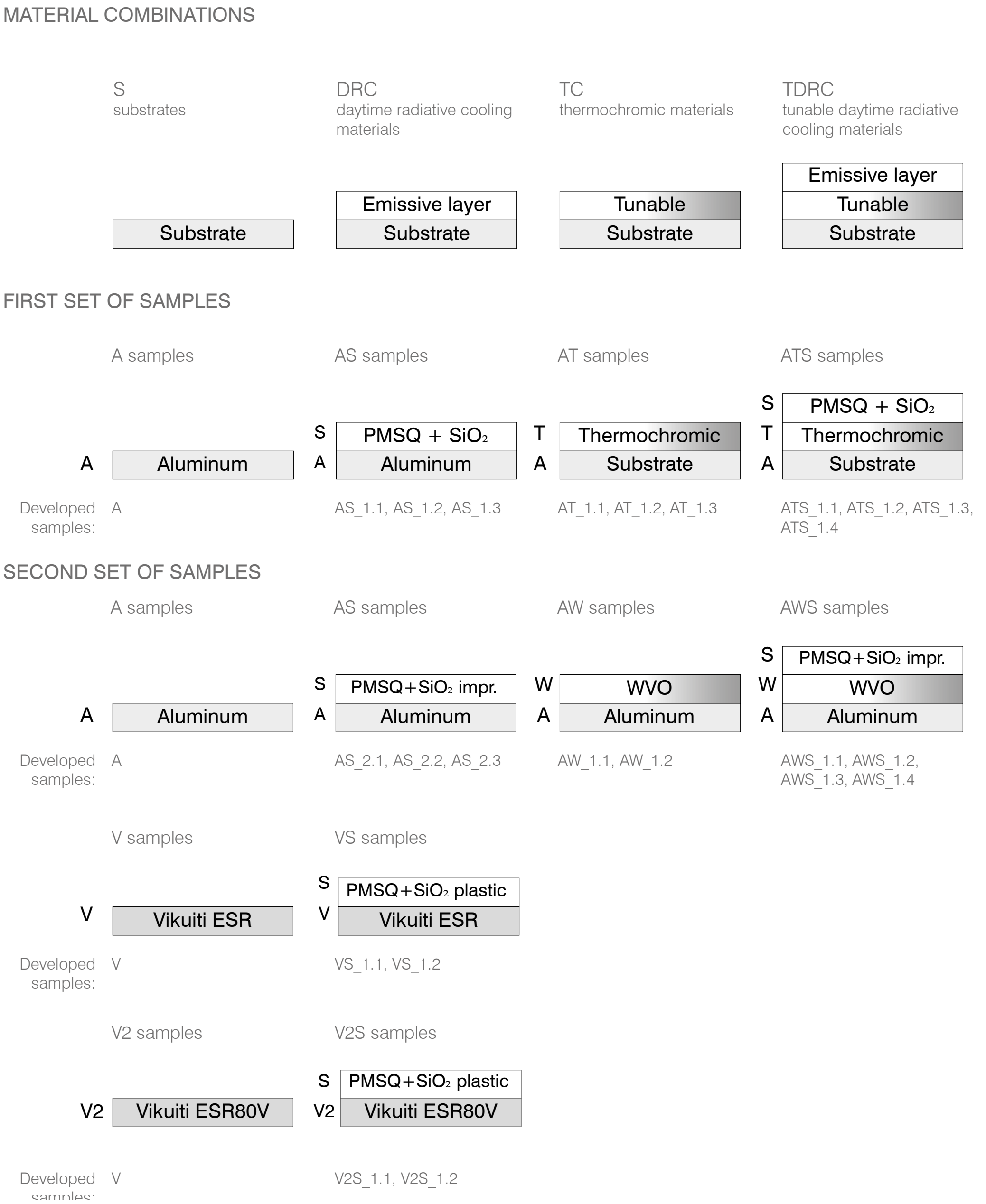

Figure 46: Configuration of the different fabricated samples.

4.3.1 Samples

Two sets of samples were finally developed. The first set arrived in March 2020 (Table 6), the second presented some improvements in the formulation of the emissive coating and arrived to be characterized at the beginning of August 2020 (Table 7); however, the synthesis of $V_{1-x}W_xO_2$ (see APPENDIX 5: Synthesis of vanadium dioxide doped with tungsten) took longer than expected and the samples containing the thermochromic pigment arrived in mid-November 2020.

Table 6: Summary of the first batch of samples. S, TC, RDC, and TDRC stand for substrate, thermochromic, daytime radiative cooling, and tunable daytime radiative cooling, respectively.

		Substrate	**Tunable layer**		**Emissive layer**		
	Sample code	**Material**	**Material**	**Thickness (μm)**	**Material**	**Thickness (μm)**	**Mass (mg)**
S	A	Al (1 mm)	-	-	-	-	-
TC	AT_1.1	Aluminum (1 mm)	Commercial thermochromic	6.88	-	-	-
	AT_1.2			6.53			
	AT_1.3			6.09			
DRC	AS_1.1	Aluminum (1 mm)	-	-	PMSQ $+SiO_2$	1.58	-
	AS_1.2					1.62	
	AS_1.3					1.68	
TDRC	ATS_1.1	Aluminum (1 mm)	Commercial thermochromic	-	PMSQ $+SiO_2$	2.37	-
	ATS_1.2					2.63	
	ATS_1.3					1.88	
	ATS_1.4					1.33	

Figure 47 shows the bare aluminum sample, the sample with the emissive coating, the sample with the thermochromic green pigment encapsulated in the matrix, and finally, the thermochromic pigment encapsulated plus an emissive layer on top. As shown in the picture, the emissive coat had a white color and is not entirely transparent. As a result, the expected solar reflectivity (visible to the human eye) was lower than the bare aluminum without the coating. The samples containing the thermochromic pigment were whitish as well, but once heated above their transition temperature (26 °C), they turned from light green to completely white.

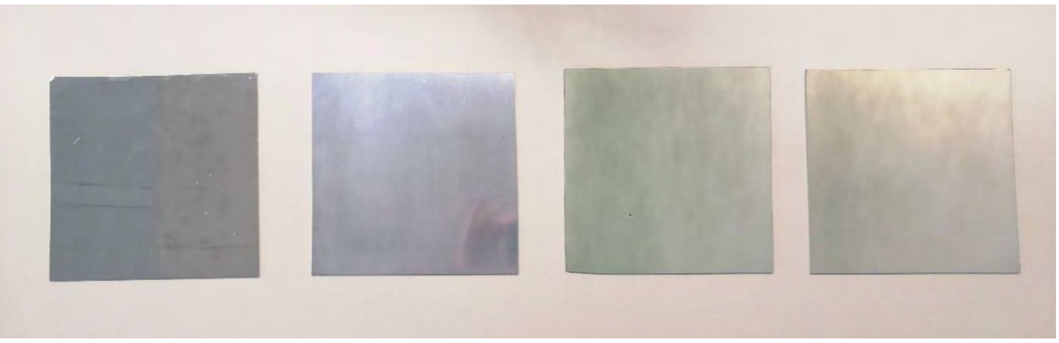

Figure 47: Photo of the first types of samples, from left to right: aluminum (A), aluminum with SiO_2. (AS), encapsulated thermochromic (AT) and encapsulated thermochromic pigment with emissive layer (ATS).

The second batch of samples introduced several improvements due to the bare aluminum's low reflectivity and improvements in the transparency in the visible wavelength range of the emissive coat. First, some attempts were made to improve the aluminum's reflectance using acids and polishes. Nevertheless, the substrates were damaged, and the reflectivity was not improved. The addition of a very reflective substrate was deemed necessary to test the structure, so two 3M substrates were selected as their reflectivity is around 0.97 in solar wavelengths. As a result, reformulations were made in the emissive coating to apply them in plastic substrates.

Table 7: Summary of the second batch of samples. S, TC, RDC, and TDRC stand for substrate, thermochromic, daytime radiative cooling, and tunable daytime radiative cooling, respectively.

		Substrate	**Tunable layer**		**Emissive layer**		
	Sample code	**Material**	**Material**	**Thickness (µm)**	**Material**	**Thickness (µm)**	**Mass (mg)**
S	A	Al (1 mm)	-	-	-	-	-
	V	Vikuiti ESR	-	-	-	-	-
	V2	Vikuiti ESR 80V2	-	-	-	-	-
DRC	AS_2.1	Aluminum (1 mm)	-	-	Improved PMSQ $+SiO_2$	0.5±0.3	6.2
	AS_2.2					1.5 ± 0.6	13.3
	AS_2.3						22.5
	VS_1.1	Vikuiti ESR	-		Plastic PMSQ $+SiO_2$		17.4
	VS_1.2						36.6
	V2S_1.1		-				11.2

		Substrate	Tunable layer		Emissive layer		
	Sample code	Material	Material	Thickness (μm)	Material	Thickness (μm)	Mass (mg)
	V2S_1.2	Vikuiti ESR 80V2			Plastic PMSQ +SiO_2		19.5
TC	AW_1.1	Aluminum (1 mm)	$V_{1-x}W_xO_2$	2.5 ± 0.8	-	-	-
	AW_1.2			1.9 ± 0.5			
TDRC	AWS_1.1	Aluminum (1 mm)	$V_{1-x}W_xO_2$	-	Improved PMSQ +SiO_2	2.7 ± 0.5	-
	AWS_1.2			-		2.1 ± 0.8	
	AWS_1.3			-		1.8 ± 0.4	
	AWS_1.4			-		1.6 ± 0.3	

As can be seen in Figure 48, the sample with the aluminum sample is less reflective visually than the Vikuiti samples. From the visual inspection, the predicted solar reflectance is lower in the case of the metallic substrate. The Vikuiti samples are a very thin film whose reflectance might not be suitable for some applications due to glaring.

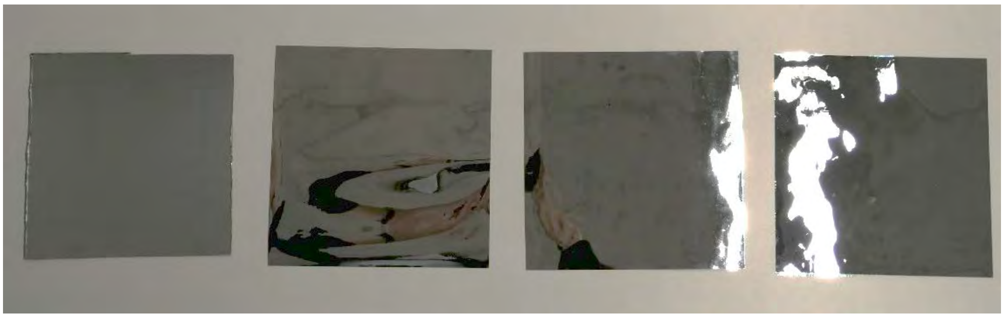

Figure 48: Photo of the second DRC samples, from left to right: aluminum with improved PMSQ and SiO_2 (AS_2), Vikuiti Substrate (V), emissive layer on Vikuiti ESR (VS1), emissive layer on Vikuiti ESR 80V2 (VS2).

Finally, two aluminum samples were coated with $V_{1-x}W_xO_2$ encapsulated in the PMSQ matrix, and four were coated with an emissive layer on top of the thermochromic layer (Figure 49). Ideally, the thermochromic layer should not be encapsulated but applied directly as another coating; nevertheless, the spray coating technique needed a carrier agent to be applied onto the substrate.

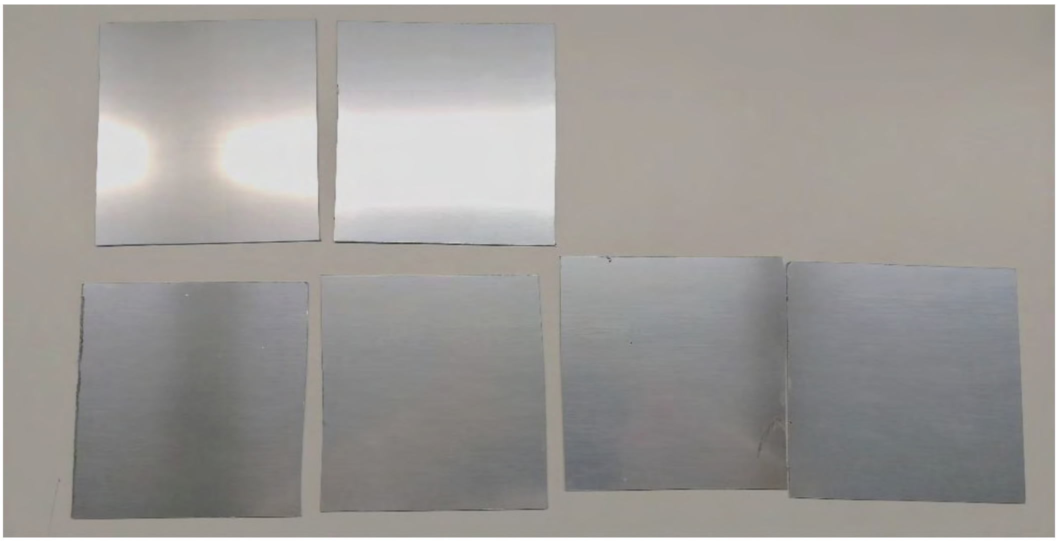

Figure 49: Photo of the second TC and TDRC set of samples. The top row has the samples with vanadium dioxide and no emissive layer, AW_1.1and AW_1.2, and the bottom layer from left to right, AWS_1.1, AWS_1.2, AWS_1.3, and AWS_1.4.

4.3.2 Characterizations

Among the first set of samples, the substrate (A), two materials with thermochromic pigment (AT_1.2 and AT_1.3), two samples with the emissive coating (AS_1.2, AS_1.3), and two others with a layer of thermochromic and a layer of emissive coating (ATS_1.1 and ATS_1.4) were characterized using the instruments and techniques presented in 4.2.4. Among all the developed samples, the ones with the highest thickness were selected since the thickness optimization showed that a larger coating resulted in a more emissive material in the atmospheric window. The emissivity of the first set of samples is presented in Figure 50. The samples with the thermochromic pigment were not previously optimized due to the inability to determine the pigment's refractive index inside the encapsulation matrix. The reflectivity of all the samples around 0.3 μm wavelength is lower than 0.8, which will lead to high incoming solar radiation absorption. The samples with thermochromic pigment have a higher emissivity in the atmospheric window, which will enable radiating heat, allowing them to achieve cooler temperatures at night. The resulting emissivity of the PMSQ and SiO_2 samples (AS_1.2 and AS_1.3) is compared with the predicted results in Figure 51; the simulated emissivity in the atmospheric transparency window is higher in the simulation results than in the samples. Moreover, the solar reflectance is worse than was predicted, reaching almost 0.4 at 0.5 μm.

The simulations and optimizations were conducted with ideal and bulk materials, whose refractive indexes were obtained from databases and literature. The differences between the simulated and the measured emissivity are due to the finally used materials. As mentioned in

4.2.3, instead of using bulk SiO_2, a polymethylsilsesquioxane (PMSQ) matrix was employed with a different refractive index from silica.

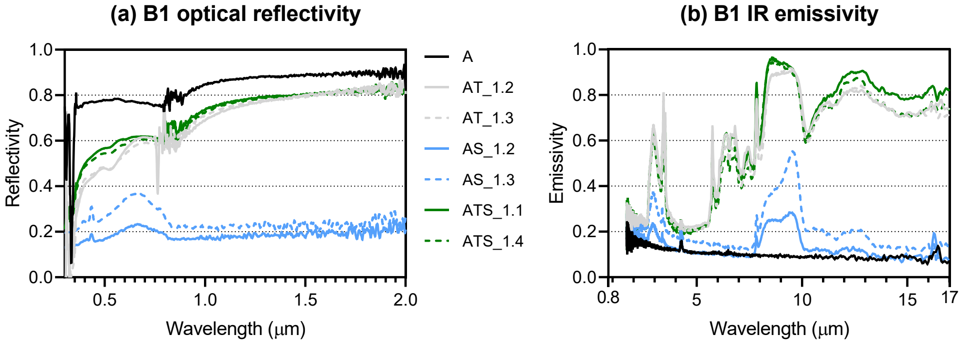

Figure 50: Measured (a)optical reflectivity and (b) infrared emissivity of the first samples set. A (aluminum), AT samples (aluminum plus thermochromic coat), AS samples (aluminum plus emissive layer), and ATS samples (aluminum, thermochromic layer, and emissive layer). See Table 6 and Figure 46 for details on the material composition.

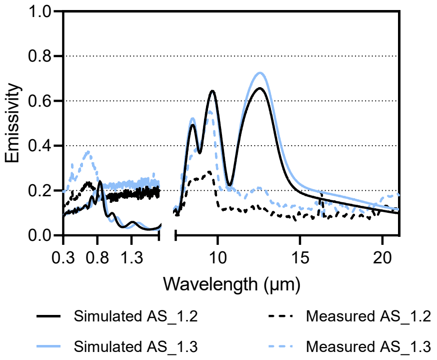

Figure 51: Comparison between the simulated (aluminum plus SiO_2) and the samples' measured emissivity with aluminum and an emissive layer made of PMSQ plus SiO_2 nanoparticles. See Table 6 and Figure 46 for details on the material composition.

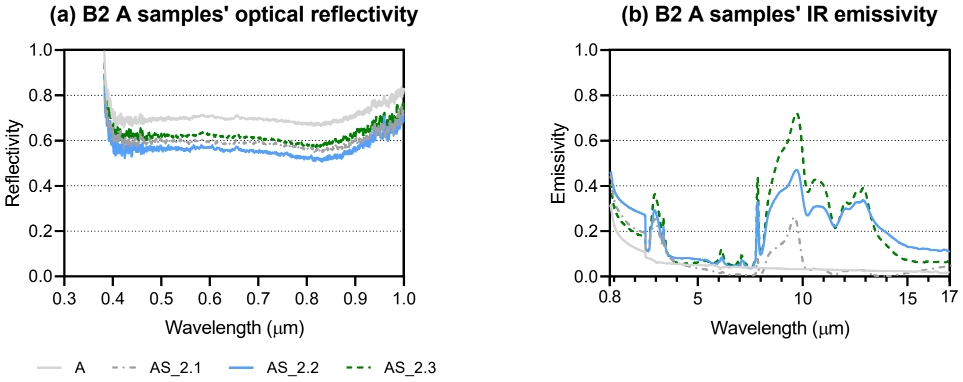

Figure 52: Measured (a) optical reflectivity and (b) infrared emissivity of the samples with an aluminum substrate (A), A aluminum substrate, and three samples with emissive coating, AS_2.1, AS_2.2, and AS_2.3. See Table 7 and Figure 46 for details on the material composition.

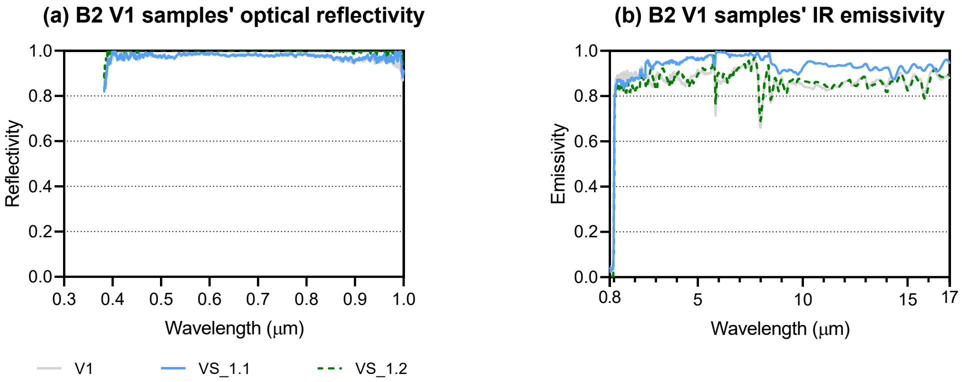

Figure 53: Measured (a) optical reflectivity and (b) infrared emissivity of the samples with Vikuiti ESR substrate (V), V bare Vikuiti substrate, and two samples with emissive coating, VS_1.1 and VS_1.2. See Table 7and Figure 46 for details on the material composition.

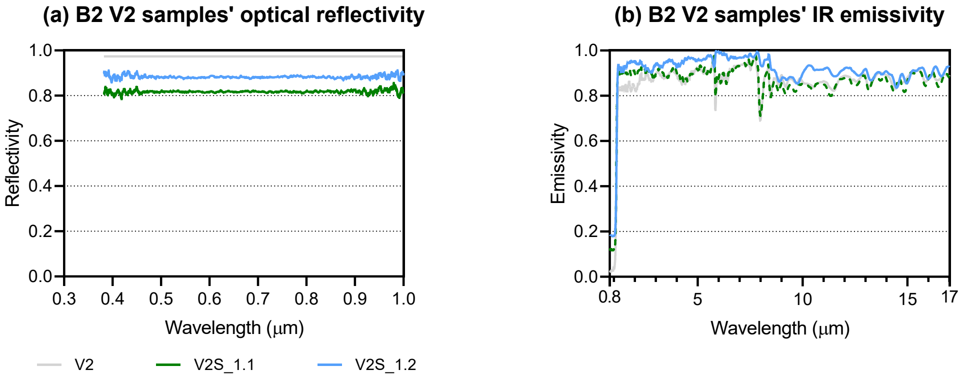

Figure 54: Measured (a) optical reflectivity and (b) infrared emissivity of the samples with Vikuiti ESR80V2 substrate (V2), V2 bare Vikuiti substrate, and two samples with emissive coating, V2S_1.1 and V2S_1.2. See Table 7 and Figure 46 for details on the material composition. See Table 7and Figure 46 for details on the material composition.

Figure 52 to Figure 54 show the samples' optical reflectivity and infrared emissivity from the second set. Figure 52a shows the optical reflectivity of the samples with the aluminum substrate, A (continuous grey line) presents the highest reflectivity among the samples; the application of the emissive coating reduces the ability to reflect in the solar wavelengths. Figure 52 b shows the emissivity where AS_2.3 (green dashed line) presents the highest infrared in the atmospheric window; the peaks correspond to the SiO_2 nanoparticle inclusion, as was previously discussed. The sample AS_2.3 did not present the lowest solar reflectivity having the best reflectivity just below A.

Figure 53a shows the optical reflectivity of the Vikuiti ESR samples; the solar reflectivity is almost 1 for all the samples, the emissive coat had a negligible effect on the ability to reflect solar light. VS_1.2 had very similar behavior to the sample without coating V1, and VS_1.1 had a slightly higher emissivity (Figure 53 b). The solar reflectivity of the Vikuiti ESR80V samples had a different behavior (Figure 54 a) than in the previous samples (Figure 53 a) in both instances with the emissive layer (V2S_1.1 and V2S_1.2) reduced the solar reflectivity.

As with the previous samples, the emissive layer shows little difference in the emissivity spectrum (Figure 54 b). The testing will determine whether the emissive layer gives any advantages to the plastic substrate.

Besides the reflectivity and emissivity of the samples, the coating thickness was measured (Table 6 and Table 7). For the metallic samples, adherence, hardness, and gloss were measured as well. The plastic samples' characterization consisted of measuring the quantity of material and the gloss; the harness, thickness, and adherence measurements were complicated since the available instrument was designed for metallic substrates. There is no visible shedding of the coating; this result was tested by analyzing the samples with a microscope.

The hardness test was based on ISO 15184 norm using different pencils and a hardness test instrument. The results show that aluminum without coating is weak, being affected by the softest pencil. However, the emissive coating significantly improves the hardness for samples AS_2.1 and AS_2.2 and F for sample AS_2.3. The gloss was measured using a gloss meter Zehntner ZGM 1110 at three angles, 20 °, 60°, and 85°. For relatively shiny materials as polished aluminum, the angles of study are 20 and 60. As seen in Table 8, the gloss is reduced with the increase of coating thickness. The samples with Vikuiti showed almost no gloss reduction with the increase of deposited mass.

Table 8: Second batch characterization: gloss, hardness, and the number of layers of emissive coatings.

	Sample code	**Gloss**		**Hardness**	**Number of layers of emissive coating**
		20°	**60°**		
S	A	1247 ± 19	721 ± 6	<9B	-
	V	-	1001 ± 2	-	-
	V2	-	978 ± 1	-	-
DRC	AS_2.1	868 ± 30	549 ± 7	H	1 layer regular speed application
	AS_2.2	684 ± 32	437 ± 23	H	1 layer slow speed application.
	AS_2.3	626 ± 45	465 ± 34	F	2 layers regular speed application
	VS_1.1	-	997 ± 7	-	2
	VS_1.2	-	992 ± 4	-	3

	Sample code	**Gloss**		**Hardness**	**Number of layers of emissive coating**
		20°	**60°**		
	V2S_1.1	-	962 ± 8	-	2
	V2S_1.2	-	957 ± 4	-	3
TC	AW_1.1	284±59	171±10	HB	
	AW_1.2	254±19	165±21	HB	
TDRC	AWS_1.1	135±38	89±13	HB	
	AWS_1.2	122±10	100±11	F	
	AWS_1.3	127±24	95±12	-	
	AWS_1.4	131±12	91±10	-	

4.4 Summary and discussion

This chapter presented the simulation, development, and characterization of two daytime radiative cooling materials: non-tunable and tunable. Two kinds of reflective layers were selected, aluminum substrate and commercial Vikuiti. The emissive layer consisted of bulk silica; however, although simulations were carried with SiO_2, the final used emissive layer consisted of a silica-derived polymeric matrix of polymethylsilsesquioxane, which has a different optical behavior than bulk silica (SiO_2), but a similar response. Two kinds of thermochromic pigments were researched to develop the tunable layer, commercial thermochromic pigments and vanadium dioxide doped with tungsten developed by sol-gel. The simulations and the finally employed materials differ due to limitations in the fabrication process. The developed $V_{1-x} W_xO_2$ particles had to be embedded into the same matrix to adhere to the substrates.

The first set of samples consisted of a DRC material made of aluminum and a silica matrix; the TDRC materials included a thermochromic layer encapsulated on the same polymeric matrix. The emissive layer consisted of SiO_2 nanosphere particles embedded in a silica-derived polymeric matrix of polymethylsilsesquioxane PMSQ; the tunable layer was made of thermochromic pigments encapsulated in the same matrix. The second batch improved the emissive layer transparency in the solar wavelengths without affecting the mid-infrared properties with a reformulation of the embedding matrix. Since the firstly developed materials were neither very solar reflective nor very emissive in the atmospheric window, another substrate was selected to improve the reflectivity in the solar wavelengths, Vikuiti. As a result, a new formulation for plastic applications was developed. Finally, vanadium dioxide doped with tungsten was fabricated by the sol-gel method, and the resulting particles were encapsulated on the same matrix.

The spray deposition used in this research presents two main advantages: speed and scalability. Drawbacks from this technique are thickness control and replicability. Deposition with these fabrication techniques should be further researched as controlling the thickness is essential for accurate and reliable results. The first set of materials had a low solar reflectivity (60%) and will lead to substantial heat gains. Their emissivity in the atmospheric window is not very high, being more significant in the materials with the thermochromic layer since they have more thickness of the PMSQ matrix. The resulting optical properties are not very promising due to the mismatch between the optimized materials and the actually developed materials.

The second batch improved the emissive layer transparency in the solar wavelengths without affecting the mid-infrared properties with a reformulation of the embedding matrix. As a result, the solar reflectivity was higher, and the emissivity was maintained. Moreover, the included commercial substrate enabled a higher reflectivity. It must be noted that using Vikuiti, the samples' spectral response showed little difference with and without coating. The experimental testing will determine whether the coating affects the substrate if it is not cured. This second set of samples, with the commercial substrate, shows a more promising result than the first set and might achieve sub-ambient cooling. The samples with the aluminum showed lower solar reflectivity than the Vikuiti samples; although the inclusion of a silver layer to improve the reflectivity was researched, it was dismissed as it would increase the costs and, therefore, scalability. If a silver layer were to be included, 100 nm thickness would be sufficient to increase the sample's solar reflectivity. The developed emissive layer of polymethylsilsesquioxane with SiO_2 approximate cost is 0.3 euros/m^2 for a 2 μm layer.

As mentioned before, the thicknesses could not be controlled as desired, leading to two consequences. First, the targeted thicknesses could not be obtained with this type of matrix due to the viscosity needed. Secondly, every time a deposition is made, the thickness will be different, leading to a replicability problem. Furthermore, the spray coating is done manually, leading to heterogeneous deposition in the samples, which could be seen clearly in the samples with encapsulated thermochromic pigments, which had darker areas. Concluding, the deposition method needs substantial changes, with a more mechanical and controlled process. It is essential to control both the application homogeneity and thickness without compromising the sample size's ability.

5 TESTING OF DAYTIME RADIATIVE COOLING MATERIALS IN DIFFERENT CLIMATES[8]

In this chapter, some of the developed radiative cooling materials based on silica-derived polymers developed in Chapter 4 were tested in two different locations, Sydney and Pamplona. A total of 10 prototype daytime radiative cooling materials and tunable radiative cooling materials were tested and compared to the substrates without any coating. During the experiments, the samples were exposed to ambient conditions without any convection barrier and were embedded in an extruded polystyrene (XPS) board to eliminate conduction. To study the samples' thermal performance, the surface temperature of the samples was monitored. The ambient meteorological conditions were recorded with a meteorological station. The first experiment in Sydney tested an initial set of samples whose reflectivity in the solar wavelengths was insufficient to achieve sub-ambient cooling. At night the samples achieved 5.54 °C below ambient temperature—the samples with the emissive coating heated up to 9 °C more than the bare aluminum. The second experiment conducted in Pamplona tested a set of improved materials whose solar reflectivity was higher. During the day, the samples had a 7.32 °C surface temperature reduction (below ambient) even with an incident solar radiation of 633 $W \cdot m^{-2}$. At night, the samples were up to 9.13 °C below the ambient. The samples with the commercial substrate achieved a mean reduction of 3.72 °C below ambient temperature. Although the aluminum samples did not achieve sub-ambient cooling throughout the day, the emissive layer reduced the sample's surface temperature to an average of 1.7 °C in Pamplona. Materials based on silicon-derived polymers such as

---

[8] The experiment conducted in Pamplona, along the material design, optimization and development, was published in Solar Energy Materials and Solar Cells journal as "Experimental development and testing of low-cost scalable radiative cooling materials for building applications.".

polymethylsilsesquioxane (PMSQ) show great potential as architecture coatings. Due to setbacks, ranging from very high wind speeds and COVID restrictions, the period lasted only a total of 5 days; more experiments should be done during more extended periods and more locations with different climate conditions.

5.1 Introduction

Urban overheating has a severe impact on the cooling energy consumption of buildings, outdoor pollution levels, heat-related mortality and morbidity, urban ecological footprint, and survivability levels (Santamouris, 2020). To counterbalance the impact of urban overheating, several mitigation technologies have been proposed and implemented in cities. Proposed technologies include reflective and chromic materials for the urban fabric, additional green infrastructure, evaporative systems, solar control devices, and the use of low temperature heat sinks (Santamouris, 2015b). Implementation of the proposed mitigation technologies in large scale projects showed that it is possible to decrease the peak temperature of cities up to 2.5-3 °C (Santamouris et al., 2016). Among the various proposed technologies, the use of reflective, thermochromic, and photonic materials seems to present the highest mitigation potential (Santamouris and Yun, 2020). Recent data have shown that the use of reflective materials in cities reduces the ambient temperature by 0.09 °C per 0.1 increase of the urban albedo while reducing heat-related mortality between 0.1 to 4 deaths per day (Santamouris and Fiorito, 2021).

The recent development of photonic and plasmonic materials has skyrocketed the mitigation potential of modern materials used in the built environment. Photonic materials or Daytime Radiative Coolers (DTRC) exhibit sub-ambient surface temperatures under the sun's daytime (Santamouris and Feng, 2018).

Daytime radiative cooling materials can be classified into multilayer photonic structures, metamaterial 2D-3D photonic structures, polymers, and paints for radiative cooling (Santamouris and Feng, 2018). Although other materials had previously achieved daytime radiative cooling, a new photonic material recently achieved 4 °C below ambient temperature under direct sunlight (Raman et al., 2014). This photonic material was a breakthrough in the field, and many authors have followed their approach. Numerical simulation of the sample inside a vacuum chamber showed a theoretical maximum reduction of 60 °C (Chen et al., 2016) below ambient temperature. Experimentally the material achieved an average temperature reduction of 37.4 °C with a sunblock. A double-layer coating composed of densely packed titanium dioxide particles on top of densely packed silicon dioxide or carbide nanoparticles can theoretically achieve 17 °C below ambient at night and 5 °C below ambient under direct solar radiation. However, experiments conducted in Shanghai did not achieve sub-ambient temperatures due to high relative humidity (Bao et al., 2017). A polymer-coated fused (PDMS) silica mirror achieved radiative cooling below ambient air temperature under direct sunlight of 8.2 °C (Kou et al., 2017). Using periodic high and low index layers, a radiative cooling power of 100 $W \cdot m^{-2}$ was attained (Kecebas et al., 2017). An optimized BN, SiC, and SiO_2 gratings on top of a metal/dielectric multilayer structure reached a mean cooling power of 55 W·m^{-2} (Hervé et al., 2018). An equilibrium daytime temperature of -13 °C and cooling power of 105 W·m^{-2} was achieved with two thermally emitting photonic crystal layers comprised of SiC and quartz, on top of a broadband solar reflector made of three sets of five bilayers made of MgF2 and TiO2 with varying periods on a silver substrate (Rephaeli et al., 2013). A complex structure of symmetrically shaped conical metamaterial pillars composed of alternating layers of aluminum and germanium can reach a daytime equilibrium temperature of 9 °C below the ambient temperature and 12 °C at night (Hossain et al., 2015).

Photonic materials sometimes include 3D volumes to improve and tune the emissivity towards the desired spectrum. A cell consisting of a thick phosphorus-doped n-type doped silicon substrate and two identical rectangular dielectric resonators numerically achieved a nighttime minimum temperature decrease of 10.29 K at thermal equilibrium and 7.36 K at daytime with a maximum net cooling power of 95.84 W·m^{-2} (Zou et al., 2017). An experiment doped 25 μm thick polyethylene (PE) with SiC and SiO_2 nanoparticles on top of aluminum, the device was covered with an IR transparent cover (10 μm PE) to avoid convective heat gains achieving an actual stagnation temperature of 17 °C below ambient in Sydney with about 3 mm of water vapor pressure (Gentle and Smith, 2010b).

Many radiative cooling materials have been developed using polymeric-derived composites. A glass-polymer hybrid material (Zhai et al., 2017b) achieved a cooling power of 93 W·m^{-2} under direct sunshine at noon. The material's performance was tested in China comparing two boxes (one with the material and the other without it) where the inside air temperature was measured, showing a 21.6 °C difference (Yi et al., 2020). A cost-effective double-layer coating embedded with titanium dioxide and black carbon particles predicted a net cooling power of 100 W·m^{-2} during the day and 180 W·m^{-2} at night (Huang and Ruan, 2017). Another test in Shanghai compared twelve samples of SiO_2 microsphere-Poly-4-methyl-1-pentene (TPX) hybrid system deposited on fluorine doped tin oxide (FTO). Substrates showed temperatures about 20 °C lower than a black surface, 12 °C lower than the silver-coated glass, and 8 °C lower than the FTO sample; however, they did not achieve sub-ambient cooling, showing an average temperature of 15 °C higher than ambient.

Paints for easy and scalable application based on a hierarchically porous poly(vinylidene fluoride-co-hexafluoropropene) have achieved a sub-ambient temperature drop of 6 °C and cooling powers of 96 W·m^{-2} (Mandal et al., 2018). A 7.3 °C sub-ambient temperature drop was reported at noontime in Beijing by spraying zinc phosphate sodium onto aluminum (Ao et al., 2019). Aperture dependency designs where the radiative cooling surfaces are shaded were introduced by Trombe (cited by (Smith, 2009)) and continued by (Aviv and Meggers, 2017; Smith, 2009; Zhou et al., 2019a, 2019b), showing temperature drops of up to 11 °C below ambient temperature.

Besides material development, several authors focused on system development (Ahmadi et al., 2016; Erell et al., 2006; Erell and Etzion, 1999, 1992; Ferrer Tevar et al., 2015; Goldstein et al., 2017; Hosseinzadeh and Taherian, 2012, 2012; Meir et al., 2002; Molina et al., 2013; Zhao et al., 2017). However, systems relying solely on fluid circulations are focused on nighttime radiative cooling. Systems that work at temperatures higher than the ambient present an advantage since convective heat exchange increases the rate at which energy is removed from the system rather than impede it. This feature of the system obviates the need for windscreens (Erell and Etzion, 1992). Convective heat gains remain a problem to be solved. If sub-ambient temperatures are reached, the convection forces tend to augment the temperature of the radiative cooler. According to (Lu et al., 2016), convective heat transfer reduction can be solved in two ways: wind covers and windshields. The most researched wind covers have been made of polyethylene (Berdahl et al., 1983; Landro and McCormick, 1980; Matsuta et al., 1987). However, its aging degradation is a challenge to be solved (Ali et al., 1998). When a thin layer of water precipitates directly on the radiator, it improves its performance since water has a high emissivity. Nevertheless, it reduces the transmittance when it is located on the cover and, therefore, the net output thermal radiation (Gentle and Smith, 2010a). Moreover, dust accumulation reduces the efficiency of radiator systems that incorporate transparent windscreens (Erell and Etzion, 1992). Finally, radiative cooling materials' optimal spectral characteristics depend on the climate conditions and the type of application (Carlosena et al., 2020). In that study, a series of daytime radiative cooling materials, theoretical materials, and existing materials were simulated under a passive and active approach in two differentiated climates, concluding that a material that performs well in a dry climate as a passive solution could perform poorly as an active solution.

This research goal is to study daytime radiative cooling and tunable daytime radiative cooling materials under two climates with different surrounding conditions (urban environment and ideal conditions) and different meteorological conditions. The performance of several materials is compared with the substrates without the coatings to prove its contribution towards lowering the surface's temperature. The materials were tested in a hot, humid climate, Sydney, and in a moderate climate, Pamplona. This study's main novelty is that it includes innovative and low-cost types of radiative cooling materials while it provides experimental information on their performance.

5.2 Methodology

In this research framework, a series of previously[9] developed radiative cooling materials samples were tested in two of the most prevalent climates worldwide (more information is available in Chapter 6). The climates are warm temperate and fully humid with hot summer (Cfa according to the Köppen-Geiger classification, (Kottek et al., 2006)) and warm temperate and fully humid with hot summer (Cfb). One location was chosen for each climate, Sydney (Cfa) and Pamplona (Cfb). Sydney[10] was chosen since it suffers from UHI (Santamouris et al., 2017). Among the Cfb locations, Pamplona was selected as the National Energy Renewable Center is located nearby is a reference center on solar calibration equipment and and facilitated access to their facilities.

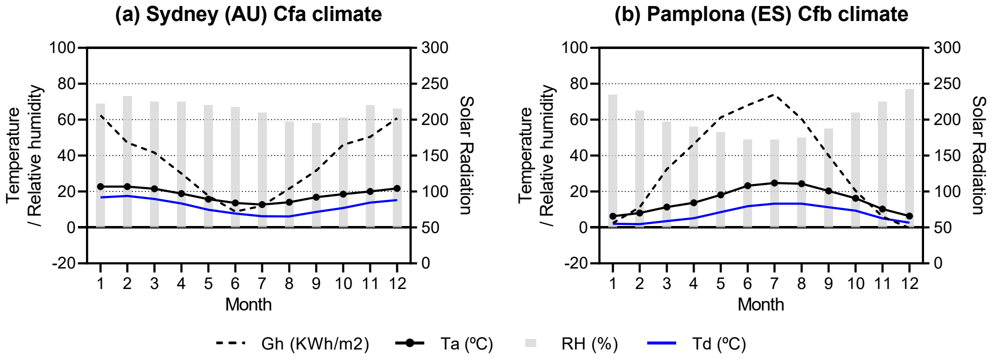

Figure 55: (a) Sydney climate and (b) Pamplona climate.

Six prototype daytime radiative cooling materials and four tunable radiative cooling materials were tested outdoors. Finally, the performance of the materials was compared to the substrates without any coating. Both experiments had a very similar setup. The samples were embedded in hollowed-out squares in an extruded polystyrene (XPS) board to eliminate heat conduction; this condition can be considered almost adiabatic. The materials were directly exposed to the ambient conditions without a convection shield or a sunshade. To study the thermal performance of the samples, the surface temperature of the samples was monitored. The essential experimental equipment consists of surface temperature sensors placed on the center of the surface of each sample, connected to a data logging system.

---

[9] The material design, optimization, fabrication, and characterization details of the samples were described in-depth in Chapter 4.

[10] Moreover, the author conducted two research stays in Sydney at the University of New South Wales.

Moreover, the ambient meteorological conditions were recorded with a meteorological station (a portable meteorological station in Sydney and a BSRN[11] weather station on a rooftop from the National Energy Renewable Center in Sarriguren, 10 km away from Pamplona). Both stations monitor ambient temperature, relative humidity, wind speed, global and diffuse solar radiation on a horizontal surface. This data is used to characterize the outdoor climatic conditions onsite. The whole measurement is based on the thermal balance of the material. To test the thermal performance, its surface temperature when exposed under the direct sun is needed alongside the meteorological data.

$$P_{out} = \varepsilon_s \cdot \sigma \cdot T_{sample}^4 \tag{21}$$

Where P_{out} is the outgoing radiating power, ε_s is the emissivity of the surface, the blackbody radiation in the wavenumber v when its temperature is T_s, $G_s(v)$ the irradiance received by the surface at a wavenumber v.

$$P_{in} = R_{solar} + (h_{conv} + h_{cond}) \cdot \left(T_{amb} - T_{sample}\right) + R_{amb} \tag{22}$$

$$\varDelta T = (\mathrm{P_{in}} - P_{out})/A_{surface} \tag{23}$$

5.2.1 Experimental setup in Sydney

Once the materials' reflectance and emissivity were characterized, as described in 4.3.2, an experiment was conducted on the 12th of April of 2020 in a Square House[12] terrace at the University of New South Wales during a research stay at this institution. During the experiment, the meteorological information was recorded (Figure 57); the radiation was measured by a 4-component net radiometer (Hukseflux NR01) with four separate measurements of global and reflected solar radiation and downwelling and upwelling longwave radiation, weather station (Gill Instruments MetPak Pro1723-2B-2-111) monitored ambient air temperature, humidity, and wind speed.

---

[11] Baseline Surface Radiation Network (BSRN) is a project of the World Climate Research Program (WCRP) and the Global Energy and Water Cycle Experiment (GEWEX) and detects important changes in the Earth's radiation field at the Earth's surface which may be related to climate changes.

[12] Due to the COVID outbreak in March 2020, many restrictions on the location and duration took place. As a result, the experiment could not be carried out longer overnight.

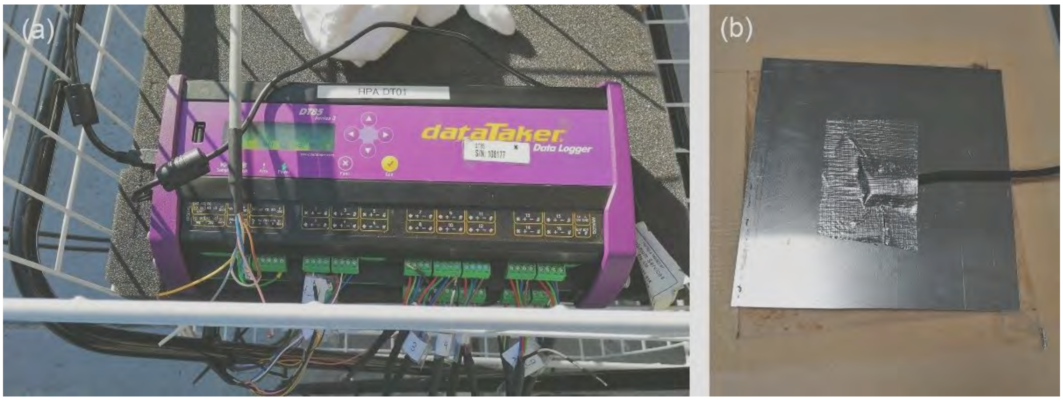

Figure 56: Photos of the experimental setup (a) DataTaker datalogger, (b) thermocouple attached with thermal paste to the samples' bottom side with conductive paste.

Seven surface temperature sensors (LSI Pt100) located at the bottom side of the samples recorded the temperature (Figure 56a); all the equipment channels went through a datalogger (dataTaker DT85 Series) (Figure 56b). Three analog channels were used for the net radiometer, 2 digital channels for the weather station, and 8 analog channels for the surface temperature sensors.

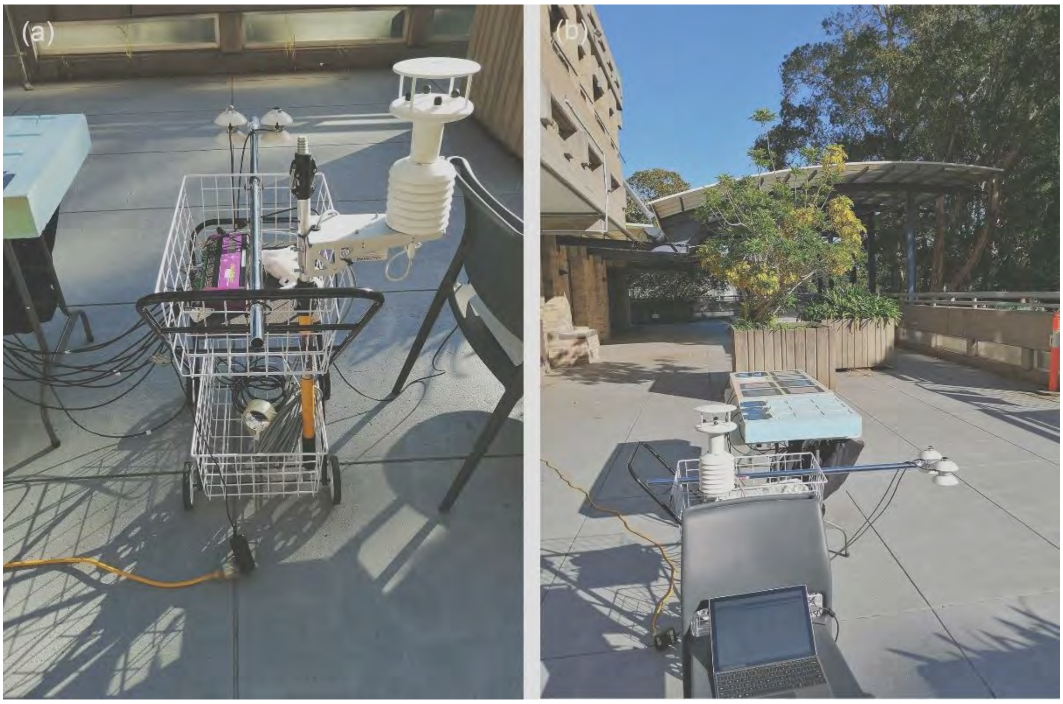

Figure 57: Photos of the experimental setup in the Square House at UNSW, Sydney, Australia. (a) Mobile meteorological weather station with radiometer (b)general photo of the samples contained in an XPS board and the weather station.

5.2.2 Experimental setup in Pamplona

The reflectance of the second samples (Table 7) was characterized as explained in 4.3.2. The experiment was conducted from the 16th to the 20th of October of 2020 on the National Renewable Energy Center (CENER)[13.] During the experiment, the meteorological data was recorded using their permanent equipment[14] part of the Baseline Surface Radiation Network. The station is composed of 3 pyranometers for global horizontal irradiance (Kipp&Zonen, CMP22), 1 shaded pyranometer for diffuse radiance (Kipp&Zonnen, CMP22), 1 pyrheliometer on a sun tracker for beam irradiance (Kipp&Zonnen, CHP1), and a shaded pyrgeometer for downwelling infrared radiation (Kipp&Zonen, CGR4). Kipp & Zonen equipment maximum uncertainty is 2% for hourly totals and 1% for daily totals. Other components are sensors to measure atmospheric pressure (Vaisala, PTB110), air temperature and relative humidity (Vaisala, HMP45C), and wind speed with an anemometer (Ammonit, P6100H). The air temperature measurements range from -39.2 °C to +60 °C, the accuracy at 20 °C is ±0.2 °C. The relative humidity measurement range is 0.8 to 100 °C with accuracy at 20 °C against factory references ± 1 %RH. The anemometer range is 0.3 to 75 $ms^{-1,}$ and ± 0.03 ms^{-1} accuracy, and the wind vane has a full 360° range, ± 2° accuracy, and 0.5° resolution.

This data was used to characterize the outdoor climatic conditions onsite. The measurement is based on the thermal balance of the material. When exposed to the sun the materials' surface temperature is recorded and complemented with the meteorological data. The six samples' surface temperature was monitored with six surface temperature sensors (thermocouples type K connector TP from Testo) connected to 3 data logging devices (Testo Saveris 2-T3 WiFi) with ± (0.5 + 0.5 % of mv) °C accuracy and range is -40 °C to 400 °C with ±0.2 °C accuracy. As seen in Figure 58, a cell phone connected to a battery was placed to generate a WiFi net to retrieve data from the dataloggers and synchronize it with the cloud. The general setup can be seen in Figure 59.

---

[13] The experiment was scheduled in August, however due to manufacturing delays and COVID related restrictions it was postponed to the month of October. Moreover, for safety reasons the experiment was disassembled the 19th of October due to high-speed winds announcements which reached up to 90 km·h^{-1} in Pamplona.

[14] CENER laboratory is the first and only one in Spain to be accredited by the ENAC entity for calibration of field pyranometers and pyrheliometers.

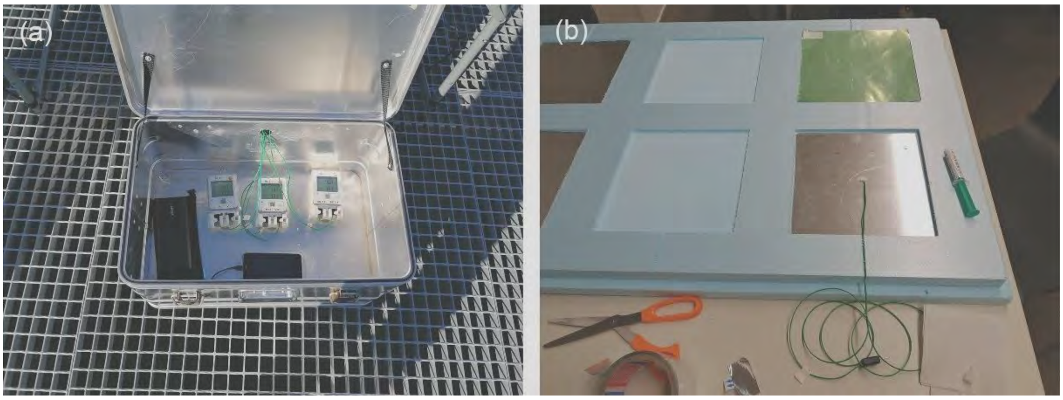

Figure 58: Photos of the experimental set up (a) 3 WI-FI dataloggers (2 thermocouples each), Wi-Fi-net created with a smartphone plugged into a power bank to allow remote monitoring during several days, (b) Thermocouple attached with thermal paste to the samples' bottom side.

Figure 59: Photos of the experimental setup in CENER, Sarriguren, Spain. The samples are contained in an XPS board and monitored with thermocouples connected to dataloggers.

5.3 Results

5.3.1 Experiment in Sydney

The experiment conducted at the University of New South Wales, as opposed to all the experiments on radiative cooling presented in the literature, had obstructed views. The samples were in a location whose surrounding building emitted infrared radiation to the samples, and the trees shadowed during brief periods of the experiment (Figure 60b). This experimental setup is, as a result, more realistic since it assimilates an urban environment. As seen in Figure 60a, a total of 7 samples from the first set of samples (Table 6) were tested, the bare aluminum substrate (A), 2 samples with encapsulated commercial thermochromic pigment (AT), 2 DRC materials of aluminum with the silica emissive layer (AS) and 2 TDRC of aluminum with the encapsulated commercial thermochromic pigment and an emissive layer (ATS). Besides the samples developed, another set of commercial samples were monitored[15].

Figure 60: Photos of the experiment at UNSW, Sydney, Australia. (a) The yellow XPS board contained the developed samples; the blue XPS board contained the commercial samples. (b) general photo of the experimental setup with the nearby Square House building.

During the experiment, the short and longwave sky radiation was monitored; during part of the day, some pictures were taken with a GoPro with a fisheye lens to check the sky view factor of the samples (Figure 61). As shown in Figure 66, at 13:00, there is a substantial decrease in solar radiation due to passing clouds during that period. This decrease of solar radiation was expressed in a reduction of samples surface temperature. At sunset, around 17:00, the solar radiation abruptly decreased, and the samples quickly achieved sub-ambient temperature from that point onwards. The bare aluminum sample without coating (A) presented a higher temperature than the rest since the emissivity in the atmospheric window of the material is negligible.

---

[15] These samples belong to Jie Feng as part of her PhD on radiative cooling.

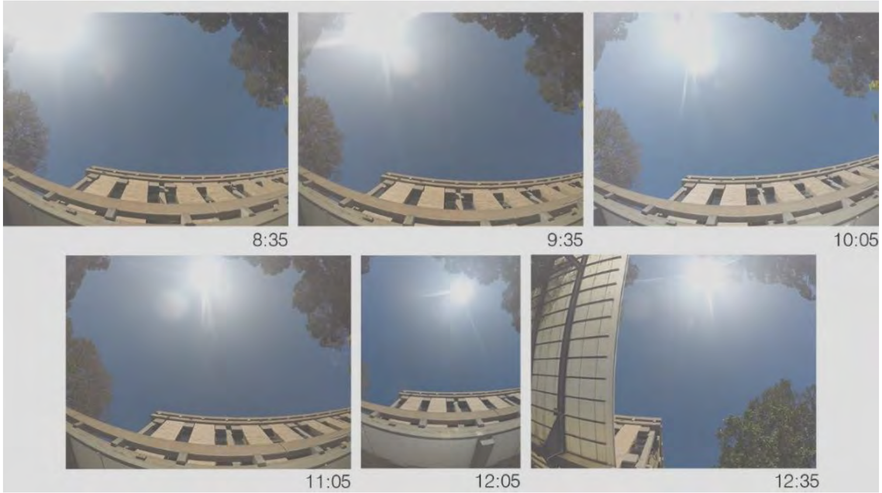

Figure 61: Sky photos during the experiment taken from the XPS board.

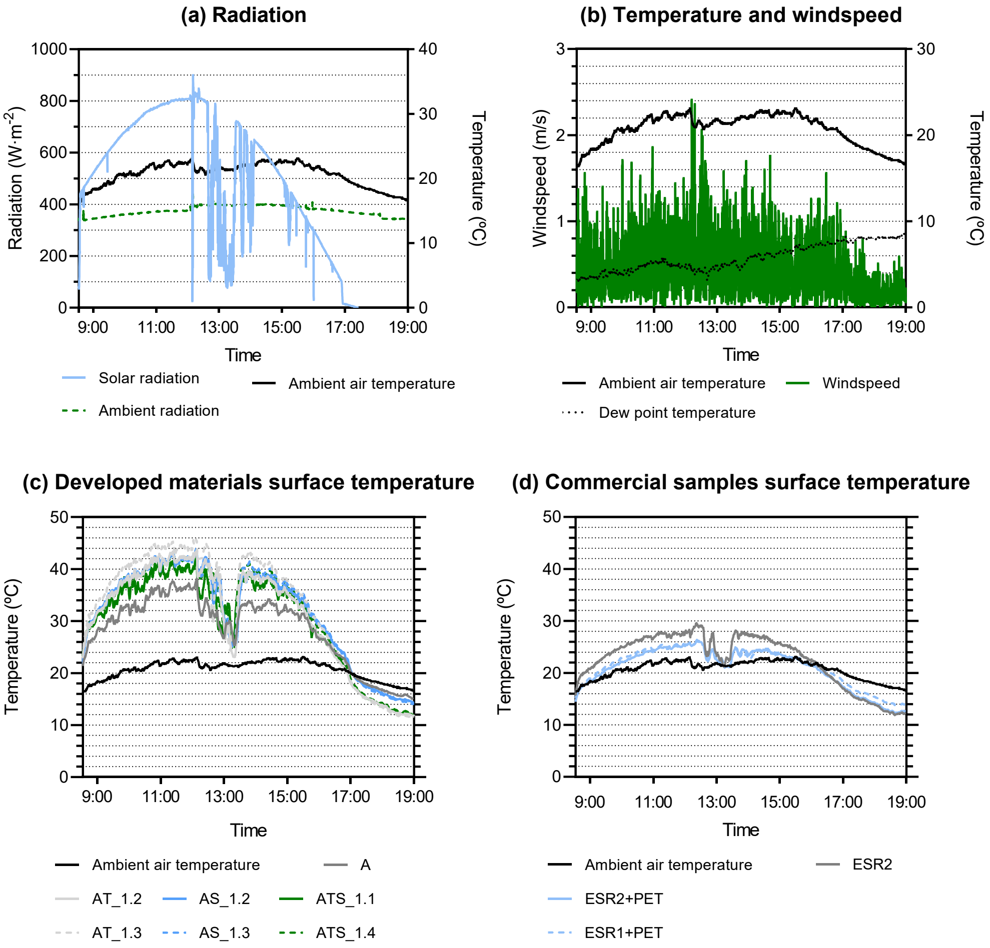

Figure 62: (a) Solar and ambient radiation (b) ambient air temperature, dewpoint temperature, and wind speed. (c) The surface temperature of the developed samples and (d) Surface temperature commercial samples during the Sydney experiment. See Table 6 and Figure 46 for details on the material composition.

Figure 62 a and b show the recorded meteorological data, the solar radiation peaked up to 900 W·m$^{-2,}$ and the longwave 451 W·m^{-2} with an average of 368 W·m^{-2} the maximum registered ambient temperature was 28 °C with a minimum of 14 °C and an average of 22 °C. The average dew point temperature was 6.4 °C, the wind speed was relatively low with a maximum of 2.4 m·s^{-1} and an average of 0.4 m·s^{-1} (Figure 62b).

Table 9 summarizes the maximum surface temperature achieved by the samples, the minimum surface temperature, and the maximum temperature difference between the surface and the ambient (material heats up), and the difference between the ambient temperature and the surface's temperature (material cools down below the ambient). All the samples heated up considerably, the bare aluminum (A) was up to 15.11 °C above the ambient temperature, the samples with the emissive coating performed worse than the bare aluminum. During the day, the worst performing sample was AT_1.3 sample, reaching up to 23.43 °C above the ambient or a surface temperature of 45.72 °C. The highest temperature was achieved at noon when the solar radiation was around 800 W·m^{-2}. This is consistent with the solar reflectivity reduction caused by the emissive coating's application; the thicker the coating is, the higher the emissivity and the lower the reflectivity. Therefore, this sample achieved the lowest temperature at night, 9.75 °C being up to 5.11 °C below the ambient temperature. All the samples achieved sub-ambient cooling from sunset onwards but were especially significant in the samples with a thicker emissive coat (Figure 62 c). As seen in Figure 62 d, the commercial samples registered temperatures above the ambient air; however, the difference was less significant than the developed samples.

Table 9: Summary of the main experimental data in Sydney.

12th April (11:00 - 24:00) sunset 17:36							
	A	**AT_1.2**	**AT_1.3**	**AS_1.2**	**AS_1.3**	**ATS_1.1**	**ATS_1.4**
Max surface T (°C)	38.10	43.61	45.72	43.38	43.81	42.22	43.65
Min surface T (°C)	12.40	9.75	9.36	11.98	11.58	9.76	10.12
ΔT Max (T_{surf-} T_{amb})	15.11	20.65	23.45	20.69	20.91	19.32	20.75
ΔT Min (T_{amb}-T_{surf}) [16]	-2.02	-5.11	-5.54	-2.50	-2.88	-5.04	-4.70

The samples with commercial thermochromic pigment degraded in an hour, turning reddish. An hour later, they had lost their reversibility properties and turned completely white (see

---

[16] The difference between the ambient temperature and the samples is negative, which means that the samples achieve sub-ambient cooling.

Figure 63 and Figure 64). This result was expected as durability when exposed to weather and aging is one of the main constraints of thermochromic paints (Karlessi and Santamouris, 2013). However, this process happened at a faster pace than initially predicted.

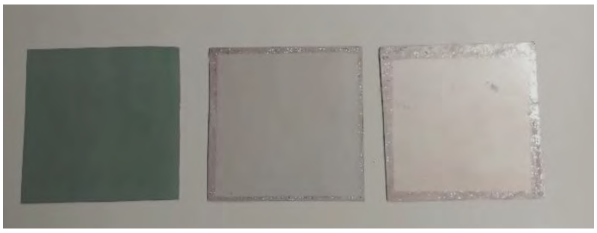

Figure 63: Photo of the samples with thermochromic pigment (AT) from left to right AT1.1, AT1.2, and AT1.3. See Table 6 and Figure 46 for details on the material composition.

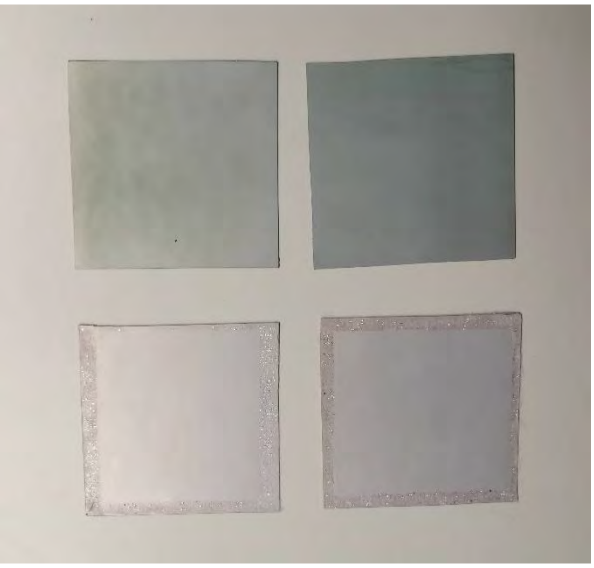

Figure 64: Photo of the samples with thermochromic pigment (ATS), starting from the top left corner: ATS1.1, ATS 1.2, degraded ATS1.3 sample, and degraded ATS1.4. See Table 6 and Figure 46 for details on the material composition.

5.3.2 Experiment in Pamplona

The experiment conducted in the National Renewable Energy Center (CENER) rooftop allowed the samples' direct exposure to the sky without unobstructed views since the facility is designed to test solar photovoltaic and thermal panels (Figure 65). A total of 6 samples from Table 7 were tested, the bare aluminum substrate (A), the Vikuti sample (V), 2 DTRC materials of aluminum with the silica emissive layer (AS_2.2 and AS_2.3), and 2 two samples the emissive layer formulated for plastic deposition on top of a Vikuiti film (VS1 and VS2). The experiment was monitored for five consecutive days with different meteorological conditions. Figure 66 shows the meteorological data from those five days.

The samples' surface temperature was recorded and compared to the ambient air temperature in Figure 67. All the samples achieved subambient cooling by noon even with an incident solar radiation of 633 W·m^{-2} and infrared atmospheric radiation ranging from 280 to 320 W·m^{-2}. The higher ambient temperatures induced by the solar radiation heated the samples. Before noon, the aluminum sample A was 3.62 °C below ambient. The samples with emissive coating, AS_2.2, and AS_2.3, achieved 3.62 °C and 3.92 °C, respectively. The samples with the commercial substrate, V, V_1.1, and V_1.2, had a higher solar reflectivity and achieved 6.12 °C, 7.32 °C, and 7.12 °C below ambient temperature. From 12:55 onwards, the samples with the aluminum substrate were hotter than the ambient air temperature due to the high absorption of solar radiation in the 0.3-2 μm range.

Nevertheless, the AS samples were up to 5 °C cooler than the aluminum sample and an average of 1 °C lower than the sample without coating. The materials with coating showed a better behavior due to their ability to radiate heat in the infrared wavelengths. The Vikuiti samples' low surface temperature led to surface water condensations, as seen in Figure 69. These samples had an almost ideal solar reflectivity and a broadband emissivity in the infrared wavelengths since the materials reflected all the incident heat and emitted any possible heat gains, leading to substantial temperature drops.

Figure 65: Photos of the experimental set-up, (a) Day 1: sunny day, and (b) Day 5: rainy day.

The materials presented three distinct behaviors (Figure 66) corresponding to different climatic conditions (Figure 67). Day 1 was sunny with low temperature (mean of 10.5 °C day and 4°C at night) and high humidity (62%), the aluminum samples heated up during the day and attained subambient cooling at night; the same happened with the V samples. The aluminum samples behaved better than on any other day; as discussed in (Feng et al., 2020a), the cooling performance of the materials has an almost linear response to changes in the ambient air temperature.

Day 2 and 3 were similar, sunny with high passing clouds, moderate daytime temperature (mean of 15 °C days and 7 °C at night), medium relative humidity (55%) and low wind speeds

(0.78 m·s^{-1}); as a result, all the samples had a similar thermal response both days. Day 2 had a slightly higher relative humidity than day 3, translated into lower temperatures during day 2 and higher during day 3. The aluminum samples heated up more significantly than the previous days due to higher temperatures and similar relative humidity. The plastic samples achieved subambient cooling during both days (Figure 67 (b)) since the relatively low humidity favors the thermal exchange. In cloudy days, broadband emitters end up absorbing radiation coming from the clouds, and as a result, the thermal equilibrium is achieved at higher temperatures.

(a) Temperature, solar and ambient radiation

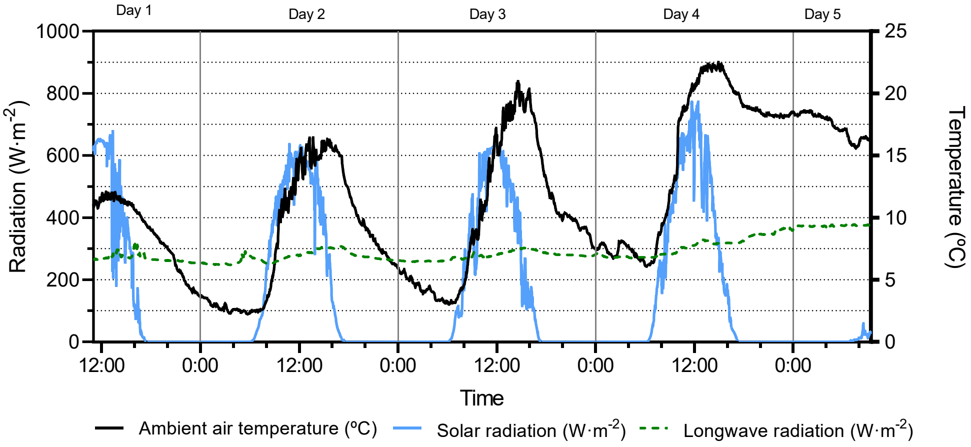

(b) Temperature, relative humidity, and wind speed

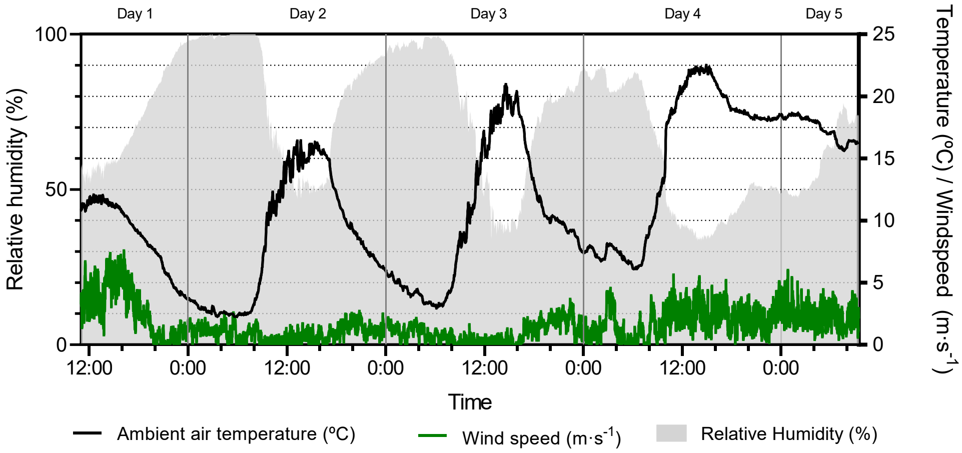

Figure 66: Climate data during the five consecutive days of the experiment. (a)Temperature, solar and ambient radiation, and (b) ambient air temperature, relative humidity, and wind speed.

(a) Surface temperature aluminum samples

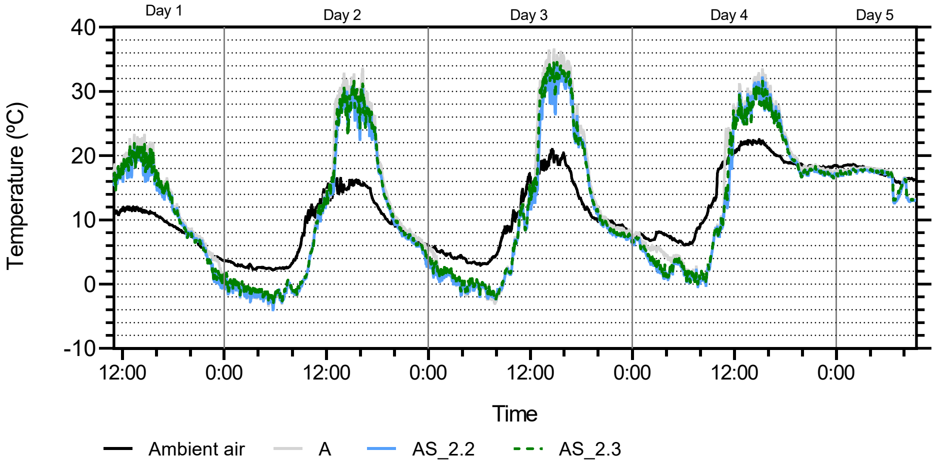

(b) Surface temperature vikuiti samples

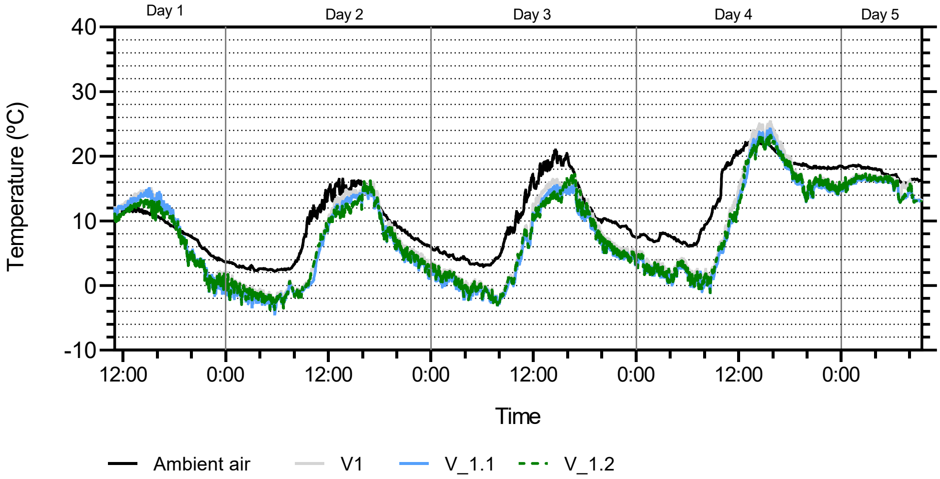

Figure 67: Samples surface temperature throughout the five days of the experiment. (a) aluminum samples and (b) samples with Vikuiti substrate. See Table 7 and Figure 46 for details on the material composition.

Finally, day 4 was very sunny during the daytime and very cloudy at night with high temperatures, 20.6 °C during the day and 18 °C at night, and low relative humidity (39%), and higher ambient radiation (323 W·m^{-2}). Although the temperatures reached up to 22.3 °C during the day and were higher than the previous days, the aluminum samples were cooler, 9 °C (AS_2.2 and AS_2.3) over ambient temperature. Outgoing radiation evacuated from the materials was favored by low relative humidity. On the contrary, in the previous days, as seen in Figure 67 (a), AS_2.2 and AS_2.3 had reached 18 °C above ambient (day 2 and day 3) since water vapor inhibits outgoing radiation. The V samples achieved higher temperatures than in the previous days and surpassed ambient temperature. This phenomenon might be explained because the longwave radiation increases from noon onwards and lower wind speeds, making the convective heat exchange lower, penalizing the broadband emitters (VS1 and VS2) while benefitting the strictly spectrally selective materials (AS_2.2 and AS_2.3). When surfaces are above ambient air temperature, wind helps to reduce the surface temperature. The night leading to day 5 was cloudy with higher longwave radiation (Figure 66 (a)); thus, the samples did not cool down as much as in the previous days. Moreover, on day 4, higher convection led the Vikuiti samples below ambient air temperature to increase their temperature around and above ambient air temperature.

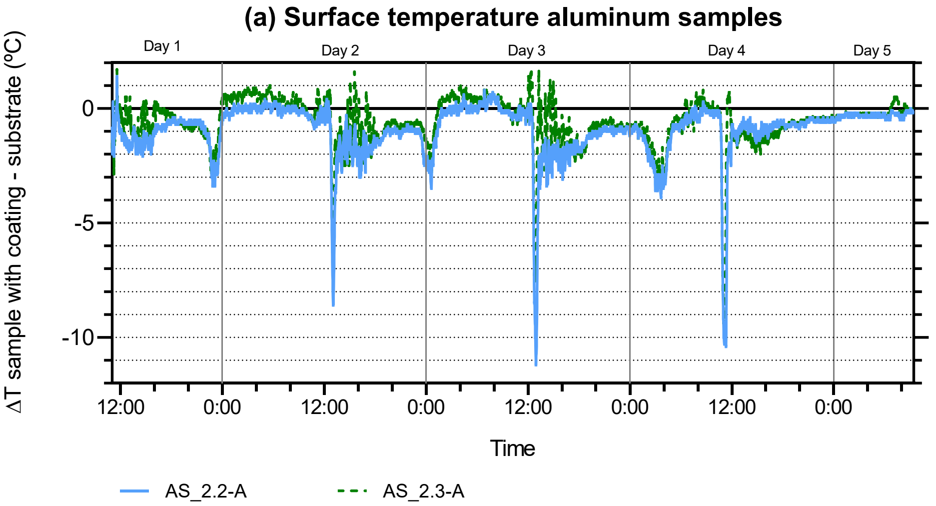

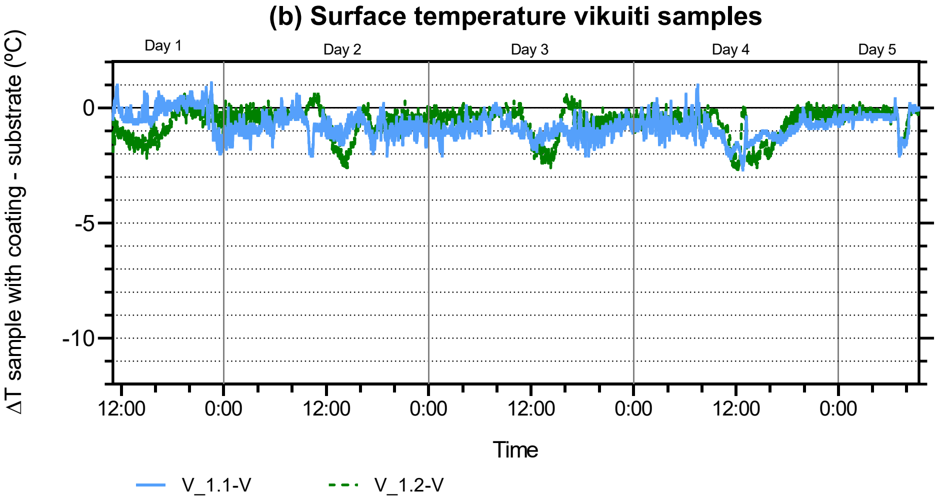

Figure 68: DTRC sample’s surface temperature difference with the bare substrates (a) comparison of AS_2.2 and AS_2.3 with bare aluminum (A) (b) comparison of V_1.1 and V_1.2 with bare Vikuiti substrate (V). Negative values reflect when the samples with coating are below the substrate’s temperature. See Table 7 and Figure 46 for details on the material composition.

Finally, to see the emissive coating effect, the samples' surface temperature was compared to the bare substrate in Figure 68. Although AS_2.2 had a lower solar reflectivity and lower emissivity in the transparency window than AS_2.3 (see Figure 52), which is considered a worse optical behavior, it performed better throughout all the days, as seen in Figure 68 (a). This behavior might be related to high relative humidity values. V samples are broadband emitters in the infrared wavelengths (Figure 53), V and V_1.2 had a very similar response, and V_1.1 had a higher emissivity. Nevertheless, V_1.2 achieved more punctual temperature drops than V_1.1, but it was V_1.1 that achieved a more stable lower temperature during all the experiment days except day 1, probably due to low temperatures and high humidity (Figure 68 (b)). Several significant temperature drops in the AS samples (Figure 62(a)) can be explained because of water condensation on the samples' surface before noon. Water condensation augments emissivity, and the evaporation of this layer might lead to some significant temperature decrease due to evaporative cooling. Although the temperature difference is less significant, it can be observed in the Vikuiti samples around noon.

Figure 69a shows the general experimental, the two samples in the middle were the samples with the emissive coating; the sample below furthest to the left was the Vikuiti sample without the coating, which showed tiny water drops on top. More detail of V_1.1 and V_1.2 is seen in a closer photo in Figure 69 b.

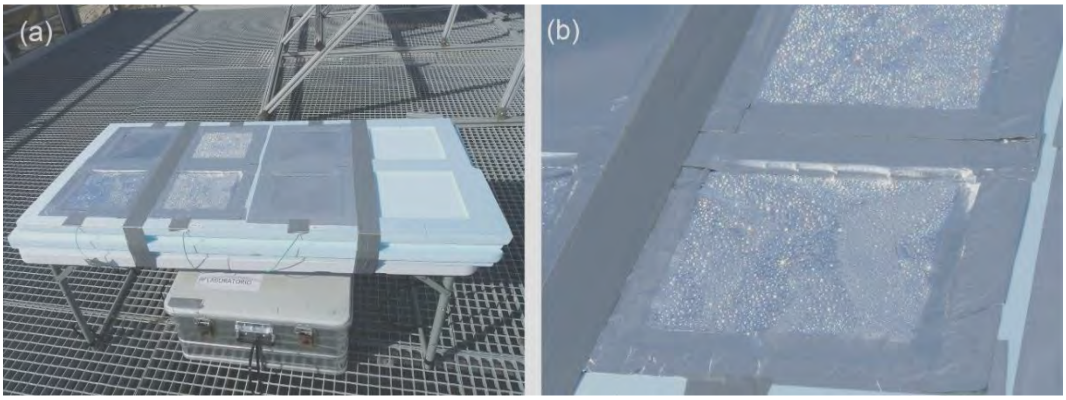

Figure 69: Photos taken Day 4 at 12:12 (a) all the samples in the insulation board, showing condensation in the samples with the plastic substrate (b) the Vikuiti samples with the emissive coating and condensed water.

Table 10 to Table 14 summarize the surface's maximum and minimum temperatures, the maximum and minimum difference between surface temperature and ambient temperature. Positive values correspond to materials heating and negative values when materials cool down below ambient temperatures.

Table 10: Summary of the measured surface temperature, data from day 1. See Table 7 and Figure 46 for details on the material composition.

Day 1 (11:00-24:00)						
	A	AS_2.2	AS_2.3	V	V_1.1	V_1.2
Max surface T (°C) ±0.2 °C	23.2	21.6	21.9	15	15	13.7
Min surface T (°C) ±0.2 °C	0.2	-0.6	0.2	-1.2	-1.5	-1.2
ΔT Max (T_{surf}-T_{amb}) ±0.4 °C	11.86	9.86	10.46	3.92	3.94	2.52
ΔT Min (T_{surf}-T_{amb}) ±0.4 °C	-3.43	-4.41	-3.71	-5.73	-5.83	-6.13

Table 11: Summary of the measured surface temperature, data from day 2. See Table 7 and Figure 46 for details on the material composition.

Day 2 (00:00-24:00)						
	A	AS_2.2	AS_2.3	V	V_1.1	V_1.2
Max surface T (°C) ±0.2 °C	33.5	30.6	31.6	16.1	15.5	16.2
Min surface T (°C) ±0.2 °C	5.3	2.8	3.8	2	1.1	1.4
ΔT Max (T_{surf}-T_{amb}) ±0.4 °C	18.15	15.37	15.94	1.88	0.53	1.20
ΔT Min (T_{surf}-T_{amb}) ±0.4 °C	-2.96	-3.37	-2.66	-5.83	-6.63	-5.97

Table 12: Summary of the measured surface temperature, data from day 3. See Table 7 and Figure 46 for details on the material composition.

Day 3 (00:00-24:00)						
	A	AS_2.2	AS_2.3	V	V_1.1	V_1.2
Max surface T (°C) ±0.2 °C	36.5	34.2	34.6	16.8	15.8	17.2
Min surface T (°C) ±0.2 °C	7.6	6.4	6.6	4.1	3.1	3.3
ΔT Max (T_{surf}-T_{amb}) ±0.4 °C	17.47	15.17	15.21	1.28	-0.10	0.43
ΔT Min (T_{surf}-T_{amb}) ±0.4 °C	-6.49	-6.63	-6.63	-8.23	-9.13	-9.13

Table 13: Summary of the measured surface temperature, data from day 4. See Table 7 and Figure 46 for details on the material composition.

Day 4 (00:00-24:00)						
	A	AS_2.2	AS_2.3	V	V_1.1	V_1.2
Max surface T (°C) ±0.2 °C	33.4	32.1	31.6	25.3	24.2	23.5
Min surface T (°C) ±0.2 °C	17	11.9	13.2	11.5	9.7	9.9
ΔT Max (T_{surf}-T_{amb}) ±0.4 °C	11.23	9.93	9.43	3.75	2.55	1.84
ΔT Min (T_{surf}-T_{amb}) ±0.4 °C	-1.36	-7.21	-5.91	-8.31	-10.11	-7.21

Table 14: Summary of measured surface temperature, data from day 5. See Table 7 and Figure 46 for details on the material composition.

Day 5 (00:00-09:25)						
	A	AS_2.2	AS_2.3	V	V_1.1	V_1.2
Max surface T (°C) ±0.2 °C	18.2	17.9	17.9	17.2	16.8	17.3
Min surface T (°C) ±0.2 °C	12.9	12.7	13	13.1	13	12.9
ΔT Max (T_{surf}-T_{amb}) ±0.4 °C	0.84	0.55	0.55	0.29	-0.45	-0.06
ΔT Min (T_{surf}-T_{amb}) ±0.4 °C	-3.40	-3.57	-3.40	-3.31	-3.81	-3.70

5.4 Summary and discussion

Two experiments were conducted in different locations: Sydney and Pamplona - Cfa warm temperature, fully humidy with hot summer, and Cfb warm temperate, fully humid with warm summer, respectively Köppen-Geiger classification. The experimental settings were similar in both locations. The samples were contained inside hollowed-out squares in a rigid extruded polystyrene foam (XPS). The samples' temperature was monitored with probes located at the bottom of the samples. Moreover, the ambient air temperature, longwave and shortwave radiation, wind speed, and pressure were measured. The first experiment in Sydney tested, during a fall day (12th April), samples made of a bare aluminum substrate (A), aluminum with an emissive coating (AS), aluminum with encapsulated thermochromic pigment (AT), and aluminum with encapsulated thermochromic pigment and an emissive coating (ATS). The experiment, as opposed to the literature, is tested in an urban environment with obstructed views. As a result, the samples received longwave radiation from the surrounding buildings; during the experiment preparation in Sydney, the thermochromic samples degraded in less than an hour, losing their reversibility properties due to the pigment's organic composition. During the day, the samples were up to 23.45 °C above ambient, averaging 2°C higher than the bare aluminum substrate. This observation is consistent with their measured spectral properties, a low reflectivity in the solar wavelengths, and an average emissivity in the atmospheric window. However, at night, the samples' high infrared emissivity led to sub-ambient cooling in all of them, being especially significant in the ATS samples (aluminum with encapsulated thermochromic pigment and emissive layer) and related to the emissive layer's thickness; the higher the coating based on silica, the higher the emissivity but, the lower the solar reflectance.

The second set of samples were tested in Pamplona during four consecutive fall days (16th to 20th October), consisting of DRC materials with two different substrates. To test the emissive coating's efficiency, the samples without the coatings were tested alongside bare aluminum and one Vikuiti film (A and V). The samples based on Vikuiti V, V_1.1, and V_1.2, dropped their temperature during the daytime (12:00-15:00) an average of 1 °C, 2.05 °C and 2.70 °C below ambient, respectively, and a maximum of 6.26 °C, 7.45 °C and, 7.97 °C. The samples with the aluminum substrate did not reach sub-ambient cooling during the day; nevertheless, the ones with the emissive coating were during the daytime 1.5 °C (AS_2.2) and 0.7 °C (AS_2.3) below the bare aluminum substrate. All the samples achieved nighttime radiative cooling since they were emissive in the atmospheric window. Due to manufacturing problems, the samples arrived in the middle of September, changing the experiment's schedule originally intended in August. This second experiment was expected to last for at least two weeks, but due to high wind speeds and COVID restrictions, it was disassembled after four days; however, various climatic conditions were evaluated, sunny days with passing clouds and cloudy days with some showers.

Ideally, all the samples should have been tested in both experiments; however, it was deemed unnecessary to test the first set of samples again since they were an average of 20.96 °C higher than the ambient temperature in Sydney. Although the experiments on radiative cooling should be extended in time to evaluate their potential throughout the year, Sydney's first experiment was unsuccessful. It was not considered worthwhile to continue measuring the samples after the first day's results. However, since some of the samples were exposed outdoors, they might have degraded. The reflectivity and emissivity will be measured again to see whether there has been any degradation.

The results show a promising path in using PMSQ (polymethylsilsesquioxane) as an emissive coating for radiative cooling. The set of samples with commercial substrates achieved daytime sub-ambient cooling. The samples made of aluminum plus the emissive coating achieved a 1.88 °C reduction compared to the bare aluminum and a maximum temperature difference of 11.2 °C (18th at 12:55). Although both experiments were scheduled for summer conditions due to several mishaps, they had to take place in the fall months. Further testing on sprayed coating techniques should be made for applications over different substrates as they might help to reduce the overall temperature of any compatible material. Besides the cooling potential, the heating penalty during the cold season should be evaluated in any application of these products as it is location dependent. Extended periods with different meteorological conditions can show the path towards achieving the ideal material for each climate and application. Besides the cooling potential or temperature reduction, degradation and aging should be carefully studied, especially when including organic components such as polymers. Finally, other experimental settings with circulation fluids should be made to test whether these materials can be integrated into active systems.

5.5 Conclusions

This research has studied scalable daytime radiative cooling materials in two temperate climates, in the first setting in an urban context and in the second throughout different meteorological conditions far from the usual experiments done under real conditions and ideal settings (minimizing convection and relative humidity). This study presents the simulation, development, characterization, and testing of two kinds of daytime radiative cooling materials based on silica-derived emissive layers. The material design and simulation helped understand the structures' optical behavior, providing the necessary insight to tailor the material's thickness and validate the proposed structures before fabrication.

We have proved, for the first time to our knowledge, that low cost (0.3 euros/m^2 for a layer of 2 μm of PMSQ and SiO_2 particles), scalable and sprayable coatings provide significant radiative cooling, as to reduce its temperature significantly over bare substrates in actual climatic conditions.

The following conclusions can be obtained:

(1) Under most climatic conditions, the materials can cool down a metallic substrate a mean of least 1.7 °C with up to 12 °C temperature drops.

(2) The samples based on Vikuiti dropped their temperature during the highest solar radiation and maximum ambient temperatures, an average of 2.70 °C below ambient and a maximum of 7.97 °C during the day.

(3) The substrates presented, in both cases, a better thermal behavior than the materials without treatment.

(4) Although the materials' spectra were not ideal 0.7 (solar reflectivity) and 0.34 (emissivity in the AW), the materials could stay below the ambient temperature at least until noon.

(5) The cost and deposition system presented are good candidates for future broad application in the built environment and architecture.

The path has proven promising for future scalable material development. Further testing on sprayed coating techniques should be made:

(1) Applicating on different substrates present in the built environment (e.g., concrete, ceramic, and glass). The potential substrates need to have sky access to evacuate heat—especially critical applications in roofs and other exposed horizontal building surfaces.
(2) Testing under different meteorological conditions to determine the ideal material for each climate and application.
(3) Incorporating low-cost switchable technologies to avoid overcooling during the heating seasons.
(4) Studying their degradation and aging as they will be exposed to extreme weather conditions and prolonged periods.

These new scalable polymeric materials could lower the cooling demands of buildings and alleviate heat buildup in cities, aiding in lowering the Urban Heat Island phenomenon. Moreover, the technique might be of significant interest for building retrofitting as a spraying technique can be applied onsite or as industrialized elements.

6 WORLDWIDE POTENTIAL OF RADIATIVE COOLING[17]

This chapter presents the worldwide potential of different daytime radiative cooling materials as a strategy to reduce buildings' cooling demand. To evaluate climate dependency, several daytime radiative cooling materials were simulated throughout a typical meteorological year. Using the heat transfer model presented in Chapter 3, eleven materials were simulated in fourteen different climates; different cities suffering from the Urban Heat Island were selected. The chosen materials were some of the previously developed radiative cooling materials in Chapter 4 and tested in Chapter 5 made of aluminum samples with an emissive coating and Vikuiti samples with an emissive coating, two daytime radiative cooling materials from the literature, and four theoretical materials presented in Chapter 3. The background condition assimilated an active system, where a radiative cooling material was placed on top of a conductive surface with a fluid circulating at a constant temperature of 25 °C. The goal is to calculate the amount of radiated heat per material and climate. These simulations' results show the suitability of the different materials for each climate and location under an active approach.

The studied materials indicated a great potential of heat evacuation; the higher the ambient temperatures are, the more strictly selective the material needs to be. In arid climates, one of the literature materials (RC2) and a theoretical material (M8) worked better than in temperate climates since they are more strictly selective. Almost all materials showed good behavior; therefore, choosing the materials based on Vikuiti with an emissive layer would be sufficient. Climates with a higher relative humidity led to even materials' radiative behavior, seeing little

---

[17] The worldwide simulations were run by Dr. Álvaro Ruiz-Pardo and Dr. Enrique from University of Cadiz using the model developed in Chapter 3.

difference among them. Convection had an essential role in the total heat loss or gains. In some locations, such as Phoenix, Alice Springs, and Monterrey, where the outside temperature is higher, adding a convection barrier would make the system more applicable throughout the most demanding periods.

6.1 Introduction

The emissions of CO_2 due to the burning of coal, oil, and gas have continuously increased and are believed to lead to global warming and rising sea levels (IPCC, 2018). According to the International Energy Agency (IEA), cooling accounts nowadays for 20% of the total electricity used in buildings around the world, and this tendency is predicted to increase in the hottest areas of the world with the demand for greater thermal control, population growth, and climate change (IEA, 2018a). The annual sales of air conditioning (AC) units have grown consistently over the years, with only a recess during the 2008 financial crisis; between 1990 and 2016, they quadrupled to 135 million ("About Montreal Protocol | Ozonaction," n.d.). The most widespread system of air conditioning is based on vapor compression. This kind of air conditioning discharges latent waste heat to the ambient air. It has shown an increase in the street air temperature in central Paris's urbanized areas, ranging from 0.5 °C to 2 °C depending on the AC equipment employed (Munck et al., 2013). Besides the rejection of excess heat to the ambient, the main contribution of emissions of GHGs of air conditioning systems is energy use. In 2016, the energy used for cooling accounted for 65% of the total generation (coal for 37%, gas 24%, and oil 4%), resulting in average emissions of around 505 grams of carbon dioxide (CO_2) per kWh (gCO_2/kWh) of generation (IEA, 2018a). The measured concentration of carbon dioxide in the Earth's atmosphere raised from 315 ppm at the end of 1950 to the current 412 ppm (US Department of Commerce, n.d.). Moreover, the leakage or improper disposal of refrigerants contributes to emissions since they are usually comprised of hydrofluorocarbons (HFCs). The Montreal Protocol of 1987 and the Kigali Amendment aimed at progressively phasing down the production and use of chlorofluorocarbons (CFCs) and hydrochlorofluorocarbons (HCFCs) around the world ("About Montreal Protocol | Ozonaction," n.d.). The cooling demand increases notably with heatwaves, where the situation is worsened by the use of air conditioning equipment, leading to large energy consumption and worsening outdoor heat stress (Viguie et al., 2020). AC systems release heat into the street, warming the outside air and increasing the heatwave (Munck et al., 2013; Y. Wang et al., 2018). During the hot spell of 2018 in Beijing, 50% of the power capacity went to air conditioning (Buranyi, 2019).

Envelope materials of buildings and urban structures significantly influence the urban thermal balance; they absorb solar and infrared radiation and evacuate part of the accumulated heat to the ambient air and atmosphere increasing ambient temperature (Santamouris et al., 2011). The Urban Heat Island Effect (UHI) has been studied in terms of the temperature differences between rural and urban locations (Kolokotroni et al., 2012). The first reference to point out this phenomenon dates from 1833, in which the evidence of higher temperatures in cities was reported (Oke, 1982).

Extensive urban expansion and population growth have aggravated environmental problems such as local climate, resource depletion, and air pollution change (Yin et al., 2018). Moreover, this phenomenon can significantly alter the local microclimate, producing enduring high temperatures (Fabiani et al., 2019). Heatwaves aggravate UHI; Brooke Anderson and Bell (Brooke Anderson and Bell, 2011) found that mortality risk increased during prolonged periods of extreme heat compared with the community's usual climate. UHI is highly interlinked to amplified cooling loads during the summer period (Vardoulakis et al., 2013). Another study presented data supporting that neighborhoods with higher proportions of concrete and higher dense infrastructure exacerbate urban heat (O'Brien et al., 2019) despite being more walkable. To avoid using traditional heat-absorbing materials, solutions with high albedo have been proposed, such as coolmaterials (Kolokotsa et al., 2018), greenery (Foustalieraki et al., 2017; Gao et al., 2020), and phosphorescent materials (Kousis et al., 2020; Rosso et al., 2019). A recent study (Bartesaghi-Koc et al., 2021) compared several mitigation techniques on an urban street canyon, concluding that on its own, radiative cooling materials applied on shading devices decreased up to 1.6 °C ambient temperature and 24.2 °C surface temperature, being one of the most efficient strategies.

Daytime radiative cooling materials have been proposed as a mitigation strategy for the Urban Heat Island as a passive technique. The average UHI varies between 0.5 °C to 7 °C, where 90% of the data is below 4.5 °C (Santamouris, 2020). The magnitude of UHI varies in Asian and Australian cities from 0.5 °C to 11 °C (Santamouris, 2015a) and between 1 °C and 10 °C in Europe (Santamouris, 2016b), where the increase of cooling load per degree of UHI is between 0.5 to 8 kWh/m^2/C/y (Santamouris, 2020). In Sydney, the UHI has a peak intensity of up to 6 °C, leading to an increase of up to three times the cooling demand of buildings (Santamouris et al., 2018). On the one hand, as ambient air temperature increases, electric power cables' carrying capacity decreases; this event occurrence rises during the summer with the augment of electricity load caused by air-conditioned usage (Bartos et al., 2016). During the summer, power plants have to respond to the increase of the electricity load, which leads to augmenting the pollutants released into the air (Lo and Quattrochi, 2003). In Phoenix, mesoscale simulations predicted an increase in the ozone concentration between 10 to 30 ppb during the nighttime (Li et al., 2014). On the other hand, the UHI and heatwaves have a relevant environmental and financial impact, especially on vulnerable and low-income populations (Santamouris and Kolokotsa, 2015). Exposures to high ambient temperature represent a severe health danger (Brooke Anderson and Bell, 2011). An augment of the mean surface temperature by 1 °C caused a 32% increase in the odds of death from heat exposure in Phoenix, Arizona (Harlan Sharon L. et al., 2013).

The effects of higher temperature on energy, health, pollution, and vulnerability could be aggravated depending on the emissions' path model and the technological, socioeconomic, and demographic developments (Santamouris, 2020). If today's trends are followed, the atmosphere's temperature could increase between 1 °C and 4 °C by the end of the 21st Century (Fiorito and Santamouris, 2017), hindering the thermal exchange of cities. During COP25, energy scenarios were discussed to keep global temperatures from rising more than 1.5°C ("COP25 • UN Climate Change Conference," 2020). As pointed out in (IPCC, 2018), achieving the goal is possible but requires strong transitions in many social aspects. Nevertheless, global warming is not impacting all world areas in the same way due to differentiated multifaceted events occurring at the regional scale (Arnell et al., 2016).

The climate conditions of a specific location will significantly impact the cooling demands and the cooling potential. Some climates require cooling but lack the harvesting potential, others are favorable for production, but refrigeration is unnecessary. For example, some locations may have restraints such as high humidity (condensation problems depending on the operation temperature) and unsuitable despite high cooling demands. The climate needs to be understood by considering many broad aspects like urban morphology, land cover, moisture availability, anthropogenic heat, and materials properties (Santamouris et al., 2016). One common drawback detected among the literature (Fernandez et al., 2015; Raman et al., 2014; Vall et al., 2018; Zhai et al., 2017b) is to evaluate the daytime radiative cooling potential, authors assume clear sky conditions, ignoring factors such as cloudiness. Clouds can act as an insulation barrier preventing the material or panel from losing its heat since the atmosphere reradiates the emitted energy back towards the source, reducing or, in extreme cases, neutralizing radiative cooling. The increase of atmospheric emissive spectral irradiance in the sky window leads the radiative cooler to absorb more atmospheric radiation and restrains its cooling performance (C. Liu et al., 2019).

There are some precedents of savings simulations using new materials for radiative cooling (W. Wang et al., 2018; Zhang et al., 2018), cool materials (Synnefa et al., 2007), high albedo roofing, tree plantation, greenery, and optimized irrigation (Garshasbi et al., 2020a). This research pretends to establish the first approach in energy savings under realistic weather conditions across the globe. New constructive norms, standards, and directives lead toward high-efficient buildings and near-zero energy buildings (nZEB). Passive approaches, plus adequate construction, optimized technology, and installations, with the application of daytime radiative cooling materials, might contribute to lowering buildings' cooling load. Applying the knowledge of radiative cooling and new efficient materials in certain climates might positively impact energy balance, increasing user comfort. As a result, it will steer towards achieving the target of reducing CO_2 emissions.

This research studies the worldwide potential of daytime radiative cooling realistically by simulating several daytime radiative cooling materials in cities with UHI. It uses the developed energy model (Carlosena et al., 2020) that considers the material's spectral selectivity, the incoming spectral solar, and atmospheric radiation. Software for energy modeling, such as EnergyPlus, does not consider spectral discretization. In chapter 3, two different background conditions were simulated, an active system and a passive system. Daytime radiative cooling materials applied as building coatings (passive approach) might lead to heat penalties during the winter. Moreover, new construction norms lead towards a highly insulated envelope; therefore, applying a daytime radiative cooling material on a highly insulated rooftop would not make much difference inside a building since the heat exchange between the interior and the exterior of the envelope is negligible. As reported with cool roofs, their effectiveness for the improvement of building indoor thermal comfort conditions was found to be less significant with lower thermal transmittance (U-value) roofing systems (Giuseppe and D'Orazio, 2015; Synnefa et al., 2007).

The performance of several theoretical radiative cooling materials, two materials in the literature, and the materials developed in Chapter 4 and tested in Chapter 5 were compared. The materials were studied over a highly conductive to assimilate an active solution (for future integration in AC systems). A fluid is maintained at 25 °C throughout the entire cooling period. As a result, considerations for choosing the appropriate are given for each city and climate. Some research has focused on integrating these materials on active systems (Fernandez et al., 2015; W. Wang et al., 2018; Zhang et al., 2018; D. Zhao et al., 2019a); however, before doing so, the materials' potential as active systems should be studied independently of the application system. This study's main novelty is the potential cooling comparison of different daytime radiative cooling materials across the most critical world climates and specifies each heat transfer mechanism's contribution.

6.2 Methodology

The research followed the next steps to obtain the cooling potential of several daytime radiative cooling materials under different climates. First, the Köppen-Geiger climate classification's central global climates were selected according to their prevalence determined by the settlement number. For each climate, at least one representative city that suffers from UHI was chosen. Secondly, eleven materials were selected, two from the literature, Radicool and Skycool (RC1and RC2), four theoretical materials (M5 to M8), four among the previously developed radiative cooling materials in Chapter 4 and tested in Chapter 5 (AS_2.2, AS_2.3, V_1.1, and V1.2), and the aluminum substrate (A). The simulations considered the entire year as some locations might need cooling outside the summer solstice. The cooling potential for every material was calculated in every city, using the previously developed model presented in Chapter 3 and published (Carlosena et al., 2020). Finally, the results were compared according to their radiative cooling potential, and conclusions, suitability, and limitations for each material and climate are drawn.

6.2.1 Materials spectra

Figure 70 to Figure 72 show the materials' spectra discretized per wavelength band and grouped by type of material, theoretical materials (Figure 70) used previously in Chapter 3, materials from the literature (Figure 71), and a selection of the developed materials (Figure 72) from Chapter 4 and tested in Chapter 5. APPENDIX 7: Materials spectral emissivity contains the detail of the optical information for each band.

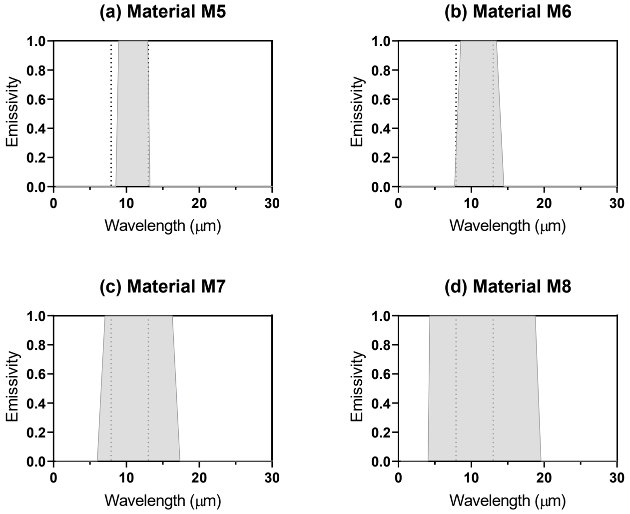

Figure 70:Emissivity spectra of theoretical materials M5, M6, M7, and M8.

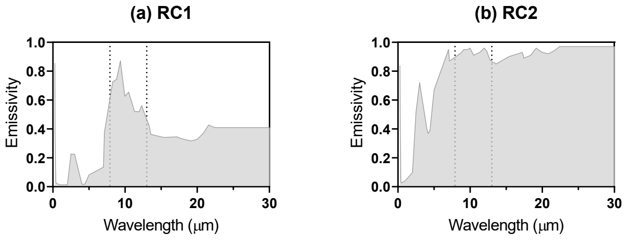

Figure 71:Emissivity spectra of radiative cooling materials from the literature RC1 (Skycool) and RC2 (Radicool).

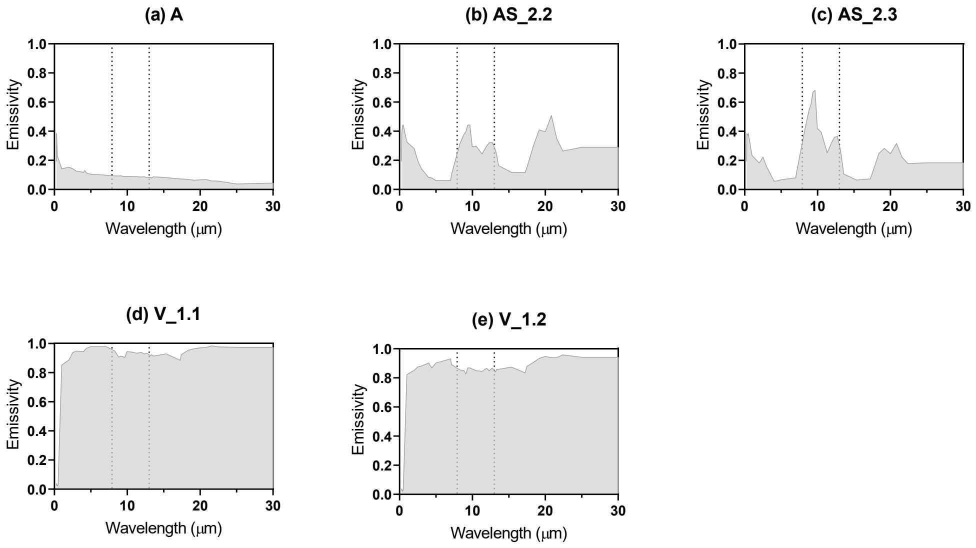

Figure 72: Emissivity spectra of A (aluminum), aluminum with an emissive coating (AS_2.2 and AS_2.3), samples with Vikuiti (V_1.1 and V_1.2).

6.2.2 City selection criteria

In 1973, Oke (Oke, 1973) demonstrated the existing relationship between an urban settlement's size and the magnitude of its heat island. Radiative cooling is of particular interest in cities suffering from UHI. The accumulated heat during the day will be rejected to the outer space instead of to the streets, alleviating the heat buildup in cities and breaking the vicious cycle, augmenting cooling demand by heating the exterior; this can be accomplished independently of the type of application, active or passive. According to Oke, villages of about 1,000 inhabitants exhibit heat islands (assuming 1°C is the minimum urban/rural difference of significance). As a result, the magnitude of Urban Heat Island is explained mainly by climate and population (Manoli et al., 2019).

To determine the worldwide potential application of radiative cooling, the climates of application were studied. The climates that englobe the highest number of settlements around the world were analyzed. The climate selection and representative cities resulted from combing the information from the Global Urban Heat Island Dataset (Center For International Earth Science Information Network-CIESIN-Columbia University, 2016) and the Köppen-Geiger classification by coordinates (Kottek et al., 2006). The Köppen-Geiger climate classification was selected as it considers humidity, which is a determinant factor for radiative cooling rates and potential; moreover, it is widely used in research. As a result, the relationships between the number of settlements, population, and climates were established. Climates in the Köppen classification are based upon vegetation distribution across the world in five areas: the equatorial zone (A), the arid zone (B), the warm temperate zone (C), the snow zone (D), and the polar zone (E). A second letter in the classification considers the precipitation (e.g., Df for snow and fully humid), the third letter is the air temperature (e.g., Dfc for snow, fully humid with cool summer) (Kottek et al., 2006). Equatorial climates' (A) mean of the coldest months is above 18 °C, arid climates (B) have low precipitation volume, and their annual precipitation is ten times below a dryness threshold which depends on annual temperature, and the mean temperature, the warm zone (C) mean temperature of the coldest months is between -3 °C and 18 °C, snow climates' (D) coldest months mean temperature is below -3 °C and polar climates' (E) hottest months are below 10 °C.

The Global Urban Heat Island dataset (Center For International Earth Science Information Network-CIESIN-Columbia University, 2016) presented the data regarding settlements such as their coordinates, population, extension, daytime, and nighttime temperature difference comparing with rural areas. Among the wide range of data, the information considered in this study is shown in Table 15.

Table 15: Information considered from Dataset UHI elaborated from (Center For International Earth Science Information Network-CIESIN-Columbia University, 2016).

CODE	**Description**
NAME	City or urban agglomeration name
SCHNM	City or urban agglomeration name in CAP
ES00POP	Estimated population for 2000
D_T_DIFF	The difference (in degrees Celsius) in average daytime maximum land surface temperature between the urban area and buffer area (URB_D_MEAN minus BUF_D_MEAN)
N_T_DIFF	The difference (in degrees Celsius) in average nighttime minimum land surface temperature between the urban area and buffer area (URB_N_MEAN minus BUF_N_MEAN)
LATITUDE	Latitude of the centroid of urban extent in decimal degrees
LONGITUDE	Longitude of the centroid of urban extent in decimal degrees

Figure 73a shows the complete dataset distribution with a total of 31,500 locations. The left vertical axis shows the number of settlements per climate, and the right vertical axis, the percentage of settlements grouped per climate. Several parameters were chosen to study the prevalence of city size and UHI factor, and several filters were applied. First of all, instances where the average city temperature was cooler than the urban surroundings were excluded. Figure 73b presents locations with more than 5,000 inhabitants and a positive difference in average daytime (D_T_DIFF) and nighttime (N_T_DIFF) maximum land surface temperature between the urban and buffer areas. It resulted in a total of 11,502 locations (36% of the total locations). The resulting climate distribution is very similar to Figure 73a.

Finally, Figure 73c presents the distribution of cities with more than 3,000,000 inhabitants that had a positive nighttime and daytime average maximum land surface temperature between the urban area and buffer area. The resulting 90 locations represent 0.003% of the starting data. In general terms, the three figures presented show a stable distribution in the percentages of cities per climate, as seen in Figure 76.

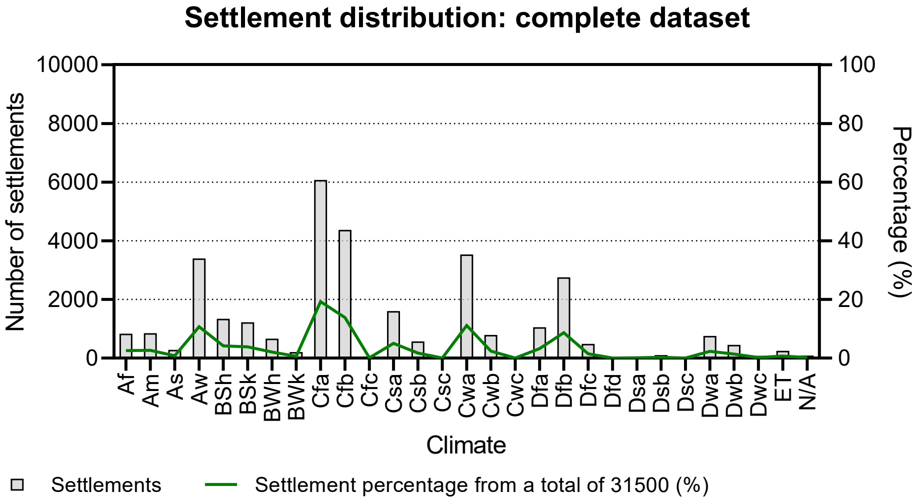

Figure 73: Prevalence per climate, includes all the information in the dataset.

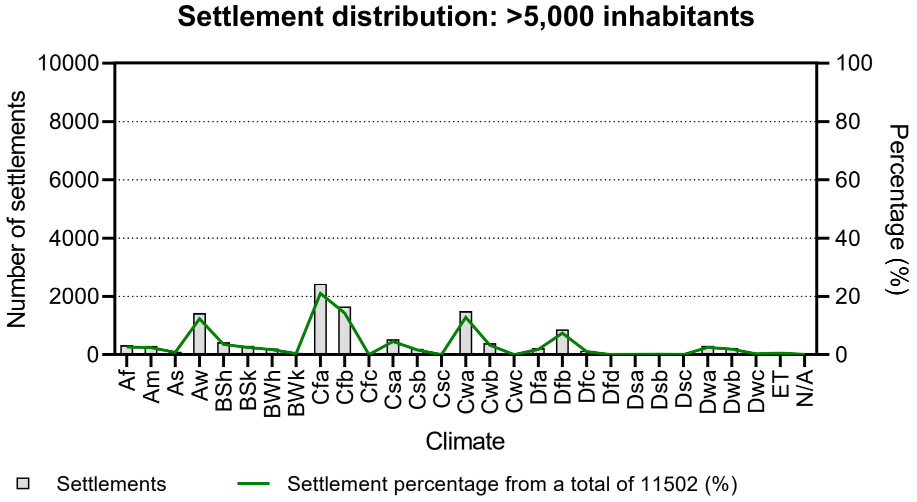

Figure 74: Location prevalence per climate and cities with more than 5,000 inhabitants and positive daytime and mean nighttime difference.

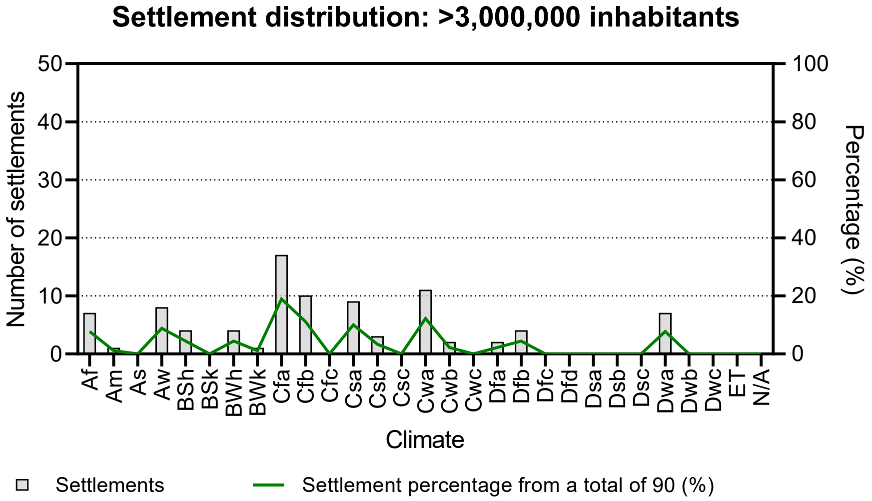

Figure 75: Location prevalence per climate and cities with more than 3,000,000 inhabitants and positive daytime and mean nighttime difference.

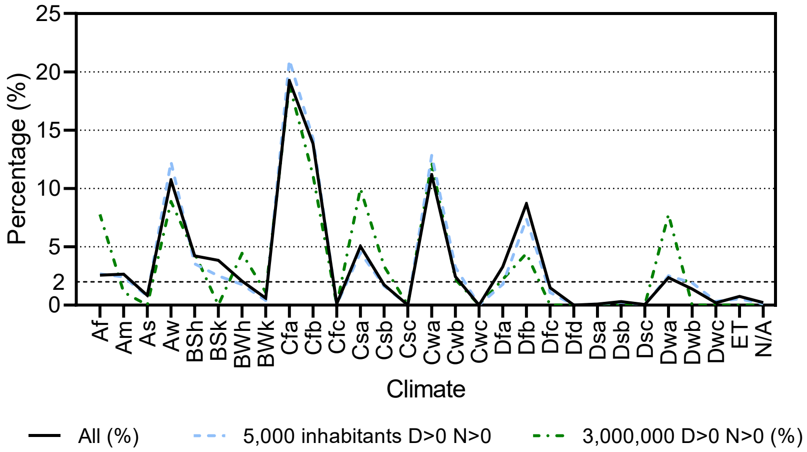

Figure 76: Climate distribution comparison in percentage for three conditions, all the cities (black line), cities with more than 5,000 inhabitants and positive daytime and nighttime temperature (blue dashed line), and cities with more than 3 million inhabitants and positive daytime and nighttime temperature (green point dashed line).

Secondly, considering the unfiltered data, with 31,500 locations, climates that grouped less than 2% (As, BWk, Cfc, Csb, Csc, Cwc, Dfc, Dfd, Dsa, Dsb, Dsc, Dwb, Dwc, and ET) of the total settlements were not considered due to their low representativity in global terms. The only exception was BSk, whose representativity was not consistent with population increase; 2.4% of cities with 1,000,000 population and positive thermal daytime and nighttime temperature difference were under this climate. However, there were no cities with more than 3,000,000 inhabitants that complied with the criteria. For that reason, one city under climate BSk in Spain was chosen. Considering the information from Figure 73c and excluding the climates that were not representative resulted in 86 cities. Lastly, to select one representative city for each climate, locations with higher daytime and nighttime temperature differences were favored (Figure 77).

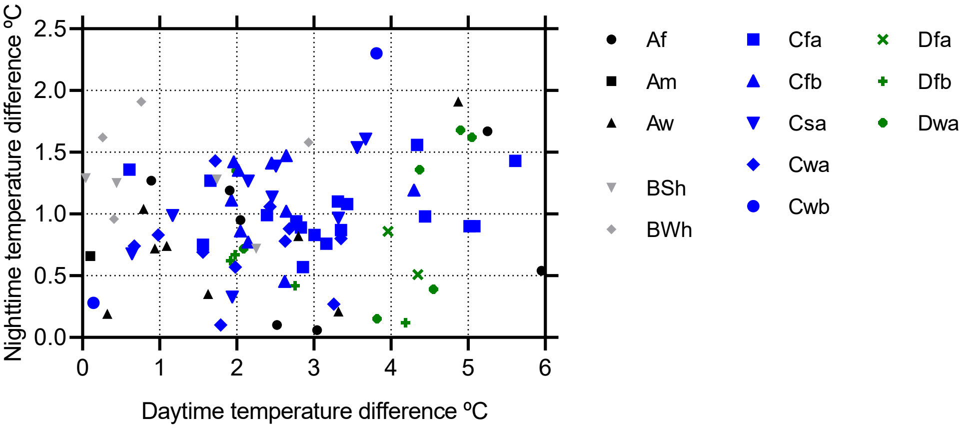

Figure 77: Daytime temperature difference (cooling need) versus nighttime temperature difference (cooling potential) from the 86 resulting cities.

Furthermore, this selection was crossed with an extensive literature review where cities with reported[18] UHI have been prioritized. The author considered a higher daytime temperature difference as a higher potential for radiative cooling and a higher nighttime temperature difference as higher demand for cooling. Some climates, such as Aw and Cfa, had a high prevalence (number of settlements), as can be seen in Figure 73a, and as a result, two cities were selected. The final city selection is presented in Table 16. Singapore, Alice Springs, and Phoenix were included since recently published papers simulated radiative cooling materials in these cities.

Table 16: City selection with climate association (based on crossing data from (Kottek et al., 2006) and (Center For International Earth Science Information Network-CIESIN-Columbia University, 2016))

KÖPPEN-GEIGER	**NAME**	**Abbr.**	**Daytime T difference (°C)**	**Nighttime T difference (°C)**
		Equatorial zone climates (A)		
Af	Bandung	BDO	5.25	1.67
Af	Singapore*	SIN	1.91	1.19
Am	Yangon City	YAN	0.10	0.66

---

[18] Most of the cities reported in present literature are found in Europe, North America, and Asia. Africa and South America have fewer reports of UHI.

* These cities were added to the selection list, as they were chosen in some recent literature. Zaragoza was chosen to represent the climate BSk even though the daytime temperature difference is negative.

KÖPPEN-GEIGER	**NAME**	**Abbr.**	**Daytime T difference (°C)**	**Nighttime T difference (°C)**
Aw	Lagos	LOS	2.80	0.82
Aw	Rio de Janeiro	RIO	4.87	1.91
		Arid zone climates (B)		
BSh	Monterrey	MTY	1.74	1.28
BSh	Phoenix*	PHX	0.10	1.18
BSk	Zaragoza*	ZAZ	-1.22	0.75
BWh	Alice Springs*	ASP	-0.83	0.38
BWh	Karachi	KHI	2.93	1.58
		Warm temperate zone (C)		
Cfa	Sydney	SYD	5.08	0.90
Cfa	Tokyo	TYO	5.61	1.43
Cfb	London	LON	2.64	1.02
Cfb	Milano	MIL	4.30	1.19
Cfb	Pamplona*	PNA	3.48	0.41
Csa	Madrid	MAD	2.15	1.27
Csa	Athens	ATH	3.67	1.61
Cwa	Dehli	DEH	2.43	1.06
Cwb	Taipei	TAY	3.81	2.30
		Snow zone climates (D)		
Dfa	Chicago	CHI	3.96	0.86
Dfb	Montréal	MON	2.76	0.42
Dwa	Beijing	BEI	4.90	1.68

Moreover, Pamplona's climate was added as an experiment of this Thesis took place there. The selected cities' climate data were obtained from Meteonorm (*Meteonorm 7*, 2017) using the typical meteorological year (file format .tm2) with hourly data and solar time. The ambient temperature, solar radiation, sky cover, relative humidity, and wind speed were used to calculate the materials' potential.

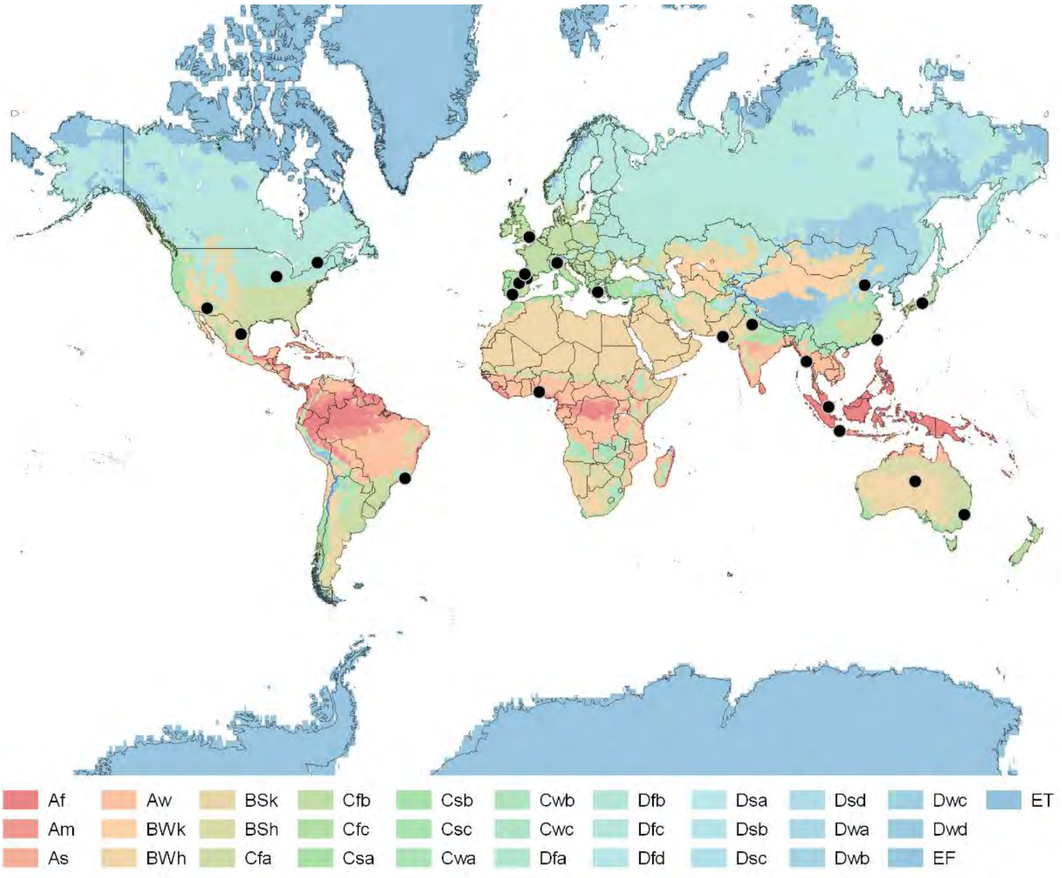

Figure 78: Map of the city selection above the Köppen-Geiger classification.

6.3 Results

As previously mentioned, an active application was simulated (Table 17) where the radiative cooling materials were placed on top of a very conductive surface with no insulation. This scenario assimilates an active system with a fluid or a heat source at a constant temperature located under the surface. The model calculates the hourly accumulated heat gains or losses used to determine the cooling potential. Below the material, the temperature is 25 °C, the exterior heat transfer coefficient is based on a linear expression from ESP-r (Mirsadeghi et al., 2013) that considers the surface's temperature, the ambient air temperature, and the wind speed, and the interior heat transfer coefficient is 1000 $W \cdot m^{-2} \cdot K^{-1}$. The following results were obtained: monthly stored heat evacuated through radiation ($kWh \cdot m^{-2}$), monthly stored heat absorbed due to incident solar radiation ($kWh \cdot m^{-2}$), monthly stored heat evacuated through convection with the air (kWh·m^{-2}), and the monthly total stored heat exchanged from the surface to the air (kWh·m^{-2}).

Moreover, some of the information regarding the climate was calculated, such as the monthly mean of the daily maximum air temperature (°C), the monthly mean of the air temperature (°C), the monthly mean of the daily minimum air temperature (°C), monthly mean incident radiation (W·m^{-2}) and monthly mean relative humidity (%). The cities climate data were obtained from Meteonorm (*Meteonorm 7*, 2017) using the standard irradiation model, the standard temperature model, and the included radiation model by Perez et al. G_h stands for global radiation, T_a, for ambient temperature, T_d for dewpoint temperature and RH for relative humidity. The typical meteorological year type of file was used (.tm2) with hourly data and solar time. The ambient temperature, solar radiation, sky cover, relative humidity, and wind speed were used to calculate the materials' cooling potential.

Table 17: Background condition substrate used in the simulation.

Background condition	**Material**	**Thickness**	**Thermal conductivity**
Conductive	Metallic sheet	0.005 m	400 W/m·K

The hourly heat gains and losses by the different heat transfer mechanisms were calculated; the monthly accumulated data is presented in Figure 79 to Figure 92. The graphs are grouped by the first letter from the climate classification. The chosen cities represent the 14 selected climates. The monthly climate data are presented, alongside the total monthly accumulated heat gains or losses for five materials (aluminum (A), AS_2.3, VS_1.1, RC2, and M8), among the eleven simulated materials. Moreover, the monthly accumulated radiated heat and the monthly accumulated total heat for each material and location are shown. The sign criterion considers positive values for heat gains and negative values for heat losses, so the lower the number is, the higher the effective cooling is. APPENDIX 8: Simulations results, presents an overview of the simulation results.

6.3.1 Equatorial zone climates (A)

The equatorial rainforest's fully humid climate (Af) is characterized by minimum precipitation above 60 mm on the driest month. In Bandung (Figure 79 a), the yearly mean ambient temperature is 19.4 °C, and the mean relative humidity is 81%, the lowest mean ambient temperature observed is 18.6 °C in February, and the lowest mean relative humidity is 75% in August. The mean wind speed is 1.3 ms$^{-1,}$ and the yearly total accumulated global horizontal radiation is 1,488 kWhm^{-2}. In Singapore (Figure 79 c), the yearly mean ambient temperature is 27.8 °C, and the mean relative humidity is 83%; the lowest mean ambient temperature observed is 26.7 °C in January, the lowest mean relative humidity is 81% in June and February. The mean wind speed is 1.9 ms$^{-1,}$ and the total global horizontal radiation is 1,641 kWhm^{-2}.

The materials had a consistent behavior throughout the year in both cities, as seen in Figure 79 b) and d). In Bandung materials, VS_1.1, RC2, and M8 could effectively evacuate heat as the mean of the total monthly heat was -33.73, -52.9, and -62.1 kWhm^{-2} (Figure 79 b). In Singapore, the system accumulated heat, a maximum of 43 kWhm^{-2} for V_1.1, 19.3 kWhm^{-2} for RC2, 8.1 kWhm^{-2} for M8, in May (Figure 79 d), so the system should be switched off, this is explained by the fact that the ambient temperature in May is 28 °C, above the operation temperature (25 °C). As seen in Figure 79 e, the radiated heat was greater in Bandung than in Singapore for all materials; the difference between both cities was more significant in materials RC2, M8, V_1.1, V_1.2, and almost identical for A and M5. The broader the emissive band was, the more the material radiates Figure 79e as shown in materials M5 to M8. Materials M5 to M8 radiated a mean of -16.1 kWhm^{-2}, -19.9 kWhm^{-2}, -21 kWhm^{-2}, -18.6 kWhm^{-2}, respectively in Singapore and -24.3 kWhm^{-2} -28.9 kWhm^{-2}, 37 kWhm^{-2}, -40 kWhm^{-2} in Bandung. Considering the solar heat gains and the convective heat gains and losses, the system could operate and evacuate heat in Bandung but not in Singapore Figure 79 f.

The equatorial rainforest climate (Am) selected representative city is Yangon (Myanmar) Figure 80 a. The yearly mean ambient temperature is 27.8 °C, the mean relative humidity 75%, the lowest mean ambient temperature is 26.5 °C in June, and the lowest mean relative humidity is 57% in February. The mean wind speed is 2.8 ms$^{-1,}$ and the total global horizontal radiation is 1,711 kWhm^{-2}. The global radiation and humidity influenced Yangon's monthly total heat; the materials present a less constant behavior throughout the year than materials in climate Af. Except for the theoretical material M8 in January (-20.8 kWhm^{-2}), June (-8 kWhm^{-2}), and December (-13 kWhm^{-2}), the system could not evacuate heat (Figure 80 b). Figure 80 (c) shows the radiated heat of the twelve months for the eleven materials, AS_2.2 (-7.9 kWhm^{-2}), AS_2.3 (-10 kWhm^{-2}), and A (mean -2.1 kWhm^{-2}) radiated almost the same heat throughout the year, the point distribution was concentrated and more disseminated for the rest of the materials. Figure 80 d all the points were primarily above zero; in this case, the developed materials behaved worse than the theoretical materials (M5-M8), RC1, and RC2.

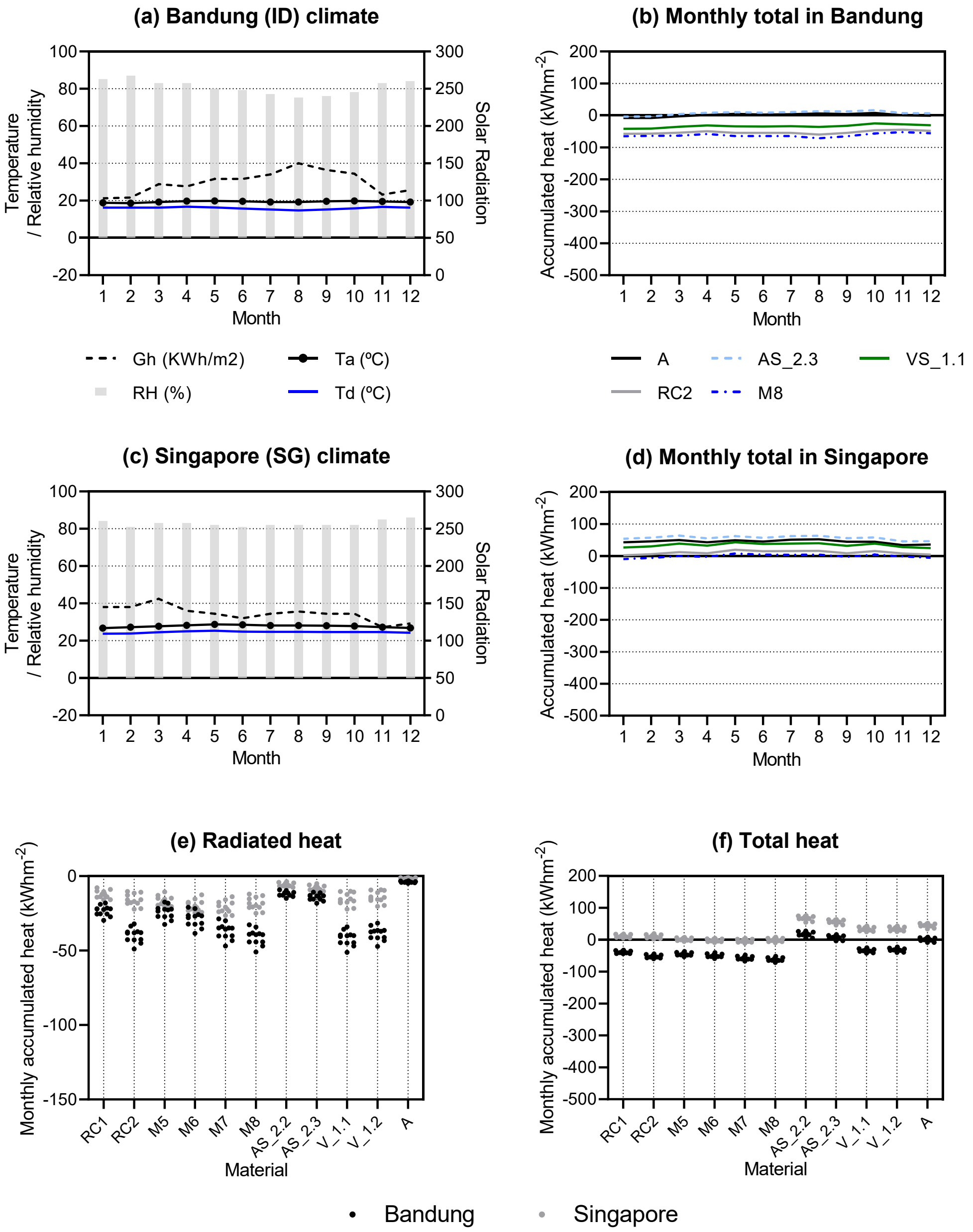

Figure 79: Af climate graphs:(a) Bandung climate, (b)Total heat accumulated per month in Bandung (c) Singapore climate (d) total heat accumulated per month in Bandung (e) Monthly accumulated radiated heat variation in Bandung and Singapore (f) Monthly accumulated total heat variation in Bandung and Singapore. Positive values are heat gains, and negative are heat losses.

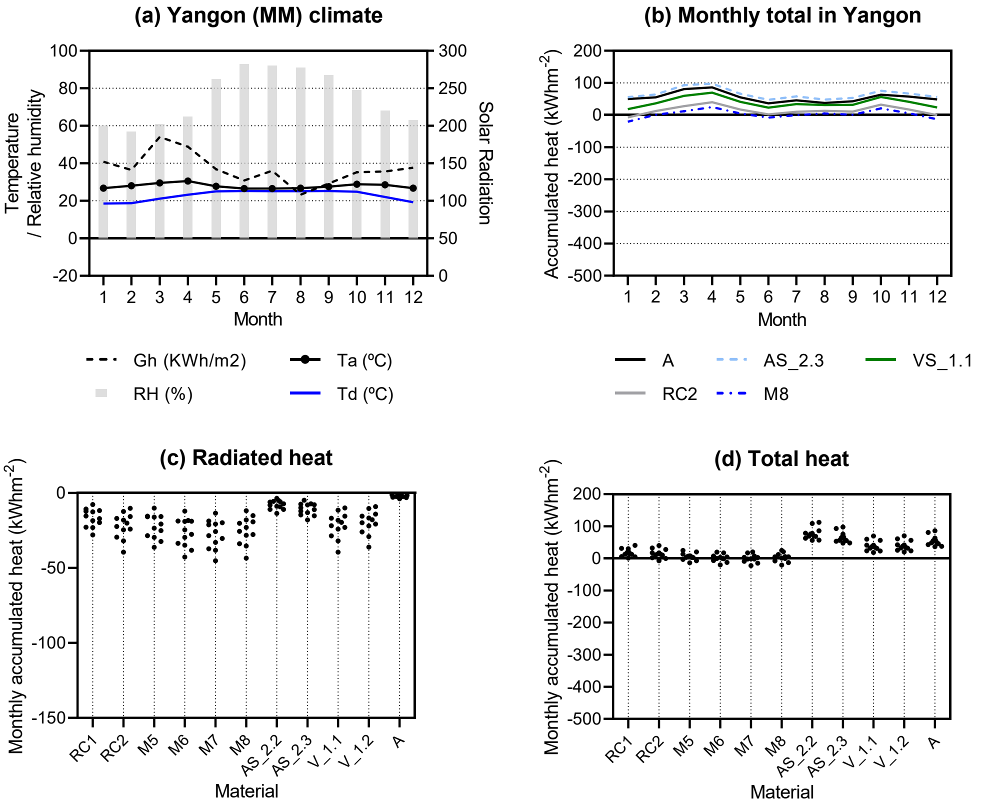

Figure 80: Am climate graphs:(a) Yangon climate, (b)Total heat accumulated per month, (c) Monthly accumulated radiated heat variation, and (d) Monthly accumulated total heat. Positive values are heat gains, and negative are heat losses.

Minimum precipitation above 60 mm in summer characterizes the equatorial savannah with a dry winter climate (Aw). In Lagos (Figure 81 a), the yearly mean ambient temperature is 27.5 °C, and the mean relative humidity is 84%, where the lowest mean ambient temperature is 25.4 °C in August and the lowest mean relative humidity 79% in January. The mean wind speed is 4.0 ms$^{-1,}$ and the total global horizontal radiation is 1,650 kWhm^{-2}. In Rio de Janeiro (Figure 81 c), the yearly mean ambient temperature is 24.2 °C, and the mean relative humidity is 77%, the lowest mean ambient temperature is 21.3 °C in July, and the lowest mean relative humidity is 75% in August. The mean wind speed is 3.0 ms$^{-1,}$ and the total global horizontal radiation is 1,692 kWhm^{-2}.

The materials had a constant behavior throughout the year in Lagos and a differentiated in Rio de Janeiro, Figure 81 (b) and (d). In Rio, material M8 (mean -37.8 kWhm^{-2}) evacuated heat throughout the entire year, closely followed by RC2 (mean -37. 6 kWhm^{-2} from March to November) and VS_1.1 (-38.3 kWhm^{-2} from May to September) that could evacuate heat with low solar radiation. As seen in Figure 81 e, the radiated heat was more disperse in Rio than in Lagos for all materials; the difference between both cities was more significant in RC2, M8, V_1.1, and V_1.2, being almost identical for A and M5.

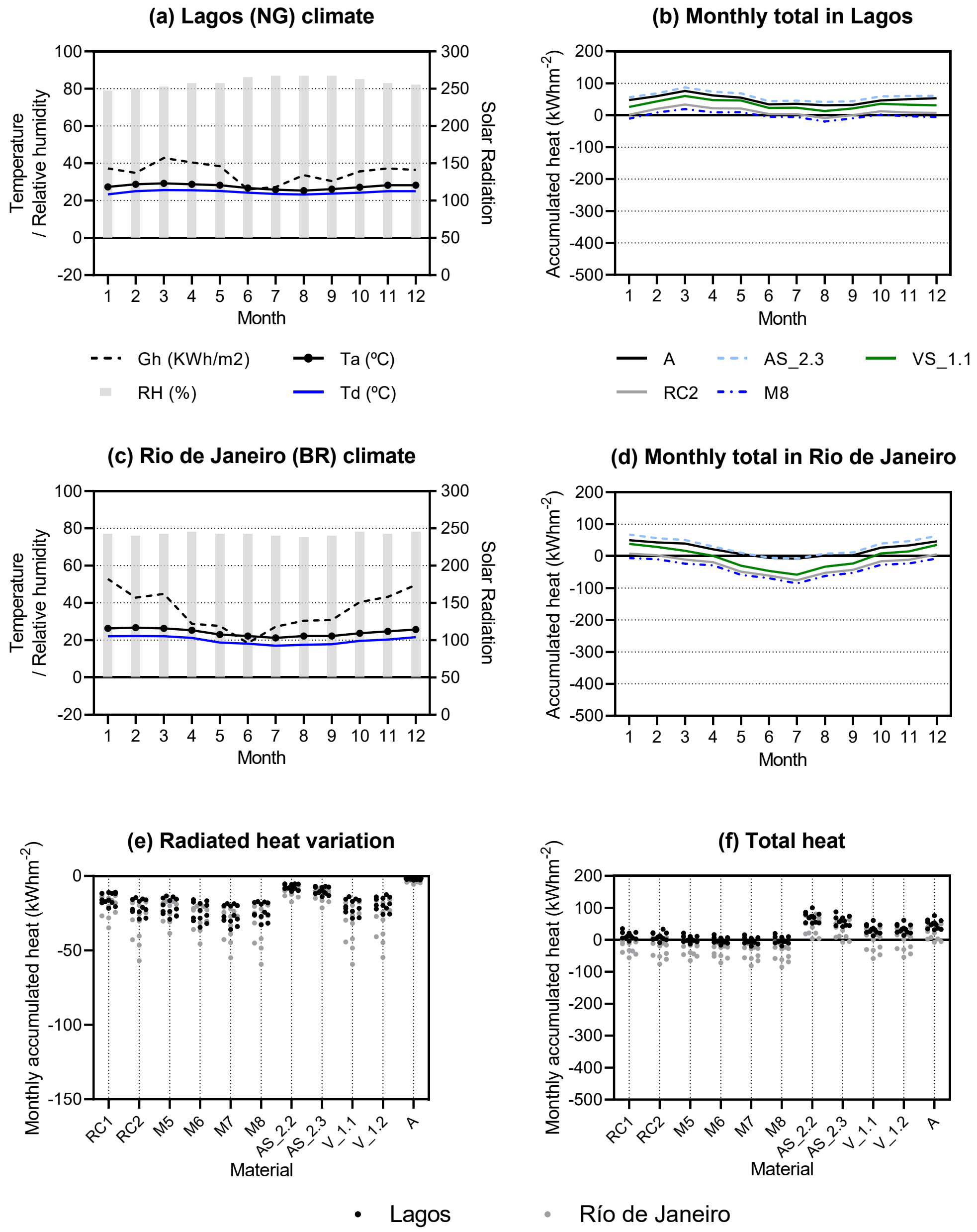

Figure 81: Aw climate graphs:(a) Lagos climate, (b)total heat accumulated per month in Lagos (c) Rio de Janeiro climate (d) total heat accumulated per month in Rio de Janeiro (e) Monthly accumulated radiated heat variation in Lagos and Rio de Janeiro (f) Monthly accumulated total heat variation in Lagos and Rio de Janeiro. Positive values are heat gains, and negative are heat losses.

Considering the solar heat gains and the convective heat gains and losses, the system could operate and evacuate heat in Río but not in Lagos Figure 81 f. In Río, all the materials except the aluminum and the ones based on aluminum (AS_2.2 and AS_2.3) succeeded in evacuating heat.

6.3.2 Arid zone climates (B)

The hot steppe (Bsh) climate is characterized by low precipitation and annual mean near-surface above 18 °C. This climate's representative cities are Monterrey (Mexico) and Phoenix (United States). In Monterrey (Figure 82 a), the yearly mean ambient temperature is 23.2 °C, and the mean relative humidity is 60%, with the lowest mean ambient temperature observed 15.2 °C in December and the lowest mean relative humidity 55% in March and April. The mean wind speed is 2.3 $ms^{-1,}$ and the total global horizontal radiation is 1,871 $kWhm^{-2}$. In Phoenix (Figure 82 c), the yearly mean ambient temperature is 24.3 °C, and the mean relative humidity is 28%, the lowest mean ambient temperature is 12.6 °C in December, and the lowest mean relative humidity is 16% in June. The mean wind speed is 2.8 $ms^{-1,}$ and the total global horizontal radiation is 2,092 $kWhm^{-2}$.

Although both cities were under the same climate classification, Monterrey had higher relative humidity than Phoenix and lower mean ambient temperatures related to lower solar radiation. The materials presented a very differentiated behavior (Figure 82 b and d). In both cities, M8 had the best behavior, followed closely by RC2 and VS_1.1, which evacuated heat from September to May in Monterrey and October to May. As seen in Figure 82e, the radiated heat was more disperse in Phoenix than in Monterrey for all materials. The difference between both cities was more significant in RC2, M8, and V_1.1, being identical for A, whose maximum radiating heat values were -59.1 $kWhm^{-2}$ (MTY) and -86 $kWhm^{-2}$ (PHX), -59.9 $kWhm^{-2}$ and -88 $kWhm^{-2}$, -62 $kWhm^{-2}$ and -90 $kWhm^{-2}$, respectively and -5.8 $kWhm^{-2}$ and -8 $kWhm^{-2}$ for aluminum. The material that radiated more heat in both cities during more time was developed material V_1.1 (Figure 82e); however, other factors counteract the total balance as seen in Figure 82 f, where RC2 and M8 had slightly better behavior than V_1.1 and V_1.2.

The cold steppe (BSk) climate is characterized by low precipitation and annual mean near-surface below 18 °C. This climate's representative selected city is Zaragoza in Spain (Figure 83 a). The yearly mean ambient temperature is 15.2 °C with a mean relative humidity of 60%. The lowest mean ambient temperature is observed in February, 1.9 °C, and the lowest mean relative humidity, 49%, occurs in June and July. The mean wind speed is 4.5 $ms^{-1,}$ and the city receives a total global horizontal radiation of 1,651 $kWhm^{-2}$.

The materials presented a diverse behavior Figure 83b, during the winter and summer months. Materials RC2, M8, and VS_1.1 could cool down all year round, except VS_1.1 heated up in July (5.5 $kWhm^{-2}$). Figure 83c shows the radiated heat of the twelve months for the eleven materials, AS_2.2, AS_2.3, and A radiated almost the same heat throughout the year as the point distribution was concentrated and more disseminated for the rest of the materials, being especially significant for RC2, and V_1.1 and V_1.2. Figure 83d shows the monthly total accumulated heat, where most of the points were below zero.

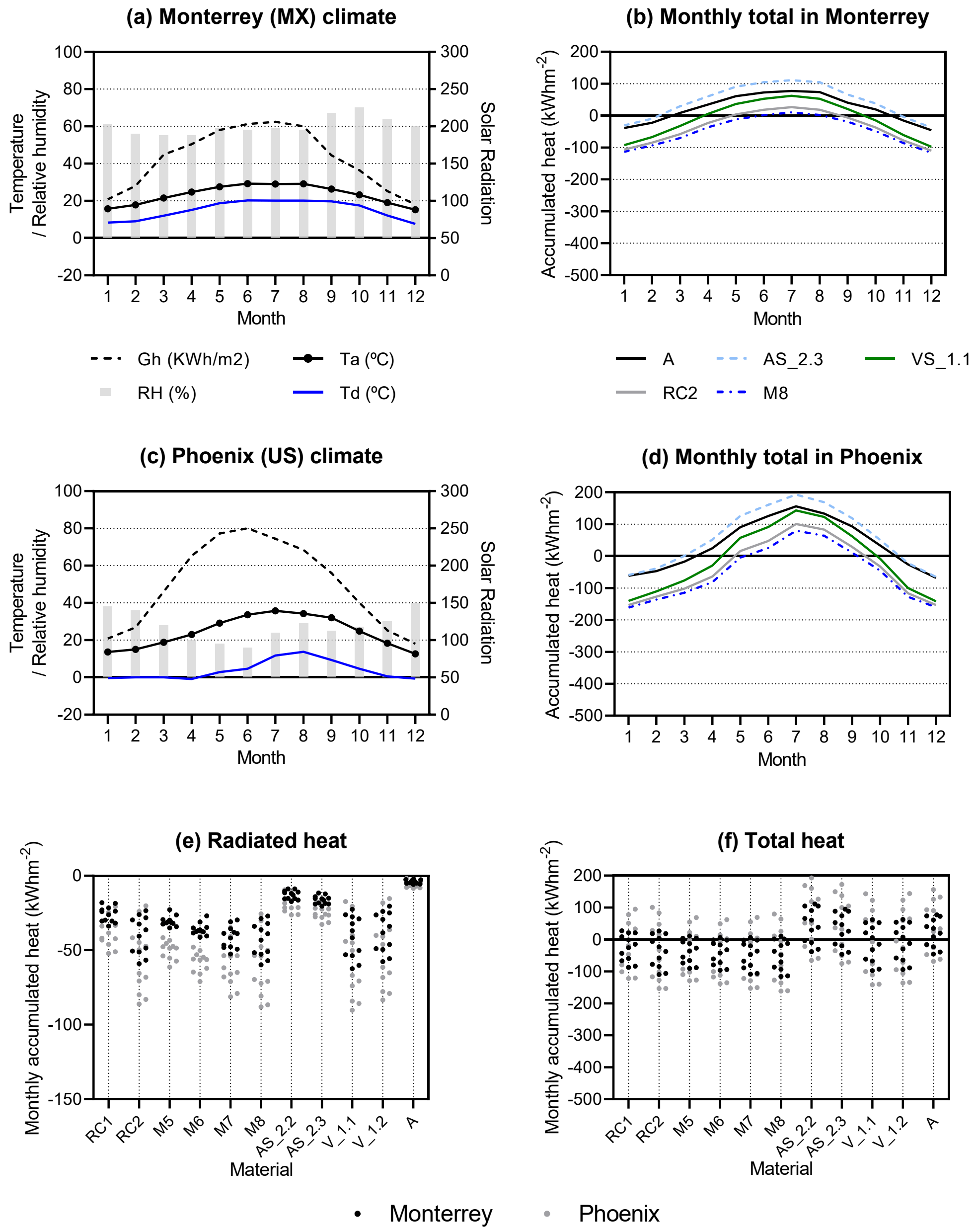

Figure 82: Bsh climate graphs:(a) Monterrey climate, (b) total heat accumulated per month in Monterrey (c) Phoenix climate (d) total heat accumulated per month in Phoenix (e) Monthly accumulated radiated heat variation in Monterrey and Phoenix (f) Monthly accumulated total heat variation in Monterrey and Phoenix. Positive values are heat gains, and negative are heat losses.

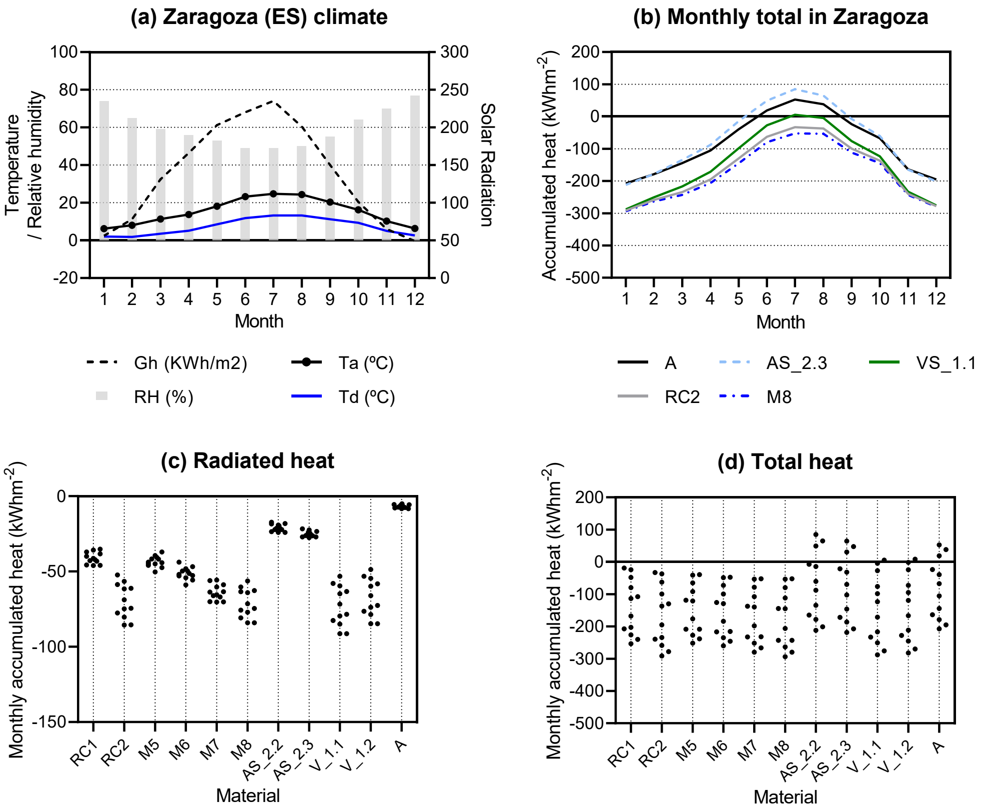

Figure 83: Bsk climate graphs: (a) Zaragoza climate, (b) total heat accumulated per month in Zaragoza (c) Monthly accumulated radiated heat variation in Zaragoza (d) Monthly accumulated total heat variation in Zaragoza. Positive values are heat gains, and negative are heat losses.

The dessert with a cold (BWh) climate is characterized by low precipitation and annual mean near-surface above 18 °C. In Alice Springs (Figure 84a), the yearly mean ambient temperature is 21.7 °C, and the mean relative humidity is 33%, with the lowest mean ambient temperature observed in June is 11.8 °C. The lowest mean relative humidity is 22% in October. The mean wind speed is 4.5 ms$^{-1,}$ and the total global horizontal radiation is 2,257 kWhm^{-2}. Karachi Figure 84c shows that the yearly mean ambient temperature is 27.0 °C, and the mean relative humidity is 57%. The lowest mean ambient temperature is 19.5 °C in January, and the lowest mean relative humidity 43% in January. The mean wind speed is 3.6 ms$^{-1,}$ and the total global horizontal radiation is 1,837 kWhm^{-2}.

Although both cities were under the same climate classification, Karachi had higher relative humidity than Alice Springs and lower mean ambient temperature. The materials presented a very differentiated behavior Figure 84b and d throughout the year due to winter and summer solstice. In both cities, M8 had an average of -113 kWhm^{-2} (ASP) and -56 kWhm^{-2} (KHI), showed the best behavior followed closely by RC2, -100 kWhm$^{-2,}$ and -53 kWhm^{-2} and VS_1.1, -100 kWhm^{-2} and -48 kWhm^{-2}. In Alice Springs, M8 cooled down from March to November, and RC2 from March to October, whereas V_1.1 cooled down from October onwards. In

Karachi, M8 and RC2 cooled down from November to March and V_1.1 from November to February. As seen in Figure 84e, the radiated heat was more disperse in Alice Springs than in Karachi for all materials. Both cities' difference was more significant in material RC2, M8, V_1.1, and V_1.2, being identical for A. The material that could radiate more heat in both cities a more significant number of months was developed material V_1.1 Figure 84e; however, other factors counteracted the total balance as seen in Figure 84f, where RC2 and M8 had slightly better behavior than V_1.1 and V_1.2.

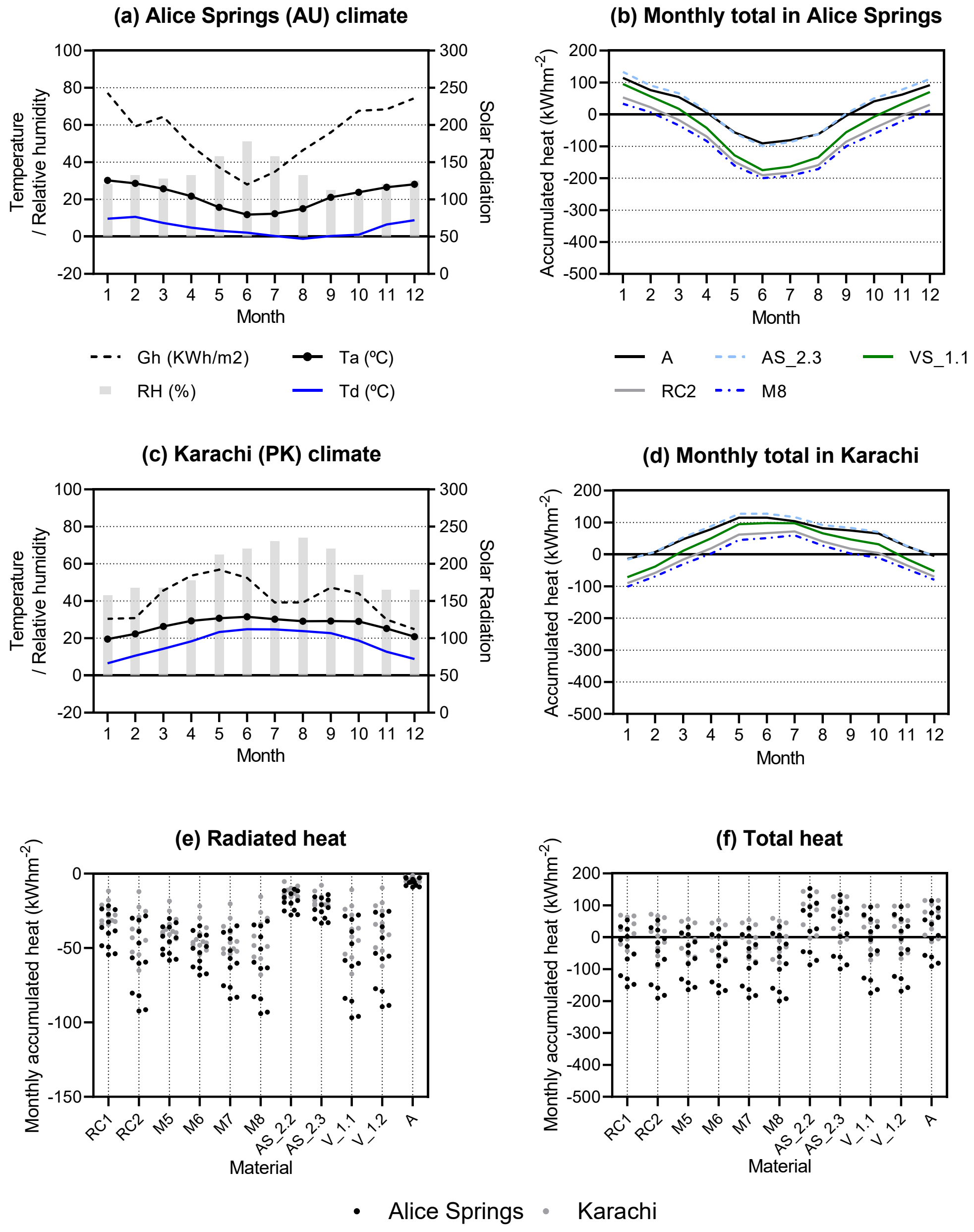

Figure 84:BWh climate graphs:(a) Alice Springs climate, (b) total heat accumulated per month in Alice Springs (c) Karachi climate (d) total heat accumulated per month in Phoenix (e) Monthly accumulated radiated heat variation in Alice Springs and Karachi (f) Monthly accumulated total heat variation in Alice Springs and Karachi. Positive values are heat gains, and negative are heat losses.

6.3.3 Warm temperate zone (C)

The warm temperate climate, fully humid and hot summer (Cfa) climate is characterized by the warmest month's mean temperature above 18 °C. This climate's representative cities are Sydney (Australia) and Tokyo (Japan). Sydney's yearly mean ambient temperature is 18.3 °C, and mean relative humidity 66%. The lowest mean ambient temperature observed is 12.7 °C in July, and the lowest mean relative humidity 59% in August (Figure 85a). The mean wind speed is 3.1 ms$^{-1,}$ and the total global horizontal radiation is 1,678 kWhm^{-2}. In Tokyo (Figure 85c), the yearly mean ambient temperature is 16.6 °C, and the mean relative humidity is 57%, with the lowest mean ambient temperature is 6.3 °C in January. The lowest mean relative humidity is 43% in January and February. The mean wind speed is 3.2 ms$^{-1,}$ and the total global horizontal radiation is 1,218 kWhm^{-2}.

The materials showed different behavior throughout the year in both cities, as seen in (Figure 85b and d). In Sydney, materials VS_1.1, RC2, and M8 could effectively evacuate heat as they were below -55 kWhm^{-2} for all months (Figure 85b), reaching up to -170 kWhm^{-2}. In Tokyo, on the other hand, those materials accumulated heat (Figure 85d) from June to August. As seen in (Figure 85e), the radiated heat was more significant in Tokyo (maximum of 93 kWhm^{-2}) than in Sydney (maximum of -77 kWhm^{-2}) for all materials. Both cities' difference was more significant in material RC2, M8, V_1.1, and V_1.2, being almost identical for A, AS_2.2, and AS_2.3. The broader the emissive band was, the greater the radiation was (Figure 85e), as shown in materials M5 to M8. Figure 85f shows that all materials except AS_2.2, AS_2.3 and A, cooled down throughout the year in Sydney, but in Tokyo, some materials were at some points above zero, having heat gains.

The warm temperate climate, fully humid with cool summer and cold winter (Cfb) representative cities are London (United Kingdom), Milano (Italy), and Pamplona (Spain). In London (Figure 86a), the yearly mean ambient temperature is 12.4 °C, the mean relative humidity is 68%, the lowest mean ambient temperature is 6.9 °C from December to February, the lowest mean relative humidity is 61% in June. The mean wind speed and the total global horizontal radiation are 3.7 ms^{-1} and 973 kWhm^{-2}, respectively. In Milan (Figure 86c), the yearly mean ambient temperature is 15.3 °C, and the mean relative humidity is 66%, with the lowest mean ambient temperature observed 4.2 °C in January and the lowest mean relative humidity 59% in June. The mean wind speed is 0.5 ms$^{-1,}$ and the total global horizontal radiation is 1,125 kWhm^{-2}. In Pamplona (Figure 86e), the yearly mean ambient temperature is 13.4 °C, and the mean relative humidity is 67%. The lowest mean ambient temperature observed is 5.5 °C in January, and the lowest mean relative humidity is 59% in June. The mean wind speed is 3.4 ms$^{-1,}$ and the total global horizontal radiation is 1,500 kWhm^{-2}.

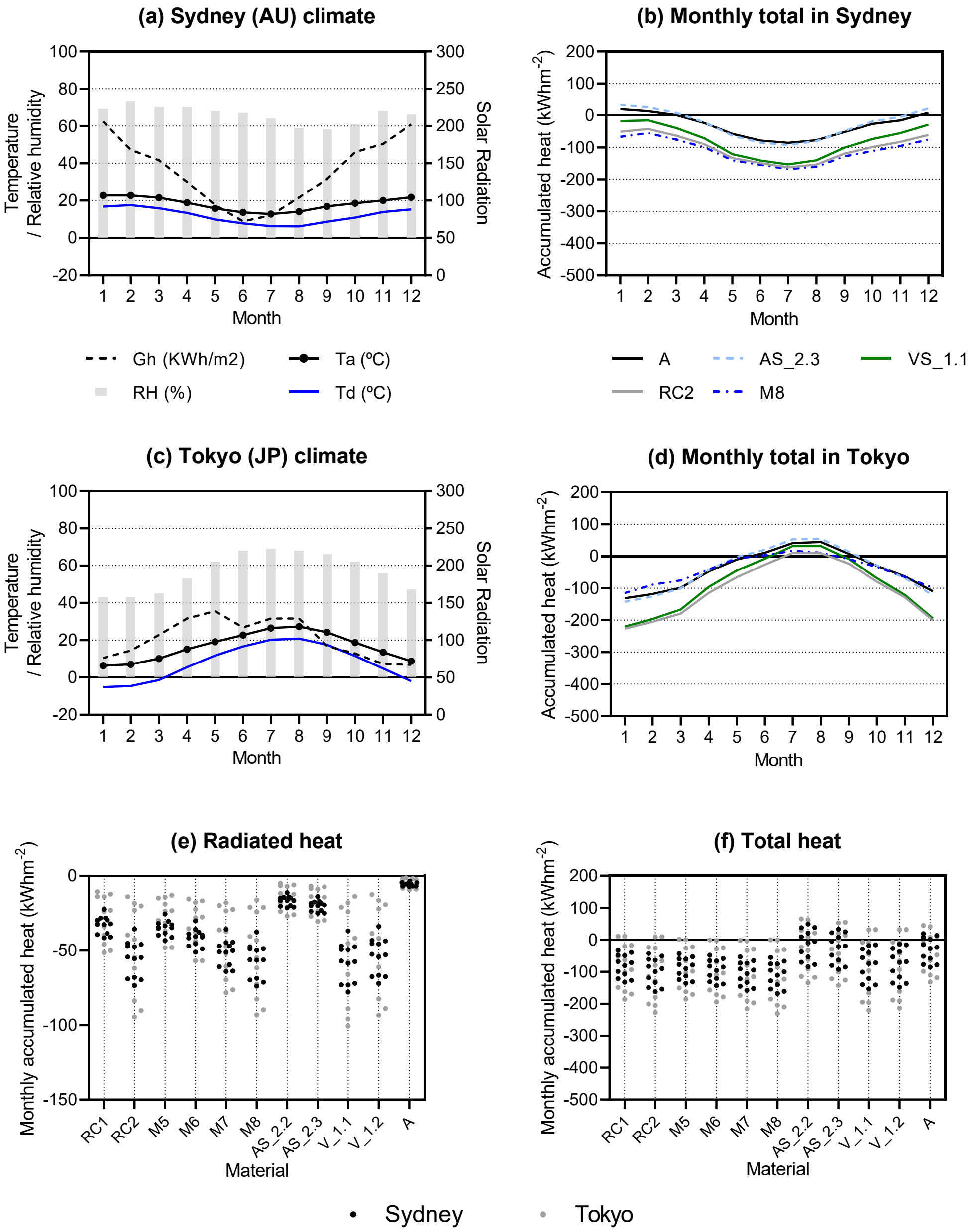

Figure 85: Cfa climate graphs:(a) Sydney climate, (b)total heat accumulated per month in Sydney (c) Tokyo climate (d) total heat accumulated per month in Tokyo (e) Monthly accumulated radiated heat variation in Sydney and Tokyo (f) Monthly accumulated total heat variation in Sydney and Tokyo. Positive values are heat gains, and negative are heat losses.

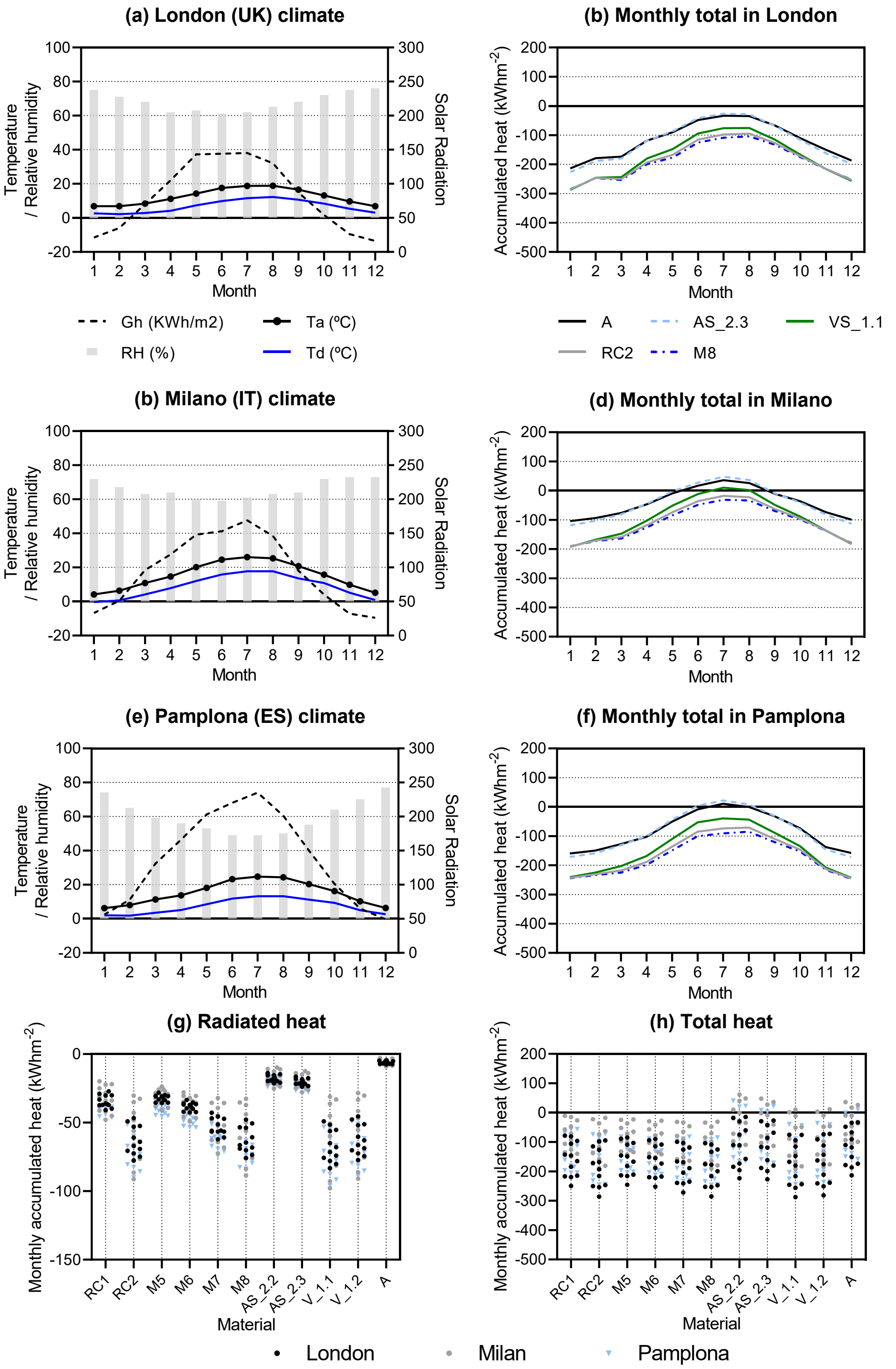

Figure 86: Cfb climate graphs:(a) London climate, (b) total heat accumulated per month in London, (c) Milano climate, (d) total heat accumulated per month in Milano, (c) Pamplona climate, (d) total heat accumulated per month in Pamplona, (g) Monthly accumulated radiated heat variation in London, Milano, and Pamplona, (h) Monthly accumulated total heat variation in London, Milano, and Pamplona. Positive values are heat gains, and negative are heat losses.

The materials showed distinct behavior in winter and summer (Figure 86b, d, and f). In London, all materials could effectively evacuate heat (Figure 86b) during all months. In Milan and Pamplona, both M8 and RC2 cool down throughout the entire year, and in Pamplona, so did V_1.1; A and AS_2.3 heated up several months, the accumulated heat gains were more significant in Milan 68 kWhm^{-2} in July. As seen in Figure 86g, the radiated heat was similar in the three cities for all materials; all materials had a different radiative potential depending on the month except AS_2.2, AS_2.3, and A with an almost constant radiative potential. The total heat was negative for most materials and all locations, leading to heat losses.

The warm temperate climate with dry, hot summer (Csa) climate is characterized by the warmest month's mean temperature above 18 °C. This climate's representative cities are Athens (Greece) and Madrid (Spain). In Athens (Figure 87a), the yearly mean ambient temperature is 18.3 °C, the mean relative humidity is 58%, the lowest mean ambient temperature is 9.4 °C in February, and the lowest mean relative humidity is 41% in July. The mean wind speed is 2.8 ms$^{-1,}$ and the total global horizontal radiation is 1,740 kWhm^{-2}. In Madrid (Figure 87c), the yearly mean ambient temperature is 16.3 °C, and the mean relative humidity is 47%, where the lowest mean ambient temperature is observed is 7 °C in January, and the lowest mean relative humidity is 30% in July. The mean wind speed and total global horizontal radiation are 1.9 ms^{-1} and 1,653 kWhm^{-2}, respectively.

As shown in Figure 88b and d, the materials had a different winter-summer behavior, almost identical in both cities. In Madrid, RC2 and M8 materials could effectively evacuate heat (Figure 87b). The same happened in Athens except in July, explained by Athens' higher relative humidity in general, especially in summer. The radiated heat was almost equal in both cities; RC2, M8, and V_1.1 achieved -82.2 kWhm^{-2}, -82 kWhm^{-2}, -87.3 kWhm^{-2} respectively in Athens and -82.8 kWhm^{-2}, -81.7 kWhm^{-2} and -88.4 kWhm^{-2} in Madrid. In Athens and Madrid, both M8 and RC2 cooled down throughout the entire year, and in Madrid, so did V_1.1; A and AS_2.3 heated up some months, being more significant in Athens 104 kWhm^{-2} in July. As seen in Figure 87g, the radiated heat was similar in both cities for all materials. All materials had a different radiative potential depending on the month except AS_2.2, AS_2.3, and A that had a stable constant radiative potential.

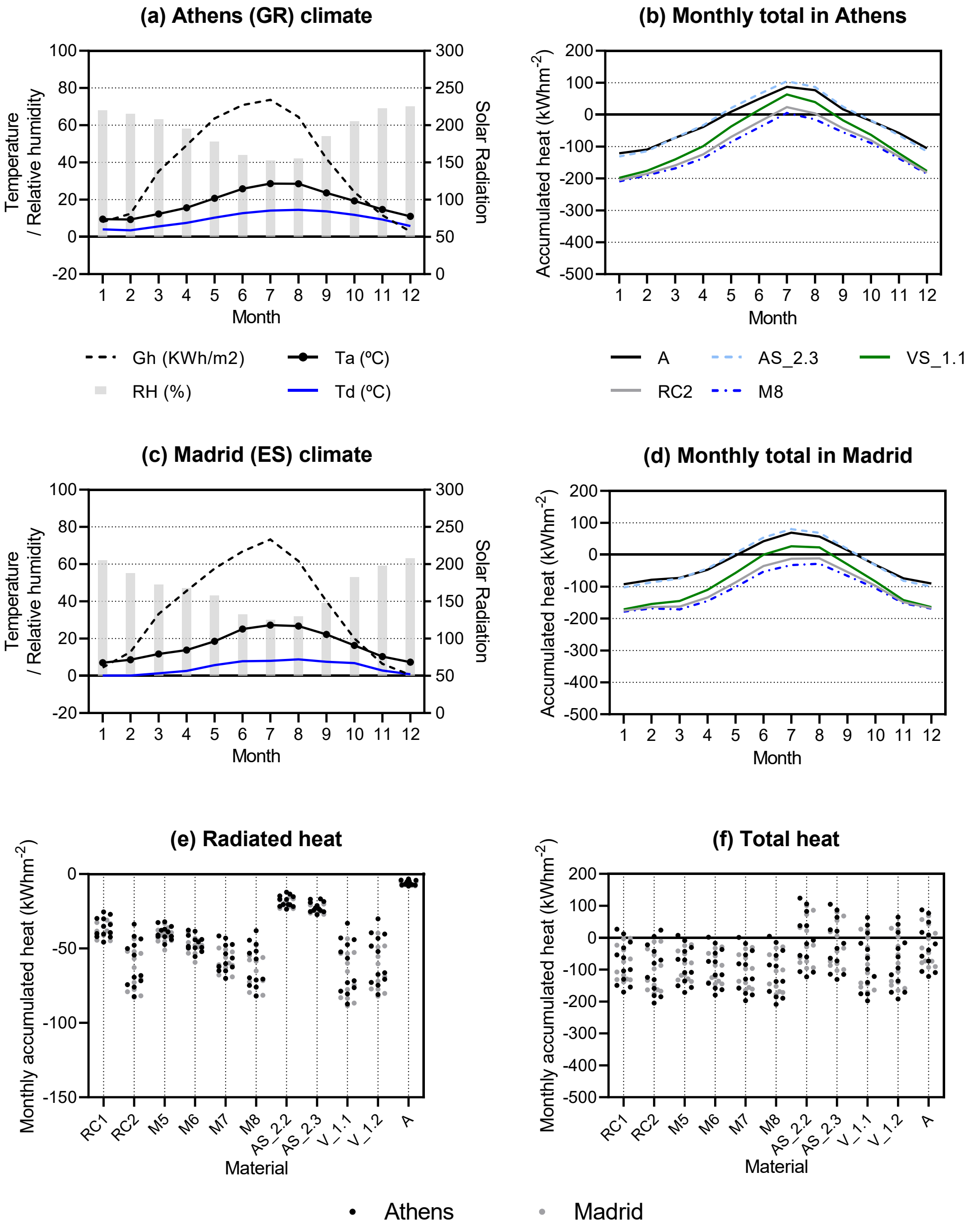

Figure 87:Csa climate graphs:(a) Athens climate, (b) total heat accumulated per month in Athens (c) Madrid climate (d) total heat accumulated per month in Madrid (e) Monthly accumulated radiated heat variation in Athens and Madrid (f) Monthly accumulated total heat variation in Athens and Madrid. Positive values are heat gains, and negative are heat losses.

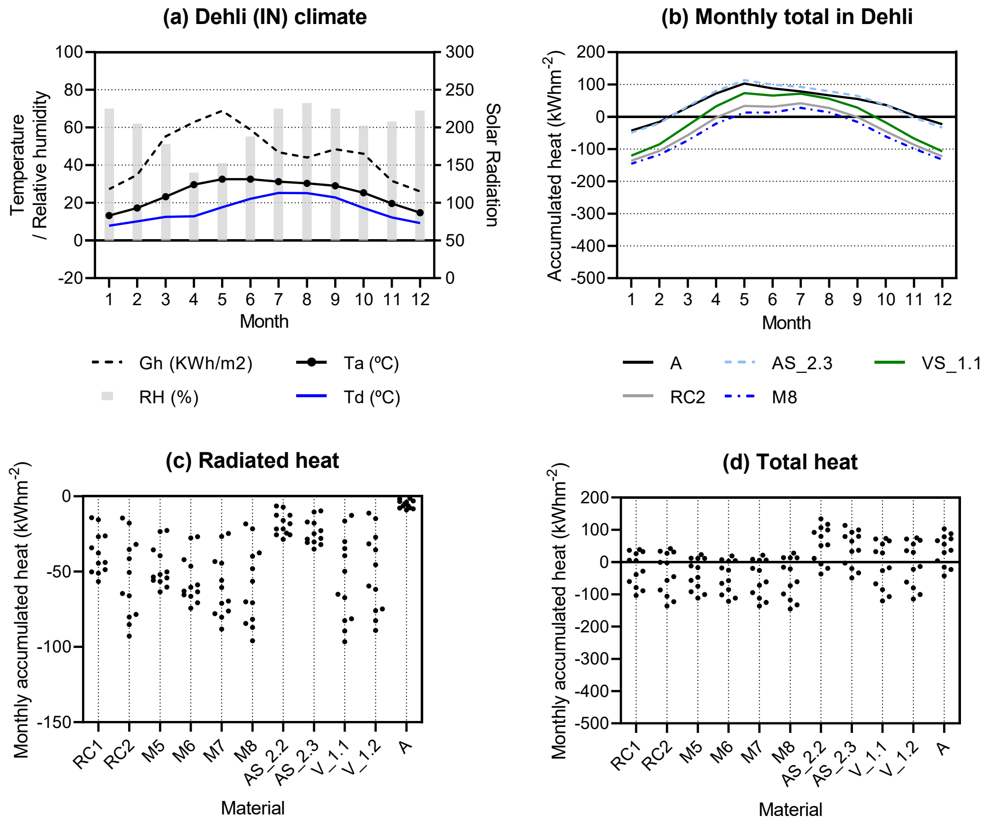

Figure 88: Cwa climate graphs: (a) Delhi climate, (b) total heat accumulated per month in Delhi (c) Monthly accumulated radiated heat variation in Delhi (d) Monthly accumulated total heat variation in Delhi. Positive values are heat gains, and negative are heat losses.

The warm temperate climate with dry winter and hot summer (Cwa) climate representative city is Delhi (India) (Figure 88a). The yearly mean ambient temperature is 24.9 °C, and the mean relative humidity is 60%, where the lowest mean ambient temperature is 13.2 °C in January, and the lowest mean relative humidity is 36% in April. The mean wind speed is 1.4 $ms^{-1,}$ and the total global horizontal radiation is 1,976 $kWhm^{-2}$.

The materials had a different summer-winter behavior, as seen in Figure 88b. In Delhi, none of the materials could evacuate heat from May to August. Nevertheless, M8 (monthly average -83 $kWhm^{-2}$) and RC2 (monthly average -69 $kWhm^{-2}$) and would be reasonable solutions for spring and autumn as they could evacuate heat (Figure 88b), the radiated heat was more significant for those materials as well, up to 95 $kWhm^{-2}$ and 92 $kWhm^{-2}$, respectively (Figure 88e). All materials evacuated heat in some months, considering all heat transfer mechanisms. However, it should be studied more in detail Figure 88f.

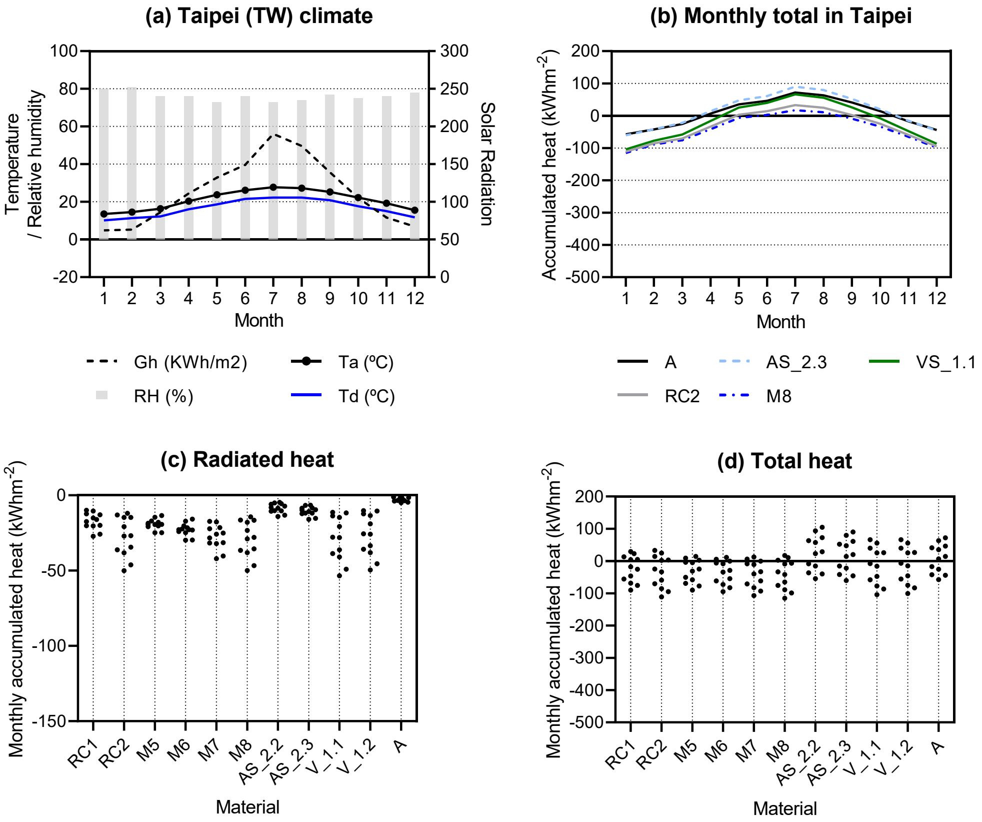

Figure 89: Cwb climate graphs: (a) Taipei climate, (b) total heat accumulated per month in Taipei (c) Monthly accumulated radiated heat variation in Taipei (d) Monthly accumulated total heat variation in Taipei. Positive values are heat gains, and negative are heat losses.

The warm temperate climate with dry cold winter and cool summer climate (Cwb) representative city is Taipei (Taiwan) (Figure 89a). The yearly mean ambient temperature is 21.0 °C, and the mean relative humidity is 76%, where the lowest mean ambient temperature observed is 13.5 °C in January, and the lowest mean relative humidity is 73% in July. The average wind speed is 3.7 ms$^{-1,}$ and the total global horizontal radiation is 1,353 kWhm^{-2}.

The materials had a different summer-winter behavior, as seen in Figure 89b. In Taipei, materials VS_1.1, RC2, and M8 could effectively evacuate heat from October to April, with averages of -57 kWhm^{-2}, -68 kWhm^{-2}, -74 kWhm^{-2}, respectively (Figure 89b). As seen in Figure 89e, the radiated heat was more significant for those three materials. The broader the emissive band was, the greater the radiative power was, as seen in materials M5 to M8 (Figure 89e).

6.3.4 Snow zone climates (D)

The snow climate, fully humid, and hot summer climate (Dfa) representative city is Chicago (United States) (Figure 90a). The yearly mean ambient temperature is 10.3 °C, and the mean relative humidity is 66%, with the lowest mean ambient temperature -3.6 °C in January, and the lowest mean relative humidity is 57% in April. The mean wind speed is 4.2 ms^{-1}, and the total global horizontal radiation is 1,404 $kWhm^{-2}$.

The materials had a significant behavior variation across the year Figure 90b. In Chicago, materials VS_1.1, RC2, and M8 could effectively evacuate heat for all months (Figure 90b). As seen in Figure 90c, the radiated heat was greater to for those materials RC2 (av. -73 $kWhm^{-2}$), M8 (av.-72 $kWhm^{-2}$), V_1.1 (av. -77 $kWhm^{-2}$) and V_1.2 (av. -72 $kWhm^{-2}$). The eleven materials' total heat gains showed a great cooling potential, especially in winter due to low ambient temperature. However, since the material was theoretically a part of an active system, it could be switched off; all materials except AS_2.2, AS_2.3, and A would cool down throughout the entire year (Figure 90d).

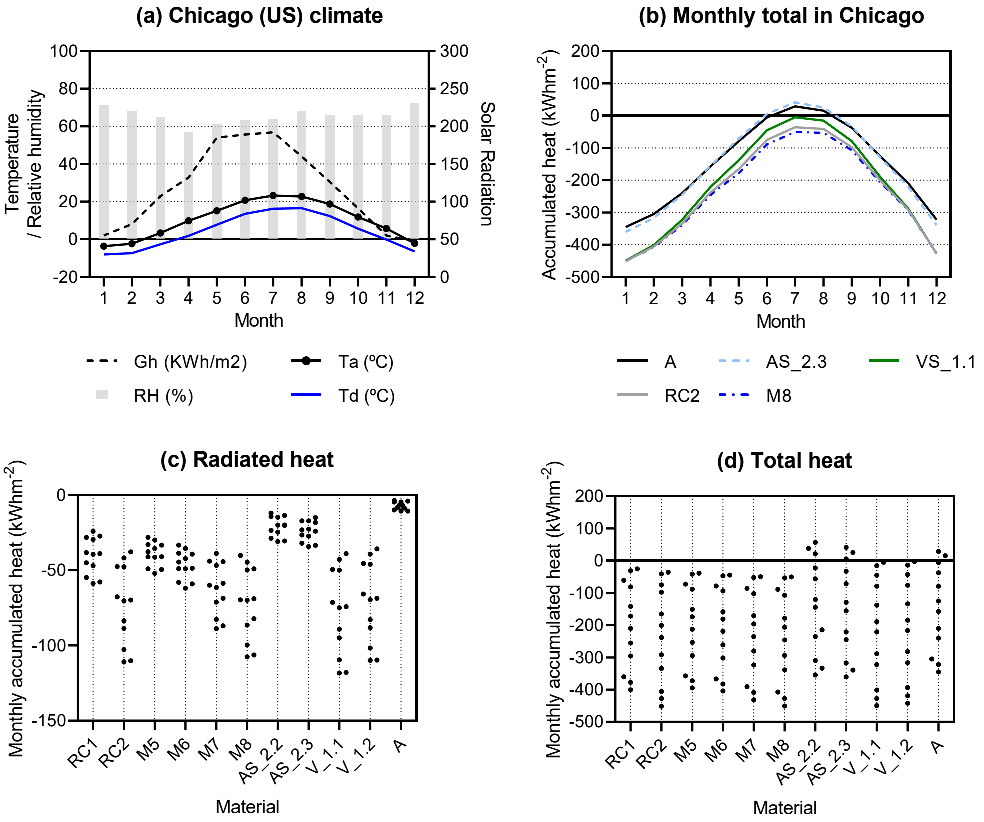

Figure 90: Dfa climate graphs: (a) Chicago climate, (b) total heat accumulated per month in Chicago (c) Monthly accumulated radiated heat variation in Chicago (d) Monthly accumulated total heat variation in Chicago. Positive values are heat gains, and negative are heat losses.

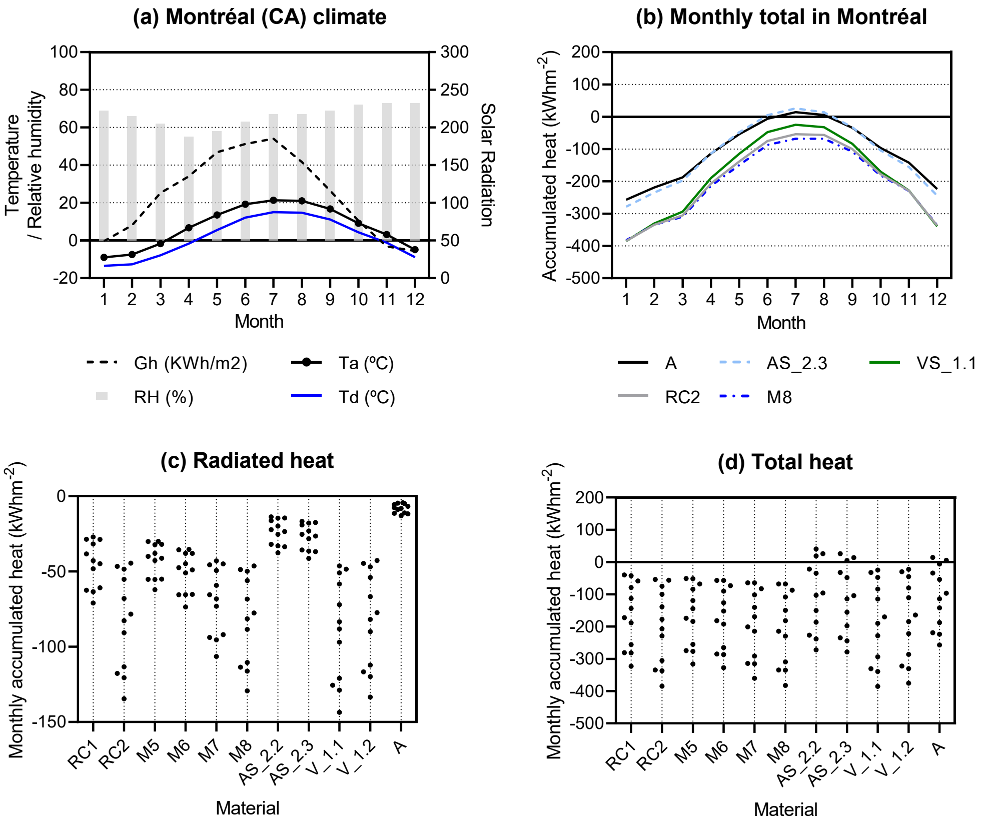

Figure 91: Dfb climate graphs: (a) Montréal climate, (b) total heat accumulated per month in Montréal (c) Monthly accumulated radiated heat variation in Montréal (d) Monthly accumulated total heat variation in Montréal. Positive values are heat gains, and negative are heat losses.

The snow climate, fully humid and warm summer climate (Dfb), selected representative city is Montréal (Canada) (Figure 91a), where the yearly mean ambient temperature is 7.3 °C, mean relative humidity is 66%. The lowest mean ambient temperature observed is -8.9 °C in January, and the lowest mean relative humidity is 55% in April. The mean wind speed is 4.4 ms$^{-1,}$ and the total global horizontal radiation is 1,318 kWhm^{-2}.

The materials presented a similar behavior in Montréal and Chicago (Dfa); in the latter, the total heating losses were more significant; nevertheless, the radiated heat losses were superior in the first city. The materials had a significant behavior variation across the year Figure 91b due to summer winter climatic differences. In Montréal, materials VS_1.1, RC2, and M8 could effectively evacuate heat for all months (Figure 91b) with an average of -88 kWhm^{-2}, -83 kWhm$^{-2,}$ and -82 kWhm^{-2}, respectively. As seen in Figure 91c, the radiated heat was higher too for those materials. The total heat gains for the eleven materials in Figure 91f showed an excellent cooling potential in winter. All materials except AS_2.2, AS_2.3, and A always cooled down.

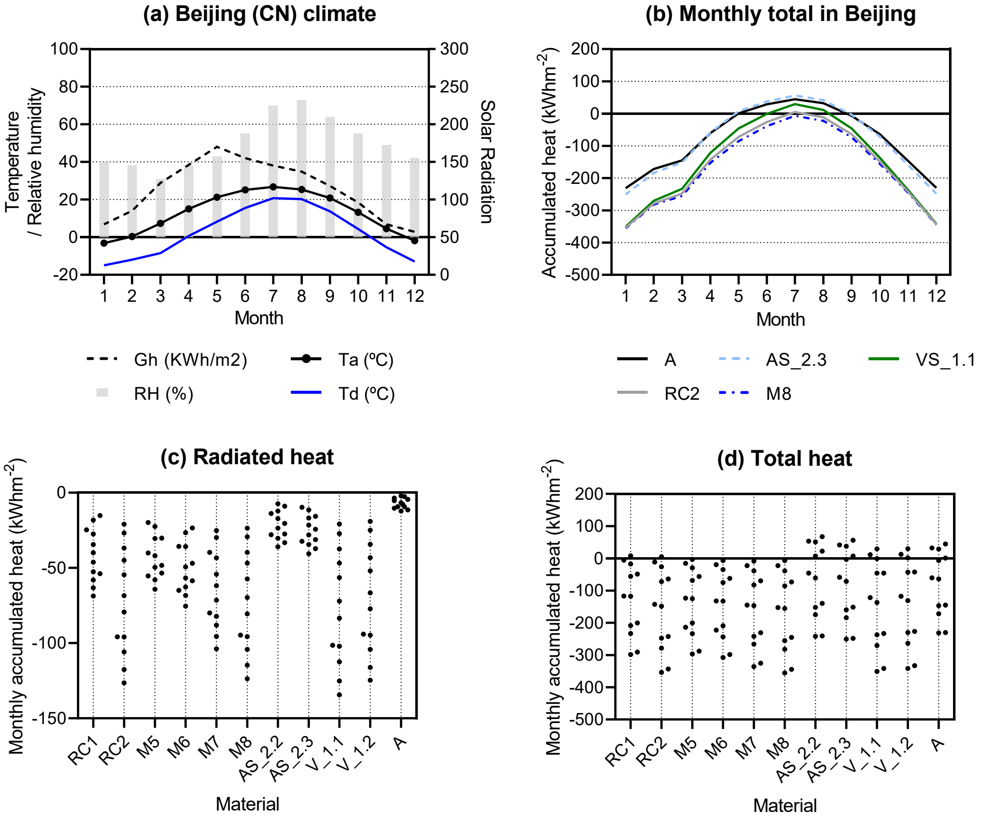

Figure 92: Dwa climate graphs: (a) Beijing climate, (b) total heat accumulated per month in Beijing (c) Monthly accumulated radiated heat variation in Beijing (d) Monthly accumulated total heat variation in Beijing. Positive values are heat gains, and negative are heat losses.

The snow climate with dry winter and hot summer climate (Dwa) representative city is Beijing (China) (Figure 92a), with a yearly mean ambient temperature of 12.9 °C and mean relative humidity of 50%. The lowest mean ambient temperature is -3.2 °C in January, and the lowest mean relative humidity is 31% in March. The mean wind speed is 2.7 ms^{-1}, and the total global horizontal radiation is 1,365 kWhm^{-2}.

The materials showed very similar behavior in this climate than in the previous two climates (Dfa and Dfb); however, the main difference was that although all materials had a higher radiative potential, including all heat transfer mechanisms, they performed slightly worse. In Beijing materials, RC2 and M8 could effectively evacuate heat for all months (Figure 92b). As seen in Figure 92c, the radiated heat was greater for those materials with a broadband emissivity RC2, M8, V_1.1, and V_1.2. The points above zero showed heat accumulations in some months. Therefore, the system should be switched off (Figure 92f).

Figure 93 to Figure 97 show the simulation boxplots results for five materials, shown in detail previously from Figure 79 to Figure 92 for every month in each selected city. In each figure, the monthly accumulated heat variation by the city is shown; graphs (a) show the radiated heat losses, (b) the solar heat gains, (c) the convective heat gains or losses, and (d) the total accumulated heat variation.

As discussed in previous chapters, the ability to radiate heat is related to the material's emissivity properties. Therefore, the more emissive the material is, the greater its ability to evacuate heat. As a result, aluminum (A) showed the least radiated heat losses (Figure 93a) among the materials (-12 $kWhm^{-2}$ in Beijing and -0.96 $kWhm^{-2}$ in Yangon), whereas VS_1.1 achieved the highest degree of radiated heat losses in all cities (Figure 95a), the lowest value is -9.3 $kWhm^{-2}$ in Yangon and -143 $kWhm^{-2}$ in Montreal.

The solar heat gains are related to the materials' reflectivity properties on the solar wavelengths (0.3 to 1 μm). The theoretical material M8 had a perfect solar reflectivity, leading to no solar gains (Figure 97 b) in any of the cities. On the contrary, the materials with the developed emissive coating had higher solar heat gains since the emissive layer partially reduces the materials' solar reflectivity (see Figure 94b and Figure 95b). RC2 had better solar behavior than V_1.1, although its emissivity is slightly worse; thus, the total balance ended up being better for RC2.

The convective heat gains in each city were the same for all the materials, as they were working on an active system with the same operating temperature graphs from Figure 93c to Figure 94c. As seen on the d graphs of all the materials, the total heat exchange was greatly dominated by convection.

The solar heat gains were higher in cities with more significant incident solar radiation, such as Phoenix, Alice Springs, Delhi, Athens, and Madrid. As mentioned before, they are related to the reflectivity of the materials in the solar wavelengths. For example, the theoretical material M8 had no solar gains as its solar reflectivity value in those wavelengths is unity. Materials VS_1.1 and RC2 showed a similar behavior across climates; the radiated cooling power was more significant in those locations where the mean ambient temperature was lower since the ambient temperature is a determinant factor (Feng et al., 2020a).

The total accumulated heat is a combination of convective heat gains or losses, radiative losses, and solar gains. Since convection was the same in each city for all materials because the surface was stable at 25 °C, the materials with almost ideal reflectivity and higher solar reflectivity had more significant heat losses.

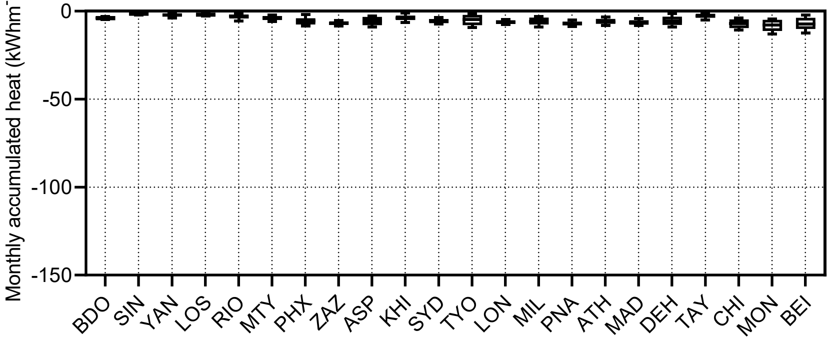
(a) A Radiated heat (losses)

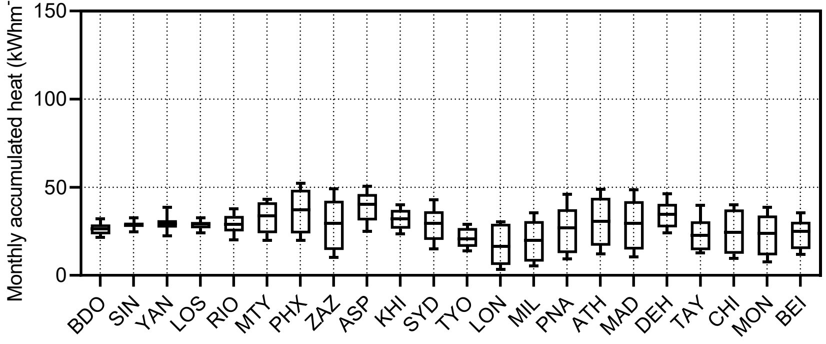
(b) A Solar heat (gains)

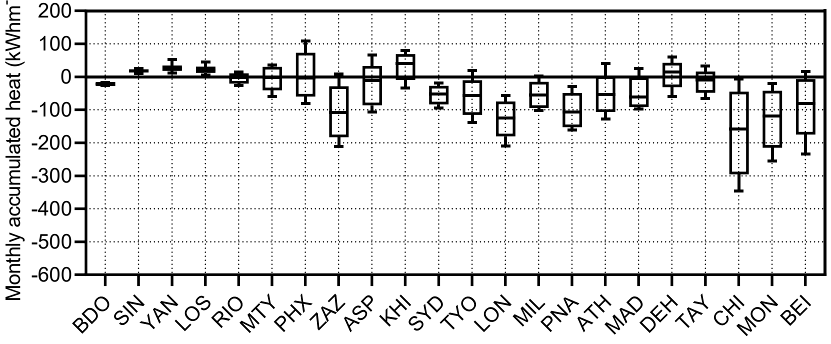
(c) A Convective heat

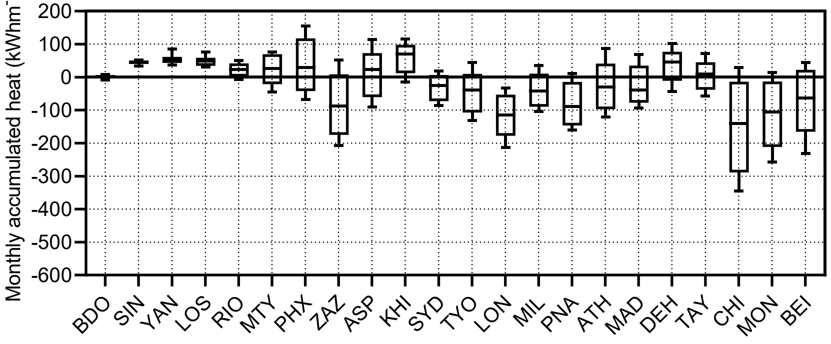
(d) A Total heat

Figure 93: Boxplots of aluminum in 22 selected cities (a) Monthly accumulated heat per city (b) Monthly solar heat gains (c) Monthly accumulated convective heat gains, and (d) Monthly accumulated total heat balance. Positive values are heat gains, and negative are heat losses—city codes presented in Table 16 and materials description in Figure 46 and Figure 72.

(a) AS_2.3 Radiated heat (losses)

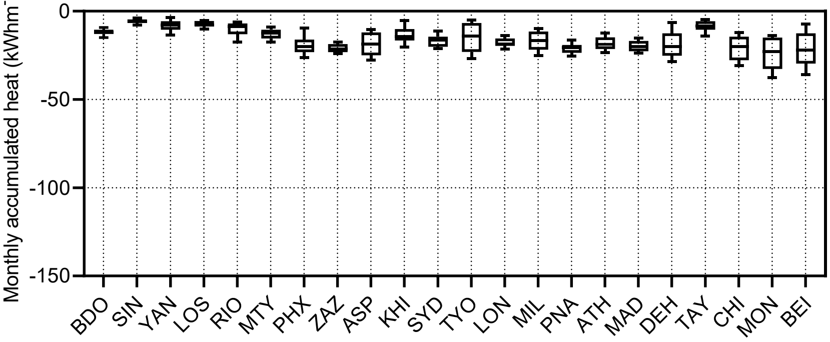

(b) AS_2.3 Solar heat (gains)

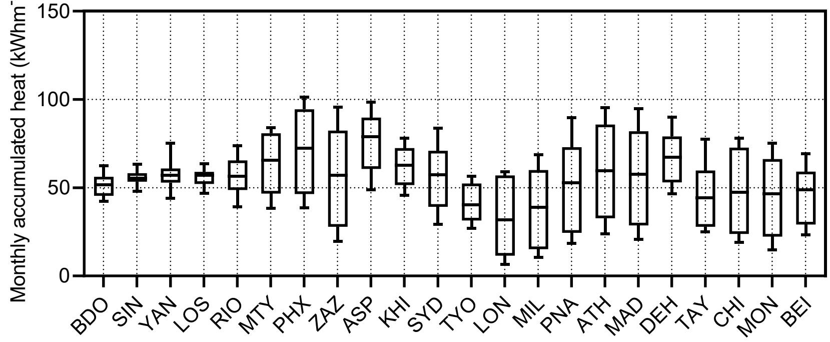

(c) AS_2.3 Convective heat

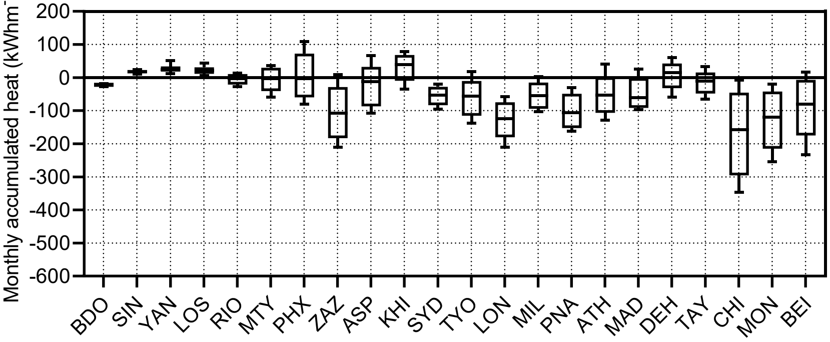

AS_2.3 Total heat

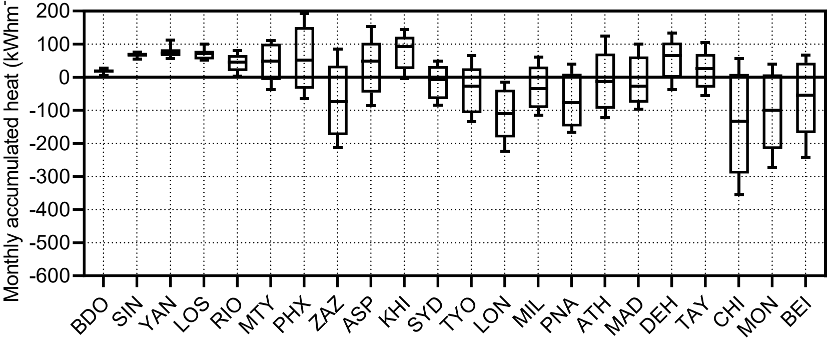

Figure 94: Boxplots of AS_2.3 in 22 selected cities (a) Monthly accumulated heat per city (b) Monthly solar heat gains (c) Monthly accumulated convective heat gains, and (d) Monthly accumulated total heat balance. Positive values are heat gains, and negative are heat losses. City codes presented in Table 16 and materials description in Figure 46 and Figure 72. City codes presented in Table 16 and materials description in Figure 46 and Figure 72.

(a) VS_1.1 Radiated heat (losses)

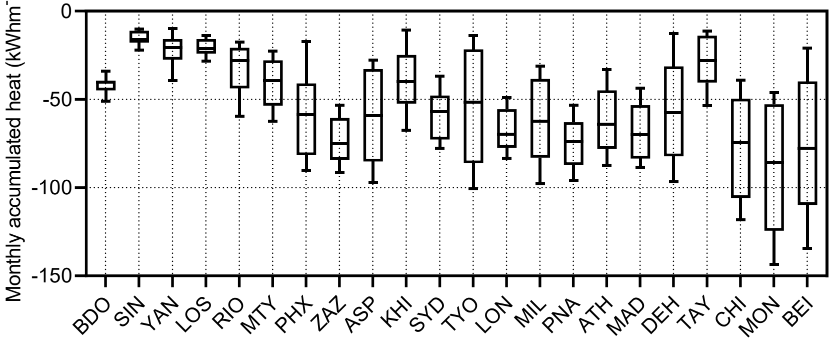

(b) VS_1.1 Solar heat (gains)

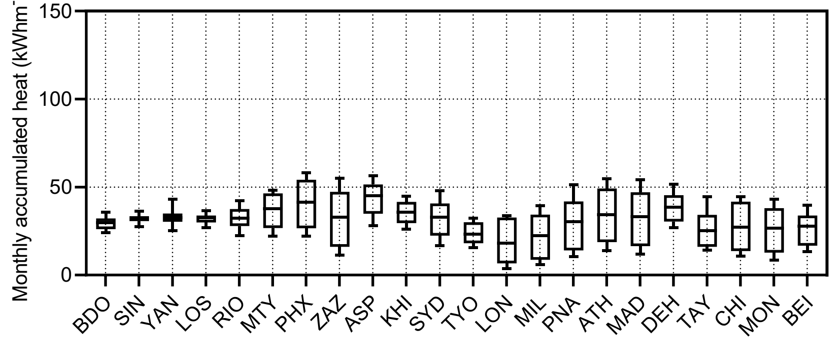

(c) VS_1.1 Convective heat

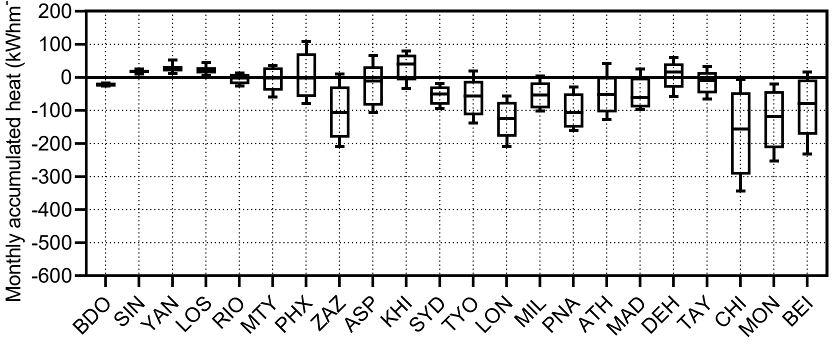

(d) VS_1.1 Total heat

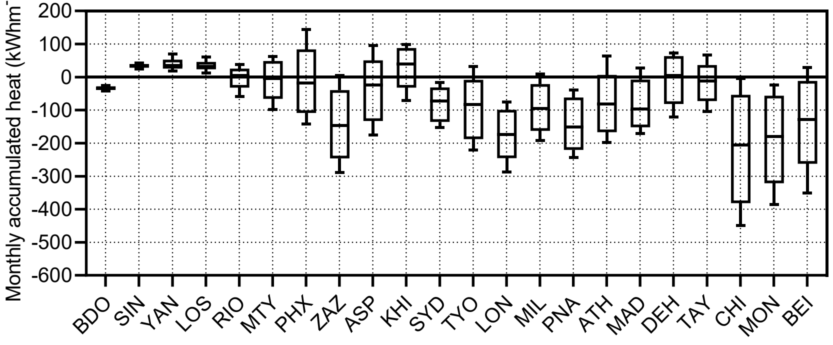

Figure 95: Boxplots of VS_1.1 in 22 selected cities (a) Monthly accumulated heat per city (b) Monthly solar heat gains (c) Monthly accumulated convective heat gains, and (d) Monthly accumulated total heat balance. Positive values are heat gains, and negative are heat losses—city codes presented in Table 16 and materials description in Figure 46 and Figure 72.

(a) RC2 Radiated heat (losses)

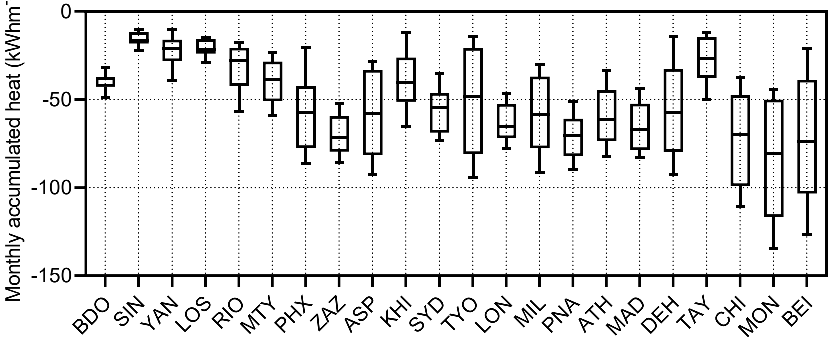

(b) RC2 Solar heat (gains)

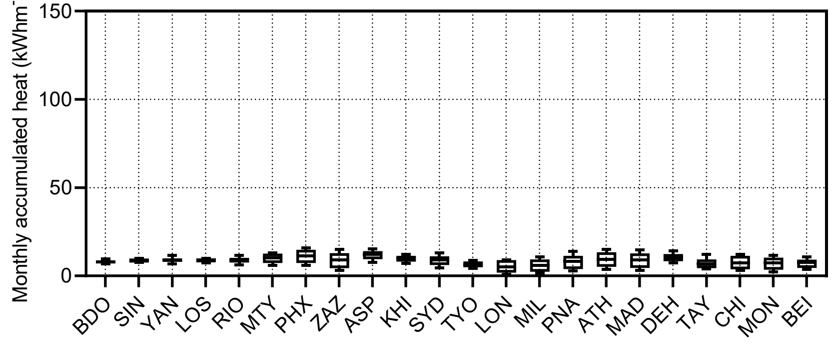

(c) RC2 Convective heat

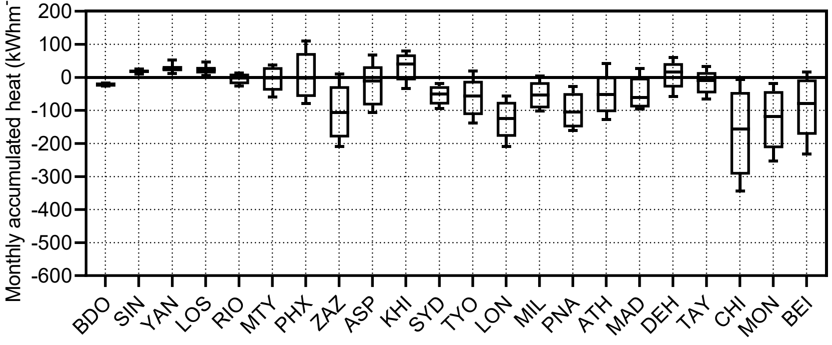

(d) RC2 Total heat

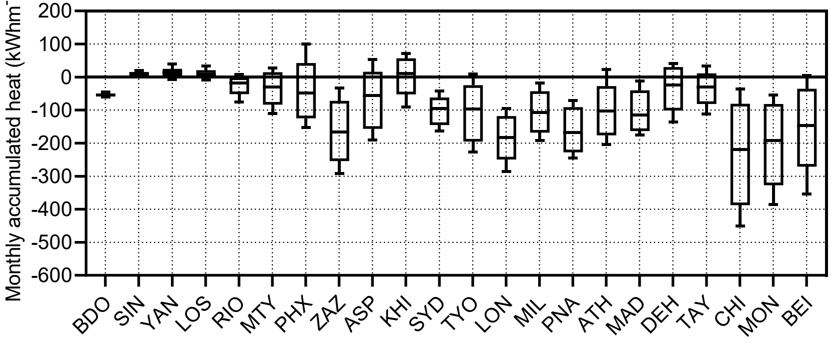

Figure 96: Boxplots of RC2 in 22 selected cities (a) Monthly accumulated heat per city (b) Monthly solar heat gains (c) Monthly accumulated convective heat gains, and (d) Monthly accumulated total heat balance. Positive values are heat gains, and negative are heat losses—city codes presented in Table 16 and materials description in Figure 46 and Figure 71.

(a) M8 Radiated heat (losses)

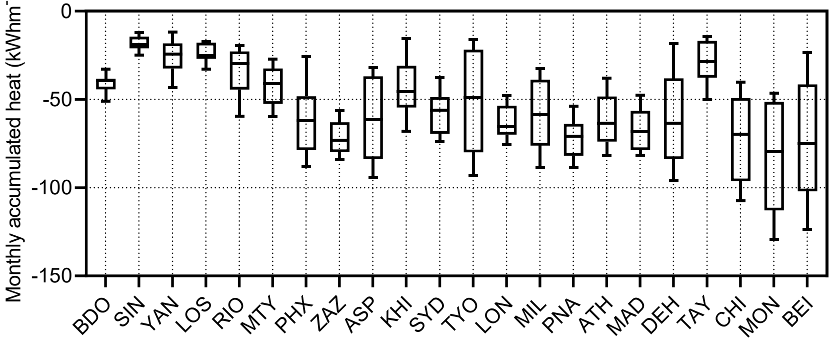

(b) M8 Solar heat (gains)

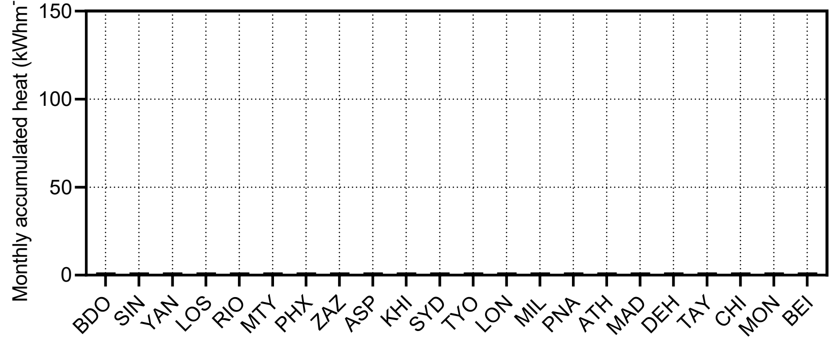

(c) M8 Convective heat

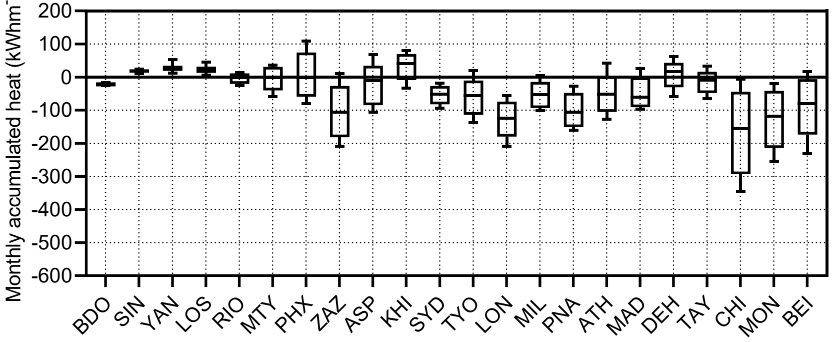

(d) M8 Total heat

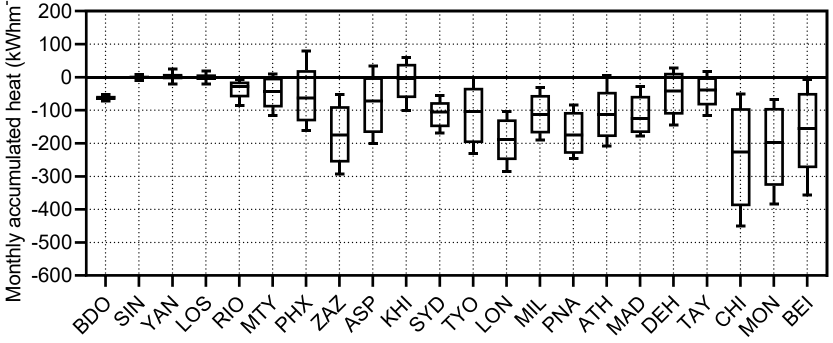

Figure 97: M8 in 22 selected cities (a) Monthly accumulated heat per city (b) Monthly solar heat gains (c) Monthly accumulated convective heat gains, and (d) Monthly accumulated total heat balance. Positive values are heat gains, and negative are heat losses—city codes presented in Table 16 and materials description in Figure 46 and Figure 70

6.4 Summary and discussion

A total of eleven materials were simulated throughout the typical meteorological year in 21 cities suffering from the UHI phenomenon, plus Pamplona, where one of the experiments in Chapter 5 took place. The climate selection was made by crossing the UHI Database from Columbia with the Köppen-Geiger classification. The 31,500 settlements included in the database were associated with their climate. As a result, the climates that grouped the most significant number of settlements were selected. The percentage of settlements per climate was preserved once the filters were applied —population, positive daytime, and nighttime temperature difference with surroundings. The filters were applied to select the most representative cities suffering from the UHI effect; it resulted in 21 cities distributed worldwide. The cities were grouped in 14 different climates from the Köppen-Geiger classification. The simulated materials were two of the most innovative radiative cooling materials presented in the literature in recent years, “Skycool” RC1 and “Radicool” RC2, four of the samples developed in this thesis (two radiative cooling materials with a metallic substrate, AS_2.2, and AS_2.3, two materials with Vikuiti substrate V_1.1 and V_1.2), a bare aluminum sample (A), and four theoretical radiative cooling materials (M5-M8).

This research is the first to simulate and calculate the potential of existing materials with already developed materials to determine the worldwide potential under the same conditions. Until now, the results of the daytime radiative cooling materials in the literature could not be directly compared since some authors referred to thermal balance temperature while others supplied heat to the samples to maintain ambient temperature. Moreover, those experiments’ locations and conditions were different and, therefore, impossible to compare. However, the present research has made it possible to compare under the same conditions and across a year using data from the typical meteorological year (TMY) from 22 cities.

Although the results presented refer to the selected cities, general conclusions can be extracted as two cities were chosen for the most prevalent climates. As opposed to most research, the meteorological data used was not ideal, as it considered covered skies with the cloudiness factor (0 to 1). Analyzing the total accumulated heat for all materials in equatorial climates (A climates: Af, Am, and Aw) cities such as Bandung, Singapore, Yangon, Lagos, and Rio de Janeiro, the system presented little benefits due to negligible radiated heat losses and some convective heat gains.

In arid climates (B climates: Bsh, Bsk, and BWh), Monterrey, Phoenix, Zaragoza, Alice Springs, and Karachi, the system might be beneficial. Sometimes, in hot arid locations, housing incorporates two different AC systems based on (vapor-compression and evaporative cooling). Radiative cooling could be operated during transition times such as fall and spring when punctual cooling is needed. Radiative cooling could be helpful in locations such as Phoenix and Alice Springs during the transition periods. In Zaragoza, the proposed solution might help achieve comfort conditions throughout the year with materials RC2 and developed material V_1.1. On the other hand, the only city where the system might not work is Karachi. The highest mean ambient temperatures coincided with the highest relative humidity values hindering the heat exchange.

In warm temperate climate cities (C climates: Cfa, Cfb, Csa, Cwa, and Cwb), the system showed a great potential to cool down during the summer months. Here, the broader band emissivity is wanted, but negligible solar gains are desired. Sydney and Tokyo are great candidates since they have more months with cooling demands. London, Milan, and Pamplona might use this system during incredibly demanding periods. However, current cooling demands are negligible compared to heating demands. Nevertheless, the rising temperatures might lead to higher temperatures making this system a great candidate.

Likewise, in temperate locations, active solutions should be favored rather than the application as a passive solution since the active system would not lead towards heat penalties during the winter months. Further research along these lines should be conducted to determine its impact. In temperate climates, the low-cost scalable developed materials V_1.1 and V_1.2 might be of high interest. Csa climates such as Madrid or Athens are great candidates that will benefit from this type of application. In climates Cwa and Cwb, the system showed a more unsatisfactory performance. The behavior might be explained because Delhi and Taipei’s higher relative humidity hindered the radiative cooling exchange in both studied locations, especially in the latter. The maximum radiated heat is -53 kWhm-2 in January for V_1.1.

In the snow zone climates (D climates: Dfa, Dfb, and Dwa), such as in locations like Chicago, Montréal, and Beijing, the system showed excellent cooling potential especially significant in winter, when heating is needed and not cooling. Nevertheless, the system could be implemented in more cooling hungry scenarios than housing.

As mentioned before, the material was only simulated as an active solution. If materials were to be applied as passive solutions, careful study of the insulation thicknesses should be made. Too much insulation could hinder any beneficial impact on the interior temperature, whereas too little insulation might lead to heat penalties. Moreover, there are precedents of unwanted effects in applying some passive strategies; as pointed out by some recent studies, cooling loads have increased due to the augment of insulation in Passivhaus buildings in some Mediterranean countries (Costanzo et al., 2018).

To conclude, this research presented a comparison of daytime radiative cooling materials under a broad selection of climates and locations worldwide. The results showed the performance of using several types of daytime radiative cooling materials. The selected simulation condition assimilates a building whose interior temperature is 25 °C, throughout the summer months, considered comfortable. The studied materials show a great potential of heat evacuation; the higher ambient temperatures are, the more strictly selective it needs to be. In arid climates, RC2 and M8 worked better than in temperate climates since they are more strictly selective. Almost all materials showed good behavior; therefore, choosing the V_1.1 or V_1.2 type would be enough. Climates with a higher relative humidity led to even materials' radiative behavior, seeing little difference among them. Convection had an essential role in the total heat loss or gains. In some locations, such as arid locations where the outside temperature is higher, adding a convection barrier would make the system more applicable throughout the most demanding periods.

It must be noted that this research interest was on the material's inherent properties to evacuate heat in some of the most relevant world climates. As a result, the material was not coupled to any specific cooling system. Once the materials' behavior and worldwide potential have been studied, the next logical step is to study integrating the optimal material with the best active system for each location. Moreover, when coupled to a system, the refrigeration cycle location should be carefully studied and the optimal fluid's temperature to obtain the maximum benefit from any radiative cooling material. Finally, including an accumulator of refrigerated fluid could store the cooled fluid during the night and broaden the application. Further research will be conducted following this line.

7 CONCLUSIONS AND FUTURE DEVELOPMENTS

This thesis “Advanced Radiative Cooling: Worldwide Potential in the Built-Environment,” brought the field of radiative cooling closer to future application in architecture to reduce the increasing cooling loads of buildings. The research approached the topic from a holistic point of view. After conducting a systematic literature review, the spectral properties of materials and the effects of climate on the ability to achieve sub-ambient cooling were studied in depth. Subsequently, this thesis centered on material design and the development of low-cost scalable coatings for easy application as building envelope coatings and part of air conditioning systems. Two sets of materials were tested under two different climate conditions, where the cooling ability of those materials was examined. Finally, the worldwide cooling potential of several daytime radiative cooling materials was studied throughout an entire year in 14 worldwide climates, and 22 cities experiencing the Urban Heat Island effect were selected as representative locations. The simulations included two of the most relevant materials from the literature, theoretical materials, and the developed materials in this research. This last point culminates the thesis investigation and highlights the importance of the spectral design of the material and the climate of application.

This final chapter summarizes the main contributions of the research and its limitations. First, the answers to the research questions are stated, and the key findings of each chapter are reviewed. Finally, future research directions are discussed under the perspective of the work contributed and the latest developments.

7.1 Introduction

The current energy context, on which this thesis is based, points to an increasing demand for cooling in the coming years. More than half of the world population lives in urban areas (*World Urbanization Prospects*, 2014) and consumes 75% of the primary energy sources ("Energy – UN-Habitat," n.d.). Expected population growth in developing countries and rising living standards present a challenging scenario (O'Neill et al., 2010). Moreover, greenhouse gas emissions are increasing the temperature of the atmosphere. Additionally, it is being reported that cities are experiencing the Urban Heat Island phenomenon, which combined with increasing heatwaves (Founda and Santamouris, 2017), present a health threat to the population and a highly demanding cooling scenario. The number of air conditioning units installed across the world has been rising consistently (IEA, 2018a), contributing to rejection of heat onto the streets and intensive energy use. The number of refrigeration devices will increase with rising temperatures and ease of access.

Although radiative cooling is a low-grade energy source, since the cooling power achieved is around 120 $W \cdot m^{-2}$, it is a free source of cooling, as it rejects the excess heat into the space passively. Radiative cooling materials that rely on particular spectral configurations could lower the energy demands of buildings when applied as passive coatings, or make the cooling cycle more efficient when integrated into active systems. This research has presented a broad overview of this technology potential through several experimental and numerical approaches, which are based on the future integration of this technology as a prerequisite in architecture.

The following details the main contributions and critical findings of this thesis; presents the answers to each research question; discusses the limitations; and finally highlights future research.

7.2 Main contributions and key findings

This thesis used different methodological approaches tailored to answer the specific objectives and research questions posed. In addition to the specific findings of each chapter, this research has contributed the following:

A material design methodology for architecture applications.

Each chapter delved into the research process of new materials, from a critical perspective. The sequence has proven to be valid for daytime radiative cooling materials and could potentially be applied in future material development for any other material or coating that aims to be used in architecture. The methodology uses the following five steps:

1. Systematic state-of-the-art analysis.

The systematic literature review critically analyzes results and findings from a list of selected publications, to find the relevant research gaps and main contributions in the field.

2. Energy potential and possible applications of the theoretical material.

Most studies report the benefits of the material in a single location. When considering low-grade energy systems or materials such as radiative cooling, it is essential to have a broad overview of their potential applicability before studying their application in architecture.

3. Material optimization, development, and characterization

Materials must be optimized before they are manufactured; otherwise, the chances of achieving the desired outcome are low. After implementing developments, materials should be adequately characterized and compared to the optimizations to detect significant differences. Critically discussing the differences between simulations and measurement is essential to make progress in the field.

4. Material testing.

Material testing under careful environmental conditions might help prove specific designs. However, if materials are to be part of the built environment, more extended periods and overall meteorological and urban conditions should be taken into account. The yearly balance is essential to see if the material is worthy of application.

After material testing, another optimization-development-characterization-testing process should be carried out to maximize potential positive outcomes during an initial experiment.

5. Worldwide potential of the material.

Another critical aspect in the urban and built environment, especially with passive mechanisms such as radiative cooling, is studying its behavior in different climates and locations in the world.

The steps mentioned above provide a systematic method that can be used as a guide for future material developments for the built environment. The methodology and the calculations of the given material should be adapted considering the specifications of the researched material. Material development requires an interdisciplinary approach, which has been a critical aspect in completing this thesis and serves as a reminder that new technical developments require a broad approach to succeed.

Potential applicability is a critical step in material development.

Climate plays a specific role in any renewable energy production and material behavior. A particular climate might benefit from applying a given material but might not be ideal in terms of its potential. In this case, other types of applications, combinations, or solutions should be favored instead of optimizing a system that is not tailored to the location or is, in the worst-case scenario, counterproductive.

The research has proven in a very concrete manner that before using any new developments, specific studies should be conducted on locations to determine their needs and suitability.

7.3 Conclusions

The research has evaluated the cooling potential of daytime radiative cooling materials experimentally and numerically in 22 locations across the world experiencing the Urban Heat Island effect. The results demonstrate that **the technology shows promise for reducing the cooling loads** of **buildings** both for active and passive applications **in the built environment**. The research focused extensively on **climate potential** since it is a **critical aspect** for success. The developed materials based on polymethylsilsesquioxane (PMSQ) show a promising path in the use of polymers for radiative cooling. During the experiment and under most climatic conditions, the materials can cool down a metallic substrate a mean of at least 1.7 °C with up to 12 °C temperature drops. In both cases, the substrates presented a better thermal behavior than the materials without treatment. The **cost** (0.3 euros/m^2 for a 2 μm layer) **and the spray coating deposition technique** used, proved to make it a **good candidate** for future broad **application** in the built environment and in **architecture**. Furthermore, the proposed material design based on a highly reflective substrate and the emissive coat could be integrated into already existing air conditioning devices to improve its efficiency.

7.3.1 Answers to the research questions

This section answers the specific research questions posed in the first chapter of the dissertation (1.3.1).

- What is the impact of each wavelength on radiative cooling? What is the theoretical temperature drop limit on a given climate? (Chapter 3)

The answer to this question was published as (Carlosena et al., 2020). The contribution of each wavelength to the ability to cool by radiation was studied with a sensitivity analysis. The radiation spectrum was divided into bands, according to the division used in the thermal model and sky emissivity model, and the **contribution of each band** in the ability to **achieve sub-ambient cooling** was calculated. The most critical bands regarding heat absorption are band 4 (0.5-1 μm), followed by band 5 (1-2 μm) and band 3 (0.4-0.5 μm). Therefore, it is essential to achieve high reflectivity in the 0.5-1 μm region and incredibly high emissivity values from 9.98 to 11.95 μm. The theoretical values of sub-ambient cooling were calculated in two locations experiencing the Urban Heat Island phenomenon with different climates – Phoenix, with an arid climate, and Sydney, with a hot and humid one.

A material that solely emits or absorbs radiation wavelengths from 0.5 to 1 μm reaches a surface temperature up to 10.6 °C higher than the ambient air temperature in Sydney and 9.9 °C in Phoenix. The theoretical materials achieved up to 5.30 °C below ambient air temperature in an arid climate (Phoenix) and 4.21 °C below ambient temperature in a hot and humid climate (Sydney). Reducing convection to 1 $W{\cdot}m^{-2}{\cdot}K^{-1}$ leads to a temperature drop of around 37 °C in Phoenix and 30 °C in Sydney.

- What kind of designs, materials, and manufacturing techniques should be used to manufacture scalable, low-cost radiative cooling materials and tunable radiative cooling materials for applications in the built environment? (Chapter 4)

Simple designs such as 1D photonics might be **preferably used for scalable applications** in the built environment, as the manufacture is more **straightforward** and, therefore, **inexpensive**. Although layers of different materials and thickness, such as Fabry-Perot resonators, can provide almost ideal results, simpler structures will ease application in the built environment.

Abundant materials or derivates that show peak absorption at the target wavelengths should be **favored**. Silica and silica-derived polymers have proven beneficial; however, their aging should be further studied when exposed to long periods.

The **developed emissive laye**r of **polymethylsilsesquioxane with SiO_2** nanoparticles had a cost of **0.3 euros/m2** for a 2 μm layer. The ability to **reduce** any **substrate temperature** in current climatic conditions and the costs make it a great candidate for the **built environment**. Moreover, the **transparent** properties of the emissive layer show the aesthetic characteristics of the substrate, making it an **ideal** solution for **refurbishment**. The design, optimization, development, characterization, and testing of these materials in a temperate climate is under peer review, titled “Experimental development and testing of low-cost scalable radiative cooling materials for building applications”.

Simple deposition techniques reduce costs; the **spray coating** technique, such as the one used in this thesis, should prevail over complex procedures such as plasma-enhanced chemical vapor deposition (PECVD), sputtering and sol-gel spin-coating. Moreover, the size sample and the resulting quantity of the deposition should be another factor to analyze.

The **tunable materials** were successfully developed; nevertheless, the tunable functionality **introduces complexity** in material design. On the one hand, the commonly available thermochromic leuco-dyes are not trustworthy. On the other hand, the manufacture of inorganic thermochromic materials such as vanadium dioxide is more sophisticated, especially when doped, increasing costs and uncertainties. More research should be conducted with these materials.

- What is the maximum temperature drop achieved by the developed materials in different climates? Are the developed tunable radiative cooling materials able to successfully switch their optical properties? (Chapter 5)

Two experiments were conducted in different **temperate climate** locations: Sydney and Pamplona - warm temperate and fully humid with hot summer (Cfa), warm temperate and fully humid with hot summer (Cfb). These climates are two of the **most prevalent** climates **worldwide**, grouping, respectively 19.2% (Cfa) and 13.8% (Cfb) of the settlements worldwide.

The experimental settings were similar in both locations to test climate dependency. Nevertheless, different sets of materials were tested in each location; since the first set of samples achieved **nighttime radiative cooling in Sydney**, a second set of samples – an improved version of the first – were tested in Pamplona. The first samples, tested in Sydney, were up to 23.45 °C higher above ambient air temperature during the day and an average of 2 °C higher than the bare aluminum sample. At **night**, the samples reached **up to 4 °C below ambient air temperature**. The second set of materials tested in Pamplona consisted of daytime radiative cooling materials with two different substrates. The samples based on the developed **emissive coating and the commercial reflective substrate**, Vikuiti, dropped their temperature during the daytime up to **2.70 °C below ambient air temp**erature and up to 7.97 °C temperature drop. The samples made of **aluminum** plus the **emissive coating** achieved a **1.88 °C reduction** compared to the bare aluminum and a maximum temperature difference of 11.2 °C.

Among the tunable radiative cooling materials, only the first set with commercial pigment was tested (Sydney), but the samples degraded in less than an hour, losing their reversibility properties due to the pigment's organic composition. Testing needs to be carried out on the samples containing the doped vanadium dioxide ($V_{1-x}W_xO_2$). However, the low quantity of the pigment within the polymethylsilsesquioxane matrix might not be enough to present a different thermal behavior in both phases.

- Which climate conditions benefit the most from a daytime radiative cooling (DRC) material? (Chapter 6)

Eleven materials were simulated as an active system in 22 locations experiencing the Urban Heat Island phenomenon, grouped in 14 of the worlds' most prevalent climates, totaling 242 simulations throughout the typical meteorological year. The **materials analyzed** show **great potential for heat evacuation**, primarily through radiation. The **higher ambient air temperatures** are, the more **strictly selective** the **material** needs to be. In **equatorial climates**, the materials and system showed **poor performance** due to the low heat radiated. In arid and temperate climates, the system proved to evacuate heat satisfactorily. In **arid climates**, the more **strictly selective** materials showed **better behavior** than in temperate climates, where less reflective materials achieve considerable cooling rates. Climates with higher relative humidity led to more constant radiative behavior in the materials, and few differences were observed among them. **Convection** played an **essential role** in the total heat loss or gain. In some locations, such as arid locations where the outside temperature is higher, adding a convection barrier would make the system more applicable throughout the most demanding periods.

- How much energy can be radiated by a radiative cooling material (active application)? (Chapter 6)

The **amount of energy radiated** by the system **depends** greatly on the **climate of application**. The colder the climate, the greater the evacuation through radiative cooling. Radicool material (RC2) achieved a monthly mean of accumulated radiated heat of -26 $kWhm^{-2}$ in equatorial climates, -48.6 $kWhm^{-2}$ in arid climates, -56 $kWhm^{-2}$ in temperate climates, and -78 $kWhm^{-2}$ in snow zone climates. The total heat balance depends on the absorption of solar radiation and the gains or losses through evacuation.

7.3.2 Limitations

The outcomes presented throughout this research have accomplished the objectives defined in the introductory chapter. The work has answered the research questions comprehensively; however, some limitations need to be addressed for future reference. Some of these limitations have already been discussed individually in each chapter.

Material optimization and development

The outcomes presented throughout this research have accomplished the objectives defined in the introductory chapter. The work has answered the research questions comprehensively.

However, some limitations need to be addressed for future reference and a few of these have already been discussed individually in each chapter.

Material optimization and development

Optimization of a given material requires a complex refractive index that is not possible to measure, as the samples do not have the properties required by the instruments. In this case, it was not possible to optimize the polymethylsilsesquioxane layer, and as a result, an approximation was given. As mentioned before, due to the inability to control deposition thickness with the presented spray coating technique, the resulting materials are not exactly replicable. However, the data presented gives enough information on replicating the materials using other deposition techniques, such as ultrasonic spraying with numeric control or flame spray pyrolysis (FSP). Thus, making the process more scalable for broad application.

Tunability

The research focused primarily on developing two types of materials: daytime radiative cooling materials (DRC) and tunable daytime radiative cooling materials (TDRC). DRC samples were successfully developed and achieved sub-ambient cooling. However, the TDRC samples that included thermochromic pigments did not achieve the desired results.

Two different approaches were considered. The first approach included commercial thermochromic pigments; they change their reflectivity behavior reversibly on the visible wavelengths. Their solar spectrum in the color phase is absorbent and highly reflective in the colorless phase. They can be absorbent during the cold periods and reflective in the heating seasons, thus decreasing the built environment's energy consumption in any season (Granqvist et al., 2009; Kanu and Binions, 2010). The thermochromic pigment was based on leuco-dyes made of organic components (1,2-Benz-6-diethylaminofluorane). Furthermore, as reported in Chapter 5.3.1, 5.3.1, they degraded very quickly, losing their reversible behavior.

The samples with doped vanadium dioxide are based on inorganic components, enabling both cooling and heating due to changes in the solar reflectivity of VO_2 and infrared emissivity (Jin et al., 1994). As opposed to the organic components, vanadium dioxide maintains its switching ability after aging in the air for five years (Zhang et al., 2020). Unfortunately, the developed samples with the doped thermochromic material have not been tested, as they arrived in winter.

Material aging

In general, the materials with spectral selectivity should be spectrally characterized before and after experiments outdoors to compare and detect any change in their spectral properties. Thus, giving information about any possible performance changes that this may lead to. Degradation is a crucial aspect when materials are applied in the built environment as they are exposed to extreme conditions over long periods.

As highlighted in the previous point, tunable daytime radiative cooling with thermochromic leuco-dye pigments degraded in less than an hour, losing their reversibility properties; this severe aging concern has been extensively discussed. It must be noted that although the degradation of the material was not explicitly tested, the daytime radiative cooling samples (DRC) maintained the same appearance after testing.

Glaring effect

The glaring effect of the radiative cooling materials developed in this research depends mainly on the substrate; when applied on top of aluminum, the emissive coat reduced the visible glaring effect. However, more reflective substrates such as Vikuiti require careful studies on location to avoid this effect. Techniques such as orienting small louvers have recently been proposed (Xia et al., 2020) to avoid this unwanted effect.

The developed emissive coat could be applied to numerous non-metallic substrates typically found in buildings, such as ceramic and concrete, to improve their thermal behavior without glaring.

Active system assimilation

The research and simulations considered only a theoretical fluid at a constant temperature of 25 °C, analyzed the potential of the material to radiate heat, and considered other thermal forces to calculate the total accumulated heat. Although the results were consistent with the predictions, in some instances, the fluid heats up since the ambient air temperature is higher than that of the fluid. Increasing the fluid temperature would have led to better results as radiation depends on the temperature at the fourth power, but the objective was to simulate a system that achieved thermal comfort inside a building. It must be noted that integrating these materials in an air conditioning system could improve efficiency and lower energy consumption, while lowering the rejection of heat into the street. Moreover, the systems were not applied on a building, requiring more complex thermal exchanges with the envelope and user energy demand patterns. Nevertheless, quantifying these aspects was out of the scope of the thesis. The goal of the thesis was to study radiative cooling performance potential across different climates and locations using different materials and conditions.

7.4 Future research

Future research lines will be briefly discussed, considering the results obtained in this research as well as the limitations described in the previous section. From the experiences of this research, the radiative cooling field offers great potential for application in temperate climates that encompass most worldwide settlements. The fields yet to explore in more depth are:

Active systems

Once the potential of radiative cooling materials has been thoroughly researched, the following natural step is to discuss integrating such materials as parts of active systems at different positions, within a vapor compression refrigeration system, or as part of a heat pump. There are several candidate systems to accommodate these radiators as part of a cooling circuit. Afterward, two aspects should be analyzed, the temperature surrounding the system and the potential energy savings. The first refers to the latent waste rejection of heat into the street; the inclusion of a radiative cooler ought to diminish the surrounding temperature and improve efficiency. Secondly, the energy performance of the system should be compared before and after including the material as part of the system. Some authors of the seminal paper (Raman et al., 2014) already implemented their panels as part of cooling systems in a series of commercial buildings in California ("Case Studies," n.d.). However, peer-reviewed results have not been published to date that report data on cooling savings.

Passive materials applications

Materials for radiative cooling should be placed in locations with exposure to the sky to radiate heat towards the space, such as rooftops, shadowing devices, louvers, overhangs, and canopies. If radiative cooling materials are applied as envelope coatings, their composition (layers) should be carefully studied. The optimal insulation thickness should be determined for each location and orientation to observe any potential benefit on the inside. This type of application might be more beneficial in locations with almost no heating period than in places with very extreme summer and winters, such as snow zone locations or even some temperate climates, where an active system or a tunable material could be more suitable. Moreover, angular spectral emissivity could be tuned to a certain inclination angle instead of having an almost Lambertian emissivity. This type of design could be applied to surfaces with less exposure to the sky, such as vertical surfaces (façades). The latest research points towards different alternatives to expand the applicability of radiative cooling materials with different assymetric transmission techniques such as gratings, arrays and chiral materials (Ulpiani et al., 2021).

As a passive application, the presented transparent emissive coating could cover any material, improving its emissivity and therefore its thermal behavior, resulting in a broader range of colors and materials to use.

Building application

Once the type of application is selected (active or passive), energy savings calculations should be made using case study buildings to determine the cooling loads when these materials are applied. Moreover, in case of passive application, unwanted penalties during the heating season should be estimated.

Both applications could be of interest in rehabilitation. A passive application of emissive coating could be sprayed onto existing surfaces with high absorptivity for a low cost. Moreover, the material design based on a highly reflective substrate and the emissive coat could be integrated into already existing air conditioning devices to improve their efficiency.

Complex urban environment

Radiative cooling materials need to be further developed for integration into pavements, to lower the Urban Heat Island effect. Moreover, in complex urban environments, other buildings, trees, or urban elements might reduce exposure to the sky, which limits the potential benefits of these materials. Research should determine the potential benefit of theoretical materials in lowering the Urban Heat Island effect without glaring. A recent publication considered radiative cooling materials among other strategies such as cool pavements, urban greenery, shading, and spray systems (Bartesaghi-Koc et al., 2021), and showed that radiative cooling shading had one of the highest mitigation potentials among those studied on a street canyon.

The author of this thesis, alongside other researchers, has already begun some investigation work to address this concern. The overcooling penalty of the passive application of daytime radiative cooling materials during the cold period was evaluated. Using a mesoscale urban modeling system, the thermal and overcooling impact of standard and optically modulated broadband radiative cooling emitters during the winter seasons at a city scale are being assessed. Moreover, the technological ways to reduce the phenomena were explored, proposing technologies to modulate their optical characteristics to reduce the overcooling penalty.

REFERENCES

3M^{TM} Enhanced Specular Reflector (3M ESR) | 3M United States [WWW Document], n.d. URL https://www.3m.com/3M/en_US/company-us/all-3m-products/~/3M-Enhanced-Specular-Reflector-3M-ESR-/?N=5002385+3293061534&rt=rud (accessed 9.8.20).

About Montreal Protocol | Ozonaction [WWW Document], n.d. URL https://www.unenvironment.org/ozonaction/who-we-are/about-montreal-protocol (accessed 11.5.19).

Addeo, A., Monza, E., Peraldo, M., Bartoli, B., Coluzzi, B., Silvestrini, V., Troise, G., 1978. Selective covers for natural cooling devices. Il Nuovo Cimento C 1, 419–429. https://doi.org/10.1007/BF02507668

Afonso, C.F.A., 2006. Recent advances in building air conditioning systems. Appl. Therm. Eng. 26, 1961–1971. https://doi.org/10.1016/j.applthermaleng.2006.01.016

Ahmadi, A., Karaei, M.A., Fallah, H., 2016. Investigation of night (radiative) cooling event and construction of experimental radiator. Int J Adv Biotechnol Res 7, 1180–1184.

Aili, A., Wei, Z., Chen, Y., Zhao, D., Yang, R., Yin, X., 2019a. Selection of polymers with functional groups for day-time radiative cooling. Mater. Today Phys. 100127. https://doi.org/10.1016/j.mtphys.2019.100127

Aili, A., Zhao, D., Lu, J., Zhai, Y., Yin, X., Tan, G., Yang, R., 2019b. A kW-scale, 24-hour continuously operational, radiative sky cooling system: Experimental demonstration and predictive modeling. Energy Convers. Manag. 186, 586–596. https://doi.org/10.1016/j.enconman.2019.03.006

Akbari, H., Bretz, S., Kurn, D.M., Hanford, J., 1997. Peak power and cooling energy savings of high-albedo roofs. Energy Build. 25, 117–126. https://doi.org/10.1016/S0378-7788(96)01001-8

Akbari, H., Cartalis, C., Kolokotsa, D., Muscio, A., Pisello, A.L., Rossi, F., Santamouris, M., Synnef, A., Wong, N.H., Zinzi, M., 2016. Local climate change and urban heat island mitigation techniques – the state of the art. J. Civ. Eng. Manag. 22, 1–16. https://doi.org/10.3846/13923730.2015.1111934

Algarni, S., Nutter, D., 2015. Survey of Sky Effective Temperature Models Applicable to Building Envelope Radiant Heat Transfer. ASHRAE Trans. 121, 351. https://doi.org/10.13140/rg.2.1.4212.5526

Ali, A.H.H., Saito, H., Taha, I.M.S., Kishinami, K., Ismail, I.M., 1998. Effect of aging, thickness and color on both the radiative properties of polyethylene films and performance of the nocturnal cooling unit. Energy Convers. Manag. 39, 87–93. https://doi.org/10.1016/S0196-8904(96)00174-4

Amma, S., Luo, J., Pantano, C.G., Kim, S.H., 2015. Specular reflectance (SR) and attenuated total reflectance (ATR) infrared (IR) spectroscopy of transparent flat glass surfaces:

A case study for soda lime float glass. J. Non-Cryst. Solids 428, 189–196. https://doi.org/10.1016/j.jnoncrysol.2015.08.015

Anderson, B., 1976. Heat Transfer Mechanisms, The 1967 Odeillo House, Integrated Collection and Storage Systems. Presented at the Passive solar heating and cooling conference and workshop proceedings, Merily H. Keller, LASL, University of New Mexico, Albuquerque, New Mexico, pp. 23–28.

Antonanzas-Torres, F., Urraca, R., Polo, J., Perpiñán-Lamigueiro, O., Escobar, R., 2019. Clear sky solar irradiance models: A review of seventy models. Renew. Sustain. Energy Rev. 107, 374–387. https://doi.org/10.1016/j.rser.2019.02.032

Ao, X., Hu, M., Zhao, B., Chen, N., Pei, G., Zou, C., 2019. Preliminary experimental study of a specular and a diffuse surface for daytime radiative cooling. Sol. Energy Mater. Sol. Cells 191, 290–296. https://doi.org/10.1016/j.solmat.2018.11.032

Aranovitch, E., Oliveira Fernandes, E. de, Institute for Systems Engineering and Informatics, Joint Research Centre at Ispra, Commission of the European Communities (Eds.), 1990. Workshop on Passive Cooling, EUR. Luxembourg.

Argiriou, A., Santamouris, M., Balaras, C., Jeter, S., 1992. Potential Of Radiative Cooling In Southern Europe. Int. J. Sol. Energy 13, 189–203. https://doi.org/10.1080/01425919208909784

Arnell, N.W., Brown, S., Gosling, S.N., Gottschalk, P., Hinkel, J., Huntingford, C., Lloyd-Hughes, B., Lowe, J.A., Nicholls, R.J., Osborn, T.J., Osborne, T.M., Rose, G.A., Smith, P., Wheeler, T.R., Zelazowski, P., 2016. The impacts of climate change across the globe: A multi-sectoral assessment. Clim. Change 134, 457–474. https://doi.org/10.1007/s10584-014-1281-2

Ascione, F., De Masi, R.F., Santamouris, M., Ruggiero, S., Vanoli, G.P., 2018. Experimental and numerical evaluations on the energy penalty of reflective roofs during the heating season for Mediterranean climate. Energy 144, 178–199. https://doi.org/10.1016/j.energy.2017.12.018

Asimakopoulos, D., Santamouris, M., 1996. Passive Cooling of Buildings. CRC Press LLC, London, UNITED KINGDOM.

Atiganyanun, S., Plumley, J.B., Han, S.J., Hsu, K., Cytrynbaum, J., Peng, T.L., Han, S.M., Han, S.E., 2018. Effective Radiative Cooling by Paint-Format Microsphere-Based Photonic Random Media. ACS Photonics 5, 1181–1187. https://doi.org/10.1021/acsphotonics.7b01492

Aviv, D., Meggers, F., 2017. Cooling oculus for desert climate-dynamic structure for evaporative downdraft and night sky cooling, in: Energy Procedia. Presented at the CISBAT International Conference-Furture Buildings & Districts- Energy Efficiency from Nano to Urban Scale, CISBAT 2017, Lausanne, Switzerland, pp. 1124–1129. https://doi.org/10.1016/j.egypro.2017.07.474

Awanou, C.N., 1986. Radiative cooling by a diode roof. Sol. Wind Technol. 3, 163–172. https://doi.org/10.1016/0741-983X(86)90030-5

Baer, S., 1976. Movable Insulation. Presented at the Passive solar heating and cooling conference and workshop proceedings, Merily H. Keller, LASL, University of New Mexico, Albuquerque, New Mexico, pp. 63–69.

Bagiorgas, H.S., Mihalakakou, G., 2008. Experimental and theoretical investigation of a nocturnal radiator for space cooling. Renew. Energy 33, 1220–1227. https://doi.org/10.1016/j.renene.2007.04.015

Bao, H., Yan, C., Wang, B., Fang, X., Zhao, C.Y., Ruan, X., 2017. Double-layer nanoparticle-based coatings for efficient terrestrial radiative cooling. Sol. Energy Mater. Sol. Cells 168, 78–84. https://doi.org/10.1016/j.solmat.2017.04.020

Bartesaghi-Koc, C., Haddad, S., Pignatta, G., Paolini, R., Prasad, D., Santamouris, M., 2021. Can urban heat be mitigated in a single urban street? Monitoring, strategies, and performance results from a real scale redevelopment project. Sol. Energy 216, 564–588. https://doi.org/10.1016/j.solener.2020.12.043

Bartos, M., Chester, M., Johnson, N., Gorman, B., Eisenberg, D., Linkov, I., Bates, M., 2016. Impacts of rising air temperatures on electric transmission ampacity and peak electricity load in the United States. Environ. Res. Lett. 11, 114008. https://doi.org/10.1088/1748-9326/11/11/114008

Bell, J.M., Smith, G.B., Lehmann, R., 2003. Advanced Roof Coatings: Materials and their Applications, in: Conference Proceedings. Presented at the SASBE 2003 - Smart and Sustainable Built Environment, 19-21 November 2003, Brisbane, Australia.

Berdahl, P., 1983. Radiative cooling with MgO and/or LiF layers. Appl. Opt. 23, 370. https://doi.org/10.1364/AO.23.000370

Berdahl, P., Bretz, S.E., 1997. Preliminary survey of the solar reflectance of cool roofing materials. Energy Build. 25, 149–158. https://doi.org/10.1016/S0378-7788(96)01004-3

Berdahl, P., Fromberg, R., 1982. The Thermal Radiance of Clear Skies. Sol. Energy 29, 299–314. https://doi.org/10.1016/0038-092X(82)90245-6

Berdahl, P., Martin, M., Sakkal, F., 1983. Thermal performance of radiative cooling panels. Int. J. Heat Mass Transf. 26, 871–880. https://doi.org/10.1016/S0017-9310(83)80111-2

Berger, X., Bathiebo, J., 1989. From spectral clear sky emissivity to total clear sky emissivity. Sol. Wind Technol. 6, 551–556. https://doi.org/10.1016/0741-983X(89)90090-8

Bhattacharyya, S.C., 2019. The Economics of Climate Change, in: Bhattacharyya, S.C. (Ed.), Energy Economics: Concepts, Issues, Markets and Governance. Springer, London, pp. 331–365. https://doi.org/10.1007/978-1-4471-7468-4_11

Bliss, R.W., 1961. Atmospheric radiation near the surface of the ground: A summary for engineers. Sol. Energy 5, 103–120. https://doi.org/10.1016/0038-092X(61)90053-6

Bosi, S.G., Bathgate, S.N., Mills, D.R., 2014. At Last! A Durable Convection Cover for Atmospheric Window Radiative Cooling Applications. Energy Procedia, 2013 ISES Solar World Congress 57, 1997–2004. https://doi.org/10.1016/j.egypro.2014.10.064

Bosomworth, K., Trundle, A., McEvoy, D., 2013. Responding to the Urban Heat Island: A Policy and Institutional Analysus. Victorian Centre for Climate Change Adaptation Research.

Brooke Anderson, G., Bell, M.L., 2011. Heat Waves in the United States: Mortality Risk during Heat Waves and Effect Modification by Heat Wave Characteristics in 43 U.S. Communities. Environ. Health Perspect. 119, 210–218. https://doi.org/10.1289/ehp.1002313

Brown, P.T., Caldeira, K., 2017. Greater future global warming inferred from Earth's recent energy budget. Nature 552, 45. https://doi.org/10.1038/nature24672

Buranyi, S., 2019. The air conditioning trap: how cold air is heating the world. The Guardian.

Cai, L., Peng, Y., Xu, J., Zhou, Chenyu, Zhou, Chenxing, Wu, P., Lin, D., Fan, S., Cui, Y., 2019. Temperature Regulation in Colored Infrared-Transparent Polyethylene Textiles. Joule 3, 1478–1486. https://doi.org/10.1016/j.joule.2019.03.015

Campbell, I., Kalanki, A., Sachar, S., n.d. How to Counter the Climate Threat from Room Air Conditioners.

Cao, C., Gao, Y., Luo, H., 2008. Pure Single-Crystal Rutile Vanadium Dioxide Powders: Synthesis, Mechanism and Phase-Transformation Property. J. Phys. Chem. C 112, 18810–18814. https://doi.org/10.1021/jp8073688

Carlosena, L., Ruiz-Pardo, Á., Feng, J., Irulegi, O., Hernández-Minguillón, R.J., Santamouris, M., 2020. On the energy potential of daytime radiative cooling for urban heat island mitigation. Sol. Energy 208, 430–444. https://doi.org/10.1016/j.solener.2020.08.015

Case Studies [WWW Document], n.d. . SkyCool Syst. URL http://m2h.b9f.myftpupload.com/case-studies/ (accessed 1.3.21).

Catalanotti, S., Cuomo, V., Piro, G., Ruggi, D., Silvestrini, V., Troise, G., 1975. The Radiative Cooling of Selective Surfaces. Sol. Energy 17, 83–89. https://doi.org/10.1016/0038-092X(75)90062-6

Center For International Earth Science Information Network-CIESIN-Columbia University, 2016. [Dataset] Global Urban Heat Island (UHI) Data Set, 2013. https://doi.org/10.7927/H4H70CRF

Chen, Z., Zhu, L., Li, W., Fan, S., 2018. Simultaneously and Synergistically Harvest Energy from the Sun and Outer Space. Joule. https://doi.org/10.1016/j.joule.2018.10.009

Chen, Z., Zhu, L., Raman, A., Fan, S., 2016. Radiative cooling to deep sub-freezing temperatures through a 24-h day–night cycle. Nat. Commun. 7, 13729. https://doi.org/10.1038/ncomms13729

Cheng-Chia Tsai, Norman Nan Shi, Crystal Ren, Julianne Pelaez, Gary D. Bernard, Nanfang Yu, Naomi Pierce, 2017. Butterflies regulate wing temperatures using radiative cooling. Presented at the Proc.SPIE. https://doi.org/10.1117/12.2274297

Clemens, M., Weiland, T., 2001. Discrete Electromagnetism With the Finite Integration Technique - Abstract. J. Electromagn. Waves Appl. 15, 79–80. https://doi.org/10.1163/156939301X00661

COP25 • UN Climate Change Conference [WWW Document], 2020. . UN Clim. Change Conf. URL https://unclimatesummit.org/ (accessed 12.5.19).

Costanzo, V., Fabbri, K., Piraccini, S., 2018. Stressing the passive behavior of a Passivhaus: An evidence-based scenario analysis for a Mediterranean case study. Build. Environ. 142, 265–277. https://doi.org/10.1016/j.buildenv.2018.06.035

Cui, Y., Wang, Y., Huang, Q., Wei, S., 2016. Effect of radiation and convection heat transfer on cooling performance of radiative panel. Renew. Energy 99, 10–17. https://doi.org/10.1016/j.renene.2016.06.025

Daniels, K., 2003. Advanced Building Systems, A Technical Guide for Architects and Engineers. Birkhäuser, Berlin, Basel.

Eicker, U., Dalibard, A., 2011. Photovoltaic–thermal collectors for night radiative cooling of buildings. Sol. Energy 85, 1322–1335. https://doi.org/10.1016/j.solener.2011.03.015

Energy – UN-Habitat, n.d. URL https://unhabitat.org/urban-themes/energy/ (accessed 11.4.19).

Erell, E., Etzion, Y., 2000. Radiative cooling of buildings with flat-plate solar collectors. Build. Environ. 35, 297–305. https://doi.org/10.1016/S0360-1323(99)00019-0

Erell, E., Etzion, Y., 1999. Analysis and experimental verification of an improved cooling radiator. Renew. Energy 16, 700–703. https://doi.org/10.1016/S0960-1481(98)00255-9

Erell, E., Etzion, Y., 1996. Heating Experiments with a Radiative Cooling System. Build. Environ. 31, 509–517. https://doi.org/10.1016/0360-1323(96)00030-3

Erell, E., Etzion, Y., 1992. A Radiative Cooling System Using Water as a Heat Exchange Medium. Archit. Sci. Rev. 35, 39–49. https://doi.org/10.1080/00038628.1992.9696712

Erell, E., Yannas, S., Molina, J.L., 2006. Roof Cooling Techniques, in: The 23rd Conference on Passive and Low Energy Architecture. Presented at the PLEA2006, Geneva, Switzerland, pp. 175–191.

Eriksson, T.S., Granqvist, C.G., 1983. Infrared optical properties of electron-beam evaporated silicon oxynitride films. Appl. Opt. 22, 3204. https://doi.org/10.1364/AO.22.003204

Eriksson, T.S., Jiang, S.-J., Granqvist, C.. G., 1985. Surface coatings for radiative cooling applications: Silicon dioxide and silicon nitride made by reactive rf-sputtering. Sol. Energy Mater. 12, 319–325. https://doi.org/10.1016/0165-1633(85)90001-2

European Commission, 2011. Communication from the Commission to the European Parliament, the Council, the European Economic and Social Committee and the Committee of the Regions- Energy Roadmap 2050.

European Parliament, Council of the European Union, 2016. Commission Regulation (EU) 2016/2281 of 30 November 2016 implementing Directive 2009/125/EC of the European Parliament and of the Council establishing a framework for the setting of ecodesign requirements for energy-related products, with regard to ecodesign requirements for air heating products, cooling products, high temperature process chillers and fan coil units (Text with EEA relevance), OJ L.

European Union, 2016. Regulations, Directives and other acts [WWW Document]. Eur. Union. URL https://europa.eu/european-union/eu-law/legal-acts_en (accessed 5.20.20).

Ezekwe, C.I., 1990. Performance of a heat pipe assisted night sky radiative cooler. Energy Convers. Manag. 30, 403–408. https://doi.org/10.1016/0196-8904(90)90041-V

Ezekwe, C.I., 1986. Nocturnal radiation measurements in Nigeria. Sol. Energy 37, 1–6. https://doi.org/10.1016/0038-092X(86)90100-3

Fabian, M., Lewis, E., Newe, T., Lochmann, S., 2010. Optical fibre cavity for ring-down experiments with low coupling losses. Meas. Sci. Technol. 21, 094034. https://doi.org/10.1088/0957-0233/21/9/094034

Fabiani, C., Pisello, A.L., Bou-Zeid, E., Yang, J., Cotana, F., 2019. Adaptive measures for mitigating urban heat islands: The potential of thermochromic materials to control roofing energy balance. Appl. Energy 247, 155–170. https://doi.org/10.1016/j.apenergy.2019.04.020

Family, R., Mengüç, M.P., 2017. Materials for Radiative Cooling: A Review. Procedia Environ. Sci., Sustainable synergies from Buildings to the Urban Scale 38, 752–759. https://doi.org/10.1016/j.proenv.2017.03.158

Fan, S., 2017. Thermal Photonics and Energy Applications. Joule 1, 264–273. https://doi.org/10.1016/j.joule.2017.07.012

Feng, J., Gao, K., Santamouris, M., Shah, K.W., Ranzi, G., 2020a. Dynamic impact of climate on the performance of daytime radiative cooling materials. Sol. Energy Mater. Sol. Cells 208, 110426. https://doi.org/10.1016/j.solmat.2020.110426

Feng, J., Santamouris, M., 2019. Numerical techniques for electromagnetic simulation of daytime radiative cooling: A review. Mater. 2019 Vol 6 Pages 1049-1064. https://doi.org/10.3934/matersci.2019.6.1049

Feng, J., Santamouris, M., Gao, K., 2020b. The radiative cooling efficiency of silica sphere embedded polymethylpentene (TPX) systems. Sol. Energy Mater. Sol. Cells 215, 110671. https://doi.org/10.1016/j.solmat.2020.110671

Fernandez, N., Wang, W., Alvine, K.J., Katipamula, S., 2015. Energy Savings Potential of Radiative Cooling Technologies (No. PNNL--24904, 1234791). Pacific Northwest National Laboratory (PNNL), Richland, WA (US). https://doi.org/10.2172/1234791

Ferrer Tevar, J.A., Castaño, S., Garrido Marijuán, A., Heras, M.R., Pistono, J., 2015. Modelling and experimental analysis of three radioconvective panels for night cooling. Energy Build. 107, 37–48. https://doi.org/10.1016/j.enbuild.2015.07.027

Fiorito, F., Santamouris, M., 2017. High performance technologies and the future of architectural design. TECHNE 13, 72–76. https://doi.org/10.13128/Techne-2113

Founda, D., Santamouris, M., 2017. Synergies between Urban Heat Island and Heat Waves in Athens (Greece), during an extremely hot summer (2012). Sci. Rep. 7. https://doi.org/10.1038/s41598-017-11407-6

Foustalieraki, M., Assimakopoulos, M.N., Santamouris, M., Pangalou, H., 2017. Energy performance of a medium scale green roof system installed on a commercial building using numerical and experimental data recorded during the cold period of the year. Energy Build. 135, 33–38. https://doi.org/10.1016/j.enbuild.2016.10.056

Fujishima, A., Zhang, X., Tryk, D.A., 2008. TiO2 photocatalysis and related surface phenomena. Surf. Sci. Rep. 63, 515–582. https://doi.org/10.1016/j.surfrep.2008.10.001

Gad, S.E., 2014. Polymers, in: Wexler, P. (Ed.), Encyclopedia of Toxicology (Third Edition). Academic Press, Oxford, pp. 1045–1050. https://doi.org/10.1016/B978-0-12-386454-3.00912-X

Gao, K., Santamouris, M., Feng, J., 2020. On the Efficiency of Using Transpiration Cooling to Mitigate Urban Heat. Climate 8, 69. https://doi.org/10.3390/cli8060069

Garshasbi, S., Haddad, S., Paolini, R., Santamouris, M., Papangelis, G., Dandou, A., Methymaki, G., Portalakis, P., Tombrou, M., 2020a. Urban mitigation and building adaptation to minimize the future cooling energy needs. Sol. Energy 204, 708–719. https://doi.org/10.1016/j.solener.2020.04.089

Garshasbi, S., Huang, S., Valenta, J., Santamouris, M., 2020b. Can quantum dots help to mitigate urban overheating? An experimental and modelling study. Sol. Energy 206, 308–316. https://doi.org/10.1016/j.solener.2020.06.010

Garshasbi, S., Santamouris, M., 2019. Using advanced thermochromic technologies in the built environment: Recent development and potential to decrease the energy consumption and fight urban overheating. Sol. Energy Mater. Sol. Cells 191, 21–32. https://doi.org/10.1016/j.solmat.2018.10.023

Gentle, A.R., Dybdal, K.L., Smith, G.B., 2013. Polymeric mesh for durable infra-red transparent convection shields: Applications in cool roofs and sky cooling. Sol. Energy Mater. Sol. Cells 115, 79–85. https://doi.org/10.1016/j.solmat.2013.03.001

Gentle, A.R., Smith, G., 2010a. Performance comparisons of sky window spectral selective and high emittance radiant cooling systems under varying atmospheric conditions. Canberra, ACT, Australia.

Gentle, A.R., Smith, G.B., 2015. A Subambient Open Roof Surface under the Mid-Summer Sun. Adv. Sci. 2. https://doi.org/10.1002/advs.201500119

Gentle, A.R., Smith, G.B., 2010b. Radiative Heat Pumping from the Earth Using Surface Phonon Resonant Nanoparticles. Nano Lett. 10, 373–379. https://doi.org/10.1021/nl903271d

Geoff B. Smith, 2011. Green nanotechnology. Presented at the Proc.SPIE. https://doi.org/10.1117/12.893114

Giuseppe, E.D., D'Orazio, M., 2015. Assessment of the effectiveness of cool and green roofs for the mitigation of the Heat Island effect and for the improvement of thermal comfort in Nearly Zero Energy Building. Archit. Sci. Rev. 58, 134–143. https://doi.org/10.1080/00038628.2014.966050

Gjessing, J., 2011. Photonic crystals for light trapping in solar cells. University of Oslo.

Goldstein, E.A., Raman, A.P., Fan, S., 2017. Sub-ambient non-evaporative fluid cooling with the sky. Nat. Energy 2, nenergy2017143. https://doi.org/10.1038/nenergy.2017.143

Goodenough, J.B., 1971. The two components of the crystallographic transition in VO2. J. Solid State Chem. 3, 490–500. https://doi.org/10.1016/0022-4596(71)90091-0

Granqvist, C., Niklasson, G., 2016. Thermochromic Oxide-Based Thin Films and Nanoparticle Composites for Energy-Efficient Glazings. Buildings 7, 3. https://doi.org/10.3390/buildings7010003

Granqvist, C.G., 2015. 16 - Fenestration for reducing building cooling needs: an introduction to spectral selectivity, thermochromics, and electrochromics, in: Pacheco-Torgal, F., Labrincha, J.A., Cabeza, L.F., Granqvist, C.-G. (Eds.), Eco-Efficient Materials for Mitigating Building Cooling Needs. Woodhead Publishing, Oxford, pp. 441–471. https://doi.org/10.1016/B978-1-78242-380-5.00016-9

Granqvist, C.G., 1981. Radiative heating and cooling with spectrally selective surfaces. Appl. Opt. 20, 2606. https://doi.org/10.1364/AO.20.002606

Granqvist, C.G., Hjortsberg, A., 1981. Radiative cooling to low temperatures: General considerations and application to selectively emitting SiO films. J. Appl. Phys. 52, 4205–4220. https://doi.org/10.1063/1.329270

Granqvist, C.G., Lansåker, P.C., Mlyuka, N.R., Niklasson, G.A., Avendaño, E., 2009. Progress in chromogenics: New results for electrochromic and thermochromic materials and devices. Sol. Energy Mater. Sol. Cells, IME-8 93, 2032–2039. https://doi.org/10.1016/j.solmat.2009.02.026

Granqvist, C.G., Niklasson, G.A., 2018. Solar energy materials for thermal applications: A primer. Sol. Energy Mater. Sol. Cells 180, 213–226. https://doi.org/10.1016/j.solmat.2018.02.004

Guadarrama-Cetina, J., Mongruel, A., Medici, M.-G., Baquero, E., Parker, A.R., Milimouk-Melnytchuk, I., González-Viñas, W., Beysens, D., 2014. Dew condensation on desert beetle skin. Eur. Phys. J. E 37, 109. https://doi.org/10.1140/epje/i2014-14109-y

Harlan Sharon L., Declet-Barreto Juan H., Stefanov William L., Petitti Diana B., 2013. Neighborhood Effects on Heat Deaths: Social and Environmental Predictors of Vulnerability in Maricopa County, Arizona. Environ. Health Perspect. 121, 197–204. https://doi.org/10.1289/ehp.1104625

Harrison, A.W., Walton, M.R., 1978. Radiative cooling of TiO2 white paint. Sol. Energy 20, 185–188. https://doi.org/10.1016/0038-092X(78)90195-0

Heltzel, A., 2017. Composite Material for Passive Radiative Cooling. United States Patent Application 20170350663 Kind Code: A1.

Herrera-Gomez, S.S., Quevedo-Nolasco, A., Pérez-Urrestarazu, L., 2017. The role of green roofs in climate change mitigation. A case study in Seville (Spain). Build. Environ. 123, 575–584. https://doi.org/10.1016/j.buildenv.2017.07.036

Herrero, J, Polo, M.J., 2012. Hydrology and Earth System Sciences Parameterization of atmospheric longwave emissivity in a mountainous site for all sky conditions. Hydrol Earth Syst Sci 16, 3139–3147. https://doi.org/10.5194/hess-16-3139-2012

Herrero, J., Polo, M.J., 2012. Parameterization of atmospheric longwave emissivity in a mountainous site for all sky conditions. Hydrol. Earth Syst. Sci. 16, 3139–3147. https://doi.org/10.5194/hess-16-3139-2012

Hervé, A., Drévillon, J., Ezzahri, Y., Joulain, K., 2018. Radiative cooling by tailoring surfaces with microstructures: Association of a grating and a multi-layer structure. J. Quant. Spectrosc. Radiat. Transf. 221, 155–163. https://doi.org/10.1016/j.jqsrt.2018.09.015

Hirata, A., Kohara, S., Asada, T., Arao, M., Yogi, C., Imai, H., Tan, Y., Fujita, T., Chen, M., 2016. Atomic-scale disproportionation in amorphous silicon monoxide. Nat. Commun. 7, 11591. https://doi.org/10.1038/ncomms11591

Hjortsberg, A., Granqvist, C.G., 1980. Infrared optical properties of silicon monoxide films. Appl. Opt. 19, 1694. https://doi.org/10.1364/AO.19.001694

Hossain, Md.M., Gu, M., 2016. Radiative Cooling: Principles, Progress, and Potentials. Adv. Sci. 3, 1500360. https://doi.org/10.1002/advs.201500360

Hossain, M.M., Jia, B., Gu, M., 2015. A Metamaterial Emitter for Highly Efficient Radiative Cooling. Adv. Opt. Mater. 3, 1047–1051. https://doi.org/10.1002/adom.201500119

Hosseini, B., Namazian, A., 2012. An Overview of Iranian Ice Repositories, an Example of Traditional Indigenous Architecture. METU J. Fac. Archit. https://doi.org/10.4305/METU.JFA.2012.2.10

Hosseinzadeh, E., Taherian, H., 2012. An Experimental and Analytical Study of a Radiative Cooling System with Unglazed Flat Plate Collectors. Int. J. Green Energy 9, 766–779. https://doi.org/10.1080/15435075.2011.641189

Huang, Z., Ruan, X., 2017. Nanoparticle embedded double-layer coating for daytime radiative cooling. Int. J. Heat Mass Transf. 104, 890–896. https://doi.org/10.1016/j.ijheatmasstransfer.2016.08.009

IEA, 2020a. CO2 Emissions from Fuel Combustion [WWW Document]. Int. Energy Agency. URL https://www.iea.org/subscribe-to-data-services/co2-emissions-statistics

IEA, 2020b. Tracking Buildings – Analysis [WWW Document]. Int. Energy Agency. URL https://www.iea.org/reports/tracking-buildings (accessed 5.27.20).

IEA, 2020c. Policy coverage of total final energy consumption in buildings, 2000-2018 – Charts – Data & Statistics [WWW Document]. Int. Energy Agency. URL https://www.iea.org/data-and-statistics/charts/policy-coverage-of-total-final-energy-consumption-in-buildings-2000-2018 (accessed 9.19.20).

IEA, 2019a. Final energy consumption by sector in the OECD, 1990-2017 – Charts – Data & Statistics [WWW Document]. Int. Energy Agency. URL https://www.iea.org/data-and-statistics/charts/final-energy-consumption-by-sector-in-the-oecd-1990-2017 (accessed 9.19.20).

IEA, 2019b. Percentage of households equiped with AC in selected countries, 2018 – Charts – Data & Statistics [WWW Document]. Int. Energy Agency. URL https://www.iea.org/data-and-statistics/charts/percentage-of-households-equiped-with-ac-in-selected-countries-2018 (accessed 9.19.20).

IEA, 2019c. Global air conditioner stock, 1990-2050 – Charts – Data & Statistics [WWW Document]. Int. Energy Agency. URL https://www.iea.org/data-and-statistics/charts/global-air-conditioner-stock-1990-2050 (accessed 9.19.20).

IEA, 2018a. The Future of Cooling: Opportunities for energy-efficient air conditioning. International Energy Agency.

IEA, 2018b. World Energy Outlook 2018. Executive Summary. International Energy Agency.

IEA, n.d. Policy database – Data & Statistics [WWW Document]. Int. Energy Agency. URL https://www.iea.org/policies (accessed 6.18.20).

IPCC, 2018. Global warming of 1.5°C An IPCC Special Report on the impacts of global warming of 1.5°C above pre-industrial levels and related global greenhouse gas emission pathways, in the context of strengthening the global response to the threat of climate change, sustainable development, and efforts to eradicate poverty.

IRENA, 2020a. Renewable power generation costs in 2019.

IRENA, 2020b. Renewable Capacity Statistics 2020. International Renewable Energy Agency, Abu Dhabi.

Ito, S., Miura, N., 1989. Studies of Radiative Cooling Systems for Storing Thermal Energy. J. Sol. Energy Eng. 111, 251. https://doi.org/10.1115/1.3268315

Jaramillo-Fernandez, J., Whitworth, G.L., Pariente, J.A., Blanco, A., Garcia, P.D., Lopez, C., Sotomayor-Torres, C.M., 2019. A Self-Assembled 2D Thermofunctional Material for Radiative Cooling. Small 0, 1905290. https://doi.org/10.1002/smll.201905290

Jin, P., Tazawa, M., Yoshimura, K., Miki, T., Igarashi, K., Tanemura, S., 1994. Thermochromism of metal-doped VO2 films deposited by dual-target sputtering, in: Wittwer, V., Granqvist, C.G., Lampert, C.M. (Eds.), . Presented at the Optical Materials Technology for Energy Efficiency and Solar Energy Conversion XIII, Freiburg, Federal Republic of Germany, pp. 415–422. https://doi.org/10.1117/12.185384

Johnson, K.C., 2005. GD-Calc [WWW Document]. KJ Innov. URL https://kjinnovation.com/ (accessed 12.5.20).

Jorgenson, G.V., Lee, J.C., 1986. Doped vanadium oxide for optical switching films. Sol. Energy Mater. 14, 205–214. https://doi.org/10.1016/0165-1633(86)90047-X

José, R.S., Pérez, J.L., Pérez, L., Gonzalez Barras, R.M., Pecci, J., Palacios, M., 2017. Climate Change Effects on Urban Level: Citizen Health and Building Energy Demand. ISPRS - Int. Arch. Photogramm. Remote Sens. Spat. Inf. Sci. XLII-3/W2, 83–89. https://doi.org/10.5194/isprs-archives-XLII-3-W2-83-2017

Kanu, S.S., Binions, R., 2010. Thin films for solar control applications. Proc. R. Soc. Math. Phys. Eng. Sci. 466, 19–44. https://doi.org/10.1098/rspa.2009.0259

Karlessi, T., Santamouris, M., 2013. Improving the performance of thermochromic coatings with the use of UV and optical filters tested under accelerated aging conditions. Int. J. Low-Carbon Technol. 10, 45–61. https://doi.org/10.1093/ijlct/ctt027

Karlessi, T., Santamouris, M., Apostolakis, K., Synnefa, A., Livada, I., 2009. Development and testing of thermochromic coatings for buildings and urban structures. Sol. Energy 83, 538–551. https://doi.org/10.1016/j.solener.2008.10.005

Kazemi, A.G., Shirvani, A.H., 2011. An Overview of Some Vernacular Techniques in Iranian Sustainable Architecture in Reference to Cisterns and Ice Houses. J. Sustain. Dev. 4, 264. https://doi.org/10.5539/jsd.v4n1p264

Kecebas, M.A., Menguc, M.P., Kosar, A., Sendur, K., 2017. Passive radiative cooling design with broadband optical thin-film filters. J. Quant. Spectrosc. Radiat. Transf. 198, 179–186. https://doi.org/10.1016/j.jqsrt.2017.03.046

Kelly, F.J., 1965. On kirchhoff's law and its generalized application to absorption andemission by cavities. J. Res. Natl. Bur. Stand. BMathematics Adn Math. Phys. 69B, 165–171. https://doi.org/10.2514/6.1965-135

Kirk, C.T., 1988. Quantitative analysis of the effect of disorder-induced mode coupling on infrared absorption in silica. Phys. Rev. B 38, 1255–1273. https://doi.org/10.1103/PhysRevB.38.1255

Ko, B., Lee, D., Badloe, T., Rho, J., 2018. Metamaterial-Based Radiative Cooling: Towards Energy-Free All-Day Cooling. Energies 12, 89. https://doi.org/10.3390/en12010089

Kolokotroni, M., Gowreesunker, B.L., Giridharan, R., 2013. Cool roof technology in London: An experimental and modelling study. Energy Build. 67, 658–667. https://doi.org/10.1016/j.enbuild.2011.07.011

Kolokotroni, M., Ren, X., Davies, M., Mavrogianni, A., 2012. London's urban heat island: Impact on current and future energy consumption in office buildings. Energy Build. 47, 302–311. https://doi.org/10.1016/j.enbuild.2011.12.019

Kolokotsa, D.– D., Giannariakis, G., Gobakis, K., Giannarakis, G., Synnefa, A., Santamouris, M., 2018. Cool roofs and cool pavements application in Acharnes, Greece. Sustain. Cities Soc. 37, 466–474. https://doi.org/10.1016/j.scs.2017.11.035

Kolokotsa, D., Santamouris, M., Zerefos, S.C., 2013. Green and cool roofs' urban heat island mitigation potential in European climates for office buildings under free floating conditions. Sol. Energy 95, 118–130. https://doi.org/10.1016/j.solener.2013.06.001

Kottek, M., Grieser, J., Beck, C., Rudolf, B., Rubel, F., 2006. World Map of the Köppen-Geiger climate classification updated. Meteorol. Z. 259–263. https://doi.org/10.1127/0941-2948/2006/0130

Kou, J., Jurado, Z., Chen, Z., Fan, S., Minnich, A.J., 2017. Daytime Radiative Cooling Using Near-Black Infrared Emitters. ACS Photonics 4, 626–630. https://doi.org/10.1021/acsphotonics.6b00991

Kousis, I., Fabiani, C., Gobbi, L., Pisello, A.L., 2020. Phosphorescent-based pavements for counteracting urban overheating – A proof of concept. Sol. Energy 202, 540–552. https://doi.org/10.1016/j.solener.2020.03.092

Laatioui, S., Benlattar, M., Mazroui, M., Saadouni, K., 2018. Zinc monochalcogenide thin films ZnX (X = S, Se, Te) as radiative cooling materials. Optik 166, 24–30. https://doi.org/10.1016/j.ijleo.2018.04.004

Landro, B., McCormick, P.G., 1980. Effect of surface characteristics and atmospheric conditions on radiative heat loss to a clear sky. Int. J. Heat Mass Transf. 23, 613–620. https://doi.org/10.1016/0017-9310(80)90004-6

Lemonsu, A., Viguié, V., Daniel, M., Masson, V., 2015. Vulnerability to heat waves: Impact of urban expansion scenarios on urban heat island and heat stress in Paris (France). Urban Clim. 14, 586–605. https://doi.org/10.1016/j.uclim.2015.10.007

Li, J., Georgescu, M., Hyde, P., Mahalov, A., Moustaoui, M., 2014. Achieving accurate simulations of urban impacts on ozone at high resolution. Environ. Res. Lett. 9, 114019. https://doi.org/10.1088/1748-9326/9/11/114019

Li, M., Coimbra, C.F.M., 2019. On the effective spectral emissivity of clear skies and the radiative cooling potential of selectively designed materials. Int. J. Heat Mass Transf. 135, 1053–1062. https://doi.org/10.1016/J.IJHEATMASSTRANSFER.2019.02.040

Li, M., Peterson, H.B., Coimbra, C.F.M., 2019. Radiative cooling resource maps for the contiguous United States. J. Renew. Sustain. Energy 11, 036501. https://doi.org/10.1063/1.5094510

Li, W., Fan, S., 2019. Radiative Cooling: Harvesting the Coldness of the Universe. Opt. Photonics News 30, 32–39. https://doi.org/10.1364/OPN.30.11.000032

Li, W., Fan, S., 2018. Nanophotonic control of thermal radiation for energy applications [Invited]. Opt. Express 26, 15995. https://doi.org/10.1364/OE.26.015995

Li, W., Shi, Y., Chen, K., Zhu, L., Fan, S., 2017. A Comprehensive Photonic Approach for Solar Cell Cooling. ACS Photonics 4, 774–782. https://doi.org/10.1021/acsphotonics.7b00089

Liu, C., Wu, Y., Wang, B., Zhao, C.Y., Bao, H., 2019. Effect of atmospheric water vapor on radiative cooling performance of different surfaces. Sol. Energy 183, 218–225. https://doi.org/10.1016/j.solener.2019.03.011

Liu, J., Zhou, Z., Zhang, J., Feng, W., Zuo, J., 2019. Advances and Challenges in Commercializing Radiative Cooling. Mater. Today Phys. 100161. https://doi.org/10.1016/j.mtphys.2019.100161

Lo, C.P., Quattrochi, D.A., 2003. Land-Use and Land-Cover Change, Urban Heat Island Phenomenon, and Health Implications: A Remote Sensing Approach. Photogramm. Eng. 11. https://doi.org/info:doi/10.14358/PERS.69.9.1053

Lu, X., Xu, P., Wang, H., Yang, T., Hou, J., 2016. Cooling potential and applications prospects of passive radiative cooling in buildings: The current state-of-the-art. Renew. Sustain. Energy Rev. 65, 1079–1097. https://doi.org/10.1016/j.rser.2016.07.058

Mahdavinejad, M., Javanrudi, K., 2012. Assessment of Ancient Fridges: A Sustainable Method to Storage Ice in Hot-Arid Climates. Asian Cult. Hist. 4. https://doi.org/10.5539/ach.v4n2p133

Malek, E., 1997. Evaluation of effective atmospheric emissivity and parameterization of cloud at local scale. Atmospheric Res. 45, 41–54. https://doi.org/10.1016/S0169-8095(97)00020-3

Mandal, J., Fu, Y., Overvig, A., Jia, M., Sun, K., Shi, N., Zhou, H., Xiao, X., Yu, N., Yang, Y., 2018. Hierarchically porous polymer coatings for highly efficient passive daytime radiative cooling. Science eaat9513. https://doi.org/10.1126/science.aat9513

Manoli, G., Fatichi, S., Schläpfer, M., Yu, K., Crowther, T.W., Meili, N., Burlando, P., Katul, G.G., Bou-Zeid, E., 2019. Magnitude of urban heat islands largely explained by climate and population. Nature 573, 55–60. https://doi.org/10.1038/s41586-019-1512-9

Martin, M., Berdahl, P., 1984. Characteristics of infrared sky radiation in the United States. Sol. Energy 33, 321–336. https://doi.org/10.1016/0038-092X(84)90162-2

Materiales inteligentes, S.L. [WWW Document], 2020. . Intel. Mater. Intel. URL https://www.inteligentes.org/ (accessed 8.26.20).

Matsuta, M., Terada, S., Ito, H., 1987. Solar heating and radiative cooling using a solar collector-sky radiator with a spectrally selective surface. Sol. Energy 39, 183–186. https://doi.org/10.1016/S0038-092X(87)80026-9

Meir, M.G., Rekstad, J.B., LØvvik, O.M., 2002. A Study of a Polymer-based Radiative Cooling System. Sol. Energy 73, 403–417.

Meteonorm 7, 2017. . Meteotest, Bern, Switzerland.

Michell, D., Biggs, K.L., 1979. Radiation cooling of buildings at night. Appl. Energy 5, 263–275. https://doi.org/10.1016/0306-2619(79)90017-5

Miller, W., Crompton, G., Bell, J., 2015. Analysis of Cool Roof Coatings for Residential Demand Side Management in Tropical Australia. Energies 8, 5303–5318. https://doi.org/10.3390/en8065303

Mirsadeghi, M., Cóstola, D., Blocken, B., Hensen, J.L.M., 2013. Review of external convective heat transfer coefficient models in building energy simulation programs: Implementation and uncertainty. Appl. Therm. Eng. 56, 134–151. https://doi.org/10.1016/j.applthermaleng.2013.03.003

Moharam, M.G., Gaylord, T.K., 1981. Rigorous coupled-wave analysis of planar-grating diffraction. JOSA 71, 811–818. https://doi.org/10.1364/JOSA.71.000811

Molina, J.L., Erell, E., Yannas, S., 2013. Roof Cooling Techniques: A Design Handbook. Routledge.

Montagnino, F.M., 2018. Renewable-energy-based Air Conditioning Systems, in: Cooling Energy Solutions For Buildings And Cities. World Scientific Publishing Company, Singapore, SINGAPORE.

Monteith, J.L., Unsworth, M.H., 2013. Principles of Environmental Physics. Plants, Animals, and the Atmosphere, Fourth. ed. Elsevier.

Munck, C. de, Pigeon, G., Masson, V., Meunier, F., Bousquet, P., Tréméac, B., Merchat, M., Poeuf, P., Marchadier, C., 2013. How much can air conditioning increase air temperatures for a city like Paris, France? Int. J. Climatol. 33, 210–227. https://doi.org/10.1002/joc.3415

Narayanaswamy, A., Mayo, J., Canetta, C., 2014. Infrared selective emitters with thin films of polar materials. Appl. Phys. Lett. 104, 183107. https://doi.org/10.1063/1.4875699

Nilsson, N.A., Eriksson, T.S., Granqvist, C.G., 1985. Infrared-transparent convection shields for radiative cooling: Initial results on corrugated polyethylene foils. Sol. Energy Mater. 12, 327–333. https://doi.org/10.1016/0165-1633(85)90002-4

Nilsson, T.M.J., Niklasson, G.A., Granqvist, C.G., 1992. A solar reflecting material for radiative cooling applications: ZnS pigmented polyethylene. Sol. Energy Mater. Sol. Cells 28, 175–193. https://doi.org/10.1016/0927-0248(92)90010-M

O'Brien, G.A., Ross, N.A., Strachan, I.B., 2019. The heat penalty of walkable neighbourhoods. Int. J. Biometeorol. https://doi.org/10.1007/s00484-018-01663-0

Oke, T.R., 1982. The energetic basis of the urban heat island. Q. J. R. Meteorol. Soc. 108, 1–24. https://doi.org/10.1002/qj.49710845502

Oke, T.R., 1973. City Size and the Urban Heat Island. Atmos. Environ. 7, 769–779.

Oke, T.R., Johnson, G.T., Steyn, D.G., Watson, I.D., 1991. Simulation of surface urban heat islands under 'ideal' conditions at night part 2: Diagnosis of causation. Bound.-Layer Meteorol. 56, 339–358. https://doi.org/10.1007/BF00119211

O'Neill, B.C., Dalton, M., Fuchs, R., Jiang, L., Pachauri, S., Zigova, K., 2010. Global demographic trends and future carbon emissions. Proc. Natl. Acad. Sci. U. S. A. 107, 17521–17526. https://doi.org/10.1073/pnas.1004581107

O'Neill, B.C., Liddle, B., Jiang, L., Smith, K.R., Pachauri, S., Dalton, M., Fuchs, R., 2012. Demographic change and carbon dioxide emissions. The Lancet 380, 157–164. https://doi.org/10.1016/S0140-6736(12)60958-1

Orel, B., Gunde, M.K., Krainer, A., 1993. Radiative cooling efficiency of white pigmented paints. Sol. Energy 50, 477–482. https://doi.org/10.1016/0038-092X(93)90108-Z

Paone, A., Sanjines, R., Jeanneret, P., Schüler, A., 2015. Temperature-dependent multiangle FTIR NIR–MIR ellipsometry of thermochromic VO2 and V1−xWxO2 films. Sol. Energy 118, 107–116. https://doi.org/10.1016/j.solener.2015.05.020

Parida, B., Iniyan, S., Goic, R., 2011. A review of solar photovoltaic technologies. Renew. Sustain. Energy Rev. 15, 1625–1636. https://doi.org/10.1016/j.rser.2010.11.032

Perez, G., Allegro, V.R., Corroto, M., Pons, A., Guerrero, A., 2018. Smart reversible thermochromic mortar for improvement of energy efficiency in buildings. Constr. Build. Mater. 186, 884–891. https://doi.org/10.1016/j.conbuildmat.2018.07.246

Phuong Dung Dan, Chinnappa, J.C.V., 1989. The cooling of water flowing over an inclined surface exposed to the night sky. Sol. Wind Technol. 6, 41–50. https://doi.org/10.1016/0741-983X(89)90036-2

Popovich, N., Migliozzi, B., Taylor, R., Williams, J., Watkins, D., 2018. How Much Hotter Is Your Hometown Than When You Were Born? N. Y. Times.

Prado, R.T.A., Ferreira, F.L., 2005. Measurement of albedo and analysis of its influence the surface temperature of building roof materials. Energy Build. 37, 295–300. https://doi.org/10.1016/j.enbuild.2004.03.009

Prieto, A., 2018. COOLFACADE – Architectural integration of solar cooling strategies in the building envelope. Delft University of Technology, Delft.

Psiloglou, B.E., Balaras, C.A., Santamouris, M., Asimakopoulos, D.N., 1996. Evaluation of Different Radiation and Albedo Models for the Prediction of Solar Radiation Incident on Tilted Surfaces, for Four European Locations. J. Sol. Energy Eng. 118, 183–189. https://doi.org/10.1115/1.2870939

Radhi, H., Sharples, S., Taleb, H., Fahmy, M., 2017. Will cool roofs improve the thermal performance of our built environment? A study assessing roof systems in Bahrain. Energy Build. 135, 324–337. https://doi.org/10.1016/j.enbuild.2016.11.048

Raeissi, S., Taheri, M., 2000. Skytherm: an approach to year-round thermal energy sufficient houses. Renew. Energy 19, 527–543. https://doi.org/10.1016/S0960-1481(99)00079-8

Raman, A.P., Anoma, M.A., Zhu, L., Rephaeli, E., Fan, S., 2014. Passive radiative cooling below ambient air temperature under direct sunlight. Nature 515, 540–544. https://doi.org/10.1038/nature13883

Rephaeli, E., Raman, A., Fan, S., 2013. Ultrabroadband Photonic Structures To Achieve High-Performance Daytime Radiative Cooling. Nano Lett. 13, 130311121615001. https://doi.org/10.1021/nl4004283

Ritchie, H., Roser, M., 2017. Renewable Energy. Our World Data.

Rosso, F., Fabiani, C., Chiatti, C., Pisello, A.L., 2019. Cool, photoluminescent paints towards energy consumption reductions in the built environment. J. Phys. Conf. Ser. 1343, 012198. https://doi.org/10.1088/1742-6596/1343/1/012198

Santamouris, M., 2020. Recent progress on urban overheating and heat island research. Integrated assessment of the energy, environmental, vulnerability and health impact. Synergies with the global climate change. Energy Build. 207, 109482. https://doi.org/10.1016/j.enbuild.2019.109482

Santamouris, M., 2019. Minimizing Energy Consumption, Energy Poverty and Global and Local Climate Change in the Built Environment: Innovating to Zero. Elsevier. https://doi.org/10.1016/C2016-0-01024-0

Santamouris, M., 2018. Cooling of Buildings: The New Energy Challenge, in: Cooling Energy Solutions For Buildings And Cities. World Scientific Publishing Company, Singapore, SINGAPORE.

Santamouris, M., 2016a. Cooling the buildings – past, present and future. Energy Build. 128, 617–638. https://doi.org/10.1016/j.enbuild.2016.07.034

Santamouris, M., 2016b. Innovating to zero the building sector in Europe: Minimising the energy consumption, eradication of the energy poverty and mitigating the local climate change. Sol. Energy, Special issue: Progress in Solar Energy 128, 61–94. https://doi.org/10.1016/j.solener.2016.01.021

Santamouris, M., 2015a. Analyzing the heat island magnitude and characteristics in one hundred Asian and Australian cities and regions. Sci. Total Environ. 512–513, 582–598. https://doi.org/10.1016/j.scitotenv.2015.01.060

Santamouris, M., 2015b. Regulating the damaged thermostat of the cities—Status, impacts and mitigation challenges. Energy Build. 91, 43–56. https://doi.org/10.1016/j.enbuild.2015.01.027

Santamouris, M., 2014. On the energy impact of urban heat island and global warming on buildings. Energy Build. 82, 100–113. https://doi.org/10.1016/j.enbuild.2014.07.022

Santamouris, M., 2013. Using cool pavements as a mitigation strategy to fight urban heat island—A review of the actual developments. Renew. Sustain. Energy Rev. 26, 224–240. https://doi.org/10.1016/j.rser.2013.05.047

Santamouris, M., Cartalis, C., Synnefa, A., Kolokotsa, D., 2015. On the impact of urban heat island and global warming on the power demand and electricity consumption of buildings—A review. Energy Build., Renewable Energy Sources and Healthy Buildings 98, 119–124. https://doi.org/10.1016/j.enbuild.2014.09.052

Santamouris, M., Ding, L., Fiorito, F., Oldfield, P., Osmond, P., Paolini, R., Prasad, D., Synnefa, A., 2016. Passive and active cooling for the outdoor built environment – Analysis and assessment of the cooling potential of mitigation technologies using performance data from 220 large scale projects. Sol. Energy 154, 14–33. https://doi.org/10.1016/j.solener.2016.12.006

Santamouris, M., Feng, J., 2018. Recent Progress in Daytime Radiative Cooling: Is It the Air Conditioner of the Future? Buildings 8, 168. https://doi.org/10.3390/buildings8120168

Santamouris, M., Fiorito, F., 2021. On the impact of modified urban albedo on ambient temperature and heat related mortality. Sol. Energy 216, 493–507. https://doi.org/10.1016/j.solener.2021.01.031

Santamouris, M., Haddad, S., Fiorito, F., Osmond, P., Ding, L., Prasad, D., Zhai, X., Wang, R., 2017. Urban Heat Island and Overheating Characteristics in Sydney, Australia. An Analysis of Multiyear Measurements. Sustainability 9, 712. https://doi.org/10.3390/su9050712

Santamouris, M., Haddad, S., Saliari, M., Vasilakopoulou, K., Synnefa, A., Paolini, R., Ulpiani, G., Garshasbi, S., Fiorito, F., 2018. On the energy impact of urban heat island in Sydney: Climate and energy potential of mitigation technologies. Energy Build. 166, 154–164. https://doi.org/10.1016/j.enbuild.2018.02.007

Santamouris, M., Kolokotsa, D., 2015. On the impact of urban overheating and extreme climatic conditions on housing, energy, comfort and environmental quality of vulnerable population in Europe. Energy Build., Renewable Energy Sources and Healthy Buildings 98, 125–133. https://doi.org/10.1016/j.enbuild.2014.08.050

Santamouris, M., Papanikolaou, N., Livada, I., Koronakis, I., Georgakis, C., Argiriou, A., Assimakopoulos, D.N., 2001. On the impact of urban climate on the energy consumption of buildings. Sol. Energy, Urban Environment 70, 201–216. https://doi.org/10.1016/S0038-092X(00)00095-5

Santamouris, M., Synnefa, A., Karlessi, T., 2011. Using advanced cool materials in the urban built environment to mitigate heat islands and improve thermal comfort conditions. Sol. Energy 85, 3085–3102. https://doi.org/10.1016/j.solener.2010.12.023

Santamouris, M., Synnefa, A., Kolokotsa, D., Dimitriou, V., Apostolakis, K., 2008. Passive cooling of the built environment - use of innovative reflective materials to fight heat islands and decrease cooling needs. Int. J. Low-Carbon Technol. 3, 71–82. https://doi.org/10.1093/ijlct/3.2.71

Santamouris, M., Yun, G.Y., 2020. Recent development and research priorities on cool and super cool materials to mitigate urban heat island. Renew. Energy 161, 792–807. https://doi.org/10.1016/j.renene.2020.07.109

Schinasi, L.H., Benmarhnia, T., De Roos, A.J., 2018. Modification of the association between high ambient temperature and health by urban microclimate indicators: A systematic review and meta-analysis. Environ. Res. 161, 168–180. https://doi.org/10.1016/j.envres.2017.11.004

Sharma, M., Whaley, M., Chamberlain, J., Oswald, T., Schroden, R., Graham, A., Barger, M., Richey, B., 2017. Evaluation of thermochromic elastomeric roof coatings for low-slope roofs. Energy Build. 155, 459–466. https://doi.org/10.1016/j.enbuild.2017.09.030

Shi, N.N., Tsai, C.-C., Camino, F., Bernard, G.D., Yu, N., Wehner, R., 2015. Keeping cool: Enhanced optical reflection and radiative heat dissipation in Saharan silver ants. Science 349, 298–301. https://doi.org/10.1126/science.aab3564

Shi, Y., Li, W., Raman, A., Fan, S., 2018. Optimization of Multilayer Optical Films with a Memetic Algorithm and Mixed Integer Programming. ACS Photonics 5, 684–691. https://doi.org/10.1021/acsphotonics.7b01136

Smith, G.B., 2009. Amplified radiative cooling via optimised combinations of aperture geometry and spectral emittance profiles of surfaces and the atmosphere. Sol. Energy Mater. Sol. Cells 93, 1696–1701. https://doi.org/10.1016/j.solmat.2009.05.015

Sugita, M., Brutsaert, W., 1993. Cloud effect in the estimation of instantaneous downward longwave radiation. Water Resour. Res. 29, 599–605. https://doi.org/10.1029/92WR02352

Sun, X., Sun, Y., Zhou, Z., Alam, M.A., Bermel, P., 2017. Radiative sky cooling: fundamental physics, materials, structures, and applications. Nanophotonics 6, 997–1015. https://doi.org/10.1515/nanoph-2017-0020

Synnefa, A., Saliari, M., Santamouris, M., 2012. Experimental and numerical assessment of the impact of increased roof reflectance on a school building in Athens. Energy Build., Cool Roofs, Cool Pavements, Cool Cities, and Cool World 55, 7–15. https://doi.org/10.1016/j.enbuild.2012.01.044

Synnefa, A., Santamouris, M., Akbari, H., 2007. Estimating the effect of using cool coatings on energy loads and thermal comfort in residential buildings in various climatic conditions. Energy Build. 39, 1167–1174. https://doi.org/10.1016/j.enbuild.2007.01.004

Taleghani, M., 2018. The impact of increasing urban surface albedo on outdoor summer thermal comfort within a university campus. Urban Clim. 24, 175–184. https://doi.org/10.1016/j.uclim.2018.03.001

Tazawa, M., Jin, P., Miki, T., Yoshimura, K., Igrashi, K., 2000. IR properties of SiO deposited on V1yxWxO2 thermochromic films by vacuum evaporation. Thin Solid Films 4.

Tazawa, M., Jin, P., Tanemura, S., 1996. Thin film used to obtain a constant temperature lower than the ambient. Thin Solid Films 281–282, 232–234. https://doi.org/10.1016/0040-6090(96)08620-8

Tazawa, M., Jin, P., Tanemura, S., 1995. Optical constants of V1-xWxO2 thermochromic films and their application to the selective radiating material, in: Optical Materials Technology for Energy Efficiency and Solar Energy Conversion XIV. Presented at the Optical Materials Technology for Energy Efficiency and Solar Energy Conversion XIV, International Society for Optics and Photonics, pp. 326–329. https://doi.org/10.1117/12.217341

Tazawa, M., Kakiuchida, H., Xu, G., Jin, P., Arwin, H., 2006. Optical constants of vacuum evaporated SiO film and an application. J. Electroceramics 16, 511–515. https://doi.org/10.1007/s10832-006-9908-y

the MOTHER EARTH NEWS editors, 1973. Steve Baer and Holly Baer: Dome Home Enthusiasts. Mother Earth News.

The Paris Agreement, 2015. . UNFCCC, Paris.

Trenberth, K.E., 2004. Earth's Energy Balance, in: Cleveland, C.J. (Ed.), Encyclopedia of Energy. Elsevier, New York, pp. 859–870. https://doi.org/10.1016/B0-12-176480-X/00050-2

Tso, C.Y., Chan, K.C., Chao, C.Y.H., 2017. A field investigation of passive radiative cooling under Hong Kong's climate. Renew. Energy 106, 52–61. https://doi.org/10.1016/j.renene.2017.01.018

Ulpiani, G., Ranzi, G., Feng, J., Santamouris, M., 2021. Expanding the applicability of daytime radiative cooling: Technological developments and limitations. Energy Build. 243, 110990. https://doi.org/10.1016/j.enbuild.2021.110990

Ulpiani, G., Ranzi, G., Shah, K.W., Feng, J., Santamouris, M., 2020. On the energy modulation of daytime radiative coolers: A review on infrared emissivity dynamic switch against overcooling. Sol. Energy 209, 278–301. https://doi.org/10.1016/j.solener.2020.08.077

UN Environment and International Energy Agency, 2018. Global Status Report: Towards a Zero-Emission, Efficient and Resilient Buildings and Construction Sector. UN Environment and International Energy Agency.

UN Environment and International Energy Agency, 2017. Global Status Report: Towards a Zero-Emission, Efficient, and Resilient Buildings and Construction Sector. UN Environment and International Energy Agency.

US Department of Commerce, N., n.d. Global Monitoring Laboratory - Carbon Cycle Greenhouse Gases [WWW Document]. URL https://www.esrl.noaa.gov/gmd/ccgg/trends/mlo.html (accessed 9.7.20).

Vall, S., Castell, A., 2017. Radiative cooling as low-grade energy source: A literature review. Renew. Sustain. Energy Rev. 77, 803–820. https://doi.org/10.1016/j.rser.2017.04.010

Vall, S., Castell, A., Medrano, M., 2018. Energy Savings Potential of a Novel Radiative Cooling and Solar Thermal Collection Concept in Buildings for Various World Climates. Energy Technol. 6, 2200–2209. https://doi.org/10.1002/ente.201800164

Vardoulakis, E., Karamanis, D., Fotiadi, A., Mihalakakou, G., 2013. The urban heat island effect in a small Mediterranean city of high summer temperatures and cooling energy demands. Sol. Energy 94, 128–144. https://doi.org/10.1016/j.solener.2013.04.016

Viguie, V., Lemonsu, A., Hallegatte, S., Beaulant, A.-L., Marchadier, C., Masson, V., Pigeon, G., Salagnac, J.-L., 2020. Early adaptation to heat waves and future reduction of air-conditioning energy use in Paris. Environ. Res. Lett. https://doi.org/10.1088/1748-9326/ab6a24

Voogt, J.A., Oke, T.R., 2003. Thermal remote sensing of urban climates. Remote Sens. Environ., Urban Remote Sensing 86, 370–384. https://doi.org/10.1016/S0034-4257(03)00079-8

Wang, W., Fernandez, N., Katipamula, S., Alvine, K., 2018. Performance assessment of a photonic radiative cooling system for office buildings. Renew. Energy 118, 265–277. https://doi.org/10.1016/j.renene.2017.10.062

Wang, Y., Li, Y., Sabatino, S.D., Martilli, A., Chan, P.W., 2018. Effects of anthropogenic heat due to air-conditioning systems on an extreme high temperature event in Hong Kong. Environ. Res. Lett. 13, 034015. https://doi.org/10.1088/1748-9326/aaa848

Weather in December 2013 in Palo Alto, California, USA [WWW Document], n.d. URL https://www.timeanddate.com/weather/usa/palo-alto/historic?month=12&year=2013 (accessed 6.26.19).

Weather Underground [WWW Document], n.d. URL https://www.wunderground.com/dashboard/pws/KAZCAVEC42/table/2017-10-16/2017-10-16/daily (accessed 6.26.19).

Wie du mit der Kälte des Weltraums kühlst [WWW Document], n.d. . Berl. Woche. URL https://www.berliner-woche.de/gatow/c-bauen/wie-du-mit-der-kaelte-des-weltraums-kuehlst_a184706 (accessed 9.19.19).

World Urbanization Prospects (No. ST/ESA/SER.A/366), 2014. . United Nations, Department of Economic and Social Affairs.

Wu, D., Liu, C., Xu, Z., Liu, Y., Yu, Z., Yu, L., Chen, L., Li, R., Ma, R., Ye, H., 2018. The design of ultra-broadband selective near-perfect absorber based on photonic structures to achieve near-ideal daytime radiative cooling. Mater. Des. 139, 104–111. https://doi.org/10.1016/j.matdes.2017.10.077

Xia, Z., fang, zhen, Zhang, Z., Shi, K., Meng, Z., 2020. An easy way to achieve the passive radiative materials' self-adaptive cooling. ACS Appl. Mater. Interfaces 12, acsami.0c05803. https://doi.org/10.1021/acsami.0c05803

Yang, J., Gao, X., Wu, Y., Zhang, T., Zeng, H., Li, X., 2020. Nanoporous silica microspheres–ploymethylpentene (TPX) hybrid films toward effective daytime radiative cooling. Sol. Energy Mater. Sol. Cells 206, 110301. https://doi.org/10.1016/j.solmat.2019.110301

Yang, Y., Taylor, S., Alshehri, H., Wang, L., 2017. Wavelength-selective and diffuse infrared thermal emission mediated by magnetic polaritons from silicon carbide metasurfaces. Appl. Phys. Lett. 111, 051904. https://doi.org/10.1063/1.4996865

Yang, Y., Zhang, Y., 2020. Passive daytime radiative cooling: Principle, application, and economic analysis. MRS Energy Sustain. 7, E18. https://doi.org/10.1557/mre.2020.18

Yellot, J.I., 1976. Early Tests of the "Skytherm" System. Presented at the Passive solar heating and cooling conference and workshop proceedings, Merily H. Keller, LASL, University of New Mexico, Albuquerque, New Mexico, pp. 54–62.

Yellot, John I., S., 1976. Solar Roof Ponds, "Early Tests of the 'Skytherm' System." Presented at the Passive solar heating and cooling conference and workshop proceedings, Merily H. Keller, LASL, University of New Mexico, Albuquerque, New Mexico, pp. 54–62.

Yi, Z., lv, Y., Xu, D., Xu, J., Qian, H., Zhao, D., Yang, R., 2020. A Transparent Radiative Cooling Film for Building Energy Saving. Energy Built Environ. https://doi.org/10.1016/j.enbenv.2020.07.003

Yin, C., Yuan, M., Lu, Y., Huang, Y., Liu, Y., 2018. Effects of urban form on the urban heat island effect based on spatial regression model. Sci. Total Environ. 634, 696–704. https://doi.org/10.1016/j.scitotenv.2018.03.350

Zeyghami, M., Goswami, D.Y., Stefanakos, E., 2018. A review of clear sky radiative cooling developments and applications in renewable power systems and passive building cooling. Sol. Energy Mater. Sol. Cells 178, 115–128. https://doi.org/10.1016/j.solmat.2018.01.015

Zhai, Y., Ma, Y., David, S., Zhao, D., Lou, R., Wu, C., Tan, G., Yang, R., Yin, X., 2017a. Large Scale Random Metamaterial for Effective Day-time Radiative Cooling, in: Conference on Lasers and Electro-Optics (2017), Paper JTh5B.5. Presented at the CLEO: QELS_Fundamental Science, Optical Society of America, p. JTh5B.5. https://doi.org/10.1364/CLEO_AT.2017.JTh5B.5

Zhai, Y., Ma, Y., David, S.N., Zhao, D., Lou, R., Tan, G., Yang, R., Yin, X., 2017b. Scalable-manufactured randomized glass-polymer hybrid metamaterial for daytime radiative cooling. Science 355, 1062–1066. https://doi.org/10.1126/science.aai7899

Zhang, H., Wu, Z., Wang, C., 2020. Comparative study of thermochromic properties on fresh and aged vanadium dioxide films. Vacuum 109462. https://doi.org/10.1016/j.vacuum.2020.109462

Zhang, K., Zhao, D., Yin, X., Yang, R., Tan, G., 2018. Energy saving and economic analysis of a new hybrid radiative cooling system for single-family houses in the USA. Appl. Energy 224, 371–381. https://doi.org/10.1016/j.apenergy.2018.04.115

Zhang, Y., Zhou, G., Lin, K., Zhang, Q., Di, H., 2007. Application of latent heat thermal energy storage in buildings: State-of-the-art and outlook. Build. Environ. 42, 2197–2209. https://doi.org/10.1016/j.buildenv.2006.07.023

Zhao, B., Hu, M., Ao, X., Chen, N., Pei, G., 2019. Radiative cooling: A review of fundamentals, materials, applications, and prospects. Appl. Energy 236, 489–513. https://doi.org/10.1016/j.apenergy.2018.12.018

Zhao, D., Aili, A., Yin, X., Tan, G., Yang, R., 2019a. Roof-integrated radiative air-cooling system to achieve cooler attic for building energy saving. Energy Build. 203, 109453. https://doi.org/10.1016/j.enbuild.2019.109453

Zhao, D., Aili, A., Zhai, Y., Xu, S., Tan, G., Yin, X., Yang, R., 2019b. Radiative sky cooling: Fundamental principles, materials, and applications. Appl. Phys. Rev. 6, 021306. https://doi.org/10.1063/1.5087281

Zhao, D., Martini, C.E., Jiang, S., Ma, Y., Zhai, Y., Tan, G., Yin, X., Yang, R., 2017. Development of a single-phase thermosiphon for cold collection and storage of radiative cooling. Appl. Energy 205, 1260–1269. https://doi.org/10.1016/j.apenergy.2017.08.057

Zheng, S., Xu, Y., Shen, Q., Yang, H., 2015. Preparation of thermochromic coatings and their energy saving analysis. Sol. Energy 112, 263–271. https://doi.org/10.1016/j.solener.2014.09.049

Zhou, L., Song, H., Liang, J., Singer, M., Zhou, M., Stegenburgs, E., Zhang, N., Ng, T.K., Yu, Z., Ooi, B., Gan, Q., 2019a. All-day radiative cooling using beam-controlled architectures, in: Conference on Lasers and Electro-Optics (2019), Paper ATh1I.2. Presented at the CLEO: Applications and Technology, Optical Society of America, p. ATh1I.2. https://doi.org/10.1364/CLEO_AT.2019.ATh1I.2

Zhou, L., Song, H., Liang, J., Singer, M., Zhou, M., Stegenburgs, E., Zhang, N., Xu, C., Ng, T., Yu, Z., Ooi, B., Gan, Q., 2019b. A polydimethylsiloxane-coated metal structure for all-day radiative cooling. Nat. Sustain. 2, 718–724. https://doi.org/10.1038/s41893-019-0348-5

Zhu, L., Fiorino, A., Thompson, D., Mittapally, R., Meyhofer, E., Reddy, P., 2019. Near-field photonic cooling through control of the chemical potential of photons. Nature 566, 239–244. https://doi.org/10.1038/s41586-019-0918-8

Zhu, L., Raman, A.P., Fan, S., 2015. Radiative cooling of solar absorbers using a visibly transparent photonic crystal thermal blackbody. Proc. Natl. Acad. Sci. 112, 12282–12287. https://doi.org/10.1073/pnas.1509453112

Zinzi, M., Agnoli, S., 2012. Cool and green roofs. An energy and comfort comparison between passive cooling and mitigation urban heat island techniques for residential buildings in the Mediterranean region. Energy Build. 55, 66–76. https://doi.org/10.1016/j.enbuild.2011.09.024

Zotero, 2006. . Center for History and New Media.

Zou, C., Ren, G., Hossain, M.M., Nirantar, S., Withayachumnankul, W., Ahmed, T., Bhaskaran, M., Sriram, S., Gu, M., Fumeaux, C., 2017. Metal-Loaded Dielectric Resonator Metasurfaces for Radiative Cooling. Adv. Opt. Mater. 5, 1700460. https://doi.org/10.1002/adom.201700460

LIST OF PUBLICATIONS

Published:

Carlosena, L., Ruiz-Pardo, Á., Feng, J., Irulegi, O., Hernández-Minguillón, R.J., Santamouris, M., 2020. On the energy potential of daytime radiative cooling for urban heat island mitigation. Sol. Energy 208, 430–444. https://doi.org/10.1016/j.solener.2020.08.015

Carlosena, L., Andueza, Á., Torres, L., Irulegi, O., Hernández-Minguillón, R.J., Sevilla, J., Santamouris, M., 2021. Experimental development and testing of low-cost scalable radiative cooling materials for building applications. Solar Energy Materials and Solar Cells 230, 111209. https://doi.org/10.1016/j.solmat.2021.111209

Solar Energy 208 (2020) 430–444

Contents lists available at ScienceDirect

Solar Energy

journal homepage: www.elsevier.com/locate/solener

On the energy potential of daytime radiative cooling for urban heat island mitigation

Laura Carlosena[a,b,d,*], Álvaro Ruiz-Pardo[c], Jie Feng[d], Olatz Irulegi[a], Rufino J. Hernández-Minguillón[a,b], Mattheos Santamouris[d,e]

[a] *Architecture Department, University of the Basque Country UPV/EHU, Plaza Oñati 2, 20018 San Sebastian, Spain*
[b] *Alonso Hernández & asociados arquitectura S.L., 31006 Pamplona, Spain*
[c] *Department of Thermal Machines and Engines, University of Cadiz, Av. Universidad de Cádiz, 10, 11519 Puerto Real, Spain*
[d] *Faculty of the Built Environment, University of New South Wales, Sydney, NSW 2052, Australia*
[e] *The Anita Lawrence Chair of High Performance Architecture, University of New South Wales, Sydney, NSW 2052, Australia*

ARTICLE INFO

Keywords:
Daytime radiative cooling
Sensitivity analysis
Spectrally selective materials
Cooling potential
Urban Heat Island

ABSTRACT

The objective of this paper is to present the potential of daytime radiative cooling materials as a strategy to mitigate the Urban Heat Island effect. To evaluate the cooling potential of daytime radiative cooling materials, 15 theoretical materials and seven existing materials were simulated: two radiative cooling materials, a cool-material, two white paints, a thermochromic paint and a construction material. The novelty of this study is that it shows that the optimal spectral characteristics of radiative cooling materials depending on the climate conditions and the type of application. A sensitivity analysis was performed to evaluate the impact of each wavelength emissivity on the ability to achieve sub-ambient radiative cooling. The sensitivity analysis comprised a total of 90 theoretical materials with 15 different wavelength combinations and 6 emissivity values. The heat transfer model, which includes conduction, convection, and radiation, was developed using a spectrally-selective sky model. Two conditions were considered: a very conductive surface and a highly insulated one. All the materials were simulated in two cities that suffer from the Urban Heat Island effect—Phoenix and Sydney. The mean surface temperature reduction achieved was 5.30 °C in Phoenix and 4.21 °C in Sydney. The results presented suggest that the type of application (active or passive) is a determinant factor in the design of radiative cooling materials. Modifying the spectra of the materials led to a substantial change in the cooling potential. A material that performs well in a dry climate as a passive solution could perform poorly as an active solution.

1. Introduction

Nowadays, half of the world's population lives in urban areas (World Urbanization Prospectsmz, 2014) and consumes 75% of the primary energy sources, emitting between 50 and 60% of greenhouse gases ("Energy – UN-Habitat," n.d.). Furthermore, the world's urban population is expected to increase by more than two-thirds by 2050, reaching 6.3 billion (World Urbanization Prospects, 2014), with nearly 90% of this rise taking place in cities across Asia and Africa. CO_2 emissions increase proportionately with population due to energy use (O'Neill et al., 2012). A 1% increase in the urban population is estimated to increase energy consumption by 2.2% (Santamouris et al., 2001). The global energy demand is predicted to increase by more than 25% if the IEA's New Policies Scenario (rising incomes and an extra 1.7 billion people) is followed (International Energy Agency, 2018).

Higher urban temperatures are due to the positive thermal balance of urban areas in comparison with rural areas, caused by (i) the significant release of anthropogenic heat, (ii) the excess storage of solar radiation by city structures, (iii) the lack of green spaces and cold sinks, (iv) the non-circulation of air in urban canyons, and (v) the reduced ability of emitted infrared radiation to escape into the atmosphere (Oke et al., 1991). This phenomenon, known as the Urban Heat Island (UHI), is well documented in more than 400 cities around the world (Santamouris, 2019), and the total number of reported cities is increasing rapidly. The average UHI varies between 0.5 °C and 7 °C, where 90% of the data is below 4.5 °C (Santamouris, 2020). As ambient air temperature increases, the carrying capacity of electric power cables decreases, a phenomenon that occurs more during the summer with the increase in electricity load caused by air-conditioning usage (Bartos et al., 2016).

---

* Corresponding author.
E-mail address: lcarlosena001@ikasle.ehu.eus (L. Carlosena).

https://doi.org/10.1016/j.solener.2020.08.015
Received 23 April 2020; Received in revised form 14 July 2020; Accepted 6 August 2020

Solar Energy Materials & Solar Cells 230 (2021) 111209

Contents lists available at ScienceDirect

Solar Energy Materials and Solar Cells

journal homepage: www.elsevier.com/locate/solmat

Experimental development and testing of low-cost scalable radiative cooling materials for building applications

Laura Carlosena [a,b,c,*], Ángel Andueza [d,e], Luis Torres [c], Olatz Irulegi [b], Rufino J. Hernández-Minguillón [b,c], Joaquín Sevilla [d,e], Mattheos Santamouris [f]

[a] Department of Engineering, Universidad Pública de Navarra, Campus de Arrosadía-31006, Pamplona, Navarra, Spain
[b] Architecture Department, University of the Basque Country UPV/EHU, Plaza Onati 2, 20018, San Sebastian, Spain
[c] Alonso Hernández & Asociados Arquitectura S.L., 31006, Pamplona, Spain
[d] Department of Electrical, Electronic and Communications Engineering, Universidad Pública de Navarra, Campus de Arrosadía-31006, Pamplona, Navarra, Spain
[e] Smart Cities Institute (SCI), Universidad Pública de Navarra, Campus de Arrosadía-31006, Pamplona, Navarra, Spain
[f] The Anita Lawrence Chair of High Performance Architecture, University of New South Wales, Sydney, NSW, 2052, Australia

ARTICLE INFO

Keywords:
Daytime radiative cooling
Spectrally selective materials
Scalable material development
Subambient cooling
Spray coating deposition

ABSTRACT

Urban overheating has a serious impact on building energy consumption. Daytime radiative cooling materials are an interesting passive solution for refrigeration. However, their costs and complex manufacturing hinder their current application. In this study, a series of scalable and lowcost daytime radiative cooling (DTRC) materials were designed, fabricated, and tested in a moderate climate (Cfb-Köppen-Geiger classification) and compared to aluminum and Vikuiti. The methodology was: i) material selection and design, (ii) optimization, (iii) fabrication, (iv) characterization, and (v) testing. The materials were fabricated using different substrates, aluminum and Vikuiti, and two kinds of formulations for the emissive layers based on silica-derived polymer polymethylsilsesquioxane (PMSQ) with embedded silica nanoparticles. The resulting aluminum DTRC materials had a mean solar reflectivity of 0.7 and 0.34 emissivity in the atmospheric window, the samples with Vikuiti had 0.97 and 0.89, respectively. During the experiment, the samples were exposed to different ambient conditions without a convection barrier and were contained in an extruded polystyrene board to eliminate conduction. The samples reached 7.32 °C and 9.13 °C maximum surface temperature reduction (below ambient) during the day and night, respectively. The samples with the commercial substrate achieved a mean reduction of 3.72 °C below ambient temperature. Although the aluminum samples did not achieve subambient cooling throughout the entire day, the emissive layer reduced the sample's surface temperature by an average of 1.7 °C. The PMSQ radiative cooling materials show great potential for future building applications. Suitability under different climates and experimental settings should be done to test broad applicability.

1. Introduction

Urban heat islands are the most documented phenomena of climate change. Urban overheating is associated with higher urban temperatures in the dense parts of the cities compared to the surrounding suburban or rural areas [1]. Overheating sources include the released anthropogenic heat, high absorption of solar radiation by the urban materials and structures, decreased airflow and urban ventilation, reduced evapotranspiration, and limited radiative losses [2]. The phenomenon is documented in more than 400 cities worldwide; the amplitude of urban overheating may range between 1 and 10 °C averaging 5 to 6 °C [3]. Synergies with the global climate change and heat waves further intensify the amplitude of urban overheating [4].

Urban overheating has a serious impact on the cooling energy consumption of buildings, outdoor pollution levels, heat related mortality and morbidity, urban ecological footprint and survivability levels [5]. It is reported that urban overheating rises the peak electricity load varies between 0.45% and 4.6%, equivalent to an electricity penalty of about 21 (±10.4) W per degree of temperature increase and per person [6]. Moreover, the additional energy penalty induced by urban overheating is close to 0.74 kWh/m^2/C, while the Global Energy Penalty per person is close to 237, (±130) kWh/p [7]. In parallel, recent research has found

---

[*] Corresponding author. Department of Engineering, Universidad Pública de Navarra, Campus de Arrosadía-31006, Pamplona, Navarra, Spain.
E-mail address: laura.carlosena@unavarra.es (L. Carlosena).

https://doi.org/10.1016/j.solmat.2021.111209
Received 11 February 2021; Received in revised form 22 April 2021; Accepted 27 May 2021
Available online 11 June 2021
0927-0248/

APPENDIX 1: Research overview methodology

Two kinds of databases and catalogs were consulted, multidisciplinary and architecture-specific (Table A. 1). This division provides information on the topic's relevance and the different approaches used in the field.

Table A. 1: Consulted databases grouped per discipline.

Multidisciplinary	ProQuest
	Google Scholar
	Web of Science
	GreenFILE
Architecture	RIBA
	ICONDA
	Archirès
	PIDGEON digital
	Masters of Architecture
	ProQuest: Arts & Humanities Database
	ProQuest: Art, Design & Architecture Collection

Keyword parameters shown in Table A. 2 correspond to the searches conducted in the databases mentioned in Table A. 1. Since the Thesis researched radiative cooling potential to reduce refrigeration demand in current increasing temperatures, the chosen words had to do with radiative cooling, passive cooling techniques, architecture, and the Urban Heat Island.

After an initial review of the results, they were classified on a reference manager, Zotero (*Zotero*, 2006). The documents were organized using specific program tools (e.g., tags, folders, and notes). The folders were divided by topic (e.g., vernacular architecture, radiative cooling, coolmaterials/coolroofs, environment, and sky models). Furthermore, two folders were created for not relevant and unrelated research. Besides the "topic tag," another tag was created to rate the articles according to their relevance, rigor, and relationship to this research's object. This rating tag went from 1 to 5 stars and were assigned to the documents. The queries were performed during September of 2017, ending with a consolidated database of 556 documents. Among them, 327 documents were selected due to their interest for the doctoral thesis[19].

Table A. 2: Keyword parameters used for database searches.

Keywords in title	**RC**	allintitle: radiative AND cooling
	ER	allintitle: enfriamiento AND radiativo
	PRC	allintitle: passive AND cooling AND radiative
	RCc	allintitle: radiative AND cooling AND coolmaterials
	RCcr	allintitle: radiative AND cooling AND coolroofs
Keywords in document	**RC**	radiative AND cooling
	ER	enfriamiento AND radiativo
	PRC	passive AND cooling AND radiative
	RCc	radiative AND cooling AND coolmaterials
	RCcr	radiative AND cooling AND coolroofs
	RCAI	radiative AND cooling AND architecture AND integration
	UHI RC	urban AND heat AND island AND radiative AND cooling

Figure A. 1 to Figure A. 4 show the search results of the mentioned queries. Multidisciplinary databases gave a higher number of entries than the architecture databases, suggesting that the field of radiative cooling has been approached from other branches of knowledge outside architecture. The results are grouped by RC, ER, PRC, RCAI, UHI RC, RCcr, and RCc which

---

[19] The library has been continuously fed with new research published received from Google Scholar, Google alerts and Science Direct. The 04th of December 2020, the library dedicated to the thesis contained 1550 research elements.

stand in for radiative cooling, “enfriamiento radiativo”, passive radiative cooling, radiative cooling architecture integration, urban heat island radiative cooling, radiative cooling coolroofs, and radiative cooling coolmaterials, respectively.

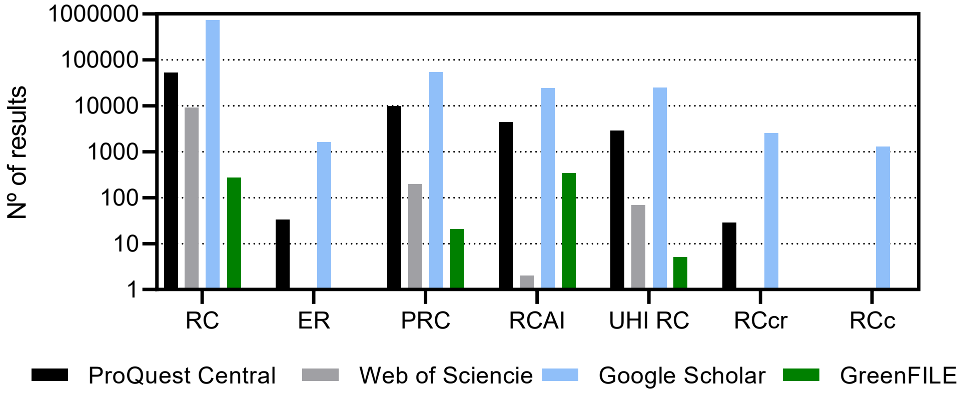

Figure A. 1: Number of results per database and word combination. The field of search has been general (e.g., “radiative AND cooling”). The vertical axis “Nº of results” is shown in a logarithmic scale. Check abbreviations in Table A. 2.

The search with the operators “radiative AND cooling” is the most numerous in results, with a constant increase in number over the last decade. However, once the results were obtained, they had to be filtered due to unrelated research in astronomy.

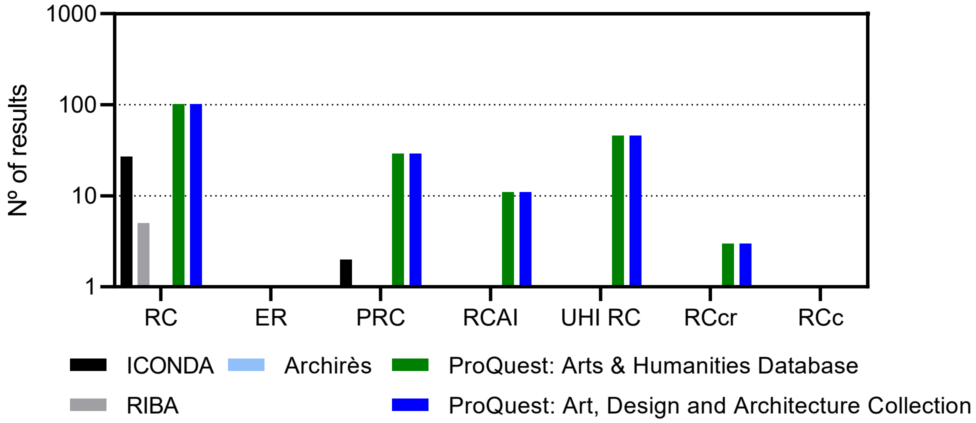

Figure A. 2: Number of results per year and database. Keywords were restricted for the title (e.g., allintitle: radiative AND cooling). Check abbreviations in Table A. 2.

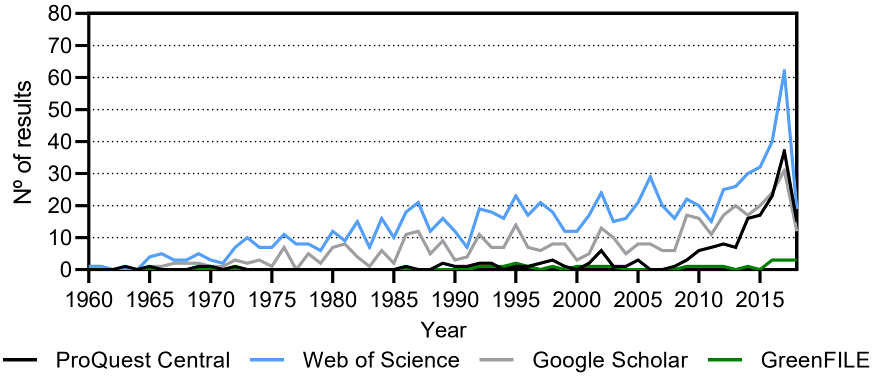

Figure A. 3: Number of entries per year and multidisciplinary databases for “radiative AND cooling”.

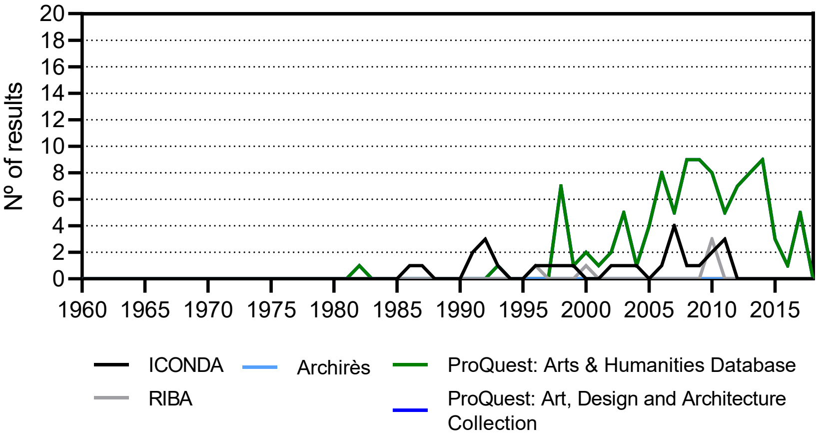

Figure A. 4: Number of entries per year and architecture databases for “radiative AND cooling”.

As shown in Figure A. 3 and Figure A. 4, radiative cooling results increased exponentially in the last years before starting this research.

APPENDIX 2: Model validation

Two materials were chosen among the literature (Raman et al., 2014; Zhai et al., 2017b); hence the information provided in the original papers regarding the experimental conditions (Table A. 3) and the spectral information (Figure A. 5). The experimental data was completed with meteorological data from the day of the experiment on the location. The selected materials reported high cooling rates even when exposed to the sun or a high temperature drop from the ambient temperature.

Table A. 3: Comparison of the two selected radiative cooling materials.

	Skycool (Raman et al., 2014)	**Radicool (Zhai et al., 2017b)**
Solar Reflectivity	0.90	0.90
Emissivity in the transparency window	0.80	0.93
Reported sub-ambient temperature	4.9 °C	-
Cooling potential	40.1 W/m^2	93 W/m^2
Location of experiment	Stanford, CA, USA	Cave Creek, AZ, USA
Köppen climate exp	Csb	BSh
Dates of the experiment	Clear winter day	16th Oct. to 19th Oct. (Fall)

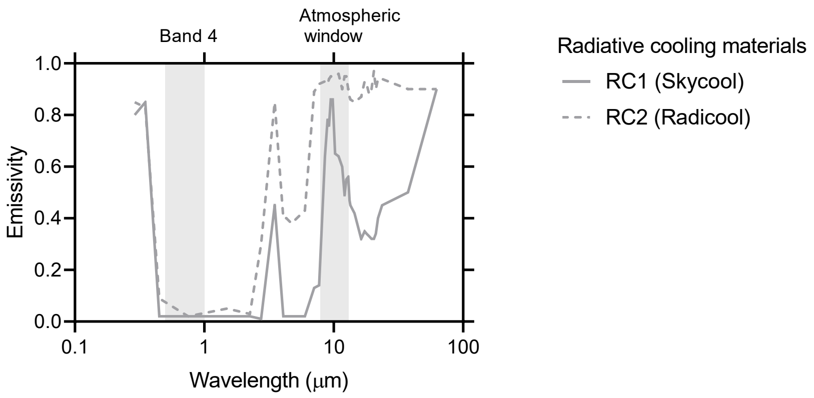

Figure A. 5: The spectral emissivity of the two daytime radiative cooling materials used for the validation.

Skycool (Raman et al., 2014)

The authors exposed the radiative cooling material to the sky, using a convection barrier: a low-density polyethylene cover. The measurements were carried throughout five hours.

The article provided the following data:

- Material's emissivity
- Ambient temperature on the location
- Location (Stanford, California)
- Dates of the experiment (clear winter day of mid-December)
- Solar radiation

The only missing information needed for the model is:

- Relative humidity

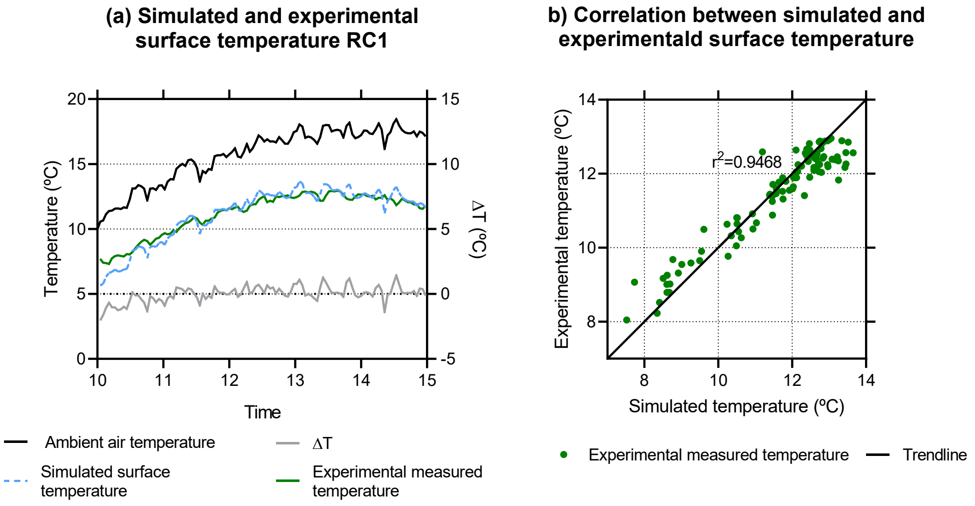

Figure A. 6: Validation of the thermal model with material 1 (RC1) “Skycool” (Raman et al., 2014).

The relative humidity values were extracted from (“Weather in December 2013 in Palo Alto, California, USA,” n.d.). Among those days, the most probable day (with the highest temperatures) is the most covered day. As a result, it was decided to use the mean values from 13th Dec. until de 17th Dec was calculated as an approximation of the relative humidity.

The surface temperature calculated with the model is quite close to the experimentally measured temperature. The simulation data show higher oscillation than the experimental surface temperature. This behavior is probably due to the thermal inertia existing in the experiment, which for this simulation was considered null. The simulation curve is very similar to the outside air temperature curve, but with a displacement, expected behavior since the thermal inertia was zero. As a result of thermal inertial, the experimental data shows a smoother surface temperature variation. Because the authors of the experiment do not give enough information to simulate the effects of thermal inertia, in this study, it was preferred not to consider it in the simulation. It could give the impression that the results could be forced by selecting convenient values for the variables that consider thermal inertia.

Radicool (Zhai et al., 2017a)

This experiment’s conditions were different from the experiment mentioned above. In this case, the material was insulated to prevent conduction and was heated to achieve the exact ambient temperature. As a result, convection forces are eliminated.

The article provided the following data:

- The emissivity of the material
- Heat input
- Ambient temperature on the location
- Cooling power
- Location (Cave Creek, Arizona (33°49′32″N, 112°1′44″W, 585 m altitude))
- Dates of the experiment (16th Oct. 2017 to 20th Oct. 2017)

The validation procedure considered the cooling power as the heat input ($W \cdot m^{-2}$). The cooling power is the energy supplied to the material to stay at ambient temperature. Otherwise, the material would drop its temperature. The information we had to infer was:

- Relative humidity
- Solar radiation

The relative humidity and the incident solar radiation were obtained from (“Weather Underground,” n.d.) for the weather station named “KAZCAVEC42” (33.80 °N, 111.98 °W, 609 m altitude), which can be considered a good approximation. No cloud cover was considered as the authors referred to the experiment days as “a series of clear autumn days in Cave Creek.”

Nevertheless, the measured ambient air temperature presents discrepancies with the data from the weather station. Therefore, there is a degree of uncertainty in the validation.

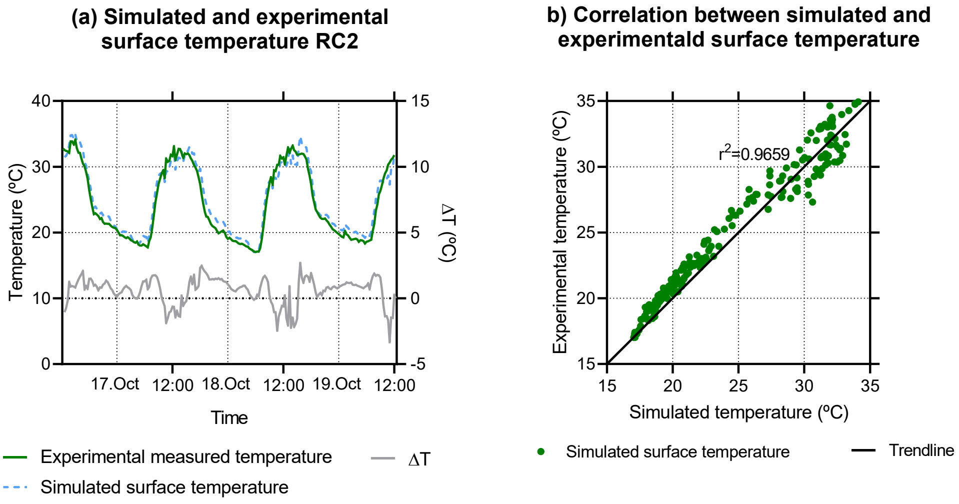

Figure A. 7: Validation of the thermal model with material 2 (RC2) “Radicool” (Zhai et al., 2017b)

In this part, we preserved all the input data and the solar radiation obtained from the weather station “KAZCAVEC42” (33.80 °N, 111.98 °W, 609 m altitude) but considered a relative humidity of 10%. The agreement is higher than in the first case.

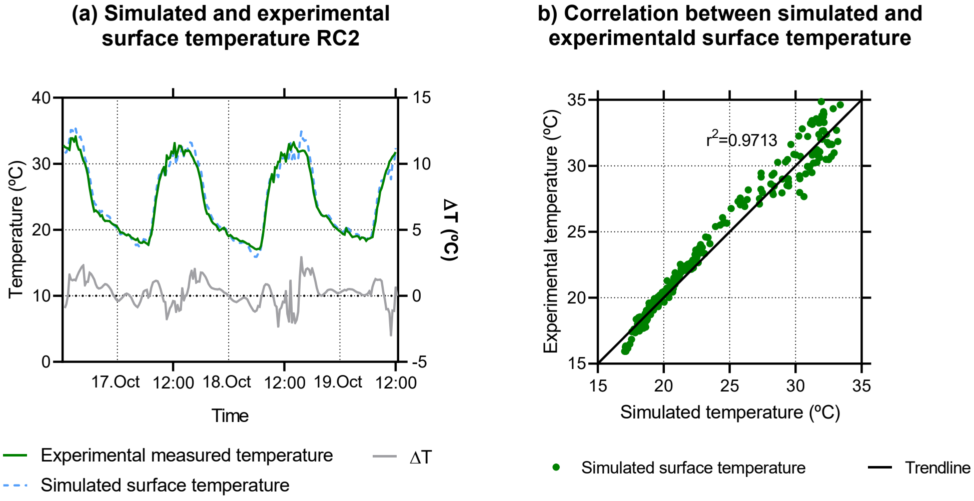

Figure A. 8: Validation of the thermal model with material 2 (RC2) “Radicool” (Zhai et al., 2017b)

APPENDIX 3: Band division

After a literature review on sky models, two spectrally selective models (Berger and Bathiebo, 1989; Li and Coimbra, 2019) were chosen and implemented in the thermal model. The models divided the sky into 21 (Table A. 4) and 7 (Table A. 5) wavelength bands. Their combination resulted in 28 wavelength bands. Nevertheless, this division was not adequate for the material's optical properties. The materials considered had subtle changes in the emissivity in the solar wavelengths. The Li-Coimbra model was not finally used due to its smaller discretization.

The ultraviolet B (0.28-0.3 μm) range was added as a band even though solar radiation in this band is low comparing to the total radiation. However, it can degrade materials. The deterioration was not considered in this research but might be of use in future research. The last two bands (25-50 μm) and (50-75 μm) were added to complete the infrared wavelengths. The thermal radiation between 75 and 1000 is almost negligible and is not considered.

Most radiative cooling materials present many spectral variations in the visible wavelengths. Therefore, the band (0.3-4 μm) was subsequently divided to better respond to changes in Table A. 6.

Table A. 4: Wavelength bands division proposed in (Berger and Bathiebo, 1989).

Range (j)	**Wavenumber (cm^{-1})**		**Wavelength (μm)**	
	V2	**v1**	**v2**	**v1**
1	1206.6	1318	8.29	7.59
2	1133.9	1206.6	8.82	8.29
3	1098.9	1133.9	9.10	8.82
4	1069.5	1098.9	9.35	9.10
5	1036.3	1069.5	9.65	9.35
6	1002.5	1036.3	9.98	9.65
7	952.4	1002.5	10.50	9.98
8	883	952.4	11.33	10.50
9	836.8	883	11.95	11.33
10	813	836.8	12.30	11.95
11	785.9	813	12.72	12.30
12	759.7	785.9	13.16	12.72
13	736	759.7	13.59	13.16
14	650.9	736	15.36	13.59
15	572.7	650.9	17.46	15.36
16	543.5	572.7	18.40	17.46
17	522.2	543.5	19.15	18.40
18	500	522.2	20.00	19.15
19	479.9	500	20.84	20.00
20	463.2	479.9	21.59	20.84
21	446.2	463.2	22.41	21.59

Table A. 5: Wavelength bands proposed in (Li and Coimbra, 2019).

Range (j)	**Wavenumber (cm^{-1})**		**Wavelength (μm)**	
	V2	**v1**	**v2**	**v1**
1	2400	2500	4.17	4.00
2	2250	2400	4.44	4.17
3	1400	2250	7.14	4.44
4	750	1400	13.33	7.14
5	580	750	17.24	13.33
6	400	580	25.00	17.24
7	0	400	-	25.00

Table A. 6: Ranges of the proposed 39 wavelength band division.

	Wavelength (μm)	
Band 1	0,28	0,30
Band 2	0,30	0,40
Band 3	0,40	0,50
Band 4	0,50	1,00
Band 5	1,00	2,00
Band 6	2,00	2,50
Band 7	2,50	3,00
Band 8	3,00	4,00
Band 9	4,00	4,17
Band 10	4,17	4,44
Band 11	4,44	5,00
Band 12	5,00	7,00
Band 13	7,00	7,14
Band 14	7,14	8,29
Band 15	8,29	8,82
Band 16	8,82	9,10
Band 17	9,10	9,35
Band 18	9,35	9,65
Band 19	9,65	9,98
Band 20	9,98	10,50
Band 21	10,50	11,33
Band 22	11,33	11,95
Band 23	11,95	12,30
Band 24	12,30	12,73
Band 25	12,73	13,16
Band 26	13,16	13,33
Band 27	13,33	13,59
Band 28	13,59	15,36
Band 29	15,36	17,24
Band 30	17,24	17,46
Band 31	17,46	18,40
Band 32	18,40	19,15
Band 33	19,15	20,00
Band 34	20,00	20,84
Band 35	20,84	21,59
Band 36	21,59	22,41
Band 37	22,41	25,00
Band 38	25,00	50,00
Band 39	50,00	75,00

APPENDIX 4: Theoretical materials

The following tables, Table A. 7 to Table A. 12, represent the 90 theoretical materials described in chapter 3. These materials were used in the sensitivity analysis to determine the impact of wavelength emissivity on achieving daytime radiative cooling, following the radiation spectrum division presented in the previous appendix (APPENDIX 2: Band division).

For each band, an emissivity value of zero or non-zero was assigned to each band resulting in fifteen wavelength combinations, M1-M15. The ideal material should emit strongly in the atmospheric window; thus, the non-zero values were established around it. Moreover, a high solar reflectivity is critical to achieving daytime sub-ambient cooling; as a result, the emissivity values were centered in the visible solar region with the highest solar irradiance. Besides the different band combinations, six non-zero values were assigned to quantify the impact of the emissivity value: 1 (Table A. 7), 0.9 (Table A. 8), 0.8 (Table A. 9), 0.7 (Table A. 10), 0.5 (Table A. 11), and 0.25 (Table A. 12).

Figure A. 9 to Figure A. 11 show the detailed simulation results of the 15 spectral configurations with the 6 emissivity values described above, the 90 theoretical materials. Figure A. 9 shows the mean temperature difference between the ambient air and the surface temperatures in the two studied locations, Phoenix (a) and Sydney (b). Figure A. 10 shows the daily gains (positive values) and losses (negative values) as an active system in Phoenix and Sydney. Finally, Figure A. 11 shows the daily radiated heat losses for both locations.

Table A. 7: Theoretical materials (M1-M15) with emissivity combinations of 1 and 0.

	[1]	[2]	MATERIAL														
			1	2	3	4	5	6	7	8	9	10	11	12	13	14	15
1	0.28	0.30	0	0	0	0	0	0	0	0	0	0	0	0	0	1	1
2	0.30	0.40	0	0	0	0	0	0	0	0	0	0	0	0	1	1	1
3	0.40	0.50	0	0	0	0	0	0	0	0	0	0	1	1	1	1	1
4	0.50	1.00	0	0	0	0	0	0	0	0	0	1	1	1	1	1	1
5	1.00	2.00	0	0	0	0	0	0	0	0	0	0	0	1	1	1	1
6	2.00	2.50	0	0	0	0	0	0	0	0	1	1	1	1	1	1	1
7	2.50	3.00	0	0	0	0	0	0	0	0	1	1	1	1	1	1	1
8	3.00	4.00	0	0	0	0	0	0	0	0	1	1	1	1	1	1	1
9	4.00	4.17	0	0	0	0	0	0	0	0	1	1	1	1	1	1	1
10	4.17	4.44	0	0	0	0	0	0	0	1	1	1	1	1	1	1	1
11	4.44	5.00	0	0	0	0	0	0	0	1	1	1	1	1	1	1	1
12	5.00	7.00	0	0	0	0	0	0	0	1	1	1	1	1	1	1	1
13	7.00	7.14	0	0	0	0	0	0	1	1	1	1	1	1	1	1	1
14	7.14	8.29	0	0	0	0	0	0	1	1	1	1	1	1	1	1	1
15	8.29	8.82	0	0	0	0	0	1	1	1	1	1	1	1	1	1	1
16	8.82	9.10	0	0	0	0	1	1	1	1	1	1	1	1	1	1	1
17	9.10	9.35	0	0	0	1	1	1	1	1	1	1	1	1	1	1	1
18	9.35	9.65	0	0	1	1	1	1	1	1	1	1	1	1	1	1	1
19	9.65	9.98	0	1	1	1	1	1	1	1	1	1	1	1	1	1	1
20	9.98	10.50	1	1	1	1	1	1	1	1	1	1	1	1	1	1	1
21	10.50	11.33	0	1	1	1	1	1	1	1	1	1	1	1	1	1	1
22	11.33	11.95	0	0	1	1	1	1	1	1	1	1	1	1	1	1	1
23	11.95	12.30	0	0	0	1	1	1	1	1	1	1	1	1	1	1	1
24	12.30	12.73	0	0	0	0	1	1	1	1	1	1	1	1	1	1	1
25	12.73	13.16	0	0	0	0	1	1	1	1	1	1	1	1	1	1	1
26	13.16	13.33	0	0	0	0	0	1	1	1	1	1	1	1	1	1	1
27	13.33	13.59	0	0	0	0	0	1	1	1	1	1	1	1	1	1	1
28	13.59	15.36	0	0	0	0	0	0	1	1	1	1	1	1	1	1	1
29	15.36	17.24	0	0	0	0	0	0	1	1	1	1	1	1	1	1	1
30	17.24	17.46	0	0	0	0	0	0	0	1	1	1	1	1	1	1	1
31	17.46	18.40	0	0	0	0	0	0	0	1	1	1	1	1	1	1	1
32	18.40	19.15	0	0	0	0	0	0	0	1	1	1	1	1	1	1	1
33	19.15	20.00	0	0	0	0	0	0	0	0	1	1	1	1	1	1	1
34	20.00	20.84	0	0	0	0	0	0	0	0	1	1	1	1	1	1	1
35	20.84	21.59	0	0	0	0	0	0	0	0	1	1	1	1	1	1	1
36	21.59	22.41	0	0	0	0	0	0	0	0	0	0	0	0	0	0	1
37	22.41	25.00	0	0	0	0	0	0	0	0	0	0	0	0	0	0	1
38	25.00	50.00	0	0	0	0	0	0	0	0	0	0	0	0	0	0	1
39	50.00	75.00	0	0	0	0	0	0	0	0	0	0	0	0	0	0	1

Table A. 8: Theoretical materials (1-15) with emissivity combinations of 0.9 and 0.

	[1]	[2]	MATERIAL														
			1	2	3	4	5	6	7	8	9	10	11	12	13	14	15
1	0.28	0.30	0	0	0	0	0	0	0	0	0	0	0	0	0	0.9	0.9
2	0.30	0.40	0	0	0	0	0	0	0	0	0	0	0	0	0.9	0.9	0.9
3	0.40	0.50	0	0	0	0	0	0	0	0	0	0	0.9	0.9	0.9	0.9	0.9
4	0.50	1.00	0	0	0	0	0	0	0	0	0	0.9	0.9	0.9	0.9	0.9	0.9
5	1.00	2.00	0	0	0	0	0	0	0	0	0	0	0	0.9	0.9	0.9	0.9
6	2.00	2.50	0	0	0	0	0	0	0	0	0.9	0.9	0.9	0.9	0.9	0.9	0.9
7	2.50	3.00	0	0	0	0	0	0	0	0	0.9	0.9	0.9	0.9	0.9	0.9	0.9
8	3.00	4.00	0	0	0	0	0	0	0	0	0.9	0.9	0.9	0.9	0.9	0.9	0.9
9	4.00	4.17	0	0	0	0	0	0	0	0	0.9	0.9	0.9	0.9	0.9	0.9	0.9
10	4.17	4.44	0	0	0	0	0	0	0	0.9	0.9	0.9	0.9	0.9	0.9	0.9	0.9
11	4.44	5.00	0	0	0	0	0	0	0	0.9	0.9	0.9	0.9	0.9	0.9	0.9	0.9
12	5.00	7.00	0	0	0	0	0	0	0	0.9	0.9	0.9	0.9	0.9	0.9	0.9	0.9
13	7.00	7.14	0	0	0	0	0	0	0.9	0.9	0.9	0.9	0.9	0.9	0.9	0.9	0.9
14	7.14	8.29	0	0	0	0	0	0	0.9	0.9	0.9	0.9	0.9	0.9	0.9	0.9	0.9
15	8.29	8.82	0	0	0	0	0	0.9	0.9	0.9	0.9	0.9	0.9	0.9	0.9	0.9	0.9
16	8.82	9.10	0	0	0	0	0.9	0.9	0.9	0.9	0.9	0.9	0.9	0.9	0.9	0.9	0.9
17	9.10	9.35	0	0	0	0.9	0.9	0.9	0.9	0.9	0.9	0.9	0.9	0.9	0.9	0.9	0.9
18	9.35	9.65	0	0	0.9	0.9	0.9	0.9	0.9	0.9	0.9	0.9	0.9	0.9	0.9	0.9	0.9
19	9.65	9.98	0	0.9	0.9	0.9	0.9	0.9	0.9	0.9	0.9	0.9	0.9	0.9	0.9	0.9	0.9
20	9.98	10.50	0.9	0.9	0.9	0.9	0.9	0.9	0.9	0.9	0.9	0.9	0.9	0.9	0.9	0.9	0.9
21	10.50	11.33	0	0.9	0.9	0.9	0.9	0.9	0.9	0.9	0.9	0.9	0.9	0.9	0.9	0.9	0.9
22	11.33	11.95	0	0	0.9	0.9	0.9	0.9	0.9	0.9	0.9	0.9	0.9	0.9	0.9	0.9	0.9
23	11.95	12.30	0	0	0	0.9	0.9	0.9	0.9	0.9	0.9	0.9	0.9	0.9	0.9	0.9	0.9
24	12.30	12.73	0	0	0	0	0.9	0.9	0.9	0.9	0.9	0.9	0.9	0.9	0.9	0.9	0.9
25	12.73	13.16	0	0	0	0	0.9	0.9	0.9	0.9	0.9	0.9	0.9	0.9	0.9	0.9	0.9
26	13.16	13.33	0	0	0	0	0	0.9	0.9	0.9	0.9	0.9	0.9	0.9	0.9	0.9	0.9
27	13.33	13.59	0	0	0	0	0	0.9	0.9	0.9	0.9	0.9	0.9	0.9	0.9	0.9	0.9
28	13.59	15.36	0	0	0	0	0	0	0.9	0.9	0.9	0.9	0.9	0.9	0.9	0.9	0.9
29	15.36	17.24	0	0	0	0	0	0	0.9	0.9	0.9	0.9	0.9	0.9	0.9	0.9	0.9
30	17.24	17.46	0	0	0	0	0	0	0	0.9	0.9	0.9	0.9	0.9	0.9	0.9	0.9
31	17.46	18.40	0	0	0	0	0	0	0	0.9	0.9	0.9	0.9	0.9	0.9	0.9	0.9
32	18.40	19.15	0	0	0	0	0	0	0	0.9	0.9	0.9	0.9	0.9	0.9	0.9	0.9
33	19.15	20.00	0	0	0	0	0	0	0	0	0.9	0.9	0.9	0.9	0.9	0.9	0.9
34	20.00	20.84	0	0	0	0	0	0	0	0	0.9	0.9	0.9	0.9	0.9	0.9	0.9
35	20.84	21.59	0	0	0	0	0	0	0	0	0.9	0.9	0.9	0.9	0.9	0.9	0.9
36	21.59	22.41	0	0	0	0	0	0	0	0	0	0	0	0	0	0	0.9
37	22.41	25.00	0	0	0	0	0	0	0	0	0	0	0	0	0	0	0.9
38	25.00	50.00	0	0	0	0	0	0	0	0	0	0	0	0	0	0	0.9
39	50.00	75.00	0	0	0	0	0	0	0	0	0	0	0	0	0	0	0.9

Table A. 9: Theoretical materials (1-15) with emissivity combinations of 0.8 and 0.

	[1]	[2]	MATERIAL														
			1	2	3	4	5	6	7	8	9	10	11	12	13	14	15
1	0.28	0.30	0	0	0	0	0	0	0	0	0	0	0	0	0	0.8	0.8
2	0.30	0.40	0	0	0	0	0	0	0	0	0	0	0	0	0.8	0.8	0.8
3	0.40	0.50	0	0	0	0	0	0	0	0	0	0	0.8	0.8	0.8	0.8	0.8
4	0.50	1.00	0	0	0	0	0	0	0	0	0	0.8	0.8	0.8	0.8	0.8	0.8
5	1.00	2.00	0	0	0	0	0	0	0	0	0	0	0	0.8	0.8	0.8	0.8
6	2.00	2.50	0	0	0	0	0	0	0	0	0.8	0.8	0.8	0.8	0.8	0.8	0.8
7	2.50	3.00	0	0	0	0	0	0	0	0	0.8	0.8	0.8	0.8	0.8	0.8	0.8
8	3.00	4.00	0	0	0	0	0	0	0	0	0.8	0.8	0.8	0.8	0.8	0.8	0.8
9	4.00	4.17	0	0	0	0	0	0	0	0	0.8	0.8	0.8	0.8	0.8	0.8	0.8
10	4.17	4.44	0	0	0	0	0	0	0	0.8	0.8	0.8	0.8	0.8	0.8	0.8	0.8
11	4.44	5.00	0	0	0	0	0	0	0	0.8	0.8	0.8	0.8	0.8	0.8	0.8	0.8
12	5.00	7.00	0	0	0	0	0	0	0	0.8	0.8	0.8	0.8	0.8	0.8	0.8	0.8
13	7.00	7.14	0	0	0	0	0	0	0.8	0.8	0.8	0.8	0.8	0.8	0.8	0.8	0.8
14	7.14	8.29	0	0	0	0	0	0	0.8	0.8	0.8	0.8	0.8	0.8	0.8	0.8	0.8
15	8.29	8.82	0	0	0	0	0	0.8	0.8	0.8	0.8	0.8	0.8	0.8	0.8	0.8	0.8
16	8.82	9.10	0	0	0	0	0.8	0.8	0.8	0.8	0.8	0.8	0.8	0.8	0.8	0.8	0.8
17	9.10	9.35	0	0	0	0.8	0.8	0.8	0.8	0.8	0.8	0.8	0.8	0.8	0.8	0.8	0.8
18	9.35	9.65	0	0	0.8	0.8	0.8	0.8	0.8	0.8	0.8	0.8	0.8	0.8	0.8	0.8	0.8
19	9.65	9.98	0	0.8	0.8	0.8	0.8	0.8	0.8	0.8	0.8	0.8	0.8	0.8	0.8	0.8	0.8
20	9.98	10.50	0.8	0.8	0.8	0.8	0.8	0.8	0.8	0.8	0.8	0.8	0.8	0.8	0.8	0.8	0.8
21	10.50	11.33	0	0.8	0.8	0.8	0.8	0.8	0.8	0.8	0.8	0.8	0.8	0.8	0.8	0.8	0.8
22	11.33	11.95	0	0	0.8	0.8	0.8	0.8	0.8	0.8	0.8	0.8	0.8	0.8	0.8	0.8	0.8
23	11.95	12.30	0	0	0	0.8	0.8	0.8	0.8	0.8	0.8	0.8	0.8	0.8	0.8	0.8	0.8
24	12.30	12.73	0	0	0	0	0.8	0.8	0.8	0.8	0.8	0.8	0.8	0.8	0.8	0.8	0.8
25	12.73	13.16	0	0	0	0	0.8	0.8	0.8	0.8	0.8	0.8	0.8	0.8	0.8	0.8	0.8
26	13.16	13.33	0	0	0	0	0	0.8	0.8	0.8	0.8	0.8	0.8	0.8	0.8	0.8	0.8
27	13.33	13.59	0	0	0	0	0	0.8	0.8	0.8	0.8	0.8	0.8	0.8	0.8	0.8	0.8
28	13.59	15.36	0	0	0	0	0	0	0.8	0.8	0.8	0.8	0.8	0.8	0.8	0.8	0.8
29	15.36	17.24	0	0	0	0	0	0	0.8	0.8	0.8	0.8	0.8	0.8	0.8	0.8	0.8
30	17.24	17.46	0	0	0	0	0	0	0	0.8	0.8	0.8	0.8	0.8	0.8	0.8	0.8
31	17.46	18.40	0	0	0	0	0	0	0	0.8	0.8	0.8	0.8	0.8	0.8	0.8	0.8
32	18.40	19.15	0	0	0	0	0	0	0	0.8	0.8	0.8	0.8	0.8	0.8	0.8	0.8
33	19.15	20.00	0	0	0	0	0	0	0	0	0.8	0.8	0.8	0.8	0.8	0.8	0.8
34	20.00	20.84	0	0	0	0	0	0	0	0	0.8	0.8	0.8	0.8	0.8	0.8	0.8
35	20.84	21.59	0	0	0	0	0	0	0	0	0.8	0.8	0.8	0.8	0.8	0.8	0.8
36	21.59	22.41	0	0	0	0	0	0	0	0	0	0	0	0	0	0	0.8
37	22.41	25.00	0	0	0	0	0	0	0	0	0	0	0	0	0	0	0.8
38	25.00	50.00	0	0	0	0	0	0	0	0	0	0	0	0	0	0	0.8
39	50.00	75.00	0	0	0	0	0	0	0	0	0	0	0	0	0	0	0.8

Table A. 10: Theoretical materials (1-15) with emissivity combinations of 0.7 and 0.

	[1]	[2]	MATERIAL														
			1	2	3	4	5	6	7	8	9	10	11	12	13	14	15
1	0.28	0.30	0	0	0	0	0	0	0	0	0	0	0	0	0	0.7	0.7
2	0.30	0.40	0	0	0	0	0	0	0	0	0	0	0	0	0.7	0.7	0.7
3	0.40	0.50	0	0	0	0	0	0	0	0	0	0	0.7	0.7	0.7	0.7	0.7
4	0.50	1.00	0	0	0	0	0	0	0	0	0	0.7	0.7	0.7	0.7	0.7	0.7
5	1.00	2.00	0	0	0	0	0	0	0	0	0	0	0	0.7	0.7	0.7	0.7
6	2.00	2.50	0	0	0	0	0	0	0	0	0.7	0.7	0.7	0.7	0.7	0.7	0.7
7	2.50	3.00	0	0	0	0	0	0	0	0	0.7	0.7	0.7	0.7	0.7	0.7	0.7
8	3.00	4.00	0	0	0	0	0	0	0	0	0.7	0.7	0.7	0.7	0.7	0.7	0.7
9	4.00	4.17	0	0	0	0	0	0	0	0	0.7	0.7	0.7	0.7	0.7	0.7	0.7
10	4.17	4.44	0	0	0	0	0	0	0	0.7	0.7	0.7	0.7	0.7	0.7	0.7	0.7
11	4.44	5.00	0	0	0	0	0	0	0	0.7	0.7	0.7	0.7	0.7	0.7	0.7	0.7
12	5.00	7.00	0	0	0	0	0	0	0	0.7	0.7	0.7	0.7	0.7	0.7	0.7	0.7
13	7.00	7.14	0	0	0	0	0	0	0.7	0.7	0.7	0.7	0.7	0.7	0.7	0.7	0.7
14	7.14	8.29	0	0	0	0	0	0	0.7	0.7	0.7	0.7	0.7	0.7	0.7	0.7	0.7
15	8.29	8.82	0	0	0	0	0	0.7	0.7	0.7	0.7	0.7	0.7	0.7	0.7	0.7	0.7
16	8.82	9.10	0	0	0	0	0.7	0.7	0.7	0.7	0.7	0.7	0.7	0.7	0.7	0.7	0.7
17	9.10	9.35	0	0	0	0.7	0.7	0.7	0.7	0.7	0.7	0.7	0.7	0.7	0.7	0.7	0.7
18	9.35	9.65	0	0	0.7	0.7	0.7	0.7	0.7	0.7	0.7	0.7	0.7	0.7	0.7	0.7	0.7
19	9.65	9.98	0	0.7	0.7	0.7	0.7	0.7	0.7	0.7	0.7	0.7	0.7	0.7	0.7	0.7	0.7
20	9.98	10.50	0.7	0.7	0.7	0.7	0.7	0.7	0.7	0.7	0.7	0.7	0.7	0.7	0.7	0.7	0.7
21	10.50	11.33	0	0.7	0.7	0.7	0.7	0.7	0.7	0.7	0.7	0.7	0.7	0.7	0.7	0.7	0.7
22	11.33	11.95	0	0	0.7	0.7	0.7	0.7	0.7	0.7	0.7	0.7	0.7	0.7	0.7	0.7	0.7
23	11.95	12.30	0	0	0	0.7	0.7	0.7	0.7	0.7	0.7	0.7	0.7	0.7	0.7	0.7	0.7
24	12.30	12.73	0	0	0	0	0.7	0.7	0.7	0.7	0.7	0.7	0.7	0.7	0.7	0.7	0.7
25	12.73	13.16	0	0	0	0	0.7	0.7	0.7	0.7	0.7	0.7	0.7	0.7	0.7	0.7	0.7
26	13.16	13.33	0	0	0	0	0	0.7	0.7	0.7	0.7	0.7	0.7	0.7	0.7	0.7	0.7
27	13.33	13.59	0	0	0	0	0	0.7	0.7	0.7	0.7	0.7	0.7	0.7	0.7	0.7	0.7
28	13.59	15.36	0	0	0	0	0	0	0.7	0.7	0.7	0.7	0.7	0.7	0.7	0.7	0.7
29	15.36	17.24	0	0	0	0	0	0	0.7	0.7	0.7	0.7	0.7	0.7	0.7	0.7	0.7
30	17.24	17.46	0	0	0	0	0	0	0	0.7	0.7	0.7	0.7	0.7	0.7	0.7	0.7
31	17.46	18.40	0	0	0	0	0	0	0	0.7	0.7	0.7	0.7	0.7	0.7	0.7	0.7
32	18.40	19.15	0	0	0	0	0	0	0	0.7	0.7	0.7	0.7	0.7	0.7	0.7	0.7
33	19.15	20.00	0	0	0	0	0	0	0	0	0.7	0.7	0.7	0.7	0.7	0.7	0.7
34	20.00	20.84	0	0	0	0	0	0	0	0	0.7	0.7	0.7	0.7	0.7	0.7	0.7
35	20.84	21.59	0	0	0	0	0	0	0	0	0.7	0.7	0.7	0.7	0.7	0.7	0.7
36	21.59	22.41	0	0	0	0	0	0	0	0	0	0	0	0	0	0	0.7
37	22.41	25.00	0	0	0	0	0	0	0	0	0	0	0	0	0	0	0.7
38	25.00	50.00	0	0	0	0	0	0	0	0	0	0	0	0	0	0	0.7
39	50.00	75.00	0	0	0	0	0	0	0	0	0	0	0	0	0	0	0.7

Table A. 11: Theoretical materials (1-15) with emissivity combinations of 0.5 and 0.

	[1]	[2]	MATERIAL														
			1	2	3	4	5	6	7	8	9	10	11	12	13	14	15
1	0.28	0.30	0	0	0	0	0	0	0	0	0	0	0	0	0	0.5	0.5
2	0.30	0.40	0	0	0	0	0	0	0	0	0	0	0	0	0.5	0.5	0.5
3	0.40	0.50	0	0	0	0	0	0	0	0	0	0	0.5	0.5	0.5	0.5	0.5
4	0.50	1.00	0	0	0	0	0	0	0	0	0	0.5	0.5	0.5	0.5	0.5	0.5
5	1.00	2.00	0	0	0	0	0	0	0	0	0	0	0	0.5	0.5	0.5	0.5
6	2.00	2.50	0	0	0	0	0	0	0	0	0.5	0.5	0.5	0.5	0.5	0.5	0.5
7	2.50	3.00	0	0	0	0	0	0	0	0	0.5	0.5	0.5	0.5	0.5	0.5	0.5
8	3.00	4.00	0	0	0	0	0	0	0	0	0.5	0.5	0.5	0.5	0.5	0.5	0.5
9	4.00	4.17	0	0	0	0	0	0	0	0	0.5	0.5	0.5	0.5	0.5	0.5	0.5
10	4.17	4.44	0	0	0	0	0	0	0	0.5	0.5	0.5	0.5	0.5	0.5	0.5	0.5
11	4.44	5.00	0	0	0	0	0	0	0	0.5	0.5	0.5	0.5	0.5	0.5	0.5	0.5
12	5.00	7.00	0	0	0	0	0	0	0	0.5	0.5	0.5	0.5	0.5	0.5	0.5	0.5
13	7.00	7.14	0	0	0	0	0	0	0.5	0.5	0.5	0.5	0.5	0.5	0.5	0.5	0.5
14	7.14	8.29	0	0	0	0	0	0	0.5	0.5	0.5	0.5	0.5	0.5	0.5	0.5	0.5
15	8.29	8.82	0	0	0	0	0	0.5	0.5	0.5	0.5	0.5	0.5	0.5	0.5	0.5	0.5
16	8.82	9.10	0	0	0	0	0.5	0.5	0.5	0.5	0.5	0.5	0.5	0.5	0.5	0.5	0.5
17	9.10	9.35	0	0	0	0.5	0.5	0.5	0.5	0.5	0.5	0.5	0.5	0.5	0.5	0.5	0.5
18	9.35	9.65	0	0	0.5	0.5	0.5	0.5	0.5	0.5	0.5	0.5	0.5	0.5	0.5	0.5	0.5
19	9.65	9.98	0	0.5	0.5	0.5	0.5	0.5	0.5	0.5	0.5	0.5	0.5	0.5	0.5	0.5	0.5
20	9.98	10.50	0.5	0.5	0.5	0.5	0.5	0.5	0.5	0.5	0.5	0.5	0.5	0.5	0.5	0.5	0.5
21	10.50	11.33	0	0.5	0.5	0.5	0.5	0.5	0.5	0.5	0.5	0.5	0.5	0.5	0.5	0.5	0.5
22	11.33	11.95	0	0	0.5	0.5	0.5	0.5	0.5	0.5	0.5	0.5	0.5	0.5	0.5	0.5	0.5
23	11.95	12.30	0	0	0	0.5	0.5	0.5	0.5	0.5	0.5	0.5	0.5	0.5	0.5	0.5	0.5
24	12.30	12.73	0	0	0	0	0.5	0.5	0.5	0.5	0.5	0.5	0.5	0.5	0.5	0.5	0.5
25	12.73	13.16	0	0	0	0	0.5	0.5	0.5	0.5	0.5	0.5	0.5	0.5	0.5	0.5	0.5
26	13.16	13.33	0	0	0	0	0	0.5	0.5	0.5	0.5	0.5	0.5	0.5	0.5	0.5	0.5
27	13.33	13.59	0	0	0	0	0	0.5	0.5	0.5	0.5	0.5	0.5	0.5	0.5	0.5	0.5
28	13.59	15.36	0	0	0	0	0	0	0.5	0.5	0.5	0.5	0.5	0.5	0.5	0.5	0.5
29	15.36	17.24	0	0	0	0	0	0	0.5	0.5	0.5	0.5	0.5	0.5	0.5	0.5	0.5
30	17.24	17.46	0	0	0	0	0	0	0	0.5	0.5	0.5	0.5	0.5	0.5	0.5	0.5
31	17.46	18.40	0	0	0	0	0	0	0	0.5	0.5	0.5	0.5	0.5	0.5	0.5	0.5
32	18.40	19.15	0	0	0	0	0	0	0	0.5	0.5	0.5	0.5	0.5	0.5	0.5	0.5
33	19.15	20.00	0	0	0	0	0	0	0	0	0.5	0.5	0.5	0.5	0.5	0.5	0.5
34	20.00	20.84	0	0	0	0	0	0	0	0	0.5	0.5	0.5	0.5	0.5	0.5	0.5
35	20.84	21.59	0	0	0	0	0	0	0	0	0.5	0.5	0.5	0.5	0.5	0.5	0.5
36	21.59	22.41	0	0	0	0	0	0	0	0	0	0	0	0	0	0	0.5
37	22.41	25.00	0	0	0	0	0	0	0	0	0	0	0	0	0	0	0.5
38	25.00	50.00	0	0	0	0	0	0	0	0	0	0	0	0	0	0	0.5
39	50.00	75.00	0	0	0	0	0	0	0	0	0	0	0	0	0	0	0.5

Table A. 12: Theoretical materials (1-15) with emissivity combinations of 0.25 and 0

	[1]	[2]	MATERIAL														
			1	2	3	4	5	6	7	8	9	10	11	12	13	14	15
1	0.28	0.30	0	0	0	0	0	0	0	0	0	0	0	0	0	0.25	0.25
2	0.30	0.40	0	0	0	0	0	0	0	0	0	0	0	0	0.25	0.25	0.25
3	0.40	0.50	0	0	0	0	0	0	0	0	0	0	0.25	0.25	0.25	0.25	0.25
4	0.50	1.00	0	0	0	0	0	0	0	0	0	0.25	0.25	0.25	0.25	0.25	0.25
5	1.00	2.00	0	0	0	0	0	0	0	0	0	0	0	0.25	0.25	0.25	0.25
6	2.00	2.50	0	0	0	0	0	0	0	0	0.25	0.25	0.25	0.25	0.25	0.25	0.25
7	2.50	3.00	0	0	0	0	0	0	0	0	0.25	0.25	0.25	0.25	0.25	0.25	0.25
8	3.00	4.00	0	0	0	0	0	0	0	0	0.25	0.25	0.25	0.25	0.25	0.25	0.25
9	4.00	4.17	0	0	0	0	0	0	0	0	0.25	0.25	0.25	0.25	0.25	0.25	0.25
10	4.17	4.44	0	0	0	0	0	0	0	0.25	0.25	0.25	0.25	0.25	0.25	0.25	0.25
11	4.44	5.00	0	0	0	0	0	0	0	0.25	0.25	0.25	0.25	0.25	0.25	0.25	0.25
12	5.00	7.00	0	0	0	0	0	0	0	0.25	0.25	0.25	0.25	0.25	0.25	0.25	0.25
13	7.00	7.14	0	0	0	0	0	0	0.25	0.25	0.25	0.25	0.25	0.25	0.25	0.25	0.25
14	7.14	8.29	0	0	0	0	0	0	0.25	0.25	0.25	0.25	0.25	0.25	0.25	0.25	0.25
15	8.29	8.82	0	0	0	0	0	0.25	0.25	0.25	0.25	0.25	0.25	0.25	0.25	0.25	0.25
16	8.82	9.10	0	0	0	0	0.25	0.25	0.25	0.25	0.25	0.25	0.25	0.25	0.25	0.25	0.25
17	9.10	9.35	0	0	0	0.25	0.25	0.25	0.25	0.25	0.25	0.25	0.25	0.25	0.25	0.25	0.25
18	9.35	9.65	0	0	0.25	0.25	0.25	0.25	0.25	0.25	0.25	0.25	0.25	0.25	0.25	0.25	0.25
19	9.65	9.98	0	0.25	0.25	0.25	0.25	0.25	0.25	0.25	0.25	0.25	0.25	0.25	0.25	0.25	0.25
20	9.98	10.50	0.25	0.25	0.25	0.25	0.25	0.25	0.25	0.25	0.25	0.25	0.25	0.25	0.25	0.25	0.25
21	10.50	11.33	0	0.25	0.25	0.25	0.25	0.25	0.25	0.25	0.25	0.25	0.25	0.25	0.25	0.25	0.25
22	11.33	11.95	0	0	0.25	0.25	0.25	0.25	0.25	0.25	0.25	0.25	0.25	0.25	0.25	0.25	0.25
23	11.95	12.30	0	0	0	0.25	0.25	0.25	0.25	0.25	0.25	0.25	0.25	0.25	0.25	0.25	0.25
24	12.30	12.73	0	0	0	0	0.25	0.25	0.25	0.25	0.25	0.25	0.25	0.25	0.25	0.25	0.25
25	12.73	13.16	0	0	0	0	0.25	0.25	0.25	0.25	0.25	0.25	0.25	0.25	0.25	0.25	0.25
26	13.16	13.33	0	0	0	0	0	0.25	0.25	0.25	0.25	0.25	0.25	0.25	0.25	0.25	0.25
27	13.33	13.59	0	0	0	0	0	0.25	0.25	0.25	0.25	0.25	0.25	0.25	0.25	0.25	0.25
28	13.59	15.36	0	0	0	0	0	0	0.25	0.25	0.25	0.25	0.25	0.25	0.25	0.25	0.25
29	15.36	17.24	0	0	0	0	0	0	0.25	0.25	0.25	0.25	0.25	0.25	0.25	0.25	0.25
30	17.24	17.46	0	0	0	0	0	0	0	0.25	0.25	0.25	0.25	0.25	0.25	0.25	0.25
31	17.46	18.40	0	0	0	0	0	0	0	0.25	0.25	0.25	0.25	0.25	0.25	0.25	0.25
32	18.40	19.15	0	0	0	0	0	0	0	0.25	0.25	0.25	0.25	0.25	0.25	0.25	0.25
33	19.15	20.00	0	0	0	0	0	0	0	0	0.25	0.25	0.25	0.25	0.25	0.25	0.25
34	20.00	20.84	0	0	0	0	0	0	0	0	0.25	0.25	0.25	0.25	0.25	0.25	0.25
35	20.84	21.59	0	0	0	0	0	0	0	0	0.25	0.25	0.25	0.25	0.25	0.25	0.25
36	21.59	22.41	0	0	0	0	0	0	0	0	0	0	0	0	0	0	0.25
37	22.41	25.00	0	0	0	0	0	0	0	0	0	0	0	0	0	0	0.25
38	25.00	50.00	0	0	0	0	0	0	0	0	0	0	0	0	0	0	0.25
39	50.00	75.00	0	0	0	0	0	0	0	0	0	0	0	0	0	0	0.25

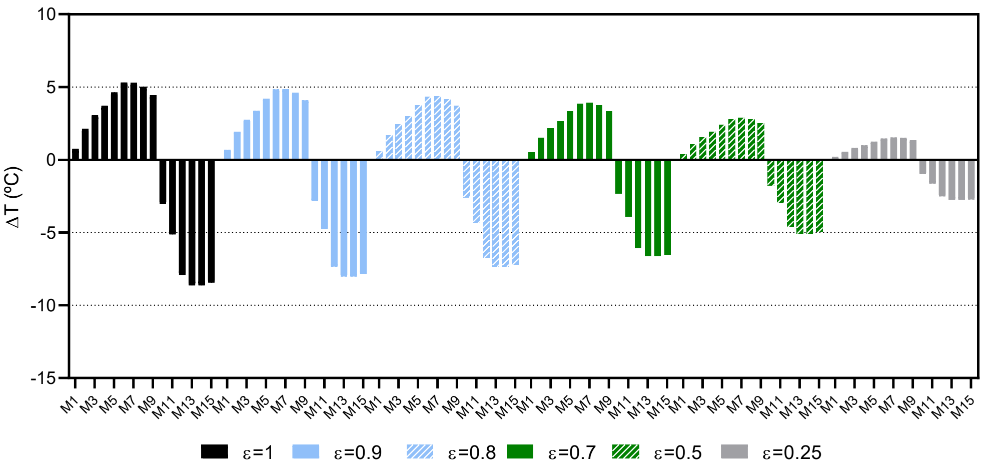
(a) Theoretical materials with emissivity variations in Phoenix

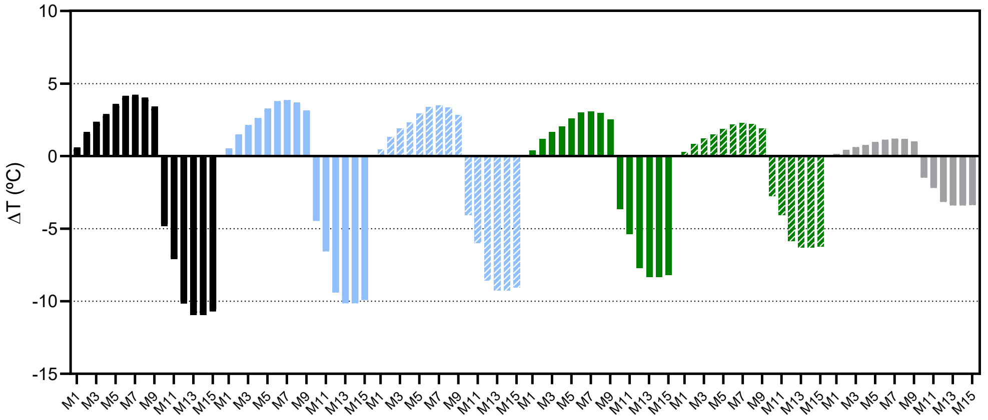
(b) Theoretical materials with emissivity variations in Sydney

Figure A. 9: Difference between mean ambient and surface temperature for theoretical materials (M1-M15) in Phoenix and Sydney. Positive values are materials that achieve sub-ambient cooling and negative values higher than ambient temperatures.

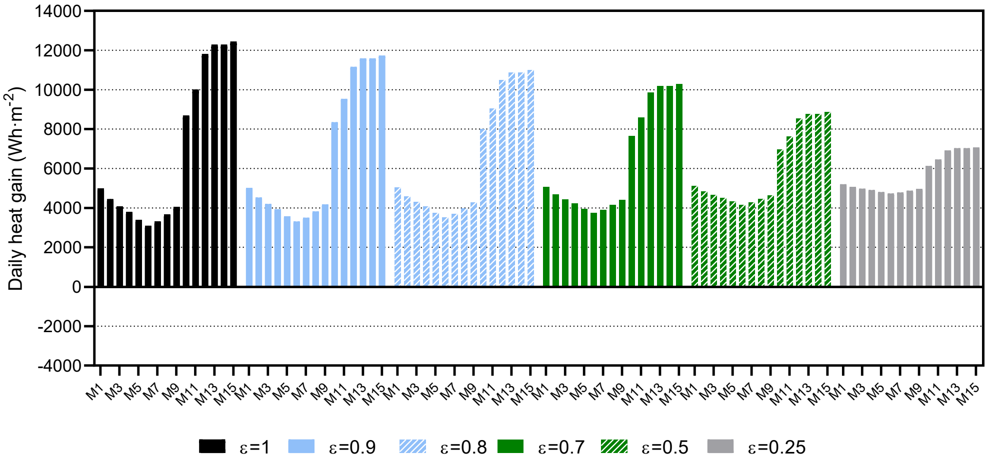
(a) Theoretical materials with emissivity variations in Phoenix

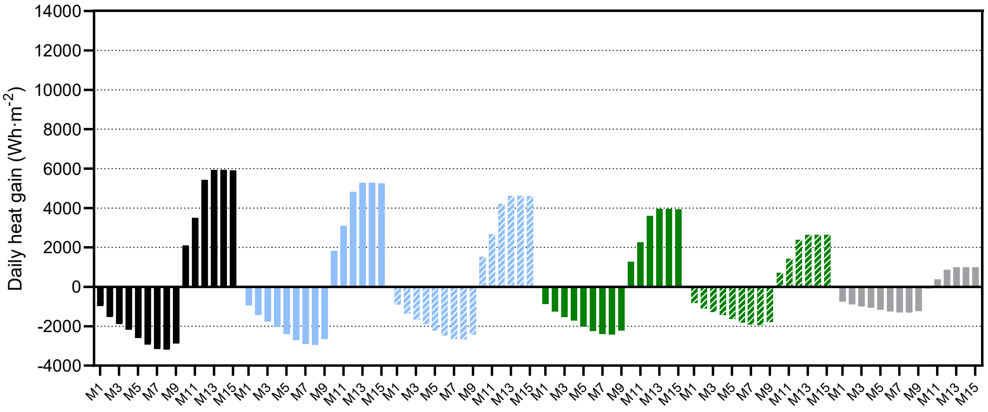
(b) Theoretical materials with emissivity variations in Sydney

Figure A. 10: Daily gains or losses for theoretical materials (M1-M15) in Phoenix and Sydney. Positive values are heat gains, and negative are heat losses.

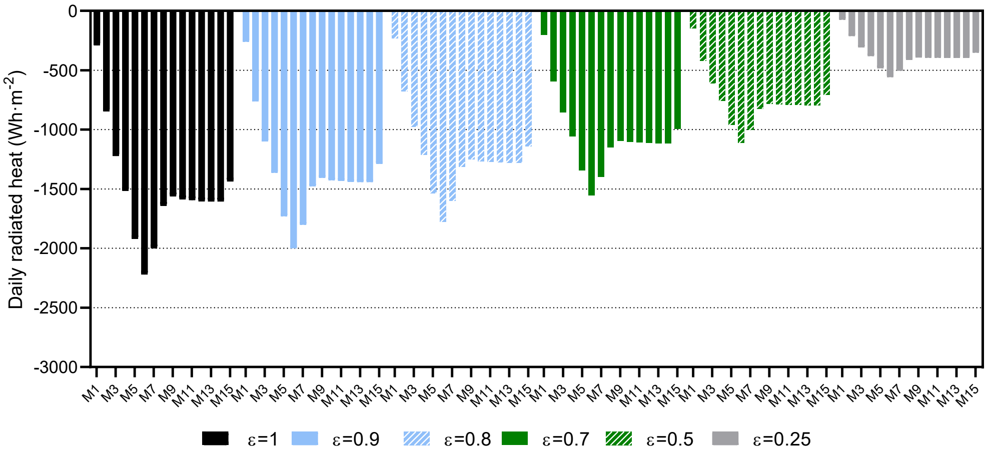
(a) Theoretical materials with emissivity variations in Phoenix

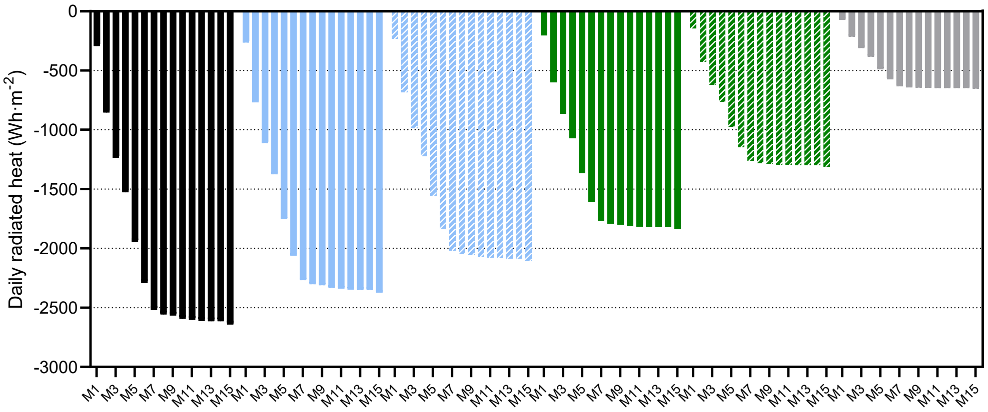
(b) Theoretical materials with emissivity variations in Sydney

Figure A. 11: Daily radiated heat for theoretical materials (M1-M15) in Phoenix and Sydney. Positive values are heat gains, and negative are heat losses.

APPENDIX 5: Synthesis of vanadium dioxide doped with tungsten[20]

Vanadium dioxide (IV) exhibits a transition phase at 68 °C, changing its electric resistivity and optical properties. Its transition can be achieved at a lower temperature by doping with high oxidation states such as tungsten. The synthesis reduced vanadium oxide (V) to vanadium oxide (IV) using oxalic acid with the presence of tungstic acid that acts as a doping agent with the procedure described in (Cao et al., 2008). The synthesis took place in Fisher-Porter immersed on a sand bath to achieve overpressure conditions (3 to 4 bars overpressure) and a constant temperature around 180 °C, maintaining these conditions during a week.

Figure A. 12: Reagents, from left to right: oxalic acid, vanadium oxide (V), and tungstic acid (IV).

---

[20] The synthesis was carried out by the technological Center L'Urederra.

The reagent's mix generates an orange dilution, as seen in Figure A. 13. Once the reaction advances, it changes towards green and blue.

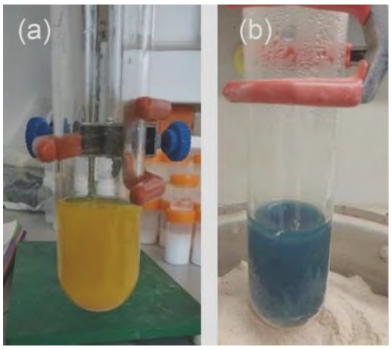

Figure A. 13: (a), initial dilution. (b), dilution after 2 hours.

After a week of reaction, a dark blue dilution is obtained with solid particles precipitated at the bottom, as shown in Figure A. 14. To obtain the vanadium oxide (IV) solid, the reaction was filtered and dried in a heater at 60 °C and was afterward collected in a filter paper. Several syntheses were made to obtain the required vanadium oxide quantity due to the reaction's efficiency and the Fisher-Porter tube capacity; the resulting quantity was not very abundant (Figure A. 15).

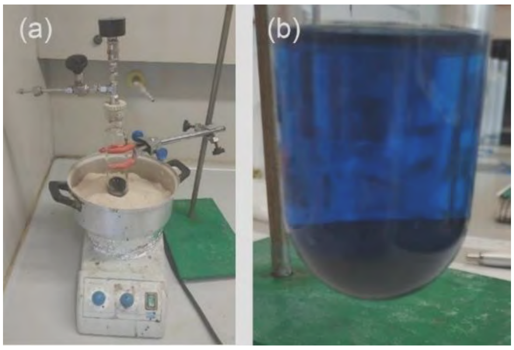

Figure A. 14: (a), reaction setting,(b): final result of the precipitated vanadium dioxide doped with tungsten.

Figure A. 15: Amount of vanadium dioxide particles obtained in one synthesis.

The two liquids obtained (Figure A. 16) formed the vanadium dioxide and emissive layers, respectively. The first consisted of the solid inside a matrix with 5% of the pigment to facilitate the aluminum adhesion. The second worked as the emissive layer.

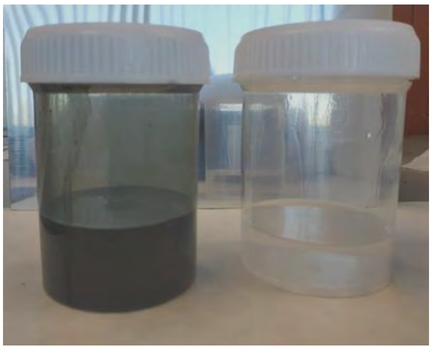

Figure A. 16: The two liquids for the tunable (left) and emissive layer (right).

The application was spray-coated in both cases, followed by a curation on a stove at 200 °C (Figure A. 17). Two layers of each product were deposited to obtain the best possible outcome.

Figure A. 17: Curation of the samples on a stove.

Finally, the inductively coupled plasma mass spectrometry (ICP-MS) was used to determine whether the doping with vanadium dioxide was successful. During the ICP-MS measurement, a liquid sample is introduced in an argon plasm, where the sample generates ions. The ions are separated according to their ratio mass/electric charge (m/z) by an analyzer (quadrupolar filter). The detector is tuned to select the goal m/z ratios. The semi-quantitative analysis sweeps the elemental spectra (48 elements), estimating the sample's element concentration. Therefore, achieving extensive information of the sample's components but with less precision. The semiquantitative analysis showed a high concentration of vanadium dioxide, saturating the sensor and the presence of tungsten around 1%, confirming the doping of vanadium dioxide with tungsten. Nevertheless, the actual percentage cannot be determined, as the measurement is not quantitative.

APPENDIX 6: Spectral characterization

As mentioned in Chapter 4, the reflectance of the first set of samples was characterized in the visible and near-infrared (0.3 to 2 μm) at the University of New South Wales, using a spectrophotometer (Agilent Technologies Cary Series UV-Vis-Nir Spectrophotometer) with an unpolarized light source and a calibrated high specular reflectance standard (Figure A. 18). Each sample measurement took around 2 minutes, and after each measurement, the machine was calibrated against a black standard sample.

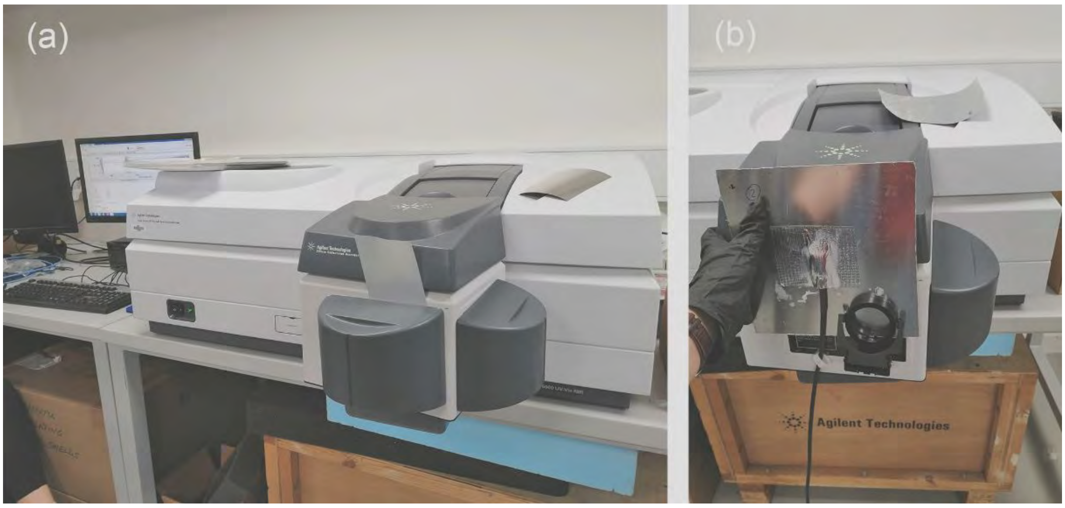

Figure A. 18: Agilent Technologies Cary Series UV-Vis-Nir Spectrophotometer (University of New South Wales).

The samples were characterized in the infrared (1.66 to 55 μm), a Fourier transform infrared spectrometer at the University of Sydney by Prof. Gianluca Ranzi and Dr. Giulia Ulpiani (Bruker Invenio R) with an unpolarized light source is used to characterize the cooler's reflectance with a gold film used as a reflectance standard (Figure A. 19). In this case, each sample's measurement took around 10 minutes, with a subsequent calibration of 2 minutes with the golden sphere. The samples with the commercial thermochromic pigments were heated up above their transition temperature, around 60 °C, and while the samples' emissivity was measured, the temperature was monitored with a probe (Table A. 13). In this case, since the heat was lost quickly, the spectrophotometer measurements were set to last only two minutes.

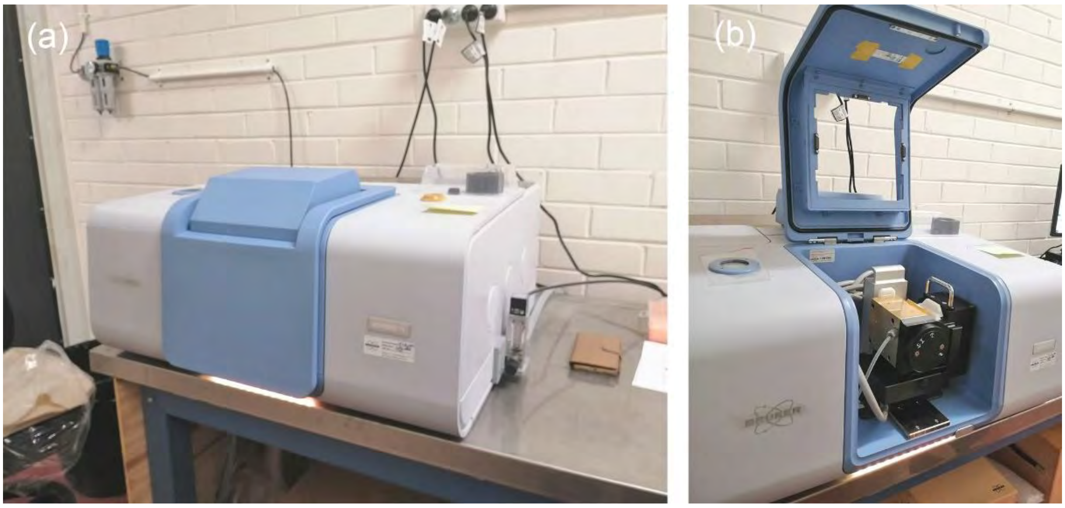

Figure A. 19: Bruker Invenio R Fourier transform infrared spectrometer (University of Sydney). (a) conducting measurement and (b)open lid to deposit the samples.

Table A. 13: Surfaces' temperature evolution of the heated samples with thermochromic pigment.

	ATS_1.1		**ATS_1.4**
% TIME	Sample T (°C)	% TIME	Sample T (°C)
5	37.7	19	34.8
11	35.6	35	33.2
19	34	38	33.6
30	33.5	45	32.9
63	35	58	32.2
70	33.8	69	31.8
82	33.1	75	31.5
90	33.8	88	31.3
		97	31.2

Although the samples were heated up well above the transition temperature, the emissivity did not show any apparent difference in the infrared wavelengths, as shown in Figure A. 20.

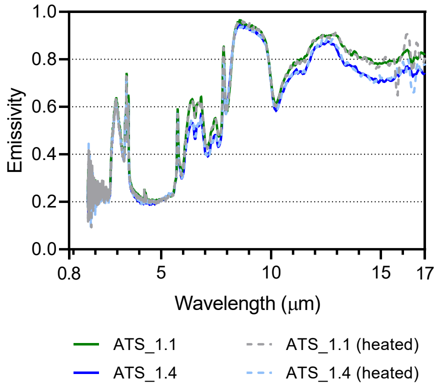

Figure A. 20: Comparison of the samples' emissivity at ambient temperature and when heated up above the transition temperature.

The reflectance of the second set of samples was characterized in the visible and near-infrared (from 200 to 1100 nm), using a combined Deuterium Halogen light source (Top Sensor System DH-2000-S) with an integrating sphere and a CCD spectrometer (OceanOptics USB2000-FLG) with an unpolarized light source and a calibrated high specular reflectance standard (Figure A. 21). The measurments were conducted with Prof. Javier Goicoeachea. The samples used as the black surface, the bare substrate. Finally, all the substrates, A, V2 were measured against the V1, which was the most reflective of the substrates. As a result, the characterization is relative to the substrates due to the impossibility to measure against a standard gold wafer like the one used for the infrared measurements.

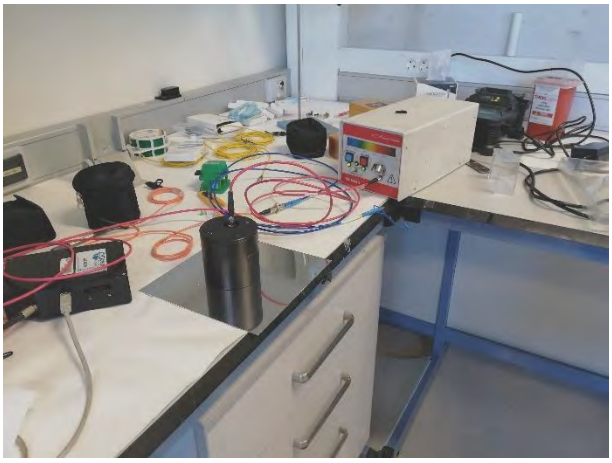

Figure A. 21: Deuterium Halogen light source (Top Sensor System DH-2000-S), Universidad Pública de Navarra.

A Fourier transform infrared spectrometer (Bruker Vertex 80V) equipped with an infrared microscope (Hyperion 3000) was employed to perform measurements in the near-infrared (NIR, 0.78-2.5 μm) and mid-infrared (MIR, 2.5-25 μm) (Figure A. 22). The excitation was done with unpolarized light sources (halogen lamp in the NIR and a Globar source in the MIR) and the detection with an InGaAs detector (NIR) and a nitrogen-cooled MCT detector (MIR). The cooler's reflectance was characterized in normal reflection with a gold mirror used as a reflectance standard. These measurements were carried out with Prof. Miguel Beruete.

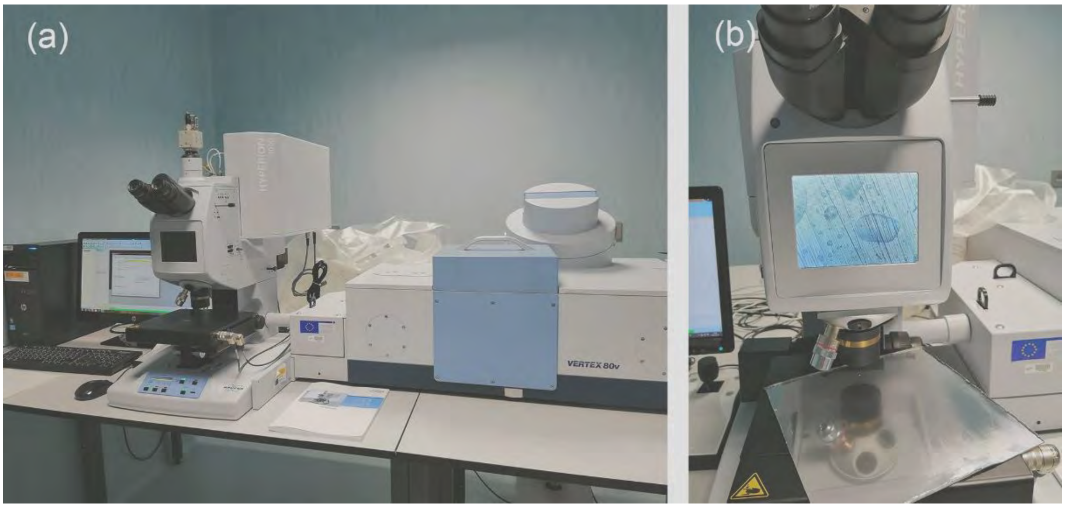

Figure A. 22: Bruker Vertex 80V Fourier transform infrared spectrometer equipped with a Hyperion 3000 infrared microscope.

As explained above, the second set of samples was characterized in the visible and near-infrared (from 200 to 1100 nm) using two experimental setups in the near-infrared (NIR, 0.78-2.5 μm) and mid-infrared (MIR, 2.5-25 μm). The second type of measurement was carried out with a normal incident ray instead of the integrating sphere. As a result, the received energy was lower than that of the integrating sphere.

Considering thermal radiation impinging on a medium of finite thickness, some irradiation will be reflected away, another fraction will be absorbed inside the layer, and the rest will be transmitted. Since all radiation must be either transmitted, absorbed, or transmitted:

$$1 = \alpha + \tau + r \tag{24}$$

Considering a medium that is sufficiently thick to be opaque, then τ=0 (the materials have no transmittance) the thermal balance is:

$$1 = \alpha + r \tag{25}$$

Kirchhoff's Law states that at a point on the surface of a thermal radiator at any temperature and wavelength, the spectral directional emittance is equal to the spectral absorptance for radiation incident from the same direction (Kelly, 1965).

$$\varepsilon_\lambda = \alpha_\lambda \tag{26}$$

Therefore, when transforming the spectral measurement of the average reflectivity to be higher, it results in lower emissivity, which is detrimental in those studied wavelengths study, presenting limitations when using the values to simulate the materials thermal behavior in Chapter 6.

The measurements from 200 to 1100 nm had some noise initially and at the end of the measurement. Besides not considering that information, a correction was deemed necessary to overlap the two measurements. Figure A. 23 (a) shows the values of the two measurements and (b) shows the correction is done and how each curve measurement is made to match using the previously described procedure. The optimization was done using the overlap from wavelengths 0.83568 μm to 0.94985 μm.

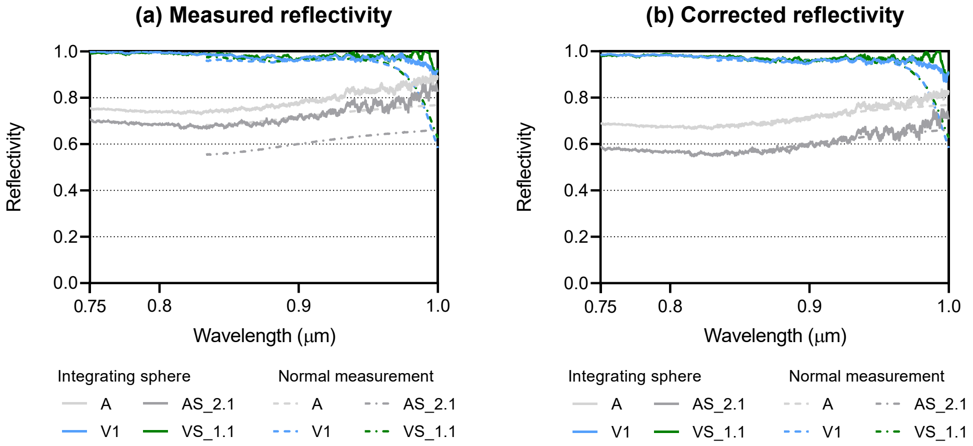

Figure A. 23: Reflectivity correction (a) measurements obtained from the integrating sphere and the normal measurements, (b) correction to overlap both measurements in the visible wavelengths.

APPENDIX 7: Materials spectral emissivity

This appendix presents the spectral emissivity values of four theoretical materials, two materials from the literature, and some of the developed materials in this thesis. The theoretical materials used are M5 to M8, described in chapter 3. The two materials from the literature are “Skycool” or RC1 and “Radicool” or RC2 that were used for validating the model (see APPENDIX 2: Model validation). Materials A, AS_2.2, AS_2.3, V_1.1, and V_1.2 developed in Chapter 4, tested in Chapter 5, and used for simulations in Chapter 6 are presented. The material’s emissivity is presented according to the 39 bands’ radiation spectrum division explained in APPENDIX 2: Band division. As a result, the developed materials’ performance was compared against the current state of the art under the same conditions.

Table A. 14: Spectral emissivity per band of the literature materials(RC1 and RC2), theoretical materials (M5-M8), and developed radiative cooling materials (A, AS_2.2, AS_2.3, V_1.1, and V_1.2.

	[1]	**[2]**	**LIT.MATERIAL**		**THEORETICAL MATERIALS**				**DEVELOPED MATERIALS**				
			RC1	**RC2**	**M5**	**M6**	**M7**	**M8**	**A**	**AS_2.2**	**AS_2.3**	**V_1.1**	**V_1.2**
1	0.28	0.30	0.8555	0.8400	0	0	0	0	0.193	0.193*	0.193*	0.024	0.024*
2	0.30	0.40	0.3714	0.5000	0	0	0	0	0.383	0.383*	0.383*	0.036	0.036*
3	0.40	0.50	0.0311	0.0320	0	0	0	0	0.229	0.436	0.375	0.022	0.000
4	0.50	1.00	0.0230	0.0260	0	0	0	0	0.216	0.443	0.384	0.029	0.000
5	1.00	2.00	0.0127	0.0410	0	0	0	0	0.142	0.325	0.234	0.852	0.822
6	2.00	2.50	0.0133	0.0980	0	0	0	0	0.153	0.281	0.182	0.887	0.852
7	2.50	3.00	0.2264	0.5200	0	0	0	0	0.142	0.196	0.223	0.938	0.875
8	3.00	4.00	0.2254	0.7200	0	0	0	0	0.126	0.142	0.158	0.948	0.881
9	4.00	4.17	0.0200	0.4000	0	0	0	0	0.118	0.081	0.060	0.944	0.902
10	4.17	4.44	0.0165	0.3700	0	0	0	1	0.129	0.081	0.056	0.956	0.886
11	4.44	5.00	0.0184	0.3900	0	0	0	1	0.111	0.079	0.060	0.968	0.869
12	5.00	7.00	0.0820	0.6700	0	0	0	1	0.105	0.061	0.067	0.979	0.902
13	7.00	7.14	0.1358	0.9500	0	0	1	1	0.099	0.062	0.080	0.979	0.930
14	7.14	8.29	0.3770	0.8700	0	0	1	1	0.097	0.105	0.123	0.978	0.891
15	8.29	8.82	0.7262	0.9100	0	1	1	1	0.094	0.315	0.420	0.949	0.854
16	8.82	9.10	0.7440	0.9300	1	1	1	1	0.093	0.376	0.544	0.907	0.852
17	9.10	9.35	0.8112	0.9500	1	1	1	1	0.094	0.395	0.586	0.913	0.828
18	9.35	9.65	0.8707	0.9500	1	1	1	1	0.091	0.441	0.668	0.911	0.868
19	9.65	9.98	0.7501	0.9500	1	1	1	1	0.089	0.443	0.681	0.904	0.869
20	9.98	10.50	0.6269	0.9600	1	1	1	1	0.090	0.295	0.420	0.945	0.861
21	10.50	11.33	0.6548	0.9100	1	1	1	1	0.089	0.298	0.394	0.942	0.850
22	11.33	11.95	0.5201	0.9300	1	1	1	1	0.088	0.244	0.252	0.934	0.845
23	11.95	12.30	0.5198	0.9600	1	1	1	1	0.085	0.299	0.325	0.940	0.865
24	12.30	12.73	0.5615	0.9400	1	1	1	1	0.088	0.320	0.358	0.928	0.850
25	12.73	13.16	0.5018	0.8800	1	1	1	1	0.080	0.323	0.366	0.933	0.867
26	13.16	13.33	0.4455	0.8600	0	1	1	1	0.084	0.272	0.269	0.915	0.841
27	13.33	13.59	0.4267	0.8600	0	1	1	1	0.079	0.238	0.207	0.924	0.857
28	13.59	15.36	0.3620	0.8500	0	0	1	1	0.087	0.164	0.106	0.914	0.859
29	15.36	17.24	0.3410	0.9000	0	0	1	1	0.081	0.118	0.065	0.929	0.874
30	17.24	17.46	0.3455	0.9300	0	0	0	1	0.073	0.116	0.073	0.885	0.835
31	17.46	18.40	0.3388	0.8900	0	0	0	1	0.072	0.147	0.103	0.925	0.878
32	18.40	19.15	0.3251	0.9100	0	0	0	1	0.069	0.305	0.247	0.955	0.908
33	19.15	20.00	0.3170	0.9600	0	0	0	0	0.064	0.409	0.283	0.964	0.934
34	20.00	20.84	0.3279	0.9300	0	0	0	0	0.066	0.397	0.246	0.970	0.947
35	20.84	21.59	0.3704	0.9200	0	0	0	0	0.068	0.507	0.317	0.974	0.939
36	21.59	22.41	0.4267	0.9400	0	0	0	0	0.059	0.347	0.222	0.984	0.940
37	22.41	25.00	0.4100	0.9700	0	0	0	0	0.058	0.264	0.178	0.977	0.958
38	25.00	50.00	0.4100	0.9700	0	0	0	0	0.038	0.290	0.184	0.974	0.941
39	50.00	75.00	0.4100	0.9700	0	0	0	0	0.070	0.290	0.184	0.974	0.941

APPENDIX 8: Simulations results

Chapter 6 simulation result values are presented in this appendix. The results are organized by city; for each, the monthly accumulated values are presented: radiative heat losses, solar heat gains, convective heat gains or losses, and total heat gains or losses ($kWh \cdot m^{-2}$). The results show the behavior of the 11 simulated materials in the 22 chosen locations grouped in 14 climates from the Köppen-Geiger classification.

The materials were simulated using the heat transfer model presented in Chapter 3 throughout a typical meteorological year. The background condition assimilated an active system, where a radiative cooling material was placed on top of a conductive surface with a fluid circulating at a constant temperature of 25 °C. Positive values are heat gains, whereas negative values are heat losses or cooling.

Bandung

Table A. 15: Bandung monthly accumulated radiative losses (kWh·m^{-2}).

	RC1	RC2	M5	M6	M7	M8	A	AS_2.2	AS_2.3	V_1.1	V_1.2
Jan	-22.0	-38.3	-22.1	-26.4	-34.9	-39.3	-3.8	-11.2	-13.2	-40.5	-37.4
Feb	-21.5	-37.3	-21.6	-25.8	-33.9	-38.2	-3.7	-10.9	-12.9	-39.4	-36.4
Mar	-22.0	-38.0	-22.3	-26.6	-34.9	-39.0	-3.7	-11.2	-13.2	-40.1	-37.0
Apr	-22.0	-37.5	-22.6	-27.0	-34.8	-38.7	-3.7	-11.1	-13.3	-39.5	-36.5
May	-27.3	-45.0	-29.9	-35.4	-43.4	-46.9	-4.4	-13.7	-16.8	-47.0	-43.3
Jun	-25.4	-42.6	-27.1	-32.2	-40.2	-44.1	-4.2	-12.8	-15.5	-44.7	-41.2
Jul	-25.3	-42.8	-26.7	-31.7	-40.1	-44.2	-4.2	-12.8	-15.4	-44.9	-41.4
Aug	-29.7	-49.0	-32.5	-38.4	-46.9	-50.9	-4.8	-15.0	-18.2	-51.1	-47.1
Sep	-25.5	-42.7	-27.2	-32.3	-40.3	-44.2	-4.2	-12.9	-15.6	-44.7	-41.3
Oct	-22.5	-38.0	-23.5	-28.0	-35.7	-39.3	-3.7	-11.4	-13.6	-40.0	-36.9
Nov	-18.1	-32.1	-17.5	-20.9	-28.7	-32.7	-3.2	-9.2	-10.8	-34.1	-31.5
Dec	-18.9	-33.6	-18.2	-21.8	-30.0	-34.2	-3.3	-9.7	-11.2	-35.7	-33.0

Table A. 16: Bandung monthly accumulated solar heat gains (kWh·m^{-2}).

	RC1	RC2	M5	M6	M7	M8	A	AS_2.2	AS_2.3	V_1.1	V_1.2
Jan	4.4	6.6	0.0	0.0	0.0	0.0	21.7	42.2	35.6	24.2	23.4
Feb	4.5	6.7	0.0	0.0	0.0	0.0	21.9	42.7	36.0	24.5	23.7
Mar	5.3	7.9	0.0	0.0	0.0	0.0	25.9	50.3	42.5	28.9	27.9
Apr	5.2	7.7	0.0	0.0	0.0	0.0	25.3	49.2	41.5	28.2	27.3
May	5.6	8.3	0.0	0.0	0.0	0.0	27.4	53.4	45.0	30.6	29.6
Jun	5.6	8.3	0.0	0.0	0.0	0.0	27.2	52.9	44.7	30.4	29.3
Jul	5.9	8.8	0.0	0.0	0.0	0.0	28.8	56.1	47.3	32.2	31.1
Aug	6.5	9.8	0.0	0.0	0.0	0.0	32.1	62.4	52.7	35.8	34.6
Sep	6.1	9.1	0.0	0.0	0.0	0.0	30.0	58.4	49.3	33.5	32.4
Oct	5.9	8.8	0.0	0.0	0.0	0.0	28.9	56.2	47.4	32.3	31.2
Nov	4.7	7.0	0.0	0.0	0.0	0.0	23.0	44.8	37.8	25.7	24.9
Dec	4.9	7.4	0.0	0.0	0.0	0.0	24.2	47.2	39.8	27.1	26.2

Table A. 17: Bandung monthly accumulated convective heat gains (positive values) and losses (negative values) (kWh·m^{-2}).

	RC1	RC2	M5	M6	M7	M8	A	AS_2.2	AS_2.3	V_1.1	V_1.2
Jan	-25.7	-25.6	-25.7	-25.7	-25.6	-25.6	-26.0	-26.1	-26.1	-25.8	-25.8
Feb	-26.2	-26.1	-26.1	-26.1	-26.0	-26.0	-26.5	-26.6	-26.5	-26.2	-26.2
Mar	-24.3	-24.2	-24.3	-24.3	-24.2	-24.2	-24.6	-24.7	-24.7	-24.4	-24.4
Apr	-19.8	-19.7	-19.8	-19.8	-19.7	-19.7	-20.1	-20.2	-20.1	-19.9	-19.9
May	-17.8	-17.7	-17.7	-17.7	-17.6	-17.6	-18.1	-18.3	-18.2	-17.9	-17.9
Jun	-20.4	-20.3	-20.4	-20.3	-20.3	-20.3	-20.7	-20.9	-20.8	-20.5	-20.5

Jul	-20.8	-20.7	-20.7	-20.7	-20.6	-20.6	-21.1	-21.3	-21.2	-20.9	-20.9
Aug	-20.8	-20.7	-20.7	-20.6	-20.6	-20.6	-21.1	-21.3	-21.2	-20.8	-20.9
Sep	-21.2	-21.1	-21.1	-21.1	-21.0	-21.0	-21.5	-21.7	-21.6	-21.2	-21.3
Oct	-17.2	-17.1	-17.1	-17.1	-17.0	-17.0	-17.5	-17.6	-17.5	-17.3	-17.3
Nov	-19.6	-19.5	-19.6	-19.6	-19.5	-19.5	-19.8	-19.9	-19.9	-19.7	-19.7
Dec	-21.9	-21.8	-21.9	-21.8	-21.8	-21.8	-22.1	-22.2	-22.2	-21.9	-21.9

Table A. 18: Bandung monthly accumulated total heat gains (positive values) and losses (negative values) (kWh·m^{-2}).

	RC1	RC2	M5	M6	M7	M8	A	AS_2.2	AS_2.3	V_1.1	V_1.2
Jan	-43.4	-57.4	-47.8	-52.1	-60.5	-64.9	-8.1	4.9	-3.6	-42.1	-39.8
Feb	-43.2	-56.7	-47.8	-51.9	-59.9	-64.2	-8.2	5.2	-3.4	-41.1	-39.0
Mar	-41.0	-54.3	-46.6	-50.9	-59.1	-63.2	-2.5	14.4	4.6	-35.6	-33.5
Apr	-36.6	-49.6	-42.4	-46.7	-54.5	-58.4	1.5	17.9	8.1	-31.2	-29.1
May	-39.5	-54.4	-47.6	-53.1	-61.0	-64.6	4.9	21.4	10.1	-34.2	-31.6
Jun	-40.3	-54.7	-47.4	-52.5	-60.5	-64.4	2.3	19.2	8.4	-34.8	-32.4
Jul	-40.2	-54.7	-47.4	-52.4	-60.7	-64.8	3.5	22.0	10.7	-33.6	-31.3
Aug	-43.9	-59.9	-53.1	-59.1	-67.5	-71.5	6.1	26.2	13.2	-36.2	-33.4
Sep	-40.5	-54.6	-48.3	-53.3	-61.3	-65.2	4.3	23.9	12.2	-32.5	-30.1
Oct	-33.7	-46.3	-40.7	-45.1	-52.7	-56.4	7.7	27.2	16.3	-25.0	-23.0
Nov	-33.0	-44.6	-37.1	-40.5	-48.2	-52.2	0.0	15.6	7.2	-28.0	-26.3
Dec	-35.8	-48.0	-40.1	-43.7	-51.7	-56.0	-1.2	15.3	6.4	-30.6	-28.8

Singapore

Table A. 19: Singapore monthly accumulated radiative heat losses (kWh·m^{-2}).

	RC1	RC2	M5	M6	M7	M8	A	AS_2.2	AS_2.3	V_1.1	V_1.2
Jan	-15.9	-22.2	-20.4	-24.3	-26.5	-24.9	-2.2	-7.6	-10.1	-22.2	-20.3
Feb	-15.9	-21.8	-20.8	-24.7	-26.4	-24.5	-2.1	-7.6	-10.2	-21.7	-19.7
Mar	-13.0	-17.1	-17.8	-21.1	-22.2	-19.7	-1.7	-6.2	-8.4	-16.7	-15.1
Apr	-12.2	-15.8	-16.8	-19.9	-20.9	-18.3	-1.5	-5.8	-7.9	-15.3	-13.9
May	-10.0	-11.5	-14.9	-17.7	-17.5	-14.1	-1.1	-4.6	-6.6	-10.6	-9.6
Jun	-10.4	-12.9	-14.8	-17.6	-18.1	-15.3	-1.2	-4.9	-6.8	-12.3	-11.1
Jul	-14.1	-18.2	-19.6	-23.2	-24.0	-21.1	-1.8	-6.7	-9.2	-17.6	-16.0
Aug	-13.9	-17.8	-19.2	-22.7	-23.5	-20.7	-1.7	-6.5	-9.0	-17.3	-15.7
Sep	-13.8	-18.3	-18.6	-22.1	-23.3	-21.0	-1.8	-6.5	-8.9	-18.0	-16.3
Oct	-9.0	-10.9	-12.9	-15.3	-15.8	-13.1	-1.0	-4.2	-5.9	-10.3	-9.3
Nov	-7.9	-10.3	-10.6	-12.5	-13.8	-12.1	-1.0	-3.7	-5.0	-10.1	-9.2
Dec	-11.7	-15.9	-15.4	-18.3	-19.9	-18.1	-1.5	-5.6	-7.5	-15.7	-14.3

Table A. 20: Singapore monthly accumulated solar heat gains (kWh·m^{-2}).

	RC1	RC2	M5	M6	M7	M8	A	AS_2.2	AS_2.3	V_1.1	V_1.2
Jan	6.2	9.2	0.0	0.0	0.0	0.0	30.2	58.9	49.7	33.8	32.6
Feb	6.2	9.2	0.0	0.0	0.0	0.0	30.2	58.8	49.6	33.7	32.6
Mar	6.6	9.9	0.0	0.0	0.0	0.0	32.5	63.3	53.4	36.3	35.1
Apr	6.0	8.9	0.0	0.0	0.0	0.0	29.2	56.8	47.9	32.6	31.5
May	5.8	8.7	0.0	0.0	0.0	0.0	28.5	55.4	46.8	31.8	30.7
Jun	5.5	8.3	0.0	0.0	0.0	0.0	27.1	52.8	44.6	30.3	29.3
Jul	5.8	8.6	0.0	0.0	0.0	0.0	28.4	55.3	46.6	31.7	30.7
Aug	5.9	8.8	0.0	0.0	0.0	0.0	28.9	56.3	47.5	32.3	31.2
Sep	5.8	8.7	0.0	0.0	0.0	0.0	28.5	55.5	46.8	31.8	30.8
Oct	5.8	8.7	0.0	0.0	0.0	0.0	28.5	55.4	46.8	31.8	30.7
Nov	5.0	7.5	0.0	0.0	0.0	0.0	24.7	48.1	40.6	27.6	26.7
Dec	5.2	7.8	0.0	0.0	0.0	0.0	25.6	49.9	42.1	28.6	27.7

Table A. 21: Singapore monthly accumulated convective heat gains (positive values) and losses (negative values) (kWh·m^{-2}).

	RC1	RC2	M5	M6	M7	M8	A	AS_2.2	AS_2.3	V_1.1	V_1.2
Jan	15.0	15.0	15.1	15.1	15.2	15.1	14.6	14.3	14.4	14.7	14.7
Feb	18.3	18.3	18.5	18.5	18.5	18.5	17.9	17.6	17.7	18.0	18.0
Mar	19.1	19.1	19.2	19.2	19.2	19.2	18.7	18.4	18.6	18.8	18.8
Apr	15.4	15.4	15.5	15.5	15.5	15.5	15.1	14.9	15.0	15.2	15.2
May	22.1	22.0	22.1	22.2	22.2	22.1	21.8	21.6	21.7	21.8	21.8
Jun	19.7	19.7	19.8	19.8	19.8	19.8	19.4	19.2	19.3	19.4	19.4
Jul	24.9	24.9	25.0	25.0	25.0	25.0	24.5	24.2	24.3	24.6	24.6
Aug	25.0	25.0	25.2	25.2	25.2	25.2	24.7	24.4	24.5	24.8	24.8
Sep	18.1	18.1	18.2	18.2	18.2	18.2	17.7	17.5	17.6	17.8	17.8
Oct	17.4	17.4	17.5	17.5	17.5	17.5	17.2	16.9	17.0	17.2	17.2
Nov	10.4	10.4	10.4	10.4	10.4	10.4	10.2	10.0	10.1	10.2	10.2
Dec	12.2	12.2	12.3	12.3	12.3	12.3	11.9	11.7	11.8	12.0	12.0

Table A. 22: Singapore monthly accumulated total heat gains (positive values) and losses (negative values) (kWh·m^{-2}).

	RC1	RC2	M5	M6	M7	M8	A	AS_2.2	AS_2.3	V_1.1	V_1.2
Jan	5.3	2.0	-5.3	-9.1	-11.3	-9.7	42.7	65.5	54.0	26.3	27.1
Feb	8.6	5.7	-2.3	-6.2	-7.9	-6.0	46.0	68.7	57.1	30.1	30.9
Mar	12.7	11.9	1.4	-1.9	-3.0	-0.5	49.6	75.6	63.5	38.4	38.8
Apr	9.1	8.5	-1.3	-4.4	-5.4	-2.8	42.8	66.0	55.0	32.4	32.8
May	17.9	19.2	7.2	4.5	4.6	8.1	49.2	72.4	61.8	43.0	43.0
Jun	14.8	15.1	4.9	2.2	1.7	4.5	45.3	67.1	57.0	37.5	37.6
Jul	16.5	15.3	5.4	1.9	1.1	3.9	51.1	72.8	61.8	38.7	39.2
Aug	17.1	16.0	6.0	2.4	1.6	4.5	51.9	74.2	63.0	39.8	40.3

Sep	10.1	8.5	-0.4	-3.9	-5.1	-2.8	44.4	66.4	55.5	31.7	32.3
Oct	14.2	15.2	4.6	2.2	1.8	4.4	44.6	68.2	57.9	38.7	38.6
Nov	7.5	7.5	-0.1	-2.1	-3.3	-1.6	33.9	54.4	45.6	27.7	27.7
Dec	5.7	4.1	-3.1	-6.0	-7.6	-5.9	36.0	56.1	46.5	24.9	25.3

Yangon

Table A. 23: Yangon monthly accumulated radiative heat losses (kWh·m^{-2}).

	RC1	RC2	M5	M6	M7	M8	A	AS_2.2	AS_2.3	V_1.1	V_1.2
Jan	-27.9	-39.4	-36.2	-42.6	-45.2	-43.4	-3.8	-13.5	-17.9	-39.4	-36.0
Feb	-18.5	-24.6	-25.1	-29.5	-30.4	-27.7	-2.4	-8.8	-12.0	-24.1	-21.9
Mar	-23.1	-29.5	-32.4	-38.2	-38.2	-33.8	-2.8	-10.9	-15.2	-28.6	-25.9
Apr	-19.7	-24.0	-28.4	-33.6	-32.9	-28.1	-2.3	-9.2	-13.0	-22.9	-20.7
May	-15.3	-20.1	-20.7	-24.5	-25.7	-23.0	-1.9	-7.2	-9.9	-19.6	-17.8
Jun	-12.6	-18.1	-15.7	-18.7	-21.2	-20.1	-1.8	-6.1	-7.9	-18.2	-16.6
Jul	-12.2	-16.9	-15.8	-18.8	-20.7	-19.1	-1.7	-5.8	-7.8	-16.9	-15.4
Aug	-7.6	-10.2	-10.1	-12.0	-13.5	-11.8	-1.0	-3.6	-4.9	-10.0	-9.1
Sep	-11.7	-15.7	-15.4	-18.4	-19.9	-18.0	-1.5	-5.5	-7.5	-15.5	-14.1
Oct	-10.8	-12.3	-16.1	-19.0	-18.7	-15.1	-1.2	-4.9	-7.1	-11.4	-10.3
Nov	-17.1	-22.4	-23.4	-27.6	-28.5	-25.5	-2.2	-8.1	-11.1	-21.8	-19.8
Dec	-22.8	-31.9	-29.5	-34.8	-37.2	-35.4	-3.1	-11.0	-14.6	-31.9	-29.1

Table A. 24: Yangon monthly accumulated solar heat gains (kWh·m^{-2}).

	RC1	RC2	M5	M6	M7	M8	A	AS_2.2	AS_2.3	V_1.1	V_1.2
Jan	6.5	9.6	0.0	0.0	0.0	0.0	31.7	61.7	52.1	35.4	34.2
Feb	6.0	9.0	0.0	0.0	0.0	0.0	29.4	57.2	48.3	32.8	31.7
Mar	7.9	11.8	0.0	0.0	0.0	0.0	38.7	75.3	63.5	43.2	41.7
Apr	7.3	10.9	0.0	0.0	0.0	0.0	35.9	69.9	58.9	40.1	38.7
May	6.1	9.1	0.0	0.0	0.0	0.0	29.7	57.9	48.8	33.2	32.1
Jun	5.4	8.1	0.0	0.0	0.0	0.0	26.6	51.8	43.7	29.7	28.7
Jul	6.0	8.9	0.0	0.0	0.0	0.0	29.2	56.8	47.9	32.6	31.5
Aug	4.6	6.9	0.0	0.0	0.0	0.0	22.5	43.8	37.0	25.2	24.3
Sep	5.3	7.8	0.0	0.0	0.0	0.0	25.7	50.1	42.3	28.7	27.8
Oct	5.9	8.8	0.0	0.0	0.0	0.0	28.8	56.0	47.3	32.1	31.1
Nov	5.9	8.8	0.0	0.0	0.0	0.0	28.9	56.3	47.5	32.3	31.2
Dec	6.1	9.1	0.0	0.0	0.0	0.0	30.1	58.5	49.4	33.6	32.4

Table A. 25: Yangon monthly accumulated convective heat gains (positive values) and losses (negative values) (kWh·m^{-2}).

	RC1	RC2	M5	M6	M7	M8	A	AS_2.2	AS_2.3	V_1.1	V_1.2
Jan	22.4	22.4	22.6	22.6	22.6	22.6	21.9	21.6	21.8	22.1	22.1
Feb	28.2	28.2	28.4	28.4	28.4	28.4	27.8	27.5	27.6	27.9	27.9
Mar	45.3	45.3	45.5	45.5	45.5	45.5	44.7	44.3	44.5	44.9	44.9
Apr	52.7	52.7	52.9	53.0	53.0	52.9	52.1	51.7	51.9	52.3	52.3
May	27.8	27.9	28.0	28.0	28.1	28.0	27.3	27.0	27.1	27.5	27.5
Jun	12.0	12.0	12.1	12.2	12.2	12.2	11.6	11.3	11.4	11.7	11.7
Jul	18.5	18.5	18.6	18.6	18.6	18.6	18.0	17.7	17.8	18.1	18.1
Aug	16.4	16.4	16.5	16.6	16.6	16.5	16.2	15.9	16.0	16.2	16.2
Sep	18.7	18.7	18.8	18.8	18.8	18.8	18.4	18.1	18.2	18.5	18.5
Oct	35.8	35.8	36.0	36.0	36.0	35.9	35.4	35.1	35.3	35.5	35.5
Nov	30.8	30.8	31.0	31.0	31.0	31.0	30.4	30.1	30.3	30.5	30.5
Dec	22.2	22.2	22.3	22.4	22.4	22.4	21.7	21.4	21.6	21.9	21.9

Table A. 26: Yangon monthly accumulated total heat gains (positive values) and losses (negative values) (kWh·m^{-2}).

	RC1	RC2	M5	M6	M7	M8	A	AS_2.2	AS_2.3	V_1.1	V_1.2
Jan	0.9	-7.3	-13.7	-20.0	-22.6	-20.8	49.7	69.8	55.9	18.1	20.3
Feb	15.8	12.6	3.3	-1.1	-2.0	0.6	54.8	75.9	63.9	36.6	37.7
Mar	30.1	27.5	13.1	7.4	7.3	11.6	80.5	108.6	92.8	59.5	60.7
Apr	40.3	39.6	24.5	19.4	20.0	24.8	85.7	112.3	97.8	69.5	70.3
May	18.6	16.8	7.3	3.5	2.4	5.0	55.1	77.6	66.1	41.1	41.8
Jun	4.9	2.0	-3.6	-6.5	-9.0	-8.0	36.4	57.0	47.2	23.2	23.8
Jul	12.2	10.4	2.8	-0.1	-2.1	-0.5	45.6	68.7	58.0	33.9	34.3
Aug	13.4	13.1	6.4	4.5	3.1	4.7	37.7	56.2	48.1	31.4	31.5
Sep	12.3	10.8	3.4	0.5	-1.0	0.9	42.6	62.7	53.0	31.7	32.1
Oct	31.0	32.3	19.9	17.0	17.3	20.9	63.1	86.2	75.4	56.2	56.3
Nov	19.7	17.3	7.6	3.4	2.5	5.4	57.2	78.4	66.7	41.0	41.9
Dec	5.6	-0.6	-7.2	-12.5	-14.8	-13.0	48.7	68.9	56.3	23.6	25.2

Rio de Janeiro

Table A. 27: Rio de Janeiro monthly accumulated radiative heat losses (kWh·m^{-2}).

	RC1	RC2	M5	M6	M7	M8	A	AS_2.2	AS_2.3	V_1.1	V_1.2
Jan	-13.1	-18.1	-17.2	-20.4	-22.1	-20.4	-1.8	-6.3	-8.4	-18.0	-16.4
Feb	-14.2	-19.7	-18.4	-21.8	-23.7	-22.1	-1.9	-6.8	-9.1	-19.7	-18.0
Mar	-20.3	-29.4	-25.6	-30.3	-33.3	-32.3	-2.9	-9.9	-12.9	-29.7	-27.1
Apr	-16.6	-25.7	-19.4	-23.0	-27.1	-27.6	-2.5	-8.2	-10.3	-26.4	-24.3
May	-26.8	-42.8	-30.3	-35.9	-42.7	-45.1	-4.2	-13.3	-16.6	-44.3	-40.8

Jun	-28.2	-46.4	-30.8	-36.6	-44.7	-48.4	-4.6	-14.2	-17.3	-48.4	-44.6
Jul	-34.8	-57.0	-38.5	-45.6	-55.0	-59.4	-5.6	-17.5	-21.4	-59.3	-54.7
Aug	-24.4	-40.4	-26.5	-31.4	-38.9	-42.1	-4.0	-12.3	-14.9	-42.2	-38.9
Sep	-18.1	-30.4	-19.1	-22.8	-29.1	-31.6	-3.0	-9.1	-11.0	-31.9	-29.4
Oct	-14.9	-23.3	-17.2	-20.4	-24.4	-25.0	-2.3	-7.4	-9.2	-24.0	-22.1
Nov	-16.5	-24.6	-19.9	-23.6	-27.0	-26.8	-2.4	-8.1	-10.3	-25.1	-23.0
Dec	-12.4	-17.4	-15.9	-18.9	-20.9	-19.5	-1.7	-6.0	-7.9	-17.5	-15.9

Table A. 28: Rio de Janeiro monthly accumulated solar heat gains (kWh·m^{-2}).

	RC1	**RC2**	**M5**	**M6**	**M7**	**M8**	**A**	**AS_2.2**	**AS_2.3**	**V_1.1**	**V_1.2**
Jan	7.7	11.5	0.0	0.0	0.0	0.0	37.9	73.8	62.3	42.3	40.9
Feb	6.7	10.0	0.0	0.0	0.0	0.0	32.7	63.7	53.7	36.5	35.3
Mar	6.9	10.3	0.0	0.0	0.0	0.0	33.9	65.9	55.6	37.8	36.6
Apr	5.2	7.7	0.0	0.0	0.0	0.0	25.4	49.5	41.8	28.4	27.4
May	5.1	7.6	0.0	0.0	0.0	0.0	24.9	48.4	40.9	27.8	26.9
Jun	4.1	6.1	0.0	0.0	0.0	0.0	20.2	39.2	33.1	22.5	21.8
Jul	5.0	7.5	0.0	0.0	0.0	0.0	24.6	47.8	40.4	27.4	26.5
Aug	5.4	8.0	0.0	0.0	0.0	0.0	26.3	51.1	43.2	29.3	28.4
Sep	5.4	8.1	0.0	0.0	0.0	0.0	26.5	51.5	43.5	29.5	28.6
Oct	6.4	9.6	0.0	0.0	0.0	0.0	31.6	61.4	51.8	35.2	34.1
Nov	6.7	10.1	0.0	0.0	0.0	0.0	33.1	64.3	54.3	36.9	35.7
Dec	7.4	11.1	0.0	0.0	0.0	0.0	36.4	70.8	59.7	40.6	39.3

Table A. 29: Rio de Janeiro monthly accumulated convective heat gains (positive values) and losses (negative values) (kWh·m^{-2}).

	RC1	**RC2**	**M5**	**M6**	**M7**	**M8**	**A**	**AS_2.2**	**AS_2.3**	**V_1.1**	**V_1.2**
Jan	14.1	14.1	14.2	14.3	14.3	14.3	13.7	13.4	13.6	13.8	13.8
Feb	12.1	12.1	12.2	12.2	12.3	12.2	11.7	11.5	11.6	11.8	11.8
Mar	8.4	8.4	8.5	8.5	8.6	8.5	8.0	7.8	7.9	8.2	8.2
Apr	-1.3	-1.3	-1.2	-1.2	-1.2	-1.2	-1.6	-1.8	-1.7	-1.4	-1.5
May	-13.7	-13.6	-13.7	-13.6	-13.6	-13.6	-14.1	-14.2	-14.1	-13.8	-13.8
Jun	-20.8	-20.7	-20.7	-20.7	-20.6	-20.6	-21.1	-21.2	-21.1	-20.8	-20.8
Jul	-26.4	-26.3	-26.3	-26.3	-26.2	-26.2	-26.8	-27.0	-26.9	-26.5	-26.5
Aug	-20.0	-19.9	-20.0	-19.9	-19.9	-19.8	-20.4	-20.6	-20.5	-20.1	-20.1
Sep	-20.6	-20.5	-20.5	-20.5	-20.5	-20.4	-20.9	-21.1	-21.0	-20.7	-20.7
Oct	-2.6	-2.6	-2.5	-2.5	-2.4	-2.4	-3.0	-3.3	-3.2	-2.9	-2.9
Nov	3.3	3.3	3.4	3.4	3.4	3.4	2.8	2.5	2.7	3.0	3.0
Dec	12.1	12.1	12.2	12.2	12.3	12.2	11.7	11.4	11.5	11.8	11.8

Table A. 30: Rio de Janeiro monthly accumulated total heat gains (positive values) and losses (negative values) (kWh·m^{-2}).

	RC1	RC2	M5	M6	M7	M8	A	AS_2.2	AS_2.3	V_1.1	V_1.2
Jan	8.7	7.6	-3.0	-6.1	-7.9	-6.1	49.9	80.9	67.4	38.2	38.4
Feb	4.6	2.3	-6.2	-9.6	-11.4	-9.9	42.5	68.3	56.2	28.7	29.2
Mar	-5.0	-10.7	-17.1	-21.8	-24.8	-23.8	39.0	63.8	50.6	16.3	17.6
Apr	-12.7	-19.2	-20.6	-24.2	-28.3	-28.8	21.3	39.5	29.7	0.5	1.7
May	-35.4	-48.9	-44.0	-49.5	-56.3	-58.7	6.6	20.9	10.2	-30.4	-27.8
Jun	-44.9	-61.0	-51.6	-57.3	-65.4	-69.0	-5.5	3.9	-5.3	-46.7	-43.7
Jul	-56.2	-75.8	-64.9	-71.9	-81.2	-85.5	-7.9	3.4	-8.0	-58.3	-54.6
Aug	-39.1	-52.3	-46.4	-51.3	-58.7	-61.9	1.9	18.3	7.7	-33.0	-30.7
Sep	-33.3	-42.8	-39.7	-43.3	-49.5	-52.1	2.5	21.3	11.4	-23.0	-21.5
Oct	-11.1	-16.3	-19.7	-22.8	-26.9	-27.4	26.2	50.7	39.4	8.4	9.1
Nov	-6.4	-11.3	-16.5	-20.2	-23.5	-23.4	33.5	58.8	46.6	14.8	15.6
Dec	7.1	5.7	-3.7	-6.6	-8.6	-7.3	46.4	76.2	63.3	35.0	35.1

Lagos

Table A. 31: Lagos monthly accumulated radiative heat losses (kWh·m^{-2}).

	RC1	RC2	M5	M6	M7	M8	A	AS_2.2	AS_2.3	V_1.1	V_1.2
Jan	-20.5	-28.3	-27.0	-31.9	-33.9	-31.7	-2.7	-9.8	-13.2	-28.1	-25.6
Feb	-17.3	-22.4	-23.8	-28.2	-29.0	-25.8	-2.2	-8.2	-11.2	-21.8	-19.8
Mar	-18.0	-22.6	-25.3	-30.1	-30.4	-26.3	-2.2	-8.4	-11.8	-21.7	-19.6
Apr	-16.2	-21.1	-22.2	-26.4	-27.4	-24.3	-2.0	-7.7	-10.5	-20.5	-18.6
May	-11.7	-14.5	-16.6	-19.7	-20.2	-17.2	-1.4	-5.5	-7.7	-13.9	-12.6
Jun	-11.0	-15.4	-14.1	-16.7	-18.7	-17.4	-1.5	-5.3	-7.0	-15.4	-14.1
Jul	-11.8	-17.0	-14.8	-17.6	-19.9	-18.9	-1.7	-5.7	-7.5	-17.1	-15.6
Aug	-16.0	-23.8	-19.4	-23.1	-26.4	-26.0	-2.3	-7.8	-10.1	-24.2	-22.2
Sep	-11.0	-16.1	-13.4	-16.0	-18.5	-17.8	-1.6	-5.3	-6.9	-16.3	-14.9
Oct	-11.7	-15.8	-15.6	-18.5	-20.0	-18.1	-1.5	-5.6	-7.5	-15.6	-14.2
Nov	-17.9	-24.0	-23.8	-28.3	-29.8	-27.2	-2.3	-8.5	-11.5	-23.7	-21.5
Dec	-21.6	-28.9	-29.0	-34.4	-35.9	-32.8	-2.8	-10.3	-14.0	-28.4	-25.9

Table A. 32: Lagos monthly accumulated solar heat gains (kWh·m^{-2}).

	RC1	RC2	M5	M6	M7	M8	A	AS_2.2	AS_2.3	V_1.1	V_1.2
Jan	6.1	9.1	0.0	0.0	0.0	0.0	29.9	58.3	49.2	33.4	32.3
Feb	5.8	8.7	0.0	0.0	0.0	0.0	28.5	55.5	46.9	31.9	30.8
Mar	6.7	10.0	0.0	0.0	0.0	0.0	32.7	63.7	53.8	36.6	35.3
Apr	6.5	9.7	0.0	0.0	0.0	0.0	31.7	61.7	52.1	35.4	34.2
May	6.2	9.3	0.0	0.0	0.0	0.0	30.5	59.3	50.0	34.0	32.9
Jun	4.9	7.3	0.0	0.0	0.0	0.0	24.1	46.9	39.6	26.9	26.0
Jul	5.0	7.5	0.0	0.0	0.0	0.0	24.7	48.1	40.6	27.6	26.7
Aug	5.7	8.5	0.0	0.0	0.0	0.0	28.0	54.6	46.0	31.3	30.3

Sep	5.4	8.0	0.0	0.0	0.0	0.0	26.4	51.3	43.3	29.4	28.4
Oct	5.9	8.8	0.0	0.0	0.0	0.0	29.1	56.6	47.7	32.5	31.4
Nov	6.1	9.1	0.0	0.0	0.0	0.0	29.8	57.9	48.9	33.2	32.1
Dec	6.0	9.0	0.0	0.0	0.0	0.0	29.5	57.5	48.5	33.0	31.9

Table A. 33: Lagos monthly accumulated convective heat gains (positive values) and losses (negative values) (kWh·m^{-2}).

	RC1	**RC2**	**M5**	**M6**	**M7**	**M8**	**A**	**AS_2.2**	**AS_2.3**	**V_1.1**	**V_1.2**
Jan	20.8	20.8	20.9	21.0	21.0	20.9	20.3	20.1	20.2	20.5	20.5
Feb	33.8	33.8	33.9	34.0	34.0	33.9	33.2	32.9	33.1	33.4	33.4
Mar	45.8	45.9	46.1	46.1	46.1	46.1	45.2	44.9	45.1	45.4	45.4
Apr	33.1	33.1	33.3	33.4	33.4	33.3	32.6	32.2	32.4	32.7	32.7
May	26.6	26.5	26.7	26.7	26.7	26.7	26.2	25.8	26.0	26.2	26.2
Jun	11.9	12.0	12.0	12.1	12.1	12.1	11.6	11.4	11.5	11.7	11.7
Jul	13.3	13.3	13.4	13.4	13.5	13.5	12.9	12.5	12.7	13.0	13.0
Aug	6.1	6.2	6.3	6.3	6.4	6.3	5.6	5.2	5.4	5.8	5.8
Sep	8.1	8.1	8.2	8.3	8.3	8.3	7.7	7.4	7.5	7.8	7.8
Oct	19.4	19.4	19.5	19.6	19.6	19.5	19.0	18.7	18.8	19.1	19.1
Nov	23.5	23.5	23.7	23.7	23.7	23.7	23.1	22.8	22.9	23.2	23.2
Dec	27.1	27.1	27.2	27.3	27.3	27.3	26.7	26.4	26.6	26.9	26.9

Table A. 34: Lagos monthly accumulated solar heat gains (positive values) and losses (negative values) (kWh·m^{-2}).

	RC1	**RC2**	**M5**	**M6**	**M7**	**M8**	**A**	**AS_2.2**	**AS_2.3**	**V_1.1**	**V_1.2**
Jan	6.3	1.6	-6.1	-11.0	-13.0	-10.8	47.5	68.5	56.2	25.9	27.2
Feb	22.3	20.1	10.2	5.8	5.0	8.2	59.6	80.3	68.7	43.5	44.4
Mar	34.5	33.3	20.7	16.0	15.7	19.7	75.8	100.2	87.1	60.3	61.1
Apr	23.4	21.7	11.1	7.0	6.0	9.0	62.3	86.3	73.9	47.6	48.3
May	21.0	21.3	10.1	7.0	6.5	9.5	55.2	79.6	68.3	46.3	46.5
Jun	5.9	3.9	-2.0	-4.6	-6.6	-5.3	34.2	53.0	44.1	23.2	23.7
Jul	6.5	3.8	-1.4	-4.2	-6.4	-5.5	35.9	54.9	45.8	23.5	24.0
Aug	-4.2	-9.1	-13.2	-16.8	-20.1	-19.7	31.3	52.0	41.4	12.9	13.9
Sep	2.5	0.1	-5.2	-7.7	-10.2	-9.6	32.4	53.3	43.9	20.9	21.3
Oct	13.6	12.5	4.0	1.1	-0.4	1.5	46.5	69.7	59.0	36.0	36.3
Nov	11.7	8.6	-0.1	-4.6	-6.1	-3.6	50.5	72.2	60.3	32.8	33.8
Dec	11.5	7.2	-1.8	-7.1	-8.6	-5.5	53.4	73.6	61.1	31.4	32.9

Monterrey

Table A. 35: Monterrey monthly accumulated radiative heat (kWh·m^{-2}).

	RC1	RC2	M5	M6	M7	M8	A	AS_2.2	AS_2.3	V_1.1	V_1.2
Jan	-33.8	-59.1	-34.2	-40.4	-52.5	-59.9	-5.8	-17.3	-20.4	-62.4	-57.7
Feb	-29.8	-50.5	-31.5	-37.2	-46.5	-51.7	-4.9	-15.1	-18.2	-53.0	-49.0
Mar	-30.5	-48.5	-35.1	-41.3	-48.2	-51.0	-4.7	-15.3	-19.0	-50.2	-46.2
Apr	-24.1	-36.3	-29.5	-34.6	-38.7	-39.0	-3.5	-11.9	-15.3	-37.0	-33.9
May	-23.8	-32.5	-31.7	-37.3	-38.8	-36.2	-3.1	-11.5	-15.4	-32.2	-29.4
Jun	-21.6	-28.2	-29.8	-35.1	-35.6	-32.0	-2.7	-10.3	-14.1	-27.5	-25.0
Jul	-18.6	-23.4	-26.4	-31.0	-31.0	-27.0	-2.2	-8.8	-12.2	-22.6	-20.4
Aug	-23.0	-29.7	-32.0	-37.6	-37.9	-33.9	-2.9	-10.9	-15.1	-29.0	-26.3
Sep	-18.1	-26.0	-22.9	-27.0	-29.7	-28.6	-2.5	-8.8	-11.5	-26.2	-24.0
Oct	-26.1	-40.6	-30.7	-36.3	-41.9	-43.2	-4.0	-12.9	-16.3	-41.7	-38.3
Nov	-30.4	-51.2	-32.5	-38.4	-47.7	-52.7	-5.0	-15.4	-18.6	-53.6	-49.5
Dec	-31.8	-56.7	-31.0	-36.8	-49.3	-57.0	-5.6	-16.4	-19.0	-60.1	-55.7

Table A. 36: Monterrey monthly accumulated solar heat gains (kWh·m^{-2}).

	RC1	RC2	M5	M6	M7	M8	A	AS_2.2	AS_2.3	V_1.1	V_1.2
Jan	4.3	6.5	0.0	0.0	0.0	0.0	21.2	41.3	34.9	23.7	22.9
Feb	5.1	7.6	0.0	0.0	0.0	0.0	24.9	48.5	41.0	27.8	26.9
Mar	6.9	10.2	0.0	0.0	0.0	0.0	33.7	65.5	55.3	37.6	36.3
Apr	7.5	11.1	0.0	0.0	0.0	0.0	36.6	71.3	60.1	40.9	39.5
May	8.3	12.4	0.0	0.0	0.0	0.0	40.7	79.2	66.9	45.5	43.9
Jun	8.7	12.9	0.0	0.0	0.0	0.0	42.5	82.6	69.7	47.4	45.8
Jul	8.8	13.2	0.0	0.0	0.0	0.0	43.2	84.1	71.0	48.3	46.6
Aug	8.5	12.7	0.0	0.0	0.0	0.0	41.8	81.4	68.6	46.7	45.1
Sep	6.9	10.3	0.0	0.0	0.0	0.0	33.7	65.6	55.4	37.7	36.4
Oct	6.0	9.0	0.0	0.0	0.0	0.0	29.5	57.4	48.5	33.0	31.8
Nov	4.8	7.2	0.0	0.0	0.0	0.0	23.6	46.0	38.8	26.4	25.5
Dec	4.0	6.0	0.0	0.0	0.0	0.0	19.7	38.4	32.4	22.0	21.3

Table A. 37: Monterrey monthly accumulated convective heat gains (positive values) and losses (negative values) (kWh·m^{-2}).

	RC1	RC2	M5	M6	M7	M8	A	AS_2.2	AS_2.3	V_1.1	V_1.2
Jan	-54.0	-53.8	-53.9	-53.9	-53.8	-53.7	-54.4	-54.5	-54.4	-54.0	-54.0
Feb	-42.2	-42.1	-42.2	-42.1	-42.0	-42.0	-42.7	-42.9	-42.8	-42.3	-42.3
Mar	-19.8	-19.7	-19.7	-19.6	-19.5	-19.5	-20.4	-20.6	-20.5	-20.0	-20.0
Apr	2.1	2.2	2.2	2.3	2.3	2.3	1.5	1.2	1.4	1.8	1.8
May	23.8	23.8	24.0	24.0	24.1	24.0	23.1	22.7	22.9	23.4	23.4
Jun	33.4	33.5	33.6	33.7	33.7	33.7	32.8	32.4	32.6	33.0	33.0
Jul	37.0	37.0	37.2	37.2	37.2	37.2	36.4	35.9	36.1	36.5	36.5

Aug	35.4	35.4	35.6	35.6	35.6	35.6	34.8	34.4	34.6	35.0	35.0
Sep	9.7	9.7	9.8	9.9	9.9	9.9	9.3	9.1	9.2	9.5	9.5
Oct	-5.8	-5.7	-5.7	-5.6	-5.6	-5.6	-6.2	-6.4	-6.3	-5.9	-6.0
Nov	-33.9	-33.8	-33.8	-33.8	-33.7	-33.7	-34.3	-34.5	-34.4	-33.9	-34.0
Dec	-59.5	-59.3	-59.5	-59.4	-59.3	-59.3	-59.9	-60.0	-59.9	-59.5	-59.5

Table A. 38: Monterrey monthly accumulated total heat gains (positive values) and losses (negative values) (kWh·m^{-2}).

	RC1	**RC2**	**M5**	**M6**	**M7**	**M8**	**A**	**AS_2.2**	**AS_2.3**	**V_1.1**	**V_1.2**
Jan	-83.5	-106.4	-88.1	-94.3	-106.3	-113.6	-39.0	-30.5	-39.9	-92.7	-88.8
Feb	-66.9	-85.0	-73.7	-79.3	-88.6	-93.7	-22.7	-9.5	-20.0	-67.5	-64.4
Mar	-43.4	-57.9	-54.8	-60.9	-67.8	-70.5	8.6	29.6	15.8	-32.6	-29.8
Apr	-14.5	-23.0	-27.2	-32.4	-36.4	-36.7	34.6	60.6	46.2	5.7	7.4
May	8.3	3.7	-7.7	-13.2	-14.7	-12.2	60.7	90.5	74.4	36.6	37.9
Jun	20.6	18.2	3.9	-1.4	-1.9	1.6	72.5	104.7	88.2	52.9	53.8
Jul	27.2	26.7	10.8	6.2	6.2	10.1	77.3	111.2	94.8	62.2	62.7
Aug	21.0	18.4	3.6	-2.0	-2.2	1.7	73.7	104.9	88.2	52.7	53.8
Sep	-1.5	-6.0	-13.0	-17.1	-19.8	-18.8	40.5	65.9	53.1	20.9	21.9
Oct	-25.9	-37.3	-36.4	-41.9	-47.4	-48.8	19.3	38.0	25.8	-14.7	-12.4
Nov	-59.5	-77.8	-66.3	-72.2	-81.4	-86.4	-15.7	-3.9	-14.1	-61.2	-58.0
Dec	-87.3	-110.0	-90.5	-96.2	-108.6	-116.3	-45.7	-37.9	-46.5	-97.6	-93.9

Phoenix

Table A. 39: Phoenix monthly accumulated radiative heat losses (kWh·m^{-2}).

	RC1	**RC2**	**M5**	**M6**	**M7**	**M8**	**A**	**AS_2.2**	**AS_2.3**	**V_1.1**	**V_1.2**
Jan	-51.1	-86.2	-55.4	-64.7	-79.0	-88.1	-8.4	-26.1	-31.4	-90.3	-83.4
Feb	-41.9	-70.6	-45.4	-53.1	-64.9	-72.3	-6.9	-21.4	-25.8	-74.0	-68.3
Mar	-42.3	-68.2	-48.6	-56.6	-66.0	-71.0	-6.7	-21.3	-26.4	-70.8	-65.2
Apr	-43.2	-65.5	-53.8	-62.1	-67.9	-69.7	-6.4	-21.6	-27.6	-66.9	-61.5
May	-33.8	-44.9	-47.5	-54.7	-54.1	-50.0	-4.3	-16.4	-22.4	-44.0	-40.1
Jun	-38.4	-47.3	-57.3	-65.9	-61.8	-54.1	-4.5	-18.4	-25.9	-45.1	-40.9
Jul	-24.6	-24.0	-41.5	-47.9	-40.8	-30.1	-2.2	-11.2	-17.2	-20.6	-18.2
Aug	-20.7	-20.2	-34.9	-40.4	-34.8	-25.6	-1.9	-9.5	-14.5	-17.4	-15.4
Sep	-33.3	-41.6	-48.6	-56.3	-53.7	-47.5	-4.0	-15.9	-22.3	-40.0	-36.3
Oct	-33.9	-49.7	-43.3	-50.2	-53.7	-53.6	-4.8	-16.7	-21.8	-50.2	-46.0
Nov	-52.2	-83.1	-61.3	-71.1	-81.3	-86.7	-8.1	-26.3	-32.7	-85.8	-79.0
Dec	-46.1	-79.9	-47.7	-56.0	-71.0	-80.8	-7.8	-23.6	-28.0	-84.2	-77.8

Table A. 40: Phoenix monthly accumulated solar heat gains (kWh·m^{-2}).

	RC1	RC2	M5	M6	M7	M8	A	AS_2.2	AS_2.3	V_1.1	V_1.2
Jan	4.3	6.5	0.0	0.0	0.0	0.0	21.3	41.4	35.0	23.8	23.0
Feb	5.0	7.4	0.0	0.0	0.0	0.0	24.4	47.4	40.0	27.2	26.3
Mar	7.1	10.5	0.0	0.0	0.0	0.0	34.6	67.3	56.7	38.6	37.3
Apr	9.1	13.5	0.0	0.0	0.0	0.0	44.4	86.5	73.0	49.6	47.9
May	10.4	15.5	0.0	0.0	0.0	0.0	50.8	98.9	83.4	56.7	54.8
Jun	10.6	15.9	0.0	0.0	0.0	0.0	52.1	101.4	85.6	58.2	56.2
Jul	10.1	15.0	0.0	0.0	0.0	0.0	49.3	96.0	81.0	55.1	53.3
Aug	9.4	14.1	0.0	0.0	0.0	0.0	46.2	89.9	75.8	51.6	49.8
Sep	8.1	12.1	0.0	0.0	0.0	0.0	39.8	77.4	65.3	44.4	42.9
Oct	6.4	9.5	0.0	0.0	0.0	0.0	31.3	60.8	51.3	34.9	33.7
Nov	4.8	7.2	0.0	0.0	0.0	0.0	23.7	46.0	38.9	26.4	25.5
Dec	4.1	6.1	0.0	0.0	0.0	0.0	19.9	38.7	32.7	22.2	21.5

Table A. 41: Phoenix monthly accumulated convective heat gains (positive values) and losses (negative values) (kWh·m^{-2}).

	RC1	RC2	M5	M6	M7	M8	A	AS_2.2	AS_2.3	V_1.1	V_1.2
Jan	-74.0	-73.7	-73.9	-73.8	-73.6	-73.6	-74.6	-74.6	-74.5	-73.8	-73.9
Feb	-64.2	-63.9	-64.1	-64.0	-63.9	-63.8	-64.8	-64.9	-64.8	-64.1	-64.2
Mar	-44.2	-43.9	-44.0	-43.9	-43.8	-43.8	-44.9	-45.1	-45.0	-44.2	-44.3
Apr	-12.1	-11.9	-11.8	-11.7	-11.7	-11.6	-13.1	-13.5	-13.2	-12.4	-12.4
May	45.0	45.1	45.4	45.4	45.4	45.4	44.1	43.6	43.9	44.5	44.5
Jun	78.9	78.9	79.3	79.4	79.3	79.2	77.9	77.4	77.7	78.3	78.3
Jul	109.5	109.4	109.9	109.9	109.8	109.7	108.7	108.1	108.4	108.8	108.8
Aug	89.4	89.3	89.7	89.8	89.7	89.6	88.6	88.1	88.4	88.8	88.8
Sep	58.1	58.1	58.3	58.4	58.4	58.3	57.3	57.0	57.2	57.7	57.7
Oct	7.8	7.9	8.0	8.1	8.1	8.1	7.2	6.9	7.1	7.6	7.6
Nov	-41.0	-40.7	-40.8	-40.7	-40.6	-40.6	-41.6	-41.7	-41.5	-40.9	-41.0
Dec	-79.7	-79.4	-79.7	-79.6	-79.5	-79.4	-80.3	-80.3	-80.2	-79.6	-79.6

Table A. 42: Phoenix monthly accumulated total heat gains (positive values) and losses (negative values) (kWh·m^{-2}).

	RC1	RC2	M5	M6	M7	M8	A	AS_2.2	AS_2.3	V_1.1	V_1.2
Jan	-120.7	-153.4	-129.2	-138.4	-152.7	-161.6	-61.7	-59.3	-70.9	-140.3	-134.3
Feb	-101.1	-127.1	-109.5	-117.1	-128.8	-136.1	-47.3	-38.9	-50.5	-110.9	-106.2
Mar	-79.4	-101.6	-92.6	-100.5	-109.8	-114.7	-17.0	0.8	-14.6	-76.4	-72.2
Apr	-46.2	-63.9	-65.6	-73.9	-79.5	-81.4	25.0	51.4	32.1	-29.7	-26.0
May	21.6	15.7	-2.1	-9.2	-8.6	-4.7	90.6	126.1	104.9	57.2	59.2
Jun	51.1	47.5	22.0	13.5	17.6	25.2	125.5	160.4	137.3	91.4	93.6
Jul	95.0	100.4	68.3	62.0	69.0	79.5	155.8	192.9	172.2	143.2	143.8

Aug	78.1	83.2	54.8	49.3	54.9	64.0	133.0	168.6	149.7	123.0	123.2
Sep	32.9	28.6	9.7	2.1	4.7	10.8	93.1	118.5	100.2	62.1	64.3
Oct	-19.7	-32.3	-35.3	-42.2	-45.6	-45.5	33.6	51.1	36.7	-7.7	-4.7
Nov	-88.3	-116.6	-102.1	-111.8	-121.9	-127.3	-26.1	-21.9	-35.4	-100.3	-94.4
Dec	-121.7	-153.3	-127.4	-135.6	-150.5	-160.2	-68.2	-65.3	-75.5	-141.6	-136.0

Zaragoza

Table A. 43: Zaragoza monthly accumulated radiative heat losses (kWh·m^{-2}).

	RC1	RC2	M5	M6	M7	M8	A	AS_2.2	AS_2.3	V_1.1	V_1.2
Jan	-46.0	-85.5	-41.8	-49.7	-70.1	-84.1	-8.4	-24.0	-27.0	-91.3	-84.7
Feb	-42.8	-77.6	-40.7	-48.2	-65.4	-77.1	-7.6	-22.2	-25.4	-82.5	-76.5
Mar	-45.6	-80.3	-45.9	-54.2	-70.3	-80.8	-7.9	-23.5	-27.5	-84.9	-78.6
Apr	-43.2	-74.5	-45.0	-53.0	-67.0	-75.6	-7.3	-22.1	-26.3	-78.4	-72.5
May	-42.2	-68.9	-47.5	-55.7	-66.1	-71.5	-6.7	-21.3	-26.2	-71.7	-66.1
Jun	-37.1	-56.6	-45.0	-52.7	-58.9	-60.3	-5.5	-18.4	-23.5	-57.9	-53.2
Jul	-39.9	-58.7	-50.3	-59.0	-63.6	-63.4	-5.7	-19.6	-25.5	-59.5	-54.5
Aug	-35.2	-52.3	-43.8	-51.4	-56.1	-56.3	-5.1	-17.3	-22.4	-53.1	-48.7
Sep	-38.3	-61.2	-44.2	-51.9	-60.3	-64.1	-6.0	-19.2	-23.9	-63.3	-58.2
Oct	-35.8	-61.5	-37.1	-43.8	-55.7	-62.7	-6.0	-18.2	-21.7	-64.8	-59.8
Nov	-41.3	-74.9	-39.4	-46.8	-63.5	-74.6	-7.3	-21.4	-24.6	-79.6	-73.8
Dec	-46.0	-85.5	-41.7	-49.7	-70.1	-84.0	-8.3	-24.0	-27.0	-91.3	-84.7

Table A. 44: Zaragoza monthly accumulated solar heat gains (kWh·m^{-2}).

	RC1	RC2	M5	M6	M7	M8	A	AS_2.2	AS_2.3	V_1.1	V_1.2
Jan	2.4	3.5	0.0	0.0	0.0	0.0	11.6	22.6	19.1	13.0	12.5
Feb	3.3	5.0	0.0	0.0	0.0	0.0	16.4	31.9	26.9	18.3	17.7
Mar	5.6	8.3	0.0	0.0	0.0	0.0	27.3	53.1	44.8	30.4	29.4
Apr	7.1	10.5	0.0	0.0	0.0	0.0	34.6	67.4	56.8	38.6	37.4
May	8.7	12.9	0.0	0.0	0.0	0.0	42.5	82.7	69.7	47.4	45.8
Jun	9.4	14.0	0.0	0.0	0.0	0.0	45.9	89.4	75.4	51.3	49.6
Jul	10.0	15.0	0.0	0.0	0.0	0.0	49.2	95.7	80.8	54.9	53.1
Aug	8.6	12.8	0.0	0.0	0.0	0.0	41.9	81.6	68.9	46.8	45.3
Sep	6.4	9.6	0.0	0.0	0.0	0.0	31.4	61.2	51.6	35.1	33.9
Oct	4.3	6.4	0.0	0.0	0.0	0.0	21.0	40.9	34.5	23.5	22.7
Nov	2.8	4.2	0.0	0.0	0.0	0.0	13.7	26.6	22.5	15.3	14.8
Dec	2.1	3.1	0.0	0.0	0.0	0.0	10.1	19.7	16.6	11.3	10.9

Table A. 45: Zaragoza monthly accumulated convective heat gains (positive values) and losses (negative values) (kWh·m^{-2}).

	RC1	RC2	M5	M6	M7	M8	A	AS2.2	AS_2.3	V_1.1	V_1.2
Jan	-210.2	-209.6	-210.2	-210.1	-209.8	-209.5	-210.9	-210.8	-210.7	-209.6	-209.7
Feb	-186.9	-186.3	-186.9	-186.7	-186.4	-186.2	-187.8	-187.8	-187.7	-186.5	-186.6
Mar	-162.6	-162.1	-162.5	-162.4	-162.1	-161.9	-163.6	-163.9	-163.6	-162.4	-162.5
Apr	-131.5	-131.1	-131.3	-131.2	-131.0	-130.8	-132.7	-133.1	-132.8	-131.6	-131.6
May	-74.1	-73.8	-73.9	-73.8	-73.6	-73.5	-75.3	-75.8	-75.5	-74.4	-74.4
Jun	-20.2	-20.0	-19.9	-19.8	-19.7	-19.7	-21.4	-22.0	-21.7	-20.7	-20.7
Jul	10.7	10.9	11.0	11.2	11.3	11.3	9.3	8.6	9.0	10.1	10.0
Aug	2.2	2.4	2.5	2.7	2.7	2.7	1.1	0.5	0.9	1.8	1.7
Sep	-48.0	-47.7	-47.8	-47.7	-47.5	-47.5	-48.9	-49.2	-49.0	-48.1	-48.1
Oct	-82.0	-81.7	-81.9	-81.8	-81.7	-81.6	-82.7	-82.9	-82.8	-82.0	-82.0
Nov	-169.1	-168.6	-169.1	-169.0	-168.7	-168.5	-169.9	-169.9	-169.8	-168.7	-168.8
Dec	-196.4	-195.8	-196.4	-196.3	-196.0	-195.8	-197.0	-197.0	-196.9	-195.9	-196.0

Table A. 46: Zaragoza monthly accumulated total heat gains (positive values) and losses (negative values) (kWh·m^{-2}).

	RC1	RC2	M5	M6	M7	M8	A	AS2.2	AS_2.3	V_1.1	V_1.2
Jan	-253.8	-291.6	-252.0	-259.8	-279.9	-293.6	-207.7	-212.3	-218.7	-288.0	-281.9
Feb	-226.3	-259.0	-227.6	-234.9	-251.9	-263.3	-179.0	-178.2	-186.2	-250.8	-245.4
Mar	-202.7	-234.1	-208.5	-216.5	-232.4	-242.8	-144.2	-134.3	-146.4	-216.9	-211.7
Apr	-167.7	-195.0	-176.3	-184.2	-197.9	-206.5	-105.4	-87.9	-102.3	-171.4	-166.8
May	-107.7	-129.7	-121.3	-129.4	-139.7	-145.0	-39.6	-14.5	-32.0	-98.6	-94.7
Jun	-47.9	-62.6	-64.9	-72.5	-78.6	-80.0	19.0	49.0	30.3	-27.3	-24.4
Jul	-19.2	-32.9	-39.3	-47.8	-52.4	-52.2	52.7	84.7	64.2	5.5	8.6
Aug	-24.4	-37.1	-41.3	-48.7	-53.3	-53.5	37.9	64.8	47.3	-4.5	-1.7
Sep	-79.9	-99.3	-92.0	-99.6	-107.9	-111.6	-23.5	-7.2	-21.2	-76.3	-72.5
Oct	-113.5	-136.8	-119.0	-125.7	-137.4	-144.3	-67.7	-60.2	-69.9	-123.2	-119.2
Nov	-207.7	-239.3	-208.5	-215.7	-232.2	-243.1	-163.5	-164.7	-171.8	-233.0	-227.8
Dec	-240.3	-278.2	-238.1	-246.0	-266.1	-279.9	-195.3	-201.2	-207.2	-275.8	-269.7

Karachi

Table A. 47: Karachi monthly accumulated radiative heat losses (kWh·m^{-2}).

	RC1	RC2	M5	M6	M7	M8	A	AS_2.2	AS_2.3	V_1.1	V_1.2
Jan	-40.5	-65.1	-46.5	-54.4	-63.4	-67.9	-6.4	-20.3	-25.2	-67.5	-62.1
Feb	-34.2	-52.7	-41.0	-48.0	-54.0	-55.9	-5.1	-17.0	-21.5	-54.1	-49.7
Mar	-31.4	-44.8	-40.7	-47.7	-50.4	-49.0	-4.3	-15.3	-20.2	-44.9	-41.1
Apr	-28.5	-38.0	-38.9	-45.7	-46.4	-42.7	-3.7	-13.6	-18.6	-37.4	-34.0

May	-23.7	-29.1	-34.0	-40.2	-39.5	-34.0	-2.8	-11.1	-15.6	-27.8	-25.1
Jun	-21.1	-25.3	-30.7	-36.3	-35.5	-29.9	-2.4	-9.8	-13.9	-23.9	-21.6
Jul	-11.6	-12.1	-18.5	-21.8	-20.4	-15.4	-1.1	-5.3	-7.9	-10.8	-9.6
Aug	-17.8	-22.5	-25.1	-29.7	-29.9	-26.1	-2.2	-8.4	-11.7	-21.6	-19.6
Sep	-27.8	-37.2	-37.4	-44.2	-45.5	-41.9	-3.6	-13.3	-18.0	-36.7	-33.4
Oct	-32.2	-43.1	-43.8	-51.5	-52.2	-48.3	-4.2	-15.4	-21.0	-42.4	-38.6
Nov	-31.6	-46.7	-39.7	-46.5	-50.5	-50.4	-4.5	-15.5	-20.2	-47.3	-43.4
Dec	-34.1	-54.5	-39.3	-46.1	-53.7	-57.1	-5.3	-17.1	-21.3	-56.3	-51.9

Table A. 48: Karachi monthly accumulated solar heat gains (kWh·m^{-2}).

	RC1	**RC2**	**M5**	**M6**	**M7**	**M8**	**A**	**AS_2.2**	**AS_2.3**	**V_1.1**	**V_1.2**
Jan	5.4	8.1	0.0	0.0	0.0	0.0	26.5	51.5	43.5	29.6	28.6
Feb	5.4	8.1	0.0	0.0	0.0	0.0	26.5	51.7	43.6	29.6	28.7
Mar	7.0	10.5	0.0	0.0	0.0	0.0	34.3	66.8	56.4	38.3	37.1
Apr	7.8	11.7	0.0	0.0	0.0	0.0	38.4	74.7	63.0	42.8	41.4
May	8.2	12.2	0.0	0.0	0.0	0.0	40.1	78.0	65.8	44.7	43.2
Jun	7.7	11.5	0.0	0.0	0.0	0.0	37.9	73.7	62.2	42.3	40.9
Jul	6.3	9.4	0.0	0.0	0.0	0.0	30.9	60.2	50.8	34.5	33.4
Aug	6.3	9.4	0.0	0.0	0.0	0.0	30.9	60.2	50.8	34.5	33.4
Sep	7.2	10.7	0.0	0.0	0.0	0.0	35.2	68.5	57.8	39.3	38.0
Oct	6.8	10.2	0.0	0.0	0.0	0.0	33.4	65.0	54.9	37.3	36.1
Nov	5.3	7.9	0.0	0.0	0.0	0.0	26.0	50.7	42.8	29.1	28.1
Dec	4.8	7.1	0.0	0.0	0.0	0.0	23.5	45.7	38.6	26.2	25.3

Table A. 49: Karachi monthly accumulated convective heat gains (positive values) and losses (negative values) (kWh·m^{-2}).

	RC1	**RC2**	**M5**	**M6**	**M7**	**M8**	**A**	**AS_2.2**	**AS_2.3**	**V_1.1**	**V_1.2**
Jan	-33.6	-33.4	-33.5	-33.4	-33.3	-33.3	-34.2	-34.4	-34.2	-33.7	-33.7
Feb	-13.8	-13.7	-13.7	-13.6	-13.5	-13.5	-14.4	-14.6	-14.4	-13.9	-14.0
Mar	18.1	18.2	18.3	18.4	18.4	18.4	17.5	17.2	17.4	17.9	17.8
Apr	45.1	45.2	45.4	45.5	45.5	45.4	44.3	43.8	44.1	44.6	44.6
May	78.7	78.7	79.0	79.1	79.1	79.0	77.7	77.0	77.4	78.0	78.0
Jun	80.4	80.4	80.8	80.9	80.8	80.7	79.5	78.9	79.2	79.8	79.8
Jul	74.6	74.6	74.9	74.9	74.9	74.8	74.0	73.5	73.7	74.1	74.1
Aug	53.7	53.7	53.9	54.0	54.0	53.9	52.9	52.5	52.7	53.2	53.2
Sep	44.4	44.5	44.7	44.8	44.8	44.7	43.6	43.1	43.4	44.0	44.0
Oct	37.1	37.1	37.3	37.4	37.4	37.3	36.5	36.2	36.4	36.8	36.8
Nov	4.8	4.9	4.9	5.0	5.0	5.0	4.4	4.2	4.3	4.7	4.7
Dec	-22.7	-22.5	-22.6	-22.5	-22.5	-22.4	-23.2	-23.3	-23.2	-22.7	-22.8

Table A. 50: Karachi monthly accumulated total heat gains (positive values) and losses (negative values) (kWh·m^{-2}).

	RC1	RC2	M5	M6	M7	M8	A	AS_2.2	AS_2.3	V_1.1	V_1.2
Jan	-68.7	-90.5	-80.0	-87.8	-96.7	-101.2	-14.1	-3.2	-16.0	-71.6	-67.3
Feb	-42.6	-58.3	-54.7	-61.6	-67.5	-69.4	7.0	20.1	7.6	-38.4	-35.0
Mar	-6.3	-16.1	-22.3	-29.3	-32.0	-30.6	47.5	68.7	53.6	11.3	13.8
Apr	24.5	18.9	6.5	-0.2	-0.9	2.7	78.9	104.8	88.5	50.1	52.0
May	63.2	61.8	45.1	39.0	39.6	45.1	114.9	143.9	127.5	95.0	96.1
Jun	67.1	66.7	50.1	44.5	45.4	50.8	115.0	142.8	127.5	98.2	99.1
Jul	69.3	71.9	56.4	53.2	54.6	59.4	103.8	128.4	116.6	97.8	97.9
Aug	42.2	40.7	28.8	24.3	24.1	27.8	81.7	104.3	91.9	66.1	67.0
Sep	23.8	18.0	7.3	0.5	-0.7	2.8	75.2	98.4	83.2	46.6	48.6
Oct	11.7	4.2	-6.5	-14.1	-14.9	-11.0	65.7	85.8	70.3	31.7	34.2
Nov	-21.5	-33.9	-34.8	-41.5	-45.4	-45.4	25.9	39.4	26.9	-13.5	-10.6
Dec	-52.0	-69.8	-61.9	-68.7	-76.2	-79.5	-5.0	5.3	-5.9	-52.8	-49.3

Alice Springs

Table A. 51: Alice Springs monthly accumulated radiative heat losses (kWh·m^{-2}).

	RC1	RC2	M5	M6	M7	M8	A	AS_2.2	AS_2.3	V_1.1	V_1.2
Jan	-24.2	-29.9	-35.7	-41.3	-39.5	-34.4	-2.8	-11.6	-16.3	-28.6	-25.9
Feb	-21.6	-28.4	-30.2	-35.1	-35.0	-31.9	-2.7	-10.4	-14.2	-27.8	-25.3
Mar	-32.5	-46.7	-42.1	-49.0	-51.7	-50.7	-4.5	-16.0	-21.0	-47.0	-43.0
Apr	-36.2	-56.6	-43.1	-50.2	-56.9	-59.6	-5.5	-18.1	-22.8	-58.3	-53.6
May	-48.4	-80.3	-53.6	-62.7	-75.3	-82.6	-7.8	-24.6	-29.9	-83.8	-77.3
Jun	-54.4	-92.4	-58.3	-68.2	-84.1	-94.0	-9.0	-27.8	-33.3	-96.8	-89.5
Jul	-53.8	-91.4	-57.5	-67.3	-83.1	-93.0	-8.9	-27.5	-32.9	-95.9	-88.6
Aug	-49.3	-82.0	-54.5	-63.5	-76.4	-84.2	-8.0	-25.1	-30.4	-85.7	-79.1
Sep	-38.4	-60.4	-45.7	-53.1	-60.2	-63.4	-5.9	-19.3	-24.2	-62.2	-57.2
Oct	-40.0	-59.5	-50.7	-58.7	-63.1	-63.7	-5.8	-19.9	-25.7	-60.4	-55.4
Nov	-27.3	-38.9	-35.9	-41.7	-43.7	-42.4	-3.8	-13.4	-17.7	-39.0	-35.6
Dec	-23.6	-31.4	-32.9	-38.2	-38.3	-35.1	-3.0	-11.4	-15.6	-30.8	-28.0

Table A. 52: Alice Springs monthly accumulated solar heat gains (kWh·m^{-2}).

	RC1	RC2	M5	M6	M7	M8	A	AS_2.2	AS_2.3	V_1.1	V_1.2
Jan	10.3	15.4	0.0	0.0	0.0	0.0	50.7	98.6	83.2	56.6	54.7
Feb	8.4	12.6	0.0	0.0	0.0	0.0	41.3	80.4	67.8	46.1	44.6
Mar	9.0	13.4	0.0	0.0	0.0	0.0	43.9	85.4	72.1	49.0	47.4
Apr	7.3	10.9	0.0	0.0	0.0	0.0	35.9	70.0	59.0	40.1	38.8
May	6.1	9.1	0.0	0.0	0.0	0.0	30.0	58.3	49.2	33.5	32.3
Jun	5.1	7.6	0.0	0.0	0.0	0.0	25.0	48.8	41.1	28.0	27.0

Jul	5.8	8.7	0.0	0.0	0.0	0.0	28.6	55.7	47.0	32.0	30.9
Aug	7.1	10.6	0.0	0.0	0.0	0.0	34.8	67.7	57.1	38.8	37.5
Sep	8.1	12.1	0.0	0.0	0.0	0.0	39.6	77.1	65.1	44.2	42.8
Oct	9.4	14.0	0.0	0.0	0.0	0.0	45.8	89.2	75.3	51.2	49.5
Nov	9.4	14.1	0.0	0.0	0.0	0.0	46.2	90.0	75.9	51.6	49.9
Dec	10.1	15.0	0.0	0.0	0.0	0.0	49.4	96.2	81.1	55.2	53.3

Table A. 53: Alice Springs monthly accumulated convective heat gains (positive values) and losses (negative values) (kWh·m^{-2}).

	RC1	RC2	M5	M6	M7	M8	A	AS2.2	AS_2.3	V_1.1	V_1.2
Jan	67.8	67.8	68.1	68.2	68.2	68.1	66.8	66.1	66.4	67.1	67.1
Feb	38.4	38.4	38.7	38.8	38.7	38.7	37.6	37.0	37.3	37.9	37.8
Mar	16.0	16.1	16.3	16.4	16.4	16.4	15.1	14.7	14.9	15.6	15.6
Apr	-23.8	-23.6	-23.6	-23.5	-23.4	-23.4	-24.6	-24.9	-24.7	-24.0	-24.0
May	-77.8	-77.5	-77.7	-77.6	-77.4	-77.3	-78.7	-78.9	-78.7	-77.8	-77.9
Jun	-106.3	-105.9	-106.2	-106.0	-105.9	-105.8	-107.1	-107.2	-107.0	-106.1	-106.2
Jul	-99.9	-99.5	-99.7	-99.6	-99.5	-99.3	-100.7	-100.9	-100.7	-99.8	-99.8
Aug	-87.9	-87.6	-87.7	-87.6	-87.5	-87.4	-88.9	-89.2	-88.9	-87.9	-88.0
Sep	-37.4	-37.1	-37.1	-37.0	-36.9	-36.9	-38.3	-38.7	-38.4	-37.6	-37.6
Oct	2.2	2.4	2.5	2.6	2.7	2.7	1.1	0.5	0.9	1.8	1.7
Nov	20.6	20.7	20.9	21.0	21.0	21.0	19.7	19.1	19.4	20.1	20.1
Dec	46.6	46.6	46.9	47.0	46.9	46.9	45.7	45.0	45.3	45.9	45.9

Table A. 54: Alice Springs monthly accumulated total heat gains (positive values) and losses (negative values) (kWh·m^{-2}).

	RC1	RC2	M5	M6	M7	M8	A	AS_2.2	AS_2.3	V_1.1	V_1.2
Jan	53.9	53.3	32.4	26.9	28.7	33.7	114.6	153.2	133.4	95.0	95.8
Feb	25.2	22.6	8.5	3.7	3.7	6.8	76.2	107.0	90.9	56.2	57.1
Mar	-7.5	-17.2	-25.8	-32.6	-35.3	-34.3	54.5	84.1	66.0	17.6	19.9
Apr	-52.6	-69.2	-66.6	-73.7	-80.3	-83.0	5.8	26.9	11.5	-42.1	-38.8
May	-120.2	-148.7	-131.3	-140.2	-152.7	-160.0	-56.6	-45.2	-59.4	-128.1	-122.8
Jun	-155.6	-190.6	-164.5	-174.3	-189.9	-199.8	-91.1	-86.2	-99.2	-175.0	-168.6
Jul	-147.8	-182.2	-157.3	-166.9	-182.5	-192.4	-81.0	-72.7	-86.6	-163.7	-157.6
Aug	-130.1	-159.0	-142.2	-151.1	-163.9	-171.6	-62.1	-46.6	-62.3	-134.8	-129.5
Sep	-67.7	-85.4	-82.8	-90.1	-97.1	-100.3	-4.6	19.1	2.4	-55.5	-52.1
Oct	-28.5	-43.1	-48.2	-56.0	-60.4	-61.0	41.1	69.9	50.4	-7.4	-4.2
Nov	2.7	-4.1	-15.0	-20.7	-22.7	-21.4	62.1	95.6	77.6	32.8	34.3
Dec	33.0	30.3	14.0	8.8	8.6	11.7	92.0	129.7	110.9	70.3	71.2

Sydney

Table A. 55: Sidney monthly accumulated radiative heat losses (kWh·m^{-2}).

	RC1	RC2	M5	M6	M7	M8	A	AS_2.2	AS_2.3	V_1.1	V_1.2
Jan	-29.4	-46.0	-34.4	-40.6	-46.9	-48.8	-4.5	-14.6	-18.4	-47.4	-43.6
Feb	-22.3	-35.5	-25.4	-30.1	-35.7	-37.5	-3.5	-11.1	-13.8	-36.8	-33.9
Mar	-29.5	-47.4	-33.5	-39.6	-46.9	-49.8	-4.7	-14.8	-18.3	-49.2	-45.3
Apr	-32.5	-54.4	-35.1	-41.5	-51.1	-56.2	-5.3	-16.5	-19.9	-56.9	-52.5
May	-40.9	-69.6	-43.3	-51.0	-63.6	-71.1	-6.8	-20.8	-24.9	-73.0	-67.5
Jun	-38.5	-68.0	-38.3	-45.3	-59.5	-68.5	-6.7	-19.8	-23.1	-71.9	-66.6
Jul	-41.5	-73.4	-41.2	-48.8	-64.0	-73.8	-7.2	-21.3	-24.9	-77.7	-71.9
Aug	-39.3	-69.0	-39.7	-46.9	-60.9	-69.7	-6.8	-20.2	-23.7	-72.9	-67.5
Sep	-32.0	-55.5	-32.9	-38.8	-49.9	-56.5	-5.4	-16.4	-19.4	-58.6	-54.1
Oct	-32.4	-54.6	-34.7	-41.0	-50.9	-56.2	-5.4	-16.5	-19.8	-57.3	-52.9
Nov	-28.2	-47.1	-30.3	-35.8	-44.4	-48.7	-4.6	-14.3	-17.2	-49.4	-45.5
Dec	-28.1	-45.2	-31.9	-37.6	-44.7	-47.5	-4.4	-14.1	-17.5	-46.9	-43.2

Table A. 56: Sidney monthly accumulated solar heat gains (kWh·m^{-2}).

	RC1	RC2	M5	M6	M7	M8	A	AS_2.2	AS_2.3	V_1.1	V_1.2
Jan	8.8	13.1	0.0	0.0	0.0	0.0	43.0	83.8	70.7	48.1	46.5
Feb	7.2	10.7	0.0	0.0	0.0	0.0	35.1	68.3	57.6	39.2	37.9
Mar	6.6	9.8	0.0	0.0	0.0	0.0	32.2	62.6	52.9	35.9	34.7
Apr	5.3	8.0	0.0	0.0	0.0	0.0	26.2	51.0	43.0	29.2	28.3
May	4.0	6.0	0.0	0.0	0.0	0.0	19.6	38.1	32.1	21.9	21.1
Jun	3.1	4.6	0.0	0.0	0.0	0.0	15.0	29.3	24.7	16.8	16.2
Jul	3.4	5.1	0.0	0.0	0.0	0.0	16.8	32.7	27.6	18.7	18.1
Aug	4.4	6.6	0.0	0.0	0.0	0.0	21.8	42.4	35.8	24.3	23.5
Sep	5.5	8.2	0.0	0.0	0.0	0.0	26.9	52.4	44.2	30.1	29.1
Oct	7.0	10.5	0.0	0.0	0.0	0.0	34.5	67.2	56.7	38.5	37.2
Nov	7.5	11.2	0.0	0.0	0.0	0.0	36.9	71.7	60.5	41.2	39.8
Dec	8.6	12.8	0.0	0.0	0.0	0.0	42.1	81.9	69.1	47.0	45.4

Table A. 57: Sidney monthly accumulated convective heat gains (positive values) and losses (negative values) (kWh·m^{-2}).

	RC1	RC2	M5	M6	M7	M8	A	AS_2.2	AS_2.3	V_1.1	V_1.2
Jan	-18.5	-18.3	-18.3	-18.2	-18.1	-18.1	-19.3	-19.7	-19.5	-18.8	-18.8
Feb	-17.9	-17.8	-17.7	-17.7	-17.6	-17.6	-18.5	-18.9	-18.7	-18.2	-18.2
Mar	-26.2	-26.0	-26.1	-26.0	-25.9	-25.9	-26.8	-27.0	-26.9	-26.3	-26.4
Apr	-44.0	-43.8	-43.9	-43.8	-43.7	-43.7	-44.5	-44.7	-44.5	-44.0	-44.0
May	-69.9	-69.6	-69.8	-69.7	-69.6	-69.5	-70.4	-70.5	-70.4	-69.8	-69.8
Jun	-86.2	-85.9	-86.2	-86.1	-85.9	-85.9	-86.7	-86.7	-86.6	-86.0	-86.1

Jul	-94.6	-94.3	-94.5	-94.4	-94.3	-94.2	-95.1	-95.2	-95.1	-94.4	-94.5
Aug	-91.8	-91.4	-91.7	-91.6	-91.5	-91.4	-92.4	-92.5	-92.4	-91.6	-91.7
Sep	-72.3	-72.0	-72.2	-72.1	-72.0	-71.9	-72.9	-73.1	-73.0	-72.3	-72.3
Oct	-55.2	-55.0	-55.1	-55.0	-54.9	-54.8	-55.9	-56.3	-56.1	-55.3	-55.4
Nov	-47.0	-46.8	-46.9	-46.8	-46.7	-46.6	-47.7	-48.1	-47.9	-47.2	-47.2
Dec	-28.6	-28.4	-28.4	-28.3	-28.2	-28.2	-29.4	-29.9	-29.6	-28.9	-28.9

Table A. 58: Sidney monthly accumulated total heat gains (positive values) and losses (negative values) (kWh·m^{-2}).

	RC1	**RC2**	**M5**	**M6**	**M7**	**M8**	**A**	**AS_2.2**	**AS_2.3**	**V_1.1**	**V_1.2**
Jan	-39.1	-51.2	-52.7	-58.8	-65.0	-66.9	19.3	49.4	32.8	-18.1	-15.9
Feb	-33.0	-42.6	-43.1	-47.8	-53.3	-55.1	13.1	38.3	25.1	-15.8	-14.2
Mar	-49.2	-63.6	-59.5	-65.6	-72.8	-75.7	0.7	20.8	7.7	-39.6	-36.9
Apr	-71.2	-90.2	-79.0	-85.3	-94.8	-99.8	-23.6	-10.2	-21.5	-71.7	-68.3
May	-106.8	-133.2	-113.1	-120.7	-133.2	-140.7	-57.7	-53.2	-63.2	-121.0	-116.2
Jun	-121.6	-149.3	-124.5	-131.4	-145.4	-154.4	-78.3	-77.2	-85.0	-141.2	-136.4
Jul	-132.6	-162.5	-135.7	-143.2	-158.3	-168.0	-85.5	-83.8	-92.4	-153.3	-148.2
Aug	-126.7	-153.8	-131.4	-138.5	-152.3	-161.1	-77.4	-70.3	-80.3	-140.3	-135.7
Sep	-98.8	-119.3	-105.1	-111.0	-121.9	-128.4	-51.4	-37.1	-48.1	-100.8	-97.4
Oct	-80.6	-99.1	-89.8	-96.0	-105.7	-111.0	-26.8	-5.6	-19.3	-74.1	-71.0
Nov	-67.7	-82.7	-77.2	-82.6	-91.1	-95.4	-15.5	9.4	-4.6	-55.4	-53.0
Dec	-48.1	-60.8	-60.3	-66.0	-72.9	-75.7	8.2	37.9	22.0	-28.9	-26.7

Tokyo

Table A. 59: Tokyo monthly accumulated radiative heat losses (kWh·m^{-2}).

	RC1	**RC2**	**M5**	**M6**	**M7**	**M8**	**A**	**AS_2.2**	**AS_2.3**	**V_1.1**	**V_1.2**
Jan	-51.4	-94.4	-47.9	-56.7	-78.1	-93.1	-9.2	-26.8	-30.4	-100.5	-93.3
Feb	-45.7	-83.5	-43.1	-50.9	-69.6	-82.6	-8.2	-23.8	-27.1	-88.9	-82.4
Mar	-39.7	-73.1	-36.8	-43.7	-60.7	-72.4	-7.2	-20.7	-23.5	-78.0	-72.4
Apr	-30.5	-54.5	-29.8	-35.3	-47.2	-54.8	-5.4	-15.7	-18.3	-57.8	-53.5
May	-22.9	-39.5	-23.5	-27.9	-36.2	-40.6	-3.9	-11.7	-13.9	-41.7	-38.6
Jun	-13.8	-22.9	-14.9	-17.6	-22.4	-24.0	-2.3	-6.9	-8.4	-23.9	-22.1
Jul	-10.5	-14.0	-14.2	-16.7	-17.9	-16.0	-1.4	-5.0	-6.8	-13.7	-12.5
Aug	-13.9	-18.4	-18.9	-22.3	-23.3	-21.0	-1.8	-6.6	-9.0	-18.0	-16.3
Sep	-12.1	-20.0	-13.0	-15.5	-19.9	-21.1	-2.0	-6.1	-7.4	-20.9	-19.2
Oct	-23.9	-42.5	-23.2	-27.6	-37.4	-43.1	-4.2	-12.2	-14.2	-45.2	-41.8
Nov	-33.8	-61.8	-31.6	-37.6	-52.0	-61.6	-6.1	-17.5	-20.0	-65.9	-61.1
Dec	-49.9	-90.2	-48.0	-56.7	-76.3	-89.6	-8.8	-25.9	-29.7	-95.8	-88.8

Table A. 60: Tokyo monthly accumulated solar heat gains (kWh·m^{-2}).

	RC1	RC2	M5	M6	M7	M8	A	AS_2.2	AS_2.3	V_1.1	V_1.2
Jan	3.2	4.8	0.0	0.0	0.0	0.0	15.9	30.9	26.0	17.7	17.1
Feb	3.7	5.5	0.0	0.0	0.0	0.0	17.9	34.9	29.5	20.0	19.4
Mar	4.6	6.8	0.0	0.0	0.0	0.0	22.3	43.4	36.6	24.9	24.1
Apr	5.5	8.2	0.0	0.0	0.0	0.0	26.9	52.3	44.2	30.0	29.0
May	5.9	8.8	0.0	0.0	0.0	0.0	29.0	56.4	47.6	32.4	31.3
Jun	5.0	7.5	0.0	0.0	0.0	0.0	24.6	47.9	40.4	27.5	26.5
Jul	5.5	8.2	0.0	0.0	0.0	0.0	26.9	52.4	44.2	30.1	29.0
Aug	5.5	8.3	0.0	0.0	0.0	0.0	27.1	52.8	44.6	30.3	29.3
Sep	3.9	5.9	0.0	0.0	0.0	0.0	19.3	37.5	31.6	21.5	20.8
Oct	3.5	5.2	0.0	0.0	0.0	0.0	17.2	33.4	28.2	19.2	18.5
Nov	2.9	4.3	0.0	0.0	0.0	0.0	14.2	27.7	23.3	15.9	15.3
Dec	2.8	4.2	0.0	0.0	0.0	0.0	14.0	27.2	22.9	15.6	15.1

Table A. 61: Tokyo monthly accumulated convective heat gains (positive values) and losses (negative values) (kWh·m^{-2}).

	RC1	RC2	M5	M6	M7	M8	A	AS2.2	AS_2.3	V_1.1	V_1.2
Jan	-137.8	-137.4	-137.8	-137.7	-137.5	-137.3	-138.3	-138.3	-138.2	-137.5	-137.5
Feb	-127.7	-127.4	-127.7	-127.6	-127.4	-127.3	-128.3	-128.3	-128.2	-127.5	-127.5
Mar	-113.5	-113.2	-113.5	-113.4	-113.2	-113.1	-114.0	-114.1	-114.0	-113.3	-113.4
Apr	-68.5	-68.3	-68.4	-68.4	-68.3	-68.2	-69.0	-69.2	-69.1	-68.5	-68.5
May	-35.1	-34.9	-35.0	-34.9	-34.9	-34.8	-35.5	-35.7	-35.6	-35.2	-35.2
Jun	-11.3	-11.3	-11.3	-11.3	-11.2	-11.2	-11.6	-11.8	-11.7	-11.5	-11.5
Jul	15.7	15.7	15.8	15.8	15.8	15.8	15.4	15.1	15.2	15.4	15.4
Aug	19.4	19.4	19.5	19.5	19.5	19.5	19.0	18.8	18.9	19.2	19.1
Sep	-9.7	-9.7	-9.7	-9.6	-9.6	-9.6	-9.9	-10.1	-10.0	-9.8	-9.8
Oct	-42.8	-42.7	-42.8	-42.7	-42.6	-42.6	-43.1	-43.2	-43.2	-42.8	-42.8
Nov	-71.4	-71.1	-71.3	-71.3	-71.2	-71.1	-71.7	-71.8	-71.7	-71.2	-71.3
Dec	-115.0	-114.7	-115.0	-114.9	-114.7	-114.6	-115.5	-115.5	-115.4	-114.7	-114.8

Table A. 62: Tokyo monthly accumulated total heat gains (positive values) and losses (negative values) (kWh·m^{-2}).

	RC1	RC2	M5	M6	M7	M8	A	AS2.2	AS_2.3	V_1.1	V_1.2
Jan	-185.9	-226.9	-185.7	-194.4	-215.6	-230.4	-131.7	-134.2	-142.6	-220.3	-213.7
Feb	-169.7	-205.4	-170.8	-178.5	-197.0	-209.9	-118.5	-117.2	-125.8	-196.3	-190.6
Mar	-148.7	-179.5	-150.3	-157.1	-174.0	-185.5	-98.9	-91.4	-100.8	-166.4	-161.6
Apr	-93.5	-114.5	-98.2	-103.7	-115.5	-123.0	-47.5	-32.6	-43.2	-96.3	-93.1
May	-52.1	-65.7	-58.5	-62.9	-71.1	-75.4	-10.4	9.0	-1.9	-44.5	-42.5
Jun	-20.2	-26.7	-26.1	-28.9	-33.7	-35.2	10.7	29.1	20.3	-7.9	-7.0
Jul	10.7	9.9	1.6	-0.9	-2.1	-0.3	40.9	62.5	52.7	31.8	32.0
Aug	11.0	9.3	0.6	-2.7	-3.8	-1.5	44.4	65.0	54.5	31.5	32.1

Sep	-17.9	-23.8	-22.6	-25.1	-29.5	-30.7	7.4	21.4	14.3	-9.2	-8.3
Oct	-63.2	-80.0	-65.9	-70.4	-80.0	-85.7	-30.2	-22.1	-29.2	-68.8	-66.1
Nov	-102.3	-128.6	-103.0	-108.9	-123.2	-132.7	-63.6	-61.6	-68.3	-121.3	-117.0
Dec	-162.0	-200.6	-163.0	-171.6	-191.0	-204.2	-110.3	-114.2	-122.2	-194.9	-188.5

London

Table A. 63: London monthly accumulated radiative heat losses (kWh·m^{-2}).

	RC1	RC2	M5	M6	M7	M8	A	AS_2.2	AS_2.3	V_1.1	V_1.2
Jan	-40.9	-77.6	-35.4	-42.4	-62.1	-75.8	-7.6	-21.4	-23.8	-83.2	-77.3
Feb	-37.2	-70.5	-32.3	-38.7	-56.6	-68.9	-6.9	-19.5	-21.6	-75.6	-70.2
Mar	-39.9	-74.8	-35.4	-42.3	-60.8	-73.5	-7.3	-20.8	-23.3	-80.1	-74.4
Apr	-36.4	-67.1	-33.6	-39.9	-55.8	-66.5	-6.6	-18.9	-21.5	-71.6	-66.4
May	-36.1	-64.1	-35.5	-42.1	-55.9	-64.5	-6.3	-18.6	-21.6	-67.9	-62.9
Jun	-30.2	-52.4	-30.9	-36.6	-47.2	-53.4	-5.1	-15.5	-18.3	-55.3	-51.1
Jul	-28.9	-49.1	-30.5	-36.0	-45.5	-50.5	-4.8	-14.7	-17.6	-51.6	-47.7
Aug	-27.2	-46.6	-28.2	-33.4	-42.8	-47.8	-4.6	-13.8	-16.5	-49.1	-45.4
Sep	-30.1	-53.1	-29.9	-35.5	-46.9	-53.8	-5.2	-15.4	-18.0	-56.2	-52.0
Oct	-33.2	-61.0	-30.8	-36.8	-51.3	-60.7	-6.0	-17.2	-19.6	-65.0	-60.3
Nov	-37.0	-69.2	-33.1	-39.6	-56.6	-68.2	-6.8	-19.3	-21.7	-74.1	-68.7
Dec	-37.3	-72.4	-30.7	-37.1	-56.6	-70.2	-7.1	-19.7	-21.5	-77.9	-72.4

Table A. 64: London monthly accumulated solar heat gains (kWh·m^{-2}).

	RC1	RC2	M5	M6	M7	M8	A	AS_2.2	AS_2.3	V_1.1	V_1.2
Jan	0.9	1.3	0.0	0.0	0.0	0.0	4.4	8.5	7.2	4.9	4.7
Feb	1.5	2.2	0.0	0.0	0.0	0.0	7.4	14.4	12.1	8.2	8.0
Mar	3.0	4.4	0.0	0.0	0.0	0.0	14.5	28.3	23.9	16.2	15.7
Apr	4.5	6.7	0.0	0.0	0.0	0.0	22.0	42.7	36.1	24.5	23.7
May	6.1	9.1	0.0	0.0	0.0	0.0	29.9	58.2	49.1	33.4	32.3
Jun	6.1	9.1	0.0	0.0	0.0	0.0	30.0	58.4	49.3	33.5	32.4
Jul	6.2	9.2	0.0	0.0	0.0	0.0	30.4	59.1	49.9	33.9	32.8
Aug	5.6	8.3	0.0	0.0	0.0	0.0	27.2	53.0	44.7	30.4	29.4
Sep	3.7	5.5	0.0	0.0	0.0	0.0	18.1	35.3	29.8	20.2	19.6
Oct	2.3	3.4	0.0	0.0	0.0	0.0	11.2	21.8	18.4	12.5	12.1
Nov	1.1	1.7	0.0	0.0	0.0	0.0	5.4	10.6	8.9	6.1	5.9
Dec	0.7	1.0	0.0	0.0	0.0	0.0	3.3	6.5	5.5	3.7	3.6

Table A. 65: London monthly accumulated convective heat gains (positive values) and losses (negative values) (kWh·m-²).

	RC1	RC2	M5	M6	M7	M8	A	AS2.2	AS_2.3	V_1.1	V_1.2
Jan	-209.9	-209.3	-209.9	-209.8	-209.5	-209.3	-210.5	-210.3	-210.2	-209.3	-209.3
Feb	-178.8	-178.3	-178.8	-178.7	-178.5	-178.3	-179.3	-179.2	-179.2	-178.3	-178.4
Mar	-180.3	-179.8	-180.3	-180.2	-179.9	-179.7	-180.9	-180.9	-180.8	-179.9	-180.0
Apr	-133.3	-132.9	-133.3	-133.2	-133.0	-132.9	-133.9	-134.1	-133.9	-133.1	-133.2
May	-113.3	-112.9	-113.2	-113.1	-112.9	-112.8	-114.0	-114.3	-114.1	-113.2	-113.3
Jun	-72.3	-72.0	-72.2	-72.1	-72.0	-71.9	-72.9	-73.1	-72.9	-72.3	-72.3
Jul	-58.4	-58.2	-58.3	-58.3	-58.1	-58.1	-59.0	-59.3	-59.1	-58.5	-58.5
Aug	-56.7	-56.5	-56.6	-56.6	-56.4	-56.4	-57.2	-57.4	-57.3	-56.7	-56.8
Sep	-79.5	-79.2	-79.4	-79.4	-79.2	-79.1	-80.0	-80.1	-80.0	-79.4	-79.4
Oct	-115.1	-114.8	-115.1	-115.0	-114.8	-114.7	-115.6	-115.6	-115.5	-114.8	-114.9
Nov	-148.7	-148.3	-148.7	-148.6	-148.4	-148.3	-149.1	-149.1	-149.0	-148.3	-148.3
Dec	-182.6	-182.1	-182.7	-182.6	-182.3	-182.1	-183.1	-182.9	-182.9	-182.1	-182.1

Table A. 66: London monthly accumulated total heat gains (positive values) and losses (negative values) (kWh·m-²).

	RC1	RC2	M5	M6	M7	M8	A	AS2.2	AS_2.3	V_1.1	V_1.2
Jan	-249.8	-285.6	-245.3	-252.2	-271.7	-285.1	-213.7	-223.2	-226.8	-287.6	-281.9
Feb	-214.5	-246.6	-211.1	-217.4	-235.0	-247.2	-178.8	-184.4	-188.7	-245.7	-240.7
Mar	-217.2	-250.2	-215.7	-222.5	-240.8	-253.3	-173.7	-173.5	-180.3	-243.8	-238.7
Apr	-165.2	-193.3	-166.9	-173.2	-188.9	-199.4	-118.6	-110.3	-119.3	-180.2	-175.9
May	-143.2	-167.9	-148.7	-155.2	-168.8	-177.3	-90.4	-74.6	-86.6	-147.7	-143.9
Jun	-96.4	-115.3	-103.1	-108.7	-119.2	-125.3	-48.0	-30.1	-41.9	-94.1	-91.0
Jul	-81.2	-98.1	-88.8	-94.3	-103.6	-108.6	-33.5	-14.9	-26.9	-76.2	-73.4
Aug	-78.4	-94.8	-84.9	-90.0	-99.2	-104.2	-34.6	-18.3	-29.1	-75.4	-72.8
Sep	-105.9	-126.8	-109.3	-114.9	-126.1	-132.9	-67.1	-60.2	-68.2	-115.3	-111.8
Oct	-146.1	-172.3	-145.9	-151.8	-166.1	-175.4	-110.4	-111.0	-116.7	-167.4	-163.1
Nov	-184.6	-215.9	-181.8	-188.2	-205.0	-216.5	-150.5	-157.8	-161.8	-216.3	-211.2
Dec	-219.2	-253.5	-213.4	-219.7	-238.9	-252.4	-186.8	-196.1	-198.9	-256.3	-251.0

Milan

Table A. 67: Milan monthly accumulated radiative heat losses (kWh·m-²).

	RC1	RC2	M5	M6	M7	M8	A	AS_2.2	AS_2.3	V_1.1	V_1.2
Jan	-47.9	-91.3	-41.1	-49.2	-72.5	-88.7	-8.9	-25.2	-27.8	-97.9	-90.9
Feb	-41.3	-78.1	-36.2	-43.3	-62.7	-76.2	-7.6	-21.7	-24.1	-83.6	-77.6
Mar	-41.9	-76.4	-39.4	-46.7	-64.2	-75.9	-7.5	-21.7	-24.8	-81.4	-75.5
Apr	-33.8	-61.1	-32.2	-38.3	-52.2	-61.2	-6.0	-17.5	-20.1	-65.1	-60.3
May	-28.5	-48.2	-30.0	-35.6	-44.8	-49.6	-4.7	-14.5	-17.3	-50.7	-46.8

Jun	-22.3	-35.1	-25.9	-30.5	-35.7	-37.2	-3.4	-11.1	-13.9	-36.2	-33.3
Jul	-22.0	-32.6	-27.1	-31.9	-35.6	-35.3	-3.2	-10.8	-13.9	-33.1	-30.4
Aug	-19.8	-30.3	-23.6	-27.9	-32.1	-32.5	-3.0	-9.8	-12.4	-31.0	-28.5
Sep	-24.9	-42.8	-25.7	-30.6	-39.3	-43.9	-4.2	-12.7	-15.1	-45.1	-41.6
Oct	-30.9	-56.1	-29.2	-34.8	-47.9	-56.1	-5.5	-15.9	-18.3	-59.7	-55.3
Nov	-34.2	-66.1	-28.4	-34.3	-52.1	-64.4	-6.5	-18.0	-19.7	-71.2	-66.1
Dec	-45.0	-86.4	-38.1	-45.7	-68.2	-83.9	-8.4	-23.7	-26.0	-92.8	-86.2

Table A. 68: Milan monthly accumulated solar heat gains (kWh·m^{-2}).

	RC1	**RC2**	**M5**	**M6**	**M7**	**M8**	**A**	**AS_2.2**	**AS_2.3**	**V_1.1**	**V_1.2**
Jan	1.4	2.1	0.0	0.0	0.0	0.0	6.8	13.2	11.2	7.6	7.3
Feb	2.2	3.3	0.0	0.0	0.0	0.0	10.7	20.9	17.6	12.0	11.6
Mar	4.1	6.1	0.0	0.0	0.0	0.0	20.0	38.9	32.8	22.3	21.6
Apr	5.1	7.5	0.0	0.0	0.0	0.0	24.8	48.2	40.7	27.7	26.7
May	6.3	9.4	0.0	0.0	0.0	0.0	30.9	60.1	50.7	34.5	33.3
Jun	6.6	9.8	0.0	0.0	0.0	0.0	32.1	62.5	52.7	35.8	34.6
Jul	7.2	10.8	0.0	0.0	0.0	0.0	35.4	68.8	58.1	39.5	38.2
Aug	6.3	9.3	0.0	0.0	0.0	0.0	30.6	59.6	50.3	34.2	33.1
Sep	4.1	6.1	0.0	0.0	0.0	0.0	20.0	38.9	32.8	22.3	21.6
Oct	2.6	3.8	0.0	0.0	0.0	0.0	12.5	24.4	20.6	14.0	13.5
Nov	1.4	2.0	0.0	0.0	0.0	0.0	6.7	13.0	11.0	7.4	7.2
Dec	1.1	1.6	0.0	0.0	0.0	0.0	5.4	10.5	8.9	6.0	5.8

Table A. 69: Milan monthly accumulated convective heat gains (positive values) and losses (negative values) (kWh·m^{-2}).

	RC1	**RC2**	**M5**	**M6**	**M7**	**M8**	**A**	**AS2.2**	**AS_2.3**	**V_1.1**	**V_1.2**
Jan	-102.1	-101.8	-102.1	-102.1	-101.9	-101.8	-102.4	-102.3	-102.3	-101.8	-101.9
Feb	-96.4	-96.2	-96.5	-96.4	-96.3	-96.2	-96.8	-96.7	-96.7	-96.2	-96.3
Mar	-88.4	-88.1	-88.4	-88.3	-88.2	-88.1	-88.8	-88.9	-88.8	-88.2	-88.3
Apr	-64.8	-64.6	-64.7	-64.7	-64.6	-64.5	-65.2	-65.3	-65.2	-64.7	-64.8
May	-35.1	-34.9	-35.0	-34.9	-34.9	-34.8	-35.5	-35.7	-35.6	-35.1	-35.2
Jun	-10.9	-10.9	-10.8	-10.8	-10.8	-10.7	-11.3	-11.5	-11.4	-11.1	-11.1
Jul	4.0	4.0	4.1	4.1	4.1	4.1	3.5	3.3	3.4	3.7	3.7
Aug	-1.3	-1.3	-1.3	-1.2	-1.2	-1.2	-1.7	-1.8	-1.7	-1.5	-1.5
Sep	-26.3	-26.2	-26.3	-26.2	-26.2	-26.1	-26.6	-26.6	-26.6	-26.3	-26.3
Oct	-43.2	-43.1	-43.2	-43.2	-43.1	-43.0	-43.4	-43.4	-43.4	-43.1	-43.1
Nov	-73.6	-73.4	-73.6	-73.6	-73.5	-73.4	-73.8	-73.8	-73.8	-73.4	-73.4
Dec	-96.1	-95.9	-96.2	-96.1	-96.0	-95.9	-96.4	-96.3	-96.3	-95.9	-95.9

Table A. 70: Milan monthly accumulated total heat gains (positive values) and losses (negative values) (kWh·m^{-2}).

	RC1	RC2	M5	M6	M7	M8	A	AS2.2	AS_2.3	V_1.1	V_1.2
Jan	-148.6	-191.0	-143.2	-151.3	-174.4	-190.5	-104.5	-114.3	-118.9	-192.1	-185.5
Feb	-135.6	-171.0	-132.7	-139.7	-159.0	-172.4	-93.7	-97.6	-103.2	-167.9	-162.3
Mar	-126.2	-158.5	-127.8	-135.1	-152.4	-164.0	-76.3	-71.7	-80.8	-147.4	-142.2
Apr	-93.5	-118.2	-96.9	-103.0	-116.8	-125.7	-46.4	-34.6	-44.7	-102.2	-98.3
May	-57.2	-73.8	-65.0	-70.5	-79.7	-84.5	-9.4	9.9	-2.2	-51.4	-48.6
Jun	-26.7	-36.2	-36.7	-41.3	-46.5	-47.9	17.3	39.8	27.4	-11.4	-9.7
Jul	-10.8	-17.8	-23.1	-27.8	-31.4	-31.2	35.7	61.3	47.6	10.1	11.5
Aug	-14.9	-22.3	-24.9	-29.1	-33.3	-33.8	26.0	48.0	36.1	1.7	3.1
Sep	-47.2	-62.9	-52.0	-56.8	-65.5	-70.0	-10.8	-0.4	-8.9	-49.0	-46.4
Oct	-71.5	-95.3	-72.3	-77.9	-90.9	-99.2	-36.4	-35.0	-41.1	-88.8	-84.9
Nov	-106.5	-137.5	-102.0	-107.9	-125.6	-137.8	-73.6	-78.8	-82.5	-137.1	-132.4
Dec	-140.1	-180.7	-134.2	-141.8	-164.2	-179.7	-99.4	-109.5	-113.4	-182.6	-176.3

Pamplona

Table A. 71: Pamplona monthly accumulated radiative heat losses (kWh·m^{-2}).

	RC1	RC2	M5	M6	M7	M8	A	AS_2.2	AS_2.3	V_1.1	V_1.2
Jan	-45.5	-85.6	-40.2	-48.0	-69.2	-83.7	-8.4	-23.8	-26.6	-91.6	-85.0
Feb	-43.9	-80.5	-40.9	-48.5	-67.0	-79.5	-7.9	-22.8	-25.9	-85.7	-79.5
Mar	-46.2	-82.6	-45.2	-53.4	-71.0	-82.6	-8.1	-23.9	-27.6	-87.6	-81.2
Apr	-40.7	-72.8	-39.7	-47.0	-62.7	-72.9	-7.1	-21.0	-24.4	-77.3	-71.6
May	-39.4	-67.4	-41.3	-48.7	-61.3	-68.8	-6.6	-20.1	-24.0	-71.0	-65.6
Jun	-32.6	-52.9	-36.5	-43.0	-51.4	-55.2	-5.2	-16.4	-20.2	-55.1	-50.8
Jul	-38.1	-59.8	-44.6	-52.4	-60.2	-63.1	-5.9	-19.0	-23.9	-61.7	-56.8
Aug	-32.2	-51.3	-37.1	-43.7	-51.1	-53.9	-5.0	-16.1	-20.1	-53.1	-48.9
Sep	-38.9	-63.9	-43.2	-50.8	-60.9	-66.2	-6.3	-19.6	-24.0	-66.6	-61.4
Oct	-38.6	-67.0	-39.3	-46.5	-59.9	-68.0	-6.6	-19.7	-23.3	-70.7	-65.4
Nov	-40.4	-74.7	-37.1	-44.2	-61.9	-73.8	-7.3	-21.0	-23.8	-79.7	-73.9
Dec	-48.7	-89.9	-45.0	-53.4	-74.3	-88.6	-8.8	-25.4	-28.7	-95.9	-88.9

Table A. 72: Pamplona monthly accumulated solar heat gains (kWh·m^{-2}).

	RC1	RC2	M5	M6	M7	M8	A	AS_2.2	AS_2.3	V_1.1	V_1.2
Jan	2.1	3.1	0.0	0.0	0.0	0.0	10.3	20.1	17.0	11.5	11.2
Feb	2.8	4.2	0.0	0.0	0.0	0.0	13.8	26.8	22.6	15.4	14.8
Mar	5.0	7.5	0.0	0.0	0.0	0.0	24.6	47.8	40.3	27.4	26.5
Apr	6.4	9.6	0.0	0.0	0.0	0.0	31.4	61.2	51.6	35.1	33.9
May	7.7	11.5	0.0	0.0	0.0	0.0	37.7	73.3	61.9	42.1	40.7
Jun	8.7	13.0	0.0	0.0	0.0	0.0	42.7	83.1	70.2	47.7	46.1

Jul	9.4	14.0	0.0	0.0	0.0	0.0	46.0	89.6	75.6	51.4	49.7
Aug	7.6	11.3	0.0	0.0	0.0	0.0	37.0	72.0	60.8	41.3	39.9
Sep	6.1	9.1	0.0	0.0	0.0	0.0	29.8	58.0	48.9	33.3	32.1
Oct	3.9	5.9	0.0	0.0	0.0	0.0	19.3	37.5	31.6	21.5	20.8
Nov	2.5	3.7	0.0	0.0	0.0	0.0	12.2	23.7	20.0	13.6	13.2
Dec	1.9	2.9	0.0	0.0	0.0	0.0	9.5	18.4	15.6	10.6	10.2

Table A. 73: Pamplona monthly accumulated convective heat gains (positive values) and losses (negative values) (kWh·m^{-2}).

	RC1	**RC2**	**M5**	**M6**	**M7**	**M8**	**A**	**AS2.2**	**AS_2.3**	**V_1.1**	**V_1.2**
Jan	-161.1	-160.6	-161.1	-161.0	-160.8	-160.6	-161.6	-161.5	-161.4	-160.6	-160.7
Feb	-154.9	-154.5	-154.9	-154.8	-154.6	-154.4	-155.5	-155.5	-155.4	-154.6	-154.6
Mar	-143.0	-142.6	-143.0	-142.9	-142.6	-142.5	-143.8	-143.9	-143.8	-142.8	-142.9
Apr	-126.1	-125.8	-126.0	-125.9	-125.7	-125.6	-127.0	-127.3	-127.1	-126.1	-126.2
May	-80.8	-80.5	-80.6	-80.6	-80.4	-80.3	-81.6	-82.0	-81.8	-80.9	-80.9
Jun	-45.4	-45.2	-45.3	-45.2	-45.1	-45.0	-46.3	-46.7	-46.5	-45.7	-45.7
Jul	-28.5	-28.3	-28.2	-28.1	-28.0	-28.0	-29.6	-30.1	-29.8	-28.9	-28.9
Aug	-31.4	-31.2	-31.2	-31.1	-31.0	-31.0	-32.2	-32.6	-32.3	-31.6	-31.6
Sep	-54.9	-54.6	-54.8	-54.7	-54.6	-54.5	-55.6	-55.8	-55.7	-54.9	-55.0
Oct	-85.3	-85.0	-85.2	-85.1	-84.9	-84.9	-85.9	-86.0	-85.9	-85.1	-85.2
Nov	-141.5	-141.1	-141.6	-141.5	-141.2	-141.1	-142.1	-142.1	-142.0	-141.2	-141.3
Dec	-158.1	-157.7	-158.1	-158.1	-157.8	-157.7	-158.6	-158.6	-158.5	-157.7	-157.8

Table A. 74: Pamplona monthly accumulated total heat gains (positive values) and losses (negative values) (kWh·m^{-2}).

	RC1	**RC2**	**M5**	**M6**	**M7**	**M8**	**A**	**AS2.2**	**AS_2.3**	**V_1.1**	**V_1.2**
Jan	-204.4	-243.0	-201.3	-209.0	-229.9	-244.3	-159.6	-165.2	-171.0	-240.7	-234.6
Feb	-196.0	-230.7	-195.8	-203.3	-221.5	-233.9	-149.7	-151.6	-158.8	-224.9	-219.3
Mar	-184.2	-217.7	-188.2	-196.3	-213.6	-225.1	-127.3	-120.0	-131.1	-203.0	-197.5
Apr	-160.4	-189.0	-165.8	-173.0	-188.5	-198.5	-102.7	-87.2	-99.8	-168.3	-163.8
May	-112.5	-136.5	-122.0	-129.3	-141.7	-149.1	-50.6	-28.8	-43.9	-109.8	-105.8
Jun	-69.3	-85.2	-81.7	-88.1	-96.4	-100.2	-8.8	20.0	3.5	-53.1	-50.4
Jul	-57.2	-74.1	-72.8	-80.5	-88.2	-91.1	10.6	40.5	21.9	-39.2	-36.0
Aug	-56.1	-71.2	-68.3	-74.8	-82.1	-84.9	-0.2	23.3	8.3	-43.4	-40.6
Sep	-87.7	-109.5	-97.9	-105.5	-115.5	-120.7	-32.1	-17.5	-30.8	-88.3	-84.2
Oct	-119.9	-146.1	-124.5	-131.6	-144.8	-152.9	-73.2	-68.3	-77.5	-134.4	-129.8
Nov	-179.5	-212.1	-178.6	-185.7	-203.1	-214.9	-137.2	-139.4	-145.8	-207.3	-202.1
Dec	-204.9	-244.7	-203.1	-211.5	-232.2	-246.3	-157.9	-165.5	-171.7	-243.0	-236.5

Madrid

Table A. 75: Madrid monthly accumulated radiative heat losses (kWh·m^{-2}).

	RC1	RC2	M5	M6	M7	M8	A	AS_2.2	AS_2.3	V_1.1	V_1.2
Jan	-44.5	-82.8	-40.3	-47.9	-67.8	-81.4	-8.1	-23.2	-26.1	-88.5	-82.1
Feb	-45.8	-81.8	-45.2	-53.3	-70.3	-81.7	-8.0	-23.7	-27.5	-86.6	-80.2
Mar	-44.9	-79.1	-45.1	-53.2	-69.1	-79.5	-7.7	-23.1	-27.0	-83.6	-77.4
Apr	-40.6	-70.7	-41.7	-49.0	-62.8	-71.5	-6.9	-20.9	-24.6	-74.6	-69.0
May	-38.3	-62.8	-42.8	-50.1	-59.9	-65.0	-6.1	-19.4	-23.7	-65.4	-60.3
Jun	-35.3	-52.0	-44.6	-52.0	-56.0	-56.0	-5.1	-17.4	-22.6	-52.7	-48.3
Jul	-38.2	-53.4	-51.1	-59.3	-61.0	-58.6	-5.2	-18.7	-24.9	-53.3	-48.6
Aug	-31.0	-43.5	-41.1	-47.8	-49.7	-47.7	-4.2	-15.1	-20.1	-43.5	-39.7
Sep	-33.2	-51.9	-39.3	-46.0	-52.3	-54.8	-5.1	-16.6	-20.9	-53.4	-49.1
Oct	-32.6	-56.8	-33.2	-39.2	-50.7	-57.6	-5.6	-16.7	-19.7	-59.9	-55.4
Nov	-40.0	-72.9	-37.7	-44.8	-61.3	-72.4	-7.1	-20.7	-23.7	-77.6	-71.9
Dec	-41.1	-77.6	-36.1	-43.2	-62.6	-76.0	-7.6	-21.5	-24.0	-83.1	-77.1

Table A. 76: Madrid monthly accumulated solar heat gains (kWh·m^{-2}).

	RC1	RC2	M5	M6	M7	M8	A	AS_2.2	AS_2.3	V_1.1	V_1.2
Jan	2.6	3.9	0.0	0.0	0.0	0.0	12.7	24.6	20.8	14.1	13.7
Feb	3.5	5.2	0.0	0.0	0.0	0.0	17.2	33.5	28.2	19.2	18.6
Mar	5.7	8.5	0.0	0.0	0.0	0.0	27.8	54.2	45.7	31.1	30.0
Apr	7.0	10.4	0.0	0.0	0.0	0.0	34.3	66.7	56.3	38.2	37.0
May	8.3	12.3	0.0	0.0	0.0	0.0	40.4	78.7	66.4	45.1	43.6
Jun	9.3	13.8	0.0	0.0	0.0	0.0	45.4	88.4	74.6	50.7	49.0
Jul	9.9	14.8	0.0	0.0	0.0	0.0	48.6	94.7	79.9	54.3	52.5
Aug	8.7	13.0	0.0	0.0	0.0	0.0	42.7	83.1	70.2	47.7	46.1
Sep	6.4	9.5	0.0	0.0	0.0	0.0	31.4	61.1	51.5	35.0	33.9
Oct	4.3	6.4	0.0	0.0	0.0	0.0	20.9	40.7	34.4	23.4	22.6
Nov	2.8	4.2	0.0	0.0	0.0	0.0	13.9	27.0	22.8	15.5	15.0
Dec	2.2	3.2	0.0	0.0	0.0	0.0	10.6	20.7	17.5	11.9	11.5

Table A. 77: Madrid monthly accumulated convective heat gains (positive values) and losses (negative values) (kWh·m^{-2}).

	RC1	RC2	M5	M6	M7	M8	A	AS_2.2	AS_2.3	V_1.1	V_1.2
Jan	-96.9	-96.7	-96.9	-96.9	-96.7	-96.6	-97.3	-97.3	-97.2	-96.7	-96.8
Feb	-87.2	-86.9	-87.1	-87.1	-86.9	-86.8	-87.6	-87.6	-87.6	-87.0	-87.0
Mar	-92.4	-92.1	-92.3	-92.2	-92.1	-92.0	-93.0	-93.1	-93.0	-92.2	-92.3
Apr	-73.9	-73.6	-73.8	-73.7	-73.6	-73.5	-74.6	-74.8	-74.6	-73.9	-74.0
May	-36.5	-36.3	-36.4	-36.3	-36.2	-36.2	-37.1	-37.4	-37.2	-36.6	-36.7
Jun	2.7	2.8	2.9	2.9	3.0	3.0	2.0	1.7	1.9	2.4	2.4

Jul	26.1	26.1	26.3	26.4	26.4	26.4	25.3	24.9	25.1	25.7	25.7
Aug	18.9	19.0	19.1	19.2	19.2	19.2	18.3	18.0	18.2	18.6	18.6
Sep	-11.8	-11.7	-11.7	-11.7	-11.6	-11.6	-12.3	-12.4	-12.3	-11.9	-11.9
Oct	-47.1	-47.0	-47.1	-47.0	-46.9	-46.9	-47.5	-47.6	-47.5	-47.1	-47.1
Nov	-80.0	-79.8	-80.0	-80.0	-79.8	-79.8	-80.4	-80.4	-80.4	-79.9	-79.9
Dec	-93.1	-92.9	-93.2	-93.1	-93.0	-92.9	-93.4	-93.4	-93.4	-92.9	-92.9

Table A. 78: Madrid monthly accumulated total heat gains (positive values) and losses (negative values) (kWh·m^{-2}).

	RC1	RC2	M5	M6	M7	M8	A	AS_2.2	AS_2.3	V_1.1	V_1.2
Jan	-138.8	-175.6	-137.2	-144.8	-164.5	-178.1	-92.7	-95.9	-102.6	-171.0	-165.2
Feb	-129.5	-163.4	-132.3	-140.3	-157.2	-168.5	-78.4	-77.9	-86.8	-154.4	-148.7
Mar	-131.5	-162.6	-137.4	-145.4	-161.2	-171.5	-72.9	-62.0	-74.3	-144.8	-139.6
Apr	-107.5	-133.9	-115.5	-122.8	-136.4	-145.0	-47.2	-29.0	-43.0	-110.3	-106.0
May	-66.5	-86.8	-79.1	-86.4	-96.1	-101.2	-2.8	21.9	5.5	-57.0	-53.4
Jun	-23.3	-35.4	-41.8	-49.0	-53.0	-53.0	42.4	72.7	53.9	0.4	3.1
Jul	-2.2	-12.4	-24.8	-32.9	-34.6	-32.2	68.8	100.9	80.1	26.7	29.5
Aug	-3.4	-11.5	-22.0	-28.6	-30.5	-28.6	56.8	86.0	68.2	22.9	25.0
Sep	-38.6	-54.0	-51.0	-57.6	-63.9	-66.3	14.1	32.1	18.4	-30.3	-27.2
Oct	-75.4	-97.3	-80.2	-86.2	-97.6	-104.5	-32.2	-23.6	-32.8	-83.7	-80.0
Nov	-117.2	-148.4	-117.7	-124.7	-141.1	-152.2	-73.7	-74.2	-81.3	-142.0	-136.9
Dec	-132.1	-167.2	-129.3	-136.3	-155.5	-168.9	-90.4	-94.3	-99.9	-164.1	-158.6

Athens

Table A. 79: Athens monthly accumulated radiative heat losses (kWh·m^{-2}).

	RC1	RC2	M5	M6	M7	M8	A	AS_2.2	AS_2.3	V_1.1	V_1.2
Jan	-45.6	-82.3	-44.0	-52.1	-70.0	-82.0	-8.0	-23.6	-27.2	-87.4	-80.9
Feb	-39.3	-71.7	-37.0	-44.0	-60.2	-71.2	-7.0	-20.4	-23.3	-76.3	-70.7
Mar	-42.0	-74.3	-41.8	-49.5	-64.9	-74.8	-7.3	-21.6	-25.3	-78.7	-72.8
Apr	-39.9	-68.2	-42.1	-49.6	-62.1	-69.6	-6.7	-20.4	-24.4	-71.7	-66.3
May	-33.9	-54.5	-38.8	-45.6	-53.5	-57.0	-5.3	-17.0	-21.1	-56.5	-52.0
Jun	-29.8	-43.5	-37.8	-44.2	-47.8	-47.2	-4.2	-14.6	-19.1	-44.0	-40.3
Jul	-25.5	-33.7	-35.3	-41.2	-41.6	-38.0	-3.3	-12.2	-16.7	-33.1	-30.1
Aug	-35.1	-47.8	-47.3	-55.4	-56.5	-53.1	-4.6	-16.9	-22.9	-47.4	-43.2
Sep	-27.0	-41.8	-32.1	-37.7	-43.1	-44.5	-4.1	-13.4	-17.0	-42.9	-39.4
Oct	-30.0	-50.0	-32.5	-38.4	-47.3	-51.8	-4.9	-15.2	-18.4	-52.4	-48.3
Nov	-40.3	-69.3	-41.8	-49.4	-62.5	-70.5	-6.8	-20.5	-24.4	-73.0	-67.4
Dec	-42.3	-75.9	-41.0	-48.5	-65.0	-75.9	-7.4	-21.8	-25.2	-80.6	-74.7

Table A. 80: Athens monthly accumulated solar heat gains (kWh·m^{-2}).

	RC1	RC2	M5	M6	M7	M8	A	AS_2.2	AS_2.3	V_1.1	V_1.2
Jan	3.0	4.5	0.0	0.0	0.0	0.0	14.8	28.9	24.4	16.6	16.0
Feb	3.5	5.3	0.0	0.0	0.0	0.0	17.3	33.6	28.4	19.3	18.6
Mar	5.9	8.8	0.0	0.0	0.0	0.0	28.8	56.1	47.3	32.2	31.1
Apr	7.3	10.9	0.0	0.0	0.0	0.0	36.0	70.0	59.1	40.2	38.8
May	8.9	13.3	0.0	0.0	0.0	0.0	43.6	84.9	71.7	48.7	47.1
Jun	9.6	14.4	0.0	0.0	0.0	0.0	47.2	91.9	77.5	52.7	51.0
Jul	10.0	14.9	0.0	0.0	0.0	0.0	49.0	95.3	80.4	54.7	52.8
Aug	9.0	13.5	0.0	0.0	0.0	0.0	44.2	86.0	72.6	49.4	47.7
Sep	6.6	9.9	0.0	0.0	0.0	0.0	32.5	63.2	53.3	36.3	35.0
Oct	4.8	7.1	0.0	0.0	0.0	0.0	23.3	45.3	38.3	26.0	25.1
Nov	3.4	5.1	0.0	0.0	0.0	0.0	16.7	32.5	27.4	18.6	18.0
Dec	2.5	3.7	0.0	0.0	0.0	0.0	12.3	23.9	20.2	13.7	13.3

Table A. 81: Athens monthly accumulated convective heat gains (positive values) and losses (negative values) (kWh·m^{-2}).

	RC1	RC2	M5	M6	M7	M8	A	AS2.2	AS_2.3	V_1.1	V_1.2
Jan	-127.5	-127.1	-127.5	-127.4	-127.2	-127.1	-128.1	-128.1	-128.0	-127.2	-127.3
Feb	-119.1	-118.7	-119.1	-119.0	-118.8	-118.7	-119.7	-119.7	-119.6	-118.9	-118.9
Mar	-93.8	-93.5	-93.7	-93.6	-93.5	-93.4	-94.4	-94.6	-94.4	-93.7	-93.7
Apr	-67.4	-67.2	-67.3	-67.2	-67.1	-67.0	-68.1	-68.4	-68.2	-67.5	-67.5
May	-28.9	-28.7	-28.7	-28.6	-28.5	-28.5	-29.6	-30.0	-29.8	-29.1	-29.2
Jun	6.8	6.9	7.0	7.1	7.1	7.1	6.0	5.5	5.7	6.4	6.3
Jul	42.3	42.4	42.6	42.7	42.7	42.7	41.5	40.9	41.2	41.8	41.7
Aug	37.9	38.0	38.2	38.3	38.3	38.2	36.9	36.5	36.8	37.4	37.4
Sep	-11.1	-11.0	-11.0	-10.9	-10.8	-10.8	-11.7	-11.9	-11.8	-11.3	-11.3
Oct	-37.2	-37.1	-37.2	-37.1	-37.0	-37.0	-37.7	-37.9	-37.8	-37.3	-37.3
Nov	-67.1	-66.9	-67.1	-67.0	-66.9	-66.8	-67.6	-67.6	-67.6	-67.0	-67.0
Dec	-109.8	-109.5	-109.8	-109.7	-109.6	-109.4	-110.4	-110.3	-110.3	-109.6	-109.6

Table A. 82: Athens monthly accumulated total heat gains (positive values) and losses (negative values) (kWh·m^{-2}).

	RC1	RC2	M5	M6	M7	M8	A	AS2.2	AS_2.3	V_1.1	V_1.2
Jan	-170.1	-204.9	-171.5	-179.5	-197.2	-209.1	-121.3	-122.8	-130.8	-198.0	-192.2
Feb	-154.9	-185.1	-156.1	-162.9	-179.0	-189.8	-109.4	-106.5	-114.6	-175.9	-171.0
Mar	-129.9	-159.0	-135.5	-143.1	-158.4	-168.2	-72.9	-60.1	-72.3	-140.2	-135.5
Apr	-100.0	-124.4	-109.4	-116.8	-129.2	-136.7	-38.8	-18.8	-33.5	-99.1	-95.0
May	-53.9	-69.9	-67.5	-74.2	-82.1	-85.5	8.7	37.9	20.7	-36.9	-34.1
Jun	-13.4	-22.3	-30.7	-37.1	-40.7	-40.1	48.9	82.7	64.2	15.0	17.0
Jul	26.8	23.6	7.4	1.5	1.1	4.6	87.2	123.9	104.8	63.3	64.5
Aug	11.8	3.6	-9.2	-17.1	-18.2	-14.9	76.5	105.6	86.5	39.4	41.9

Sep	-31.5	-42.9	-43.0	-48.6	-53.9	-55.3	16.7	37.9	24.6	-17.9	-15.7
Oct	-62.5	-80.0	-69.7	-75.5	-84.3	-88.8	-19.4	-7.8	-17.9	-63.6	-60.5
Nov	-104.0	-131.1	-108.9	-116.3	-129.4	-137.3	-57.7	-55.7	-64.6	-121.3	-116.5
Dec	-149.6	-181.7	-150.8	-158.3	-174.6	-185.4	-105.5	-108.2	-115.3	-176.4	-171.0

Dehli

Table A. 83: Dehli monthly accumulated radiative heat losses (kWh·m^{-2}).

	RC1	RC2	M5	M6	M7	M8	A	AS_2.2	AS_2.3	V_1.1	V_1.2
Jan	-50.2	-85.2	-53.5	-62.9	-77.9	-87.0	-8.3	-25.6	-30.7	-89.4	-82.6
Feb	-48.7	-78.4	-55.9	-65.5	-76.2	-81.7	-7.7	-24.5	-30.3	-81.3	-74.8
Mar	-43.9	-66.0	-54.1	-63.4	-69.5	-70.7	-6.4	-21.7	-27.9	-67.3	-61.8
Apr	-37.7	-50.6	-51.9	-60.5	-60.6	-56.4	-4.9	-18.2	-24.8	-49.8	-45.4
May	-34.2	-41.5	-50.2	-58.8	-55.8	-48.1	-3.9	-16.1	-22.8	-39.4	-35.6
Jun	-26.8	-31.9	-39.5	-46.5	-44.5	-37.5	-3.0	-12.5	-17.8	-30.1	-27.2
Jul	-14.2	-14.4	-22.7	-26.8	-24.6	-18.4	-1.3	-6.4	-9.6	-12.6	-11.2
Aug	-15.6	-17.8	-23.5	-27.7	-26.7	-21.6	-1.7	-7.2	-10.4	-16.5	-14.8
Sep	-26.4	-35.3	-35.5	-42.0	-43.3	-39.8	-3.4	-12.6	-17.1	-34.7	-31.6
Oct	-44.5	-64.5	-56.5	-66.5	-71.0	-70.1	-6.3	-21.7	-28.5	-65.1	-59.6
Nov	-51.1	-80.2	-60.3	-70.7	-80.3	-84.4	-7.8	-25.5	-32.1	-82.6	-75.9
Dec	-56.6	-92.8	-63.4	-74.3	-88.1	-96.0	-9.1	-28.6	-35.0	-96.6	-89.0

Table A. 84: Dehli monthly accumulated solar heat gains (kWh·m^{-2}).

	RC1	RC2	M5	M6	M7	M8	A	AS_2.2	AS_2.3	V_1.1	V_1.2
Jan	5.0	7.5	0.0	0.0	0.0	0.0	24.7	48.0	40.5	27.5	26.6
Feb	5.8	8.7	0.0	0.0	0.0	0.0	28.6	55.6	47.0	31.9	30.9
Mar	8.0	12.0	0.0	0.0	0.0	0.0	39.3	76.5	64.6	43.9	42.4
Apr	8.8	13.1	0.0	0.0	0.0	0.0	43.1	84.0	70.9	48.2	46.6
May	9.5	14.1	0.0	0.0	0.0	0.0	46.3	90.2	76.1	51.7	50.0
Jun	8.4	12.5	0.0	0.0	0.0	0.0	41.1	79.9	67.4	45.9	44.3
Jul	7.1	10.6	0.0	0.0	0.0	0.0	34.8	67.7	57.1	38.9	37.6
Aug	6.8	10.2	0.0	0.0	0.0	0.0	33.4	64.9	54.8	37.2	36.0
Sep	7.3	10.8	0.0	0.0	0.0	0.0	35.6	69.3	58.5	39.8	38.4
Oct	7.0	10.5	0.0	0.0	0.0	0.0	34.3	66.9	56.4	38.4	37.1
Nov	5.5	8.2	0.0	0.0	0.0	0.0	26.8	52.1	44.0	29.9	28.9
Dec	4.9	7.3	0.0	0.0	0.0	0.0	24.0	46.7	39.4	26.8	25.9

Table A. 85: Dehli monthly accumulated convective heat gains (positive values) and losses (negative values) (kWh·m^{-2}).

	RC1	RC2	M5	M6	M7	M8	A	AS_2.2	AS_2.3	V_1.1	V_1.2
Jan	-58.6	-58.4	-58.6	-58.5	-58.4	-58.3	-59.1	-59.2	-59.1	-58.6	-58.6
Feb	-36.5	-36.3	-36.4	-36.3	-36.2	-36.2	-37.1	-37.2	-37.1	-36.5	-36.5
Mar	-3.0	-2.9	-2.8	-2.7	-2.7	-2.7	-3.6	-3.9	-3.7	-3.2	-3.2
Apr	34.5	34.6	34.7	34.8	34.8	34.8	33.9	33.5	33.7	34.2	34.2
May	61.0	61.0	61.3	61.4	61.3	61.3	60.3	59.9	60.1	60.6	60.6
Jun	50.4	50.4	50.6	50.7	50.7	50.6	49.9	49.5	49.7	50.0	50.0
Jul	45.6	45.6	45.8	45.8	45.8	45.7	45.2	44.9	45.0	45.2	45.2
Aug	35.0	34.9	35.1	35.1	35.1	35.1	34.6	34.3	34.5	34.7	34.7
Sep	23.2	23.3	23.4	23.4	23.4	23.4	22.8	22.6	22.7	23.0	23.0
Oct	9.0	9.0	9.1	9.1	9.2	9.1	8.5	8.4	8.5	8.8	8.8
Nov	-15.0	-14.9	-14.9	-14.8	-14.8	-14.8	-15.4	-15.5	-15.4	-15.0	-15.0
Dec	-37.4	-37.2	-37.3	-37.2	-37.2	-37.1	-37.8	-37.9	-37.8	-37.3	-37.4

Table A. 86: Dehli monthly accumulated total heat gains (positive values) and losses (negative values) (kWh·m^{-2}).

	RC1	RC2	M5	M6	M7	M8	A	AS_2.2	AS_2.3	V_1.1	V_1.2
Jan	-103.8	-136.1	-112.1	-121.4	-136.3	-145.4	-42.8	-36.8	-49.3	-120.5	-114.6
Feb	-79.4	-106.0	-92.2	-101.8	-112.4	-117.9	-16.1	-6.0	-20.5	-85.8	-80.5
Mar	-38.9	-56.9	-57.0	-66.1	-72.2	-73.4	29.3	51.0	33.0	-26.6	-22.5
Apr	5.6	-2.9	-17.2	-25.7	-25.8	-21.7	72.1	99.3	79.8	32.5	35.3
May	36.3	33.6	11.1	2.6	5.5	13.2	102.7	134.0	113.4	72.9	74.9
Jun	32.0	31.0	11.2	4.2	6.2	13.1	87.9	116.9	99.3	65.8	67.2
Jul	38.5	41.8	23.0	19.0	21.1	27.3	78.6	106.2	92.5	71.5	71.6
Aug	26.2	27.3	11.6	7.4	8.4	13.5	66.3	92.1	78.8	55.4	55.9
Sep	4.2	-1.2	-12.1	-18.6	-19.8	-16.4	55.0	79.3	64.1	28.1	29.8
Oct	-28.5	-45.0	-47.4	-57.3	-61.9	-61.0	36.6	53.5	36.5	-17.9	-13.7
Nov	-60.6	-86.9	-75.2	-85.5	-95.0	-99.2	3.6	11.2	-3.4	-67.7	-62.1
Dec	-89.1	-122.7	-100.7	-111.6	-125.3	-133.1	-22.9	-19.7	-33.4	-107.1	-100.5

Taipei

Table A. 87: Taipei monthly accumulated radiative heat losses (kWh·m^{-2}).

	RC1	RC2	M5	M6	M7	M8	A	AS_2.2	AS_2.3	V_1.1	V_1.2
Jan	-27.1	-50.0	-24.9	-29.8	-42.1	-49.9	-4.9	-14.1	-16.0	-53.4	-49.5
Feb	-20.4	-38.2	-17.9	-21.6	-31.7	-38.0	-3.8	-10.6	-11.9	-41.0	-38.0
Mar	-19.9	-36.2	-18.6	-22.3	-31.4	-36.6	-3.6	-10.3	-11.8	-38.7	-35.8
Apr	-16.0	-26.8	-17.1	-20.3	-25.8	-28.0	-2.6	-8.1	-9.8	-28.0	-25.9
May	-10.5	-14.7	-13.4	-15.9	-17.7	-16.5	-1.4	-5.0	-6.7	-14.7	-13.4

Jun	-10.0	-11.9	-14.5	-17.1	-17.3	-14.3	-1.1	-4.6	-6.6	-11.3	-10.2
Jul	-12.3	-13.0	-19.3	-22.8	-21.5	-16.4	-1.2	-5.6	-8.3	-11.7	-10.4
Aug	-12.9	-14.7	-19.4	-22.9	-22.2	-17.9	-1.4	-5.9	-8.6	-13.7	-12.3
Sep	-15.0	-20.8	-19.5	-23.1	-25.0	-23.4	-2.0	-7.2	-9.6	-20.8	-18.9
Oct	-17.4	-27.0	-20.3	-24.1	-28.3	-29.0	-2.7	-8.6	-10.8	-27.8	-25.5
Nov	-20.2	-34.4	-20.8	-24.8	-32.0	-35.5	-3.4	-10.2	-12.2	-36.2	-33.5
Dec	-25.8	-46.2	-24.9	-29.7	-40.3	-46.6	-4.5	-13.2	-15.3	-49.0	-45.4

Table A. 88: Taipei monthly accumulated solar heat (kWh·m^{-2}).

	RC1	**RC2**	**M5**	**M6**	**M7**	**M8**	**A**	**AS_2.2**	**AS_2.3**	**V_1.1**	**V_1.2**
Jan	2.6	3.9	0.0	0.0	0.0	0.0	12.8	25.0	21.1	14.3	13.8
Feb	2.6	4.0	0.0	0.0	0.0	0.0	13.0	25.3	21.3	14.5	14.0
Mar	3.7	5.4	0.0	0.0	0.0	0.0	17.9	34.8	29.4	20.0	19.3
Apr	4.8	7.1	0.0	0.0	0.0	0.0	23.4	45.5	38.4	26.1	25.2
May	5.6	8.4	0.0	0.0	0.0	0.0	27.5	53.6	45.2	30.7	29.7
Jun	6.4	9.5	0.0	0.0	0.0	0.0	31.2	60.7	51.2	34.8	33.7
Jul	8.1	12.1	0.0	0.0	0.0	0.0	39.8	77.5	65.4	44.5	43.0
Aug	7.5	11.2	0.0	0.0	0.0	0.0	36.7	71.5	60.3	41.0	39.6
Sep	6.0	8.9	0.0	0.0	0.0	0.0	29.3	57.0	48.1	32.7	31.6
Oct	4.5	6.7	0.0	0.0	0.0	0.0	22.1	42.9	36.2	24.6	23.8
Nov	3.3	4.9	0.0	0.0	0.0	0.0	16.2	31.6	26.7	18.1	17.5
Dec	2.8	4.2	0.0	0.0	0.0	0.0	13.7	26.7	22.5	15.3	14.8

Table A. 89: Taipei monthly accumulated convective heat gains (positive values) and losses (negative values) (kWh·m^{-2}).

	RC1	**RC2**	**M5**	**M6**	**M7**	**M8**	**A**	**AS_2.2**	**AS_2.3**	**V_1.1**	**V_1.2**
Jan	-65.4	-65.2	-65.4	-65.3	-65.2	-65.2	-65.7	-65.7	-65.7	-65.3	-65.3
Feb	-51.2	-51.0	-51.2	-51.1	-51.0	-51.0	-51.4	-51.5	-51.4	-51.1	-51.1
Mar	-39.5	-39.3	-39.4	-39.4	-39.3	-39.3	-39.7	-39.8	-39.8	-39.4	-39.5
Apr	-14.1	-14.0	-14.0	-14.0	-13.9	-13.9	-14.4	-14.6	-14.5	-14.2	-14.2
May	9.3	9.3	9.4	9.4	9.5	9.4	9.0	8.8	8.9	9.1	9.1
Jun	16.8	16.8	16.9	16.9	16.9	16.9	16.5	16.3	16.4	16.6	16.6
Jul	33.6	33.6	33.8	33.8	33.8	33.8	33.3	32.9	33.1	33.3	33.3
Aug	28.4	28.3	28.5	28.5	28.5	28.5	28.0	27.7	27.9	28.1	28.1
Sep	14.1	14.2	14.2	14.3	14.3	14.3	13.7	13.5	13.6	13.9	13.9
Oct	-4.9	-4.8	-4.8	-4.8	-4.7	-4.7	-5.3	-5.5	-5.4	-5.0	-5.1
Nov	-29.7	-29.5	-29.6	-29.6	-29.5	-29.5	-30.0	-30.1	-30.0	-29.7	-29.7
Dec	-52.8	-52.6	-52.8	-52.8	-52.7	-52.6	-53.2	-53.2	-53.1	-52.7	-52.8

Table A. 90: Taipei monthly accumulated total heat gains (positive values) and losses (negative values) (kWh·m^{-2}).

	RC1	RC2	M5	M6	M7	M8	A	AS_2.2	AS_2.3	V_1.1	V_1.2
Jan	-89.9	-111.3	-90.2	-95.1	-107.3	-115.1	-57.8	-54.8	-60.6	-104.4	-101.0
Feb	-68.9	-85.3	-69.1	-72.7	-82.8	-89.0	-42.2	-36.8	-42.0	-77.6	-75.1
Mar	-55.7	-70.1	-58.0	-61.7	-70.7	-75.8	-25.4	-15.3	-22.1	-58.1	-55.9
Apr	-25.3	-33.7	-31.1	-34.3	-39.8	-41.9	6.3	22.8	14.1	-16.1	-14.8
May	4.5	3.0	-4.0	-6.4	-8.3	-7.1	35.1	57.4	47.5	25.2	25.4
Jun	13.2	14.4	2.4	-0.2	-0.4	2.5	46.6	72.4	61.0	40.1	40.1
Jul	29.5	32.7	14.5	11.0	12.3	17.3	71.9	104.9	90.2	66.1	65.9
Aug	23.0	24.8	9.1	5.7	6.3	10.5	63.3	93.3	79.6	55.4	55.4
Sep	5.1	2.2	-5.3	-8.8	-10.7	-9.1	41.0	63.3	52.1	25.8	26.6
Oct	-17.8	-25.2	-25.1	-28.8	-33.0	-33.7	14.1	28.9	20.1	-8.2	-6.8
Nov	-46.5	-59.0	-50.4	-54.4	-61.5	-65.0	-17.1	-8.7	-15.5	-47.7	-45.6
Dec	-75.8	-94.6	-77.7	-82.4	-93.0	-99.2	-44.0	-39.8	-46.0	-86.5	-83.4

Chicago

Table A. 91: Chicago monthly accumulated radiative heat losses (kWh·m^{-2}).

	RC1	RC2	M5	M6	M7	M8	A	AS_2.2	AS_2.3	V_1.1	V_1.2
Jan	-57.8	-110.2	-49.5	-59.1	-86.9	-106.3	-10.7	-30.5	-33.5	-118.0	-109.7
Feb	-54.8	-102.6	-49.0	-58.1	-82.7	-99.7	-10.0	-28.8	-32.0	-109.5	-101.7
Mar	-46.9	-88.7	-41.1	-49.0	-71.1	-86.4	-8.6	-24.7	-27.4	-95.0	-88.2
Apr	-38.3	-70.3	-35.6	-42.4	-58.7	-69.6	-6.9	-19.9	-22.7	-75.0	-69.5
May	-39.5	-67.7	-41.3	-48.7	-61.4	-69.0	-6.6	-20.2	-24.0	-71.3	-65.8
Jun	-29.5	-47.7	-33.4	-39.3	-46.8	-49.9	-4.7	-14.8	-18.3	-49.5	-45.6
Jul	-27.4	-41.8	-32.9	-38.7	-43.9	-44.7	-4.1	-13.5	-17.2	-42.8	-39.3
Aug	-24.2	-37.8	-28.2	-33.3	-38.8	-40.2	-3.7	-12.0	-15.1	-39.0	-35.8
Sep	-28.2	-47.6	-30.0	-35.4	-44.4	-49.0	-4.7	-14.3	-17.2	-49.9	-46.1
Oct	-38.9	-69.9	-37.6	-44.6	-59.9	-69.9	-6.8	-20.1	-23.2	-74.2	-68.7
Nov	-45.1	-83.6	-41.1	-48.9	-68.7	-82.2	-8.2	-23.5	-26.5	-89.2	-82.8
Dec	-58.9	-110.8	-52.1	-61.9	-88.9	-107.5	-10.7	-31.0	-34.4	-118.4	-109.9

Table A. 92: Chicago monthly accumulated solar heat gains (kWh·m^{-2}).

	RC1	RC2	M5	M6	M7	M8	A	AS_2.2	AS_2.3	V_1.1	V_1.2
Jan	2.3	3.5	0.0	0.0	0.0	0.0	11.5	22.3	18.8	12.8	12.4
Feb	3.0	4.5	0.0	0.0	0.0	0.0	14.6	28.5	24.0	16.3	15.8
Mar	4.6	6.8	0.0	0.0	0.0	0.0	22.3	43.4	36.6	24.9	24.1
Apr	5.6	8.4	0.0	0.0	0.0	0.0	27.6	53.7	45.3	30.8	29.8
May	7.9	11.8	0.0	0.0	0.0	0.0	38.7	75.2	63.5	43.2	41.7
Jun	8.1	12.0	0.0	0.0	0.0	0.0	39.4	76.8	64.8	44.1	42.6
Jul	8.2	12.2	0.0	0.0	0.0	0.0	40.0	77.9	65.7	44.7	43.2
Aug	6.8	10.2	0.0	0.0	0.0	0.0	33.4	65.1	54.9	37.4	36.1

Sep	5.4	8.0	0.0	0.0	0.0	0.0	26.3	51.2	43.2	29.4	28.4
Oct	3.9	5.8	0.0	0.0	0.0	0.0	19.1	37.1	31.3	21.3	20.6
Nov	2.3	3.5	0.0	0.0	0.0	0.0	11.4	22.3	18.8	12.8	12.3
Dec	2.0	3.0	0.0	0.0	0.0	0.0	9.8	19.0	16.1	10.9	10.6

Table A. 93: Chicago monthly accumulated convective heat gains (positive values) and losses (negative values) (kWh·m^{-2}).

	RC1	**RC2**	**M5**	**M6**	**M7**	**M8**	**A**	**AS2.2**	**AS_2.3**	**V_1.1**	**V_1.2**
Jan	-345.3	-344.4	-345.4	-345.2	-344.7	-344.4	-346.2	-346.0	-345.9	-344.4	-344.5
Feb	-308.4	-307.7	-308.5	-308.3	-307.9	-307.6	-309.4	-309.4	-309.2	-307.8	-307.9
Mar	-253.0	-252.4	-253.0	-252.9	-252.5	-252.3	-253.9	-254.0	-253.9	-252.6	-252.7
Apr	-177.0	-176.5	-176.9	-176.8	-176.5	-176.3	-178.0	-178.3	-178.0	-176.9	-176.9
May	-109.9	-109.5	-109.7	-109.6	-109.4	-109.3	-111.0	-111.4	-111.2	-110.0	-110.1
Jun	-39.7	-39.5	-39.5	-39.4	-39.3	-39.2	-40.5	-41.0	-40.7	-39.9	-40.0
Jul	-6.4	-6.2	-6.2	-6.1	-6.0	-6.0	-7.2	-7.7	-7.4	-6.7	-6.8
Aug	-13.8	-13.7	-13.7	-13.6	-13.5	-13.5	-14.5	-14.8	-14.6	-14.1	-14.1
Sep	-58.6	-58.4	-58.5	-58.4	-58.3	-58.2	-59.2	-59.4	-59.2	-58.6	-58.6
Oct	-136.6	-136.2	-136.6	-136.5	-136.3	-136.1	-137.4	-137.5	-137.3	-136.4	-136.5
Nov	-212.4	-211.8	-212.4	-212.3	-212.0	-211.8	-213.1	-213.1	-213.0	-211.9	-212.0
Dec	-320.5	-319.7	-320.6	-320.4	-320.0	-319.7	-321.4	-321.2	-321.1	-319.7	-319.8

Table A. 94: Chicago monthly accumulated total heat gains (positive values) and losses (negative values) (kWh·m^{-2}).

	RC1	**RC2**	**M5**	**M6**	**M7**	**M8**	**A**	**AS2.2**	**AS_2.3**	**V_1.1**	**V_1.2**
Jan	-400.7	-451.1	-394.9	-404.3	-431.6	-450.7	-345.4	-354.2	-360.6	-449.6	-441.8
Feb	-360.2	-405.8	-357.5	-366.4	-390.6	-407.3	-304.8	-309.7	-317.3	-401.0	-393.8
Mar	-295.4	-334.2	-294.1	-301.9	-323.7	-338.7	-240.3	-235.3	-244.6	-322.6	-316.8
Apr	-209.7	-238.4	-212.5	-219.2	-235.2	-246.0	-157.3	-144.5	-155.4	-221.0	-216.7
May	-141.5	-165.5	-151.0	-158.3	-170.8	-178.3	-79.0	-56.4	-71.7	-138.1	-134.2
Jun	-61.1	-75.1	-72.8	-78.7	-86.0	-89.1	-5.8	21.0	5.7	-45.4	-43.0
Jul	-25.6	-35.9	-39.0	-44.8	-49.9	-50.7	28.7	56.7	41.1	-4.9	-2.9
Aug	-31.2	-41.3	-41.8	-46.9	-52.3	-53.7	15.3	38.3	25.2	-15.7	-13.8
Sep	-81.4	-97.9	-88.5	-93.9	-102.7	-107.2	-37.5	-22.4	-33.2	-79.1	-76.3
Oct	-171.6	-200.3	-174.2	-181.1	-196.2	-206.0	-125.1	-120.5	-129.2	-189.3	-184.6
Nov	-255.2	-291.9	-253.5	-261.2	-280.7	-294.0	-209.9	-214.4	-220.7	-288.3	-282.4
Dec	-377.4	-427.5	-372.7	-382.3	-408.9	-427.2	-322.4	-333.2	-339.4	-427.1	-419.2

Montréal

Table A. 95: Montréal monthly accumulated radiative heat losses (kWh·m^{-2}).

	RC1	RC2	M5	M6	M7	M8	A	AS_2.2	AS_2.3	V_1.1	V_1.2
Jan	-71.0	-134.5	-62.1	-73.5	-106.5	-129.3	-13.0	-37.5	-41.3	-143.5	-133.4
Feb	-62.4	-117.7	-55.3	-65.4	-93.9	-113.6	-11.4	-33.0	-36.4	-125.6	-116.7
Mar	-60.8	-113.4	-55.1	-65.2	-92.0	-110.5	-11.0	-31.9	-35.7	-120.9	-112.2
Apr	-44.8	-82.7	-41.2	-48.9	-68.2	-81.5	-8.1	-23.4	-26.4	-88.2	-81.9
May	-38.3	-68.0	-37.9	-44.8	-59.2	-68.4	-6.7	-19.8	-23.0	-72.1	-66.7
Jun	-28.5	-48.4	-30.0	-35.6	-44.9	-49.8	-4.8	-14.5	-17.4	-50.9	-47.0
Jul	-28.7	-46.5	-32.1	-38.0	-45.6	-48.7	-4.6	-14.4	-17.8	-48.4	-44.6
Aug	-27.1	-44.4	-29.9	-35.3	-43.0	-46.3	-4.4	-13.6	-16.7	-46.3	-42.7
Sep	-31.7	-55.2	-32.0	-37.9	-49.3	-56.1	-5.4	-16.2	-19.1	-58.3	-54.0
Oct	-42.8	-78.3	-39.9	-47.4	-65.5	-77.6	-7.7	-22.2	-25.3	-83.4	-77.3
Nov	-48.2	-90.6	-42.7	-50.9	-73.1	-88.5	-8.8	-25.3	-28.2	-96.9	-90.0
Dec	-63.5	-120.6	-55.1	-65.5	-95.4	-116.2	-11.7	-33.5	-36.9	-128.9	-119.8

Table A. 96: Montréal monthly accumulated solar heat gains (kWh·m^{-2}).

	RC1	RC2	M5	M6	M7	M8	A	AS_2.2	AS_2.3	V_1.1	V_1.2
Jan	2.1	3.2	0.0	0.0	0.0	0.0	10.4	20.2	17.0	11.6	11.2
Feb	3.0	4.5	0.0	0.0	0.0	0.0	14.6	28.5	24.0	16.3	15.8
Mar	4.8	7.2	0.0	0.0	0.0	0.0	23.7	46.1	38.9	26.4	25.5
Apr	5.7	8.5	0.0	0.0	0.0	0.0	28.1	54.6	46.1	31.3	30.3
May	7.1	10.6	0.0	0.0	0.0	0.0	34.7	67.6	57.0	38.8	37.5
Jun	7.6	11.3	0.0	0.0	0.0	0.0	37.1	72.2	60.9	41.4	40.0
Jul	7.9	11.8	0.0	0.0	0.0	0.0	38.7	75.3	63.5	43.2	41.8
Aug	6.5	9.7	0.0	0.0	0.0	0.0	31.9	62.2	52.4	35.7	34.5
Sep	4.9	7.4	0.0	0.0	0.0	0.0	24.2	47.1	39.7	27.0	26.1
Oct	3.2	4.8	0.0	0.0	0.0	0.0	15.9	30.9	26.1	17.7	17.2
Nov	1.8	2.6	0.0	0.0	0.0	0.0	8.6	16.8	14.2	9.6	9.3
Dec	1.5	2.3	0.0	0.0	0.0	0.0	7.6	14.8	12.5	8.5	8.2

Table A. 97: Montréal monthly accumulated convective heat gains (positive values) and losses (negative values) (kWh·m^{-2}).

	RC1	RC2	M5	M6	M7	M8	A	AS2.2	AS_2.3	V_1.1	V_1.2
Jan	-254.0	-253.4	-254.0	-253.9	-253.6	-253.4	-254.7	-254.5	-254.5	-253.4	-253.5
Feb	-221.7	-221.1	-221.7	-221.6	-221.3	-221.1	-222.3	-222.3	-222.2	-221.2	-221.3
Mar	-199.9	-199.3	-199.9	-199.8	-199.5	-199.3	-200.6	-200.6	-200.5	-199.5	-199.5
Apr	-133.3	-132.9	-133.3	-133.2	-133.0	-132.9	-134.0	-134.1	-134.0	-133.2	-133.2
May	-81.5	-81.2	-81.4	-81.3	-81.2	-81.1	-82.1	-82.4	-82.2	-81.5	-81.5
Jun	-38.0	-37.9	-37.9	-37.9	-37.8	-37.7	-38.5	-38.8	-38.7	-38.1	-38.2

Jul	-19.3	-19.2	-19.2	-19.2	-19.1	-19.1	-19.9	-20.2	-20.0	-19.6	-19.6
Aug	-21.7	-21.6	-21.7	-21.6	-21.6	-21.5	-22.2	-22.4	-22.3	-21.9	-21.9
Sep	-52.5	-52.3	-52.4	-52.4	-52.3	-52.2	-52.9	-53.0	-52.9	-52.5	-52.5
Oct	-104.4	-104.1	-104.4	-104.3	-104.2	-104.1	-104.9	-105.0	-104.9	-104.2	-104.3
Nov	-141.5	-141.1	-141.5	-141.5	-141.3	-141.1	-141.9	-141.9	-141.8	-141.1	-141.2
Dec	-219.3	-218.8	-219.4	-219.3	-219.0	-218.8	-219.9	-219.8	-219.7	-218.8	-218.9

Table A. 98: Montréal monthly accumulated total heat gains (positive values) and losses (negative values) (kWh·m^{-2}).

	RC1	RC2	M5	M6	M7	M8	A	AS2.2	AS_2.3	V_1.1	V_1.2
Jan	-322.9	-384.7	-316.2	-327.5	-360.1	-382.6	-257.3	-271.9	-278.7	-385.3	-375.7
Feb	-281.1	-334.4	-277.0	-287.0	-315.2	-334.7	-219.1	-226.8	-234.6	-330.4	-322.1
Mar	-255.8	-305.5	-255.0	-265.0	-291.5	-309.8	-187.9	-186.5	-197.3	-293.9	-286.2
Apr	-172.3	-207.1	-174.4	-182.1	-201.2	-214.3	-114.0	-102.9	-114.3	-190.1	-184.8
May	-112.7	-138.6	-119.3	-126.2	-140.4	-149.5	-54.0	-34.5	-48.2	-114.8	-110.8
Jun	-59.0	-75.0	-67.9	-73.4	-82.6	-87.5	-6.2	18.9	4.9	-47.6	-45.1
Jul	-40.2	-54.0	-51.4	-57.2	-64.7	-67.8	14.3	40.7	25.8	-24.8	-22.4
Aug	-42.3	-56.4	-51.6	-57.0	-64.5	-67.9	5.4	26.1	13.5	-32.5	-30.1
Sep	-79.2	-100.1	-84.4	-90.3	-101.6	-108.3	-34.1	-22.1	-32.3	-83.8	-80.3
Oct	-143.9	-177.6	-144.4	-151.8	-169.7	-181.7	-96.7	-96.3	-104.1	-169.9	-164.5
Nov	-187.9	-229.1	-184.3	-192.4	-214.3	-229.6	-142.1	-150.4	-155.8	-228.4	-221.9
Dec	-281.3	-337.1	-274.5	-284.8	-314.4	-335.0	-224.0	-238.5	-244.1	-339.2	-330.4

Beijing

Table A. 99: Beijing monthly accumulated radiative heat losses (kWh·m^{-2}).

	RC1	RC2	M5	M6	M7	M8	A	AS_2.2	AS_2.3	V_1.1	V_1.2
Jan	-68.7	-126.4	-64.2	-75.4	-103.8	-123.6	-12.2	-36.0	-40.6	-134.4	-124.7
Feb	-58.0	-105.8	-55.3	-64.9	-88.1	-104.2	-10.3	-30.3	-34.5	-112.4	-104.2
Mar	-53.8	-95.9	-53.5	-62.6	-82.2	-95.6	-9.3	-27.9	-32.3	-101.5	-94.0
Apr	-39.9	-68.5	-42.0	-49.3	-61.8	-69.7	-6.7	-20.4	-24.3	-72.1	-66.6
May	-34.4	-54.6	-40.1	-46.9	-54.2	-57.3	-5.3	-17.2	-21.5	-56.4	-51.9
Jun	-24.7	-36.8	-30.5	-35.8	-39.7	-39.7	-3.6	-12.1	-15.7	-37.4	-34.3
Jul	-15.1	-21.0	-19.8	-23.4	-25.2	-23.5	-2.0	-7.3	-9.7	-20.9	-19.0
Aug	-18.2	-26.8	-22.4	-26.5	-29.8	-29.3	-2.6	-8.9	-11.5	-27.2	-24.9
Sep	-27.4	-45.0	-30.2	-35.7	-43.3	-46.8	-4.4	-13.8	-16.8	-46.9	-43.2
Oct	-46.2	-79.4	-48.3	-56.7	-71.4	-80.6	-7.8	-23.6	-28.1	-83.5	-77.2
Nov	-52.5	-96.0	-49.6	-58.6	-80.0	-94.7	-9.4	-27.4	-31.2	-102.1	-94.7
Dec	-63.2	-117.5	-57.9	-68.3	-95.6	-114.6	-11.4	-33.2	-37.2	-125.2	-116.2

Table A. 100: Beijing monthly accumulated solar heat gains (kWh·m^{-2}).

	RC1	RC2	M5	M6	M7	M8	A	AS_2.2	AS_2.3	V_1.1	V_1.2
Jan	2.9	4.3	0.0	0.0	0.0	0.0	14.0	27.3	23.0	15.6	15.1
Feb	3.6	5.4	0.0	0.0	0.0	0.0	17.8	34.7	29.3	19.9	19.2
Mar	5.2	7.7	0.0	0.0	0.0	0.0	25.4	49.5	41.8	28.4	27.5
Apr	6.2	9.3	0.0	0.0	0.0	0.0	30.4	59.2	49.9	33.9	32.8
May	7.3	10.8	0.0	0.0	0.0	0.0	35.5	69.2	58.4	39.7	38.4
Jun	6.6	9.9	0.0	0.0	0.0	0.0	32.5	63.2	53.3	36.2	35.0
Jul	6.2	9.2	0.0	0.0	0.0	0.0	30.3	58.9	49.7	33.8	32.7
Aug	5.8	8.7	0.0	0.0	0.0	0.0	28.6	55.8	47.0	32.0	30.9
Sep	5.0	7.5	0.0	0.0	0.0	0.0	24.6	47.9	40.4	27.5	26.5
Oct	4.1	6.1	0.0	0.0	0.0	0.0	19.9	38.8	32.7	22.2	21.5
Nov	2.8	4.2	0.0	0.0	0.0	0.0	13.9	27.1	22.8	15.5	15.0
Dec	2.4	3.6	0.0	0.0	0.0	0.0	12.0	23.3	19.7	13.4	12.9

Table A. 101: Beijing monthly accumulated convective heat gains (positive values) and losses (negative values) (kWh·m^{-2}).

	RC1	RC2	M5	M6	M7	M8	A	AS2.2	AS_2.3	V_1.1	V_1.2
Jan	-232.5	-231.9	-232.6	-232.4	-232.1	-231.9	-233.3	-233.2	-233.1	-231.9	-232.0
Feb	-178.6	-178.1	-178.6	-178.5	-178.2	-178.0	-179.3	-179.3	-179.2	-178.2	-178.3
Mar	-160.3	-159.8	-160.3	-160.1	-159.9	-159.7	-161.2	-161.3	-161.1	-160.0	-160.1
Apr	-83.5	-83.2	-83.4	-83.3	-83.2	-83.1	-84.3	-84.6	-84.4	-83.5	-83.6
May	-28.7	-28.5	-28.5	-28.4	-28.3	-28.3	-29.4	-29.8	-29.6	-28.9	-28.9
Jun	0.6	0.7	0.7	0.8	0.8	0.8	0.1	-0.2	0.0	0.4	0.4
Jul	16.5	16.6	16.7	16.7	16.7	16.7	16.2	15.9	16.0	16.3	16.3
Aug	6.8	6.8	6.9	6.9	7.0	7.0	6.4	6.2	6.3	6.6	6.6
Sep	-26.5	-26.4	-26.4	-26.4	-26.3	-26.3	-26.9	-27.0	-26.9	-26.5	-26.6
Oct	-75.5	-75.3	-75.5	-75.4	-75.3	-75.2	-76.1	-76.2	-76.0	-75.4	-75.5
Nov	-150.9	-150.5	-150.9	-150.8	-150.6	-150.5	-151.5	-151.5	-151.4	-150.6	-150.6
Dec	-230.3	-229.7	-230.3	-230.2	-229.9	-229.6	-231.0	-230.9	-230.8	-229.7	-229.8

Table A. 102: Beijing monthly accumulated total heat gains (positive values) and losses (negative values) (kWh·m^{-2}).

	RC1	RC2	M5	M6	M7	M8	A	AS2.2	AS_2.3	V_1.1	V_1.2
Jan	-298.3	-354.1	-296.8	-307.9	-335.9	-355.5	-231.5	-241.9	-250.7	-350.7	-341.7
Feb	-233.0	-278.5	-233.8	-243.4	-266.3	-282.2	-171.8	-174.9	-184.4	-270.7	-263.3
Mar	-208.9	-247.9	-213.7	-222.8	-242.1	-255.4	-145.1	-139.6	-151.6	-233.1	-226.7
Apr	-117.3	-142.5	-125.4	-132.6	-145.0	-152.8	-60.6	-45.8	-58.8	-121.7	-117.4
May	-55.8	-72.3	-68.6	-75.3	-82.6	-85.6	0.8	22.2	7.3	-45.6	-42.5
Jun	-17.5	-26.2	-29.8	-35.0	-38.9	-38.9	29.0	50.9	37.6	-0.8	1.1
Jul	7.6	4.8	-3.2	-6.7	-8.5	-6.8	44.4	67.5	56.0	29.2	29.9
Aug	-5.5	-11.3	-15.5	-19.6	-22.8	-22.3	32.5	53.1	41.9	11.4	12.6

Sep	-48.9	-63.8	-56.6	-62.0	-69.6	-73.1	-6.7	7.1	-3.4	-45.9	-43.2
Oct	-117.6	-148.6	-123.7	-132.1	-146.7	-155.8	-63.9	-61.0	-71.4	-136.6	-131.1
Nov	-200.6	-242.3	-200.5	-209.4	-230.6	-245.2	-147.0	-151.8	-159.7	-237.1	-230.3
Dec	-291.1	-343.5	-288.2	-298.5	-325.4	-344.3	-230.4	-240.8	-248.3	-341.5	-333.0